ADVANCED STEEL CONSTRUCTION

An International Journal

Volume 19 Number 2

June 2023

CONTENTS

Technical Papers

Website: *http://www.hkisc.org*
ISSN 1816-112X
Science Citation Index Expanded, Materials Science Citation Index and ISI Alerting
Cover: URIS Hall in Cornell University, Weathering Steel Building, Photo @ Dr. LIU Yao-Peng
e-copy of IJASC is free to download at "www.ascjournal.com" in internet and mobile apps.

ADVANCED STEEL CONSTRUCTION

VOL.19, NO.2 (2023)

ADVANCED STEEL CONSTRUCTION

an International Journal

ISSN 1816-112X

Volume 19 Number 2 *June 2023*

ISSN 1816-112X

Science Citation Index Expanded, Materials Science Citation Index and ISI Alerting

Advanced Steel Construction
an international journal

Cover: URIS Hall in Cornell University, Weathering Steel Building, Photo @ Dr. LIU Yao-Peng
e-copy of IJASC is free to download at "www.ascjournal.com" in internet and mobile apps.

General Information
Advanced Steel Construction, an international journal

Aims and scope

The International Journal of Advanced Steel Construction provides a platform for the publication and rapid dissemination of original and up-to-date research and technological developments in steel construction, design and analysis. Scope of research papers published in this journal includes but is not limited to theoretical and experimental research on elements, assemblages, systems, material, design philosophy and codification, standards, fabrication, projects of innovative nature and computer techniques. The journal is specifically tailored to channel the exchange of technological know-how between researchers and practitioners. Contributions from all aspects related to the recent developments of advanced steel construction are welcome.

Subscription inquiries and change of address. Address all subscription inquiries and correspondence to Member Records, IJASC. Notify an address change as soon as possible. All communications should include both old and new addresses with zip codes and be accompanied by a mailing label from a recent issue. Allow six weeks for all changes to become effective.

The Hong Kong Institute of Steel Construction
HKISC
c/o Department of Civil and Environmental Engineering,
The Hong Kong Polytechnic University,
Hunghom, Kowloon, Hong Kong, China.
Tel: 852- 2766 6047 Fax: 852- 2334 6389
Email: *ceslchan@polyu.edu.hk* Website: *http://www.hkisc.org/*
ISSN 1816-112X
Science Citation Index Expanded, Materials Science Citation Index and ISI Alerting

ISSN 1816-112X

Science Citation Index Expanded, Materials Science Citation Index and ISI Alerting

Advanced Steel Construction
an international journal

VOLUME 19 NUMBER 2 June 2023

Technical Papers

Advanced Steel Construction – Vol. 19 No. 2 (2023) 91–101
DOI:10.18057/IJASC.2023.19.2.1

EXPERIMENTAL STUDY ON CYCLIC BEHAVIOR OF BLIND-BOLT JOINT CONNECTING STEEL BEAM AND RECTANGULAR TUBE COLUMN

Guo-Qiang Li [1, 2], Yun-Han Jiang [1], Yuan-Zuo Wang [3, 4, *] and Chen Chen [1]

[1] *College of Civil Engineering, Tongji University, Shanghai, China*
[2] *National Key Lab for Disaster Reduction in Civil Engineering, Tongji University, Shanghai, China*
[3] *Key Laboratory of Urban Security and Disaster Engineering of Ministry of Education, Beijing University of Technology, Beijing, China*
[4] *Faculty of Engineering, Hokkaido University, Hokkaido, Sapporo, Japan*
** (Corresponding author: E-mail: yzwang@bjut.edu.cn)*

ABSTRACT

An experimental investigation on the cyclic behavior of the joints for steel H-shaped beams to steel rectangular tube columns using end-plate and blind bolts is conducted in this paper. The load-bearing capacity, rotation stiffness and hysteretic behavior of the joints are studied. In terms of the types of beams (pure steel beam and composite steel beam with concrete slab) and columns (pure steel rectangular tube column and concrete-filled steel rectangular tube column), a total of four different joints are tested and compared. It is found that filling concrete in rectangular tube columns can avoid the failure mode of column tube wall yielding under bending moment. Furthermore, due to the contribution of the concrete slab, the bending capacity and initial rotational stiffness of the composite steel beam-to-column joint are significantly greater than those of the pure steel beam-to-column joint under sagging or hogging moments. Under most circumstances, the joints demonstrate excellent ductility with the interstory displacement angle greater than 0.04 rad, which satisfies the requirement for resisting severe earthquakes.

ARTICLE HISTORY

Received: 20 September 2022
Revised: 16 January 2023
Accepted: 20 January 2023

KEYWORDS

Blind bolt;
Beam-to-column joint;
H-shaped beam;
Rectangular tube column;
Concrete-filled tube column;
Cyclic behavior

1. Introduction

Compared with the H-shaped column, the steel tube column with rectangular hollow section (RHS) exhibits more excellent static and seismic properties including higher strength and stiffness owing to its closed and symmetric cross-section. Previous research has shown that steel frame systems using RHS columns were usually able to not only reduce steel consumption but also improve space utilization[1]. The strength and ductility of the beam-to-column joints are critical for the application of such steel tube columns.

The most widely used method for connecting H-shaped beams to RHS columns is full welding, as illustrated in Fig. 1. Although the fully welded steel beam-to-RHS column connection possesses high bearing capacity and stiffness, it is easily fractured as observed in the 1994 Northbridge earthquake and the 1995 Kobe earthquake (Fig. 2)[2, 3]. Moreover, due to high technical requirements and slow speed in the construction of the welded joints, the full welding method no longer fulfils the requirements of assembly construction of steel structure buildings.

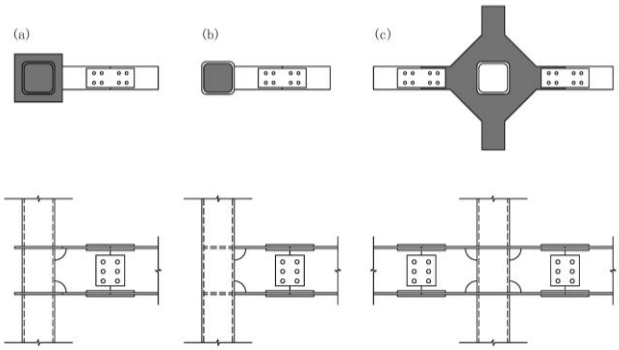

(a) through-diaphragm; (b) interior diaphragm; (c) exterior diaphragm.

Fig. 1 Typical steel beam-to-RHS column fully welded connections

(a) Northbridge earthquake[2]

(b) Kobe earthquake[3]

Fig. 2 Failure of the steel beam-to-column fully welded connections

Motivated by these incidents, bolted joints with end-plates are increasingly used to connect steel beams to columns, as shown in Fig. 3. The fracture failure of the fully welded connection can be prevented. In addition, these joints can be much more efficiently erected than those fully welded. Nevertheless, it is hard to connect H-shaped beams and RHS columns with traditional high strength bolts, which needs operation at both sides of the connected elements.

Fig. 3 Typical steel beam-to-column fully bolted connection

To solve this problem, specific blind bolts, such as Hollo-Bolt[4] and similar self-locking bolts[5, 6], as shown in Fig. 4, being able to be operated at only one side of the connected element, are proposed to replace the traditional high strength bolts. With such blind bolts, the steel beam-to-RHS column fully bolted connections can be efficiently achieved on site, as shown in Fig. 5.

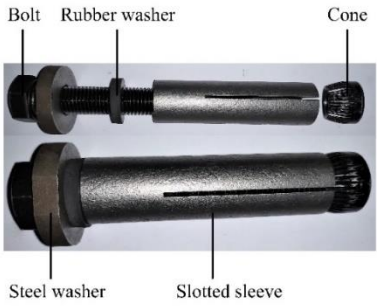

Fig. 4 Blind Bolts

Fig. 5 Steel beam-to-RHS column fully bolted connection

The joints between H-shaped steel beams and rectangular steel tubular columns using blind bolts have been extensively studied by a number of researchers that respectively analyzed the beam-to-column joints with HSBB[7, 8], Flowdrill blind bolts[9, 10], RMH blind bolts[11, 12], Hollo-bolt[13, 14] and ONESIDE Fastener blind bolts[15, 16]. These studies show that the thickness of the tube wall is an essential factor for the failure modes of the joints and the stiffness of these joints is less than those using normal high strength bolts.

In respect of filling concrete in the columns, Wang et al.[17-26] conducted static and seismic experimental investigations into H-shaped beam-to-RHS concrete-filled column end-plate connections by means of Hollo-Bolts, and Li et al.[27] completed the seismic performance tests of eight RHS concrete-filled columns and H-shaped steel beam joints connected by slip-critical blind bolts. These studies show that concrete-filled steel tubular column joints have higher initial rotational stiffness, load-bearing capacity and excellent energy dissipation capacity. Considering the effect of concrete slabs, Wang et al.[19-21] and Jiao et al.[28] studied the H-shaped steel beam with concrete floor slab and rectangular steel tube column joints using Hollo-Bolts and slip-critical blind bolts, respectively. It was found that the stiffness and bending capacity of the composite beam joints with concrete slabs are significantly increased, and the hysteretic performance of the joints was also improved.

However, in the previous studies, the failure of the beam-to-column joints with blind bolts under bending usually occurs in the joint core. This failure mode will make the wall of the rectangular steel tube column yield or even deflect out-of-plane. Unfortunately, this kind of joint failure is highly unfavorable to the vertical load-bearing capacity of the columns. To mitigate the damage of the joint zone in the columns, an end-plate yielding failure mode is introduced at the joints of steel beams to rectangular hollow section columns in this paper. Through proper design of the thickness and size of the end-plate, the yielding of the end-plate will first develop, which limits the action from the beam end to the beam-to-column joint and mitigates the damage within the joint zone of the steel rectangular tube column with blind bolts.

In this study, four different types of steel beam-to-rectangular hollow section column joints with blind bolts and end-plate yielding first are designed and experimentally studied. The effects of the steel beam with or without the composite concrete slab and rectangular steel tube column with or without infill concrete on the behavior of the beam-to-column joints under cyclic bending moments are investigated. The test results are summarized and may be used as a design guide for its application in practice.

2. Experimental program

2.1. Specimen preparation

The research objective is to identify the behavior of joints of steel beams to steel rectangular tube columns connected by blind bolts with flush end-plates. Four blind bolted flush end-plate joints to connect steel I-beams ($h \times b \times l \times t_w$ = 300×150×12×12 mm) with square CFST columns (side length = 200 mm and thickness = 12 mm) are designed. The thickness of the end-plate is 6 mm, making the end-plate the weakest element of the joint compared with the column tube wall and the blind bolts under bending due to gravity or earthquakes. In terms of the types of beams (pure steel beam and composite steel beam with concrete slab) and columns (pure steel tube columns and steel tube concrete-filled columns with rectangular section), a total of four different combinations of joints are prepared, as shown in Table 1 and Fig. 6. In Table 1, the first letter of the specimen label T represents the rectangular steel tube column and C represents the rectangular concrete-filled steel tube column. The second letter of the specimen label B represents the pure steel beam and C represents the full shear connection composite beam.

Table 1
Summary of joint specimens

Specimens	Column type	Beam type
TB	steel tube column	pure steel beam
TC	steel tube column	composite beam
CB	concrete-filled steel tube column	pure steel beam
CC	concrete-filled steel tube column	composite beam

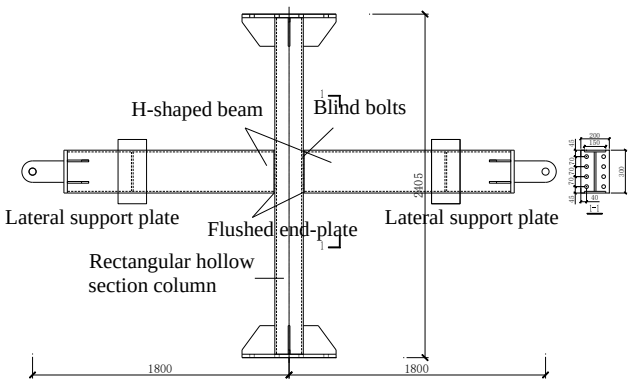

(a) Specimen TB

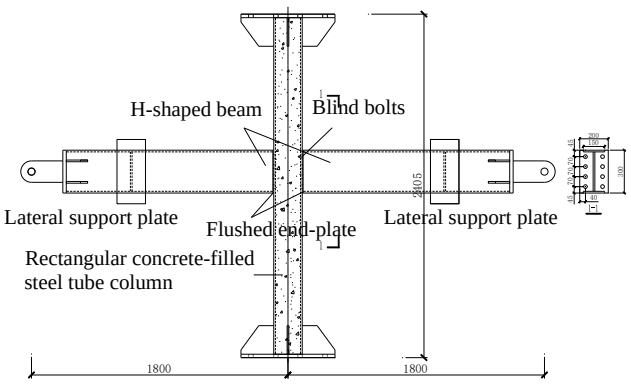

(b) Specimen CB

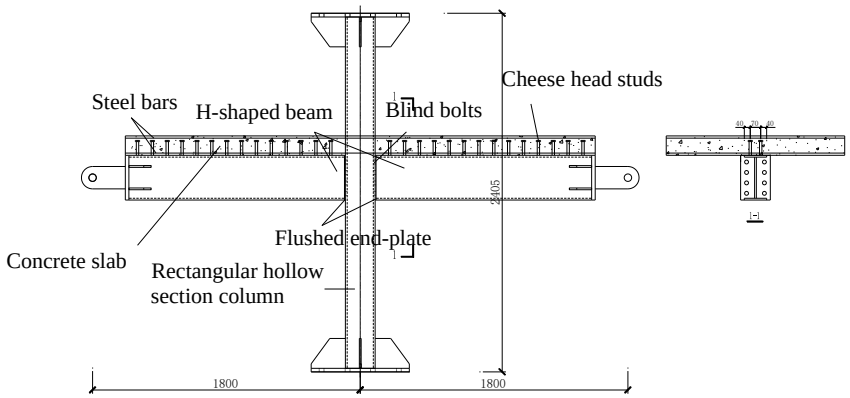

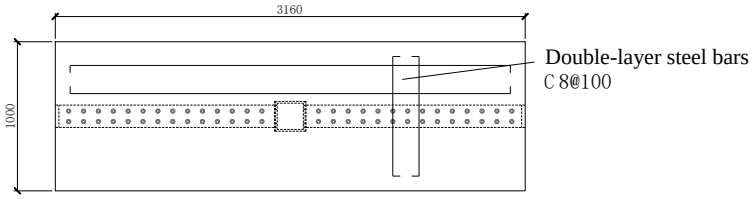

(c) Specimen TC

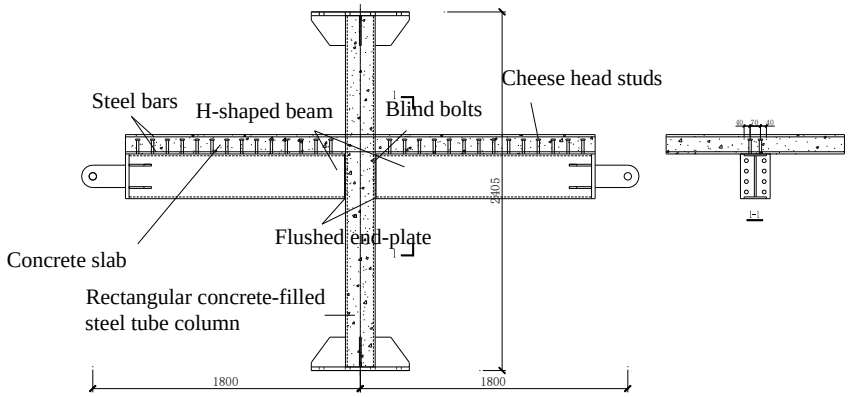

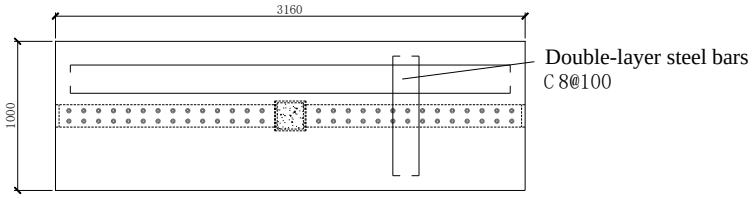

(d) Specimen CC

Fig. 6 Details of joint specimens (unit: mm)

2.2. Material properties

According to Chinese specification GB/T 228-2002[29], the mechanical properties of structural steels (elastic modulus E_s, yield strength f_y, ultimate strength f_u and elongation at fracture δ) used in the specimens are tested and summarized in Table 2. The concrete is prepared to achieve a nominal cubic strength of 40 MPa at 28 days. The mix proportion of concrete is water: cement: sand: aggregate = 0.54: 1.00: 1.30: 2.60. At the time of testing, the cubic strength and modulus of elasticity of concrete were 43.35 MPa and 35670 MPa, respectively. The reinforcement used in the test is HRB400 with a diameter of 8mm and a tensile strength of 592.49 MPa. The 8.8-NBB16 blind bolts are used in the test, and their tensile bearing capacity, shear bearing capacity and tensile stiffness are summarized in Table 3.

Table 2
Mechanical properties of structural steels

Thickness (mm)	Yield strength f_y (MPa)	Tensile strength f_u (MPa)	Elastic modulus E (GPa)	Elongation Δ (%)
6	345.72	501.36	204.82	33.66
12	387.60	520.02	194.52	37.08
25	396.04	503.94	211.02	43.36

Table 3
Mechanical properties of bolt

Bolt	Tensile bearing capacity (kN)	Shear bearing capacity (kN)	Tensile stiffness (kN/mm)
8.8-NBB16	161.13	278.89	131.98

2.3. Test setup

The test setup is shown in Fig. 7. The universal ball hinges are adopted at the top and bottom of the column of the specimens to simulate the zero moment condition at the point of contraflexure. An oil pressure actuator with 1000 kN loading capacity is used to apply the axial pressure at the top of the column, and the horizontal support is set between the column top steel base and the reaction frame to bear the horizontal reaction force from the column top. The beam end is hinged with the actuator, and the vertical load is applied at the beam end through the actuator with 500 kN loading capacity. For pure steel beam joints, the lateral support plates are welded on both sides of the steel beam, and the lateral support with rollers is arranged to restrict the out-of-plane displacement of the specimen during loading. For composite beam joints, the reaction frame is leaning against the side wall of the floor slab, which also limits the out-of-

plane displacement of the specimen.

(a) Test setup for specimens TB and CB

(b) Test setup for specimens TC and CC

Fig. 7 Test setup

The loading process is divided into three stages: (1) The pre-load with ±1mm displacement in the horizontal direction is applied to ensure that acquisition equipment works properly. (2) The actuator is used to apply the axial pressure to the square steel pipe column to the predetermined value (axial compression ratio = 0.15) and keep it constant throughout the test. (3) Finally, the vertical load is applied at two ends of the beam through the actuator. In the cyclic loading process, a lateral cyclic load is applied at the beam end, and the loading protocol is determined according to AISC 341-10[30], as plotted in Fig. 8.

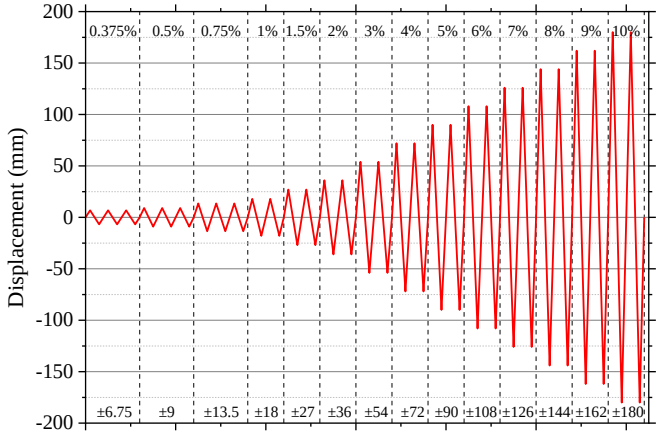

Fig. 8 Loading protocol

2.4. Measurements

To measure the local strains and displacements of joints, 79 strain gauges and 10 LVDTs are placed at critical locations of the beam, tube end plates and slab, as shown in Fig. 9.

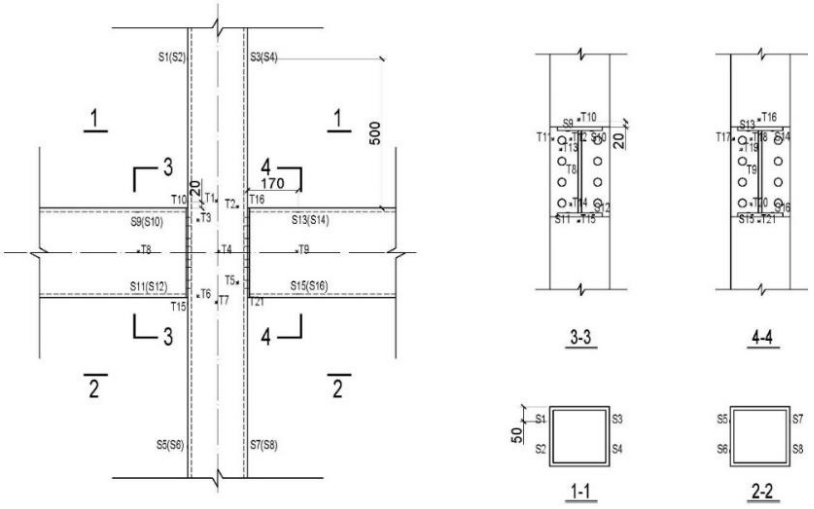

(a) Strain gauges for specimens TB and CB

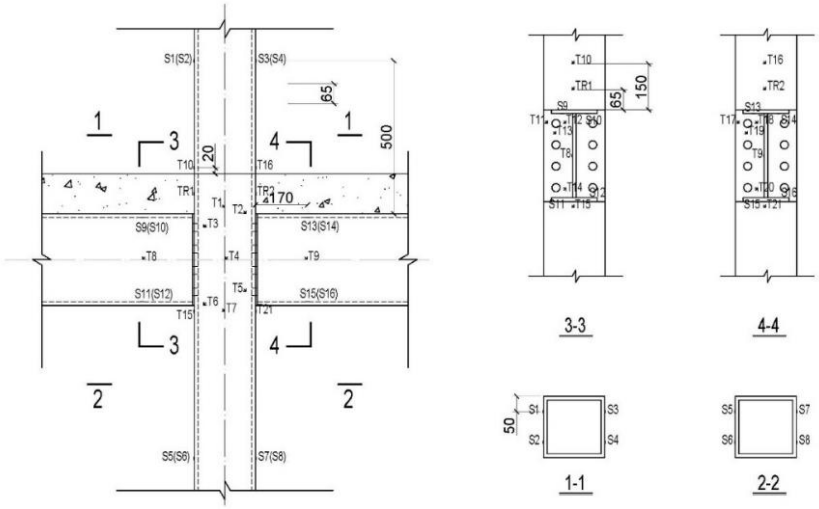

(b) Strain gauges for specimens TC and CC

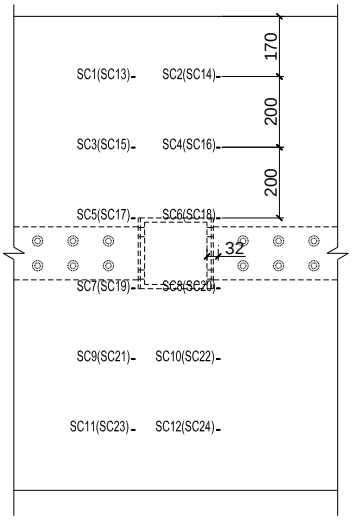

(c) Strain gauges for concrete slab

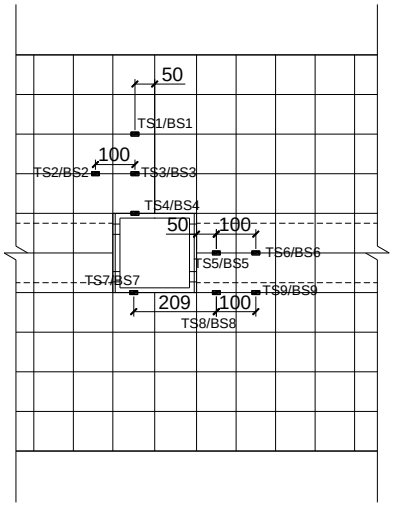

(d) Strain gauges for steel bars

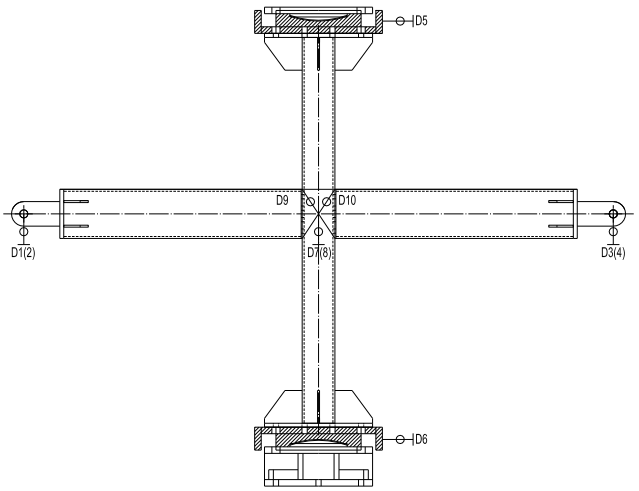

(e) LVDTs

Fig. 9 Arrangement of LVDTs and strain gauges (unit: mm)

In this test, the vertical displacement of the beam end is the key measurement object. The following five types of deformation shown in Fig. 10 can cause vertical deformations of the beam end. Only type (5) is the characteristic deformation of the joints itself, so the vertical displacement measured based on the beam end displacement meter needs to be deducted from the previous four types.

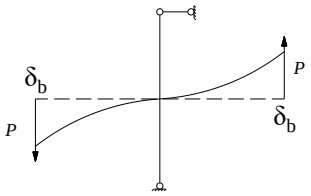

(1) Bending of beam

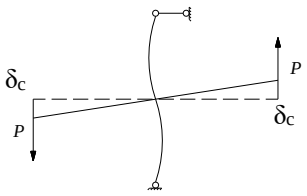

(2) Bending of column

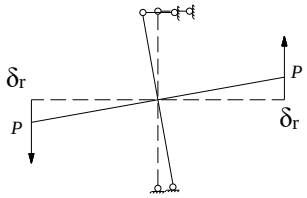

(3) Rigid body rotation

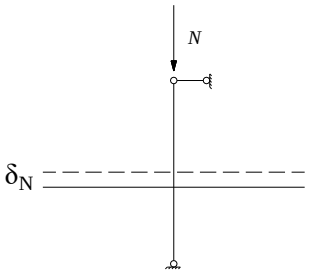

(4) Axial deformation of column

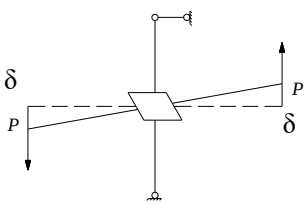

(5) Deformation of panel zone

Fig. 10 Deformation of beam-column joint

3. Test results

3.1. Typical phenomena

Typical phenomena that occurred during the tests on four joints are shown in Table 4 and Fig. 11. The story drift angles of each joint specimen corresponding to the above phenomena are summarized in Table 5.

Table 4
Typical phenomena of the joints in tests

ID	Phenomenon
A	The end-plate starts to yield
B	The column wall starts to yield
C	The first crack in the slab develops
D	A large number of floor cracks occur
E	The cracks penetrate between the upper and lower flanges of the slab
F	The floor concrete is crushed and hunched up
G	Falling of concrete block of the floor slab occurs
H	Exposed rebars in floor slab are observed
I	The topmost blind bolt loses pre-tension
J	The plasticity of blind bolt is deepened
K	Bending deformation of end-plate occurs
L	A crack on end-plate is observed
M	The crack penetrates in the thickness direction of the end plate
N	The end-plate and steel beam flange are completely torn at the crack
O	The end-plate crack develops vertically along the web of the steel beam
P	The column wall is inwardly concave and outwardly bulging

Table 5
Story drift angles corresponding to the phenomena listed in Table 4

Story drift ratio	Specimens			
	TB	TC	CB	CC
0.375%		B, C		
0.5%	A	A	A	A, B
0.75%				C
1%				
1.5%		D		
2%		B, J		
3%	J, K	G	K	
4%		L	L	F, G, I
5%	L	M, P		D, K
6%	M	F, H	M, N	E, L, H
7%		O	J	M, O
8%				
9%				
10%	N, O		O	

(a) Cracks penetrate between the upper and lower flanges of the slab

(b) The floor concrete is crushed and hunched up

(c) Falling of concrete block of floor slab

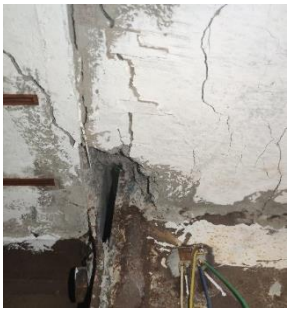

(d) Exposed rebars in floor slab

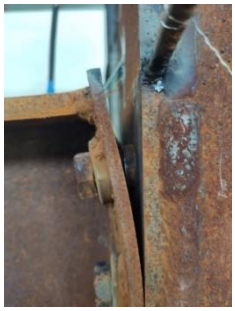

(e) Blind bolt loses pre-tension

(f) The plasticity of blind bolt is deepened

(g) Bending deformation of end plate

(h) Crack on end plate

(i) The crack penetrates in the thickness direction of the end plate

(j) The end-plate and steel beam flange are completely torn at the crack

(k) The end-plate crack develops vertically along the web of the steel beam

(l) The column wall is inwardly concave and outwardly bulging

Fig. 11 Typical phenomena of the joints in tests

3.2. Failure modes

The failure mode of the four joint specimens is the yield of the end-plate followed by fracture. When the interstory displacement angle reaches 4%, the cracks begin to appear on the end-plate of the four joints, then the crack extends to the penetration along the thickness direction of the end-plate and extends to the web of the H-shaped steel beam along the width direction of the end-plate, resulting in the tearing of the H-shaped steel beam from the end-plate. Finally, the bending moment cannot be transmitted from the H-shaped steel beam to the joint, resulting in failure. In order to avoid the joint failure mode in which the column wall is damaged before the beam end, which is highly unfavorable to the vertical bearing capacity of the column, the joint specimens in this paper are all designed to fail by end-plate yielding.

For composite beam joints with concrete floor (joint TC and CC), the floor slab cracks in tension and collapses in compression. In addition, due to the combined action of floor slabs, the column walls yield in these two joints. In particular, the column wall flange of joint TC is squeezed by the steel beam flange in the later stage of loading, resulting in obvious inward deflection and the column wall web buckling. On the contrary, the column walls of the other two joints remain elastic during loading.

The blind bolts of the four joint specimens were not fractured during the loading process. The H-shaped steel beam remained elastic, and no local buckling was found.

In summary, the failure modes of the four test specimens in the test can be divided into two types: end-plate fracture (TB and CB as shown in Fig. 11(h)-(k)), and a mixed mode of end-plate fracture, cracking and crushing of concrete slab and column wall yielding (TC and CC as shown in Fig. 11(a)-(d) and (h)-(l)).

3.3. Moment-Rotation curves

The bending moment M_0, right side and left side rotation angles θ_e and θ_w of the joints are calculated according to Eq. (1)-(5), where P is the load at the beam end; l_x=1694 mm is the distance between the loading point at the beam end and the outer edge of the end plate; δ_e and δ_w are respectively the beam end displacements caused by the deformation of the right side and left side joints; δ_1-δ_4 are respectively the readings of LVDTs D1-D4; and δ_b, δ_c, δ_r and δ_N are the vertical deformation of the beam end caused by various factors as shown in Fig. 10.

$$M_0 = Pl_x \tag{1}$$

$$\theta_e = \frac{\delta_e}{l_x} \tag{2}$$

$$\theta_w = \frac{\delta_w}{l_x} \tag{3}$$

$$\delta_e = \frac{1}{2}(\delta_1 + \delta_2) - \delta_b - \delta_c - \delta_r + \delta_N \tag{4}$$

$$\delta_w = \frac{1}{2}(\delta_3 + \delta_4) - \delta_b + \delta_c + \delta_r + \delta_N \tag{5}$$

The bending moment against rotation angle are plotted in Fig. 12. The bending moment-rotation curves of the four joints have the following characteristics:

(1) Since the sleeve part of the blind bolt has entered plasticity after installation, the hysteretic curve of the joint presents nonlinear characteristics from the beginning of loading.

(2) The bending capacity of the second circle of each load stage of the joint decreases to a certain extent compared with that of the first circle and increases with the increase of the interstory displacement angle. The reasons are as follows: with the increase of the interstory displacement angle, the plasticity of the blind bolt, especially the sleeve component, is significantly deepened. When the interstory displacement angle of a particular stage is loaded reversely, the blind bolt can no longer fit the end plate and return to its original position because it enters plasticity, demonstrating the phenomenon of separation from the end-plate. When the second circle of interstory displacement angle is positively loaded, the end-plate cannot make contact with the blind bolt properly within a specific range, resulting in the reduction of the second circle of flexural bearing capacity.

(3) The joint shows that the slope of the curve is considerably low in the middle range of each stage of loading, but the slope increases sharply at both ends. As a result, the hysteretic curve of each joint shows an inverted Z shape.

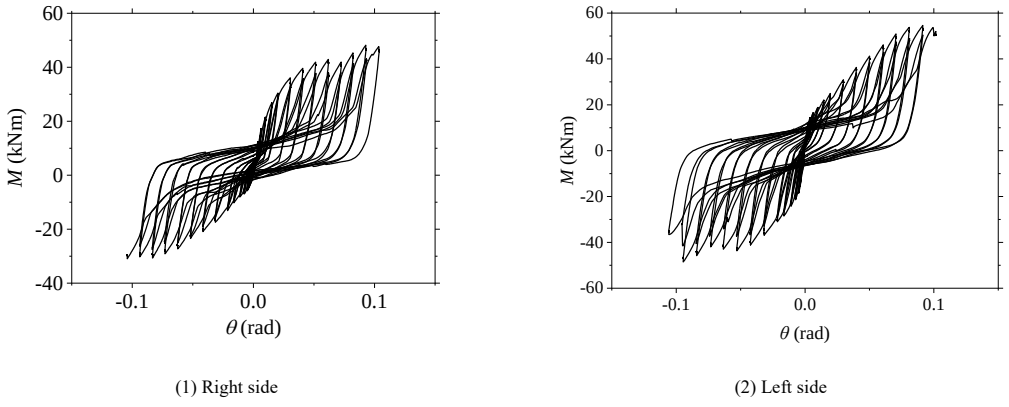

(1) Right side (2) Left side

(a) TB

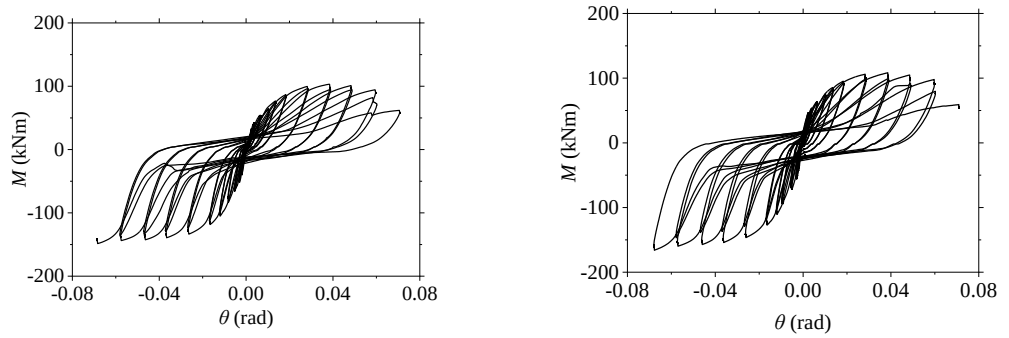

(1) Right side (2) Left side

(b) TC

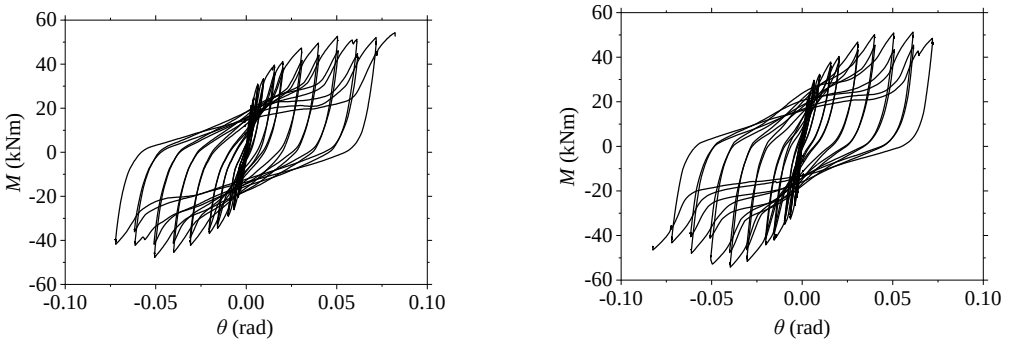

(1) Right side (2) Left side

(c) CB

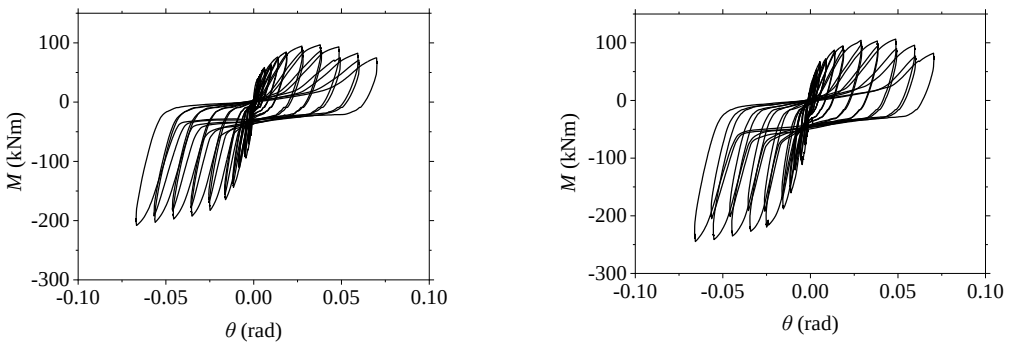

(1) Right side (2) Left side

(d) CC

Fig. 12 Moment – rotation hysteretic curves

4. Discussion

4.1. Skeleton curve and bending capacity

The skeleton curves of 4 joints are summarized as shown in Fig. 13. It can be seen from the skeleton curve of the joint that the bending moment of the pure steel joint and the full shear composite joint increases with the rotation angle until the end plate is torn, reducing the bearing capacity of the joint.

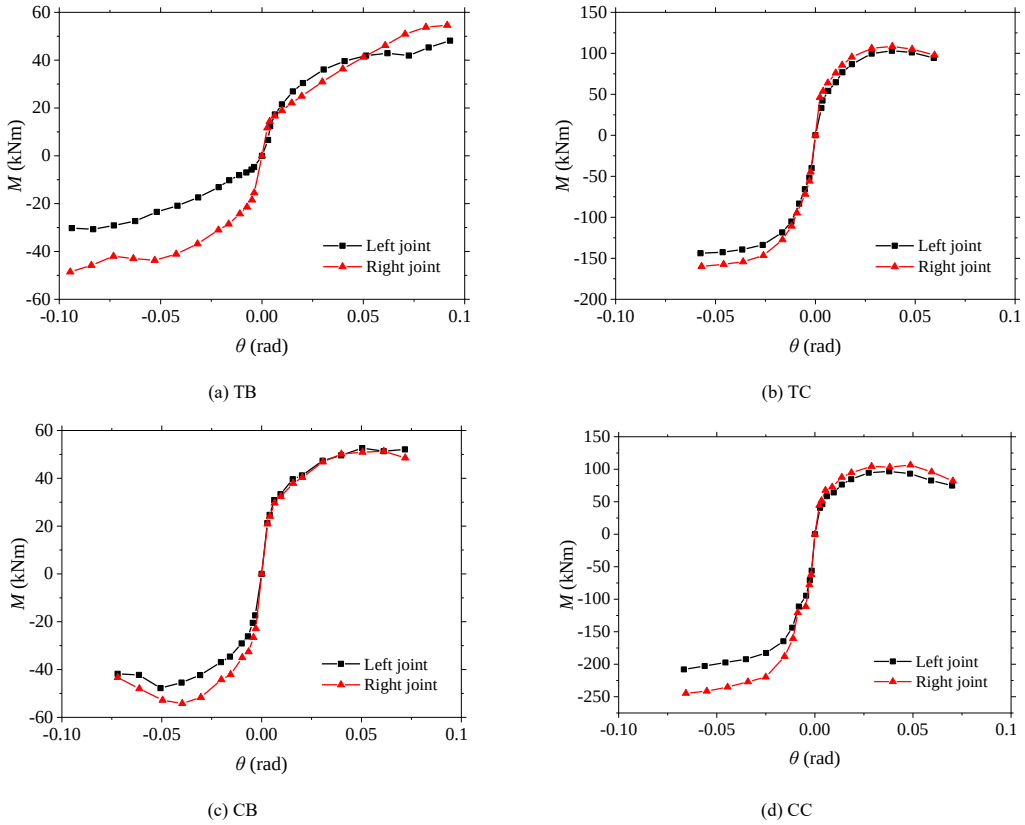

Fig. 13 Skeleton curves

According to the skeleton curve of each joint obtained, the maximum bending moments in the skeleton curve are taken as the bending capacities of the joints under the action of positive and negative bending moments. See Table 6 for the summary.

Considering that not all parts of the specimen reach their failure modes during loading, the maximum bending moment is not the ultimate bending capacity of the joint. Therefore, for each joint, the maximum values under the positive and negative bending moments are taken as its bending capacities as shown in Table 7. According to Eurocode 3[31], TC and CC are partial-strength joints, and TB and CB are hinge joints with negligible moment resistance.

Table 6
Bending capacity of each joint specimen in tests

Specimen	Right side		Left side	
	Sagging moment (kN·m)	Hogging moment (kN·m)	Sagging moment (kN·m)	Hogging moment (kN·m)
TB	48.16	30.70	54.61	48.57
TC	103.13	143.82	108.48	159.86
CB	52.65	47.77	51.29	54.21
CC	96.68	207.99	106.48	244.75

Table 7
Test value of bending capacities of joints

Specimen	Bending capacity (kN·m)	
	Sagging bending	Hogging bending
TB	54.61	48.57
TC	108.48	159.86
CB	52.65	54.21
CC	106.48	244.75

4.2. Initial rotational stiffness

For four joints in this test, the initial rotational stiffness under the action of positive and negative bending moments is different, so the initial rotational stiffness is calculated for the action of positive bending moment and negative bending moment, respectively.

Taking the load F_1 and displacement X_1 corresponding to the peak point of the bending moment angle curve after the first level interstory displacement angle loading is completed (0.375%), and the initial rotational stiffness of the joint is calculated according to Eq. (6)[31]. The summary is shown in Table 8.

$$K_1 = \frac{|F_1|}{|X_1|} \tag{6}$$

Table 8
Initial rotational stiffness of each joint specimen in tests

Specimen	Initial rotational stiffness (kN·m /rad)			
	Right side		Left side	
	Sagging bending	Hogging bending	Sagging bending	Hogging bending
TB	2198	1201	4395	4076
TC	11130	21176	20409	19006
CB	7362	5418	7005	7858
CC	15087	34829	19405	33517

Referring to the method defining the bending capacity of the joints, the maximum value of the initial rotational stiffness of each type of joints obtained by the test is also calculated, as summarized in Table 9.

Table 9
Test value of initial rotational stiffness of joints

Specimen	Initial rotational stiffness (kN·m/rad)	
	Sagging bending	Hogging bending
TB	4395	4076
TC	20409	21176
CB	7362	7858
CC	19405	34829

In this test, the loading mode of the joint is beam loading, which belongs to a non-sway frame. According to the formula of Eurocode 3[31], the stiffness of the hinge connection K_p is 2738 kN·m/rad and the stiffness of the rigid connection K_r is 43817 kN·m/rad, which can be respectively calculated by Eqs. (7) and (8), where E is the elastic modulus of steel; I_b is the second moment of inertia of the steel beam around the principal major axis and L_{b0} is the span of the steel beam.

$$K_p = \frac{0.5EI_b}{L_{b0}} \tag{7}$$

$$K_r = \frac{8EI_b}{L_{b0}} \tag{8}$$

According to the classification method by initial rotational stiffness in Eurocode 3[31], the four joints in this test are semi-rigid joints.

4.3. Ductility

The ductility coefficient of the joint is calculated according to Specification for seismic test of buildings (JGJ/T 101-2015)[32] given by

$$\mu = \frac{\theta_u}{\theta_y} \tag{9}$$

where θ_u and θ_y are respectively the ultimate deformation and yield deformation.

The definition of ultimate deformation and yield deformation of the joint is presented in Fig. 14[32]. The curve is the skeleton curve of each joint under positive and negative bending moments. The abscissa corresponding to the intersection of the straight line with the slope of the origin as the initial rotational stiffness and the horizontal line with the value of the ultimate bending moment is taken as the yield deformation of the test specimen. The abscissa corresponding to the curve point to which the bending moment of the test specimen is reduced is taken as the ultimate deformation of the test specimen. If the test specimen is not loaded to failure, the rotation angle at the loading stop time is taken as the ultimate deformation. The M_u represents the maximum bending moment obtained from moment-rotation curve. According to Specification for seismic test of buildings (JGJ/T 101-2015)[32], the rotation corresponding to bending moment equals to $0.85\times M_u$ is defined as the ultimate deformation in the present study. The yield displacement, ultimate displacement and ductility coefficient of each joint under the action of positive and negative bending moments are calculated and summarized in Table 10 and Table 11.

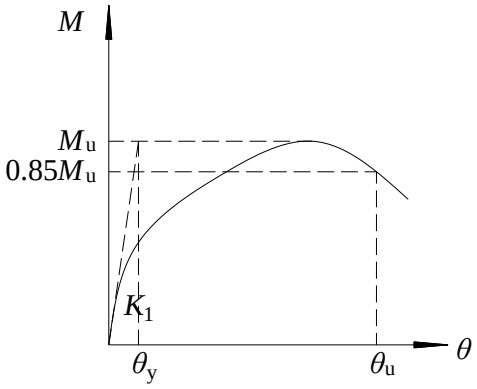

Fig. 14 Calculation method of ultimate deformation and yield deformation of joints[32]

Table 10
Ductility coefficient of each joint specimen (Right Side)

Specimen	Sagging bending			Hogging bending		
	θ_y (mrad)	θ_u (mrad)	μ	θ_y (mrad)	θ_u (mrad)	μ
TB	21.91	92.80	4.24	25.56	93.81	3.67
TC	9.27	38.33	4.14	6.79	57.52	8.47
CB	7.15	50.39	7.05	8.82	50.60	5.74
CC	6.41	37.92	5.92	5.97	66.77	11.18

Table 11
Ductility coefficient of each joint specimen (Left Side)

Specimen	Sagging bending			Hogging bending		
	θ_y (mrad)	θ_u (mrad)	μ	θ_y (mrad)	θ_u (mrad)	μ
TB	12.43	91.39	7.35	11.91	94.55	7.94
TC	5.32	38.55	7.25	8.41	56.98	6.77
CB	7.32	61.17	8.35	6.90	39.73	5.76
CC	5.49	48.71	8.88	7.30	65.70	9.00

It can be concluded that:

(1) The negative bending ductility of full shear composite joints is better than the positive bending ductility.

(2) The ductility coefficient of the rectangular steel tube column joint is close to that of the rectangular concrete-filled steel tube column joint, indicating that the type of column has a negligible effect on the ductility coefficient of the joint.

(3) American seismic code for steel structures (AISC 341-10)[30] stipulates that when the moment bearing capacity of the joint against earthquake drops to 80%, the interstory displacement angle shall not be less than 0.04 rad. Except for the composite steel beam-to-column joint, all other types of joints demonstrate excellent ductility with the interstory displacement angle greater than 0.04 rad, which meets the requirement for resisting severe earthquakes.

4.4. Influence of different structures on joint performance

The influences of the types of columns and beams on hysteretic behavior of joints are studied in this section. The skeleton curves of four joints are plotted in Fig. 15. It is observed that both the moment bearing capacity and initial rotational stiffness of composite steel beam joints with concrete slab are much higher than those of pure steel beam joints, whether the rectangular steel tube column is filled with concrete.

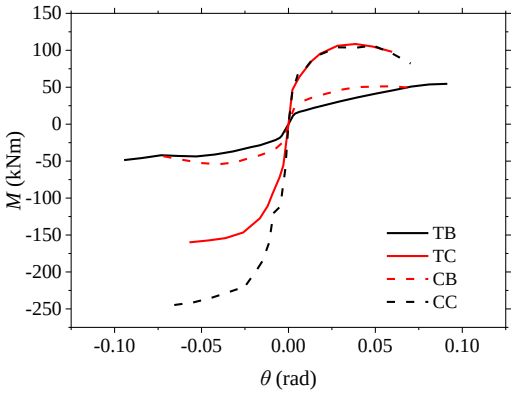

Fig. 15 Comparison of skeleton curves among four joints

For pure steel beam joints (TB and CB), it is observed that (1) The moment bearing capacities of these two joints are close. (2) The initial rotational stiffness of the joint with concrete in the column (CB) is slightly larger than that of the joint without concrete in the column (TB). It is because the failures of these two joints are both end-plate fracture. Therefore, whether concrete is in the column has negligible influence on moment bearing capacity and initial rotational stiffness.

For composite beam joints (TC and CC), it is observed that (1) The positive moment bearing capacity and positive initial rotational stiffness of these two joints are the same. (2) The negative moment bearing capacity and negative initial rotational stiffness of the joint with concrete in the column (CC) are both larger than those without concrete in the column (TC). The reasons are as follows: Under the positive bending moment, the concrete floor bears compression and the blind bolts bear tension. Therefore, whether concrete is in the column has negligible influence on the moment bearing capacity and initial rotational stiffness. However, under the negative bending moment, the reinforcements in the concrete plate bear tension and the column bears compression. Without concrete in the column, the column wall deforms significantly and enters into plasticity. On the contrary, the compression is transmitted to the concrete in the column through the column wall. Thus, the moment bearing capacity is greatly improved.

5. Conclusion

Based on the experimental investigation on the cyclic behavior of the joints for steel H-shaped beam to steel rectangular tube column connected by blind bolts with end-plate, the following conclusions can be drawn:

(1) With appropriate design, the failure mode of all the joint specimens is yielding of end-plate, which is beneficial to limit the action at the beam end transferred to the column and mitigate the failure of the column zone in the beam-to-column joint leading more severe damages to structures. The fracture will not happen on the end plate if the story-drift ratio is less than 4%.

(2) For composite beam joints, concrete in the joint core was cracked and crushed. As a result, the column wall yielded or even inwardly deflected due to its combined effect, which is not observed in pure steel beam joints.

(3) All the types of joints in this study can be classified as semi-rigid according to the criteria given in Eurocode 3. However, due to the contribution of the concrete slab, the bending capacity and initial rotational stiffness of the entire composite joints are significantly greater than those of the pure steel joints, whether under the action of sagging or hogging moments.

(4) Except for the composite beam joint under the action of positive bending moment, all the joints demonstrate excellent ductility with the interstory displacement angle greater than 0.04 rad, which satisfies the requirement for resisting severe earthquakes.

Acknowledgement

The research work presented hereinabove was supported by the National Key Research and Development Program of China (Project No. 2016YFC0701204).

References

[1] Wang HH, Cao FH. Research on Properties for Semi-Rigid Connections of H-Section Beam and RHS Column. Building Science. 2009.
[2] Miller DK. Lessons learned from the Northridge earthquake. ENG STRUCT. 1998.
[3] Tremblay R, Filiatrault A, Bruneau M, Nakashima M, Prion H, Devall R. Seismic design of steel buildings: lessons from the 1995 Hyogo-ken Nanbu earthquake. CAN J CIVIL ENG. 1996;23727-56.
[4] Lindapter International Ltd, Type HB Hollo-bolt for Blind Connection to Structural Steel and Structural Tubes, Lindapter International Ltd., UK, 1995. <http://www.lindapter.com>.
[5] ZHANG, J., Research on mechanical properties of domestic self-lock one-side bolt. 2016, Tongji University: Shanghai, China [in Chinese] [.
[6] JIANG Y, LI G, CHEN C, et al. Experimental study on tensile behavior of blind bolt[J]. ce/papers, 2021,4(2-4): 100-109.
[7] Eldin A. Behaviour of Blind Bolted Moment Connections for Square HSS Columns. Concept Development. 1993.
[8] Korol R M, Ghobarah A, Mourad S. Blind bolting W-shape beams to HSS columns[J]. Journal of Structural Engineering, 1993, 119(12): 3463-3481.
[9] France J E, Davison J B, Kirby P A. Strength and rotational stiffness of simple connections to tubular columns using flowdrill connectors[J]. Journal of Constructional Steel Research, 1999, 50(1):15-34.
[10] France JE, Davison JB, Kirby PA. Moment-capacity and rotational stiffness of endplate connections to concrete-filled tubular columns with flowdrilled connectors. J CONSTR STEEL RES. 1999;5035-48.
[11] Barnett TC, Tizani W, Nethercot DA. The practice of blind bolting connections to structural hollow sections: A review. STEEL COMPOS STRUCT. 2001;11-16.
[12] Barnett T, Tizani W, Nethercot D A. Blind bolted moment resisting connections to structural hollow sections[J]. Connections in steel structures, 2000, 4.
[13] Elghazouli AY, Malaga-Chuquitaype C, Castro JM, Orton AH. Experimental monotonic and cyclic behaviour of blind-bolted angle connections. ENG STRUCT. 2009;312540-53.
[14] Liu Y, Málaga-Chuquitaype C, Elghazouli AY. Response and component characterisation of semi-rigid connections to tubular columns under axial loads. ENG STRUCT. 2012;41510-32.
[15] Lee J, Goldsworthy HM, Gad EF. Blind bolted T-stub connections to unfilled hollow section columns in low rise structures. J CONSTR STEEL RES. 2010;66981-92.
[16] Lee J, Goldsworthy HM, Gad EF. Blind bolted moment connection to sides of hollow section columns. J CONSTR STEEL RES. 2011;671900-11.
[17] Wang J, Zhang N. Performance of circular CFST column to steel beam joints with blind bolts. J CONSTR STEEL RES. 2017;13036-52.
[18] Wang J, Zhang N, Guo S. Experimental and numerical analysis of blind bolted moment joints to CFTST columns. THIN WALL STRUCT. 2016.
[19] Wang J, Zhang H, Jiang Z. Seismic behavior of blind bolted end plate composite joints to CFTST columns. THIN WALL STRUCT. 2016;108256-69.
[20] Wang J, Li B, Wang D, Zhao C. Cyclic testing of steel beam blind bolted to CFST column composite frames with SBTD concrete slabs. ENG STRUCT. 2017.
[21] Guo L, Wang J, Wang W, Duan M. Seismic evaluation and calculation models of CFDST column blind bolted to composite beam joints with partial shear interaction. ENG STRUCT. 2019;196109261-9.
[22] Wang J, Guo L, Guo X, Ding Z. Seismic response investigation on CFDST column to steel beam blind-bolted connections. J CONSTR STEEL RES. 2019;161137-53.
[23] Wang J, Chen L, Han L. Static and Seismic Experiments and Analysis Models of Blind Bolted end Plate Joints to CFT Columns. Shanghai International Conference on Technology of Architecture & Structure2009.
[24] Wang J, Spencer BF. Experimental and analytical behavior of blind bolted moment connections. J CONSTR STEEL RES. 2013;8233-47.
[25] Wang J, Lin Z, Jr B. Seismic response of extended end plate joints to concrete-filled steel tubular columns. ENG STRUCT. 2013;49876-92.
[26] Guo L, Wang J, Wang W, Wang C. Cyclic tests and analyses of extended endplate composite connections to CFDST columns. J CONSTR STEEL RES. 2020;167105937.
[27] LI M., Research on cyclic behavior and design method of hollow section column-to-beal connections with siip-critical blind bolts. 2017, Tongji University: Shanghai, China [in Chinese].
[28] Jiao W, Wang W, Chen Y, Teh LH. Seismic performance of concrete-filled SHS column-to-beam connections with slip-critical blind bolts. J CONSTR STEEL RES. 2020;170106075.
[29] GB/T 228-2002. Code for acceptance of construction quality of steel structures. Beijing: General Administration of Quality Supervision, Inspection and Quarantine of the People's Republic of China; 2002 [in Chinese].
[30] American Institute of Steel Construction. ANSI/AISC 341-10: Seismic Provisions for Structural Steel Buildings[S]. 2010.
[31] European Committee for Standardization. EN 1993-1-8: 2005, Eurocode 3: Design of steel structures - Part 1-8: Design of joints[S]. 2005.
[32] JGJ / T 101-2015. Specification for seismic test of buildings. Beijing: Ministry of Housing and Urban-Rural Construction of the People's Republic of China; 2015 [in Chinese].

Advanced Steel Construction – Vol. 19 No. 2 (2023) 102–111
DOI:10.18057/IJASC.2023.19.2.2

THE TENSILE PERFORMANCE OF INTER-MODULE CONNECTION WITH A BOLT AND SHEAR KEY FITTING FOR MODULAR STEEL BUILDINGS

Hong-Lei Chen [1], Cao Ke [2], Chen Chen [1] and Guo-Qiang Li [1, 3, *]

[1] *College of Civil Engineering, Tongji University, Shanghai 200092, China*
[2] *School of Management Science and Real Estate, Chongqing University, Chongqing 400044, China*
[3] *National Key Laboratory for Disaster Reduction in Civil Engineering, Tongji University, Shanghai 200001, China*
** (Corresponding author: E-mail: gqli@tongji.edu.cn)*

ABSTRACT

Modular steel buildings, as one of the most integrated prefabricated construction forms, have recently received extensive attention. The connection between modules (inter-module connection) plays a vital role in modular steel buildings' overall performance. However, most of the existing inter-module connections have problems such as insufficient construction space, difficulty in disassembly, etc. This paper proposed an innovative inter-module connection with bolt and shear key fitting, which is convenient for construction and has a clear force transmission path. The proposed connection separates the load-bearing components and has a high tolerance for installation errors. The advantages of the connection in configuration and installation were introduced, and the tensile performance of the connection was investigated with the monotonic static test. A finite element model verified with the test was also proposed to simulate the performance of the connection, and the main bearing components and failure modes of the connection were obtained through parametric study with the finite element model. Combining the experimental and numerical study results, a formula was proposed for predicting the tension capacity of the connection for practical design of inter-module connection for modular steel buildings.

ARTICLE HISTORY

Received: 30 November 2021
Revised: 26 June 2022
Accepted: 26 June 2022

KEYWORDS

Modular steel buildings;
Inter-module connection;
Bolt and shear key fitting;
Tensile performance;
Monotonic static test

1. Introduction

As one of the most integrated prefabricated steel structural forms, modular steel buildings have received widespread attention in many countries. It leads to less construction time, more cost-saving, better quality control and recycling of modules [1]. The disadvantages of modular steel buildings are that the structural span is relatively small, and the design lacks guidance and specification [2]. However, due to their special advantages, various types of modular steel buildings have been developed and used in diverse applications such as hotels, hospitals and military facilities [3].

Different from traditional steel buildings, modular steel buildings are constructed by stacking steel modules, which are manufactured off-site, transported and assembled on-site. Steel modules can be grouped into corner-supported and continuously supported, and the former is more applicable in high-rise buildings for its larger vertical bearing capacity [4]. Connections in modular steel buildings play a vital role in maintaining the strength and stability of the overall structure. As shown in Fig. 1, connections are divided into three types: inter-module, intra-module and module-foundation [2].

Considering the importance of inter-module connection in construction efficiency and load transfer, various inter-module connections have been proposed and studied [4-12]. Chen [4] proposed a new type of design with beam-to-beam connections and studied its flexural performance and aseismic behavior. Results revealed that beams and connections had independent and individual bending behaviors. Annan [5, 6] evaluated the hysteretic characteristics of modular steel building, using welding as the vertical connections and field-bolting of clip angles as horizontal connections between modules. By comparing the performance between a regular braced frame and a modular braced frame, the differences indicated that the detailing requirements of the system need to be incorporated into their design. Chen [7] investigated the seismic performance of a modular frame with pretension inter-module connection, in which the columns are vertically connected by pre-stressed strands. Chen [8] studied the tensile and shear performance of a rotary inter-module connection, and simplified calculations were developed. Lee [9] proposed a new inter-module connection to form a rigidly connected modular system and verified the seismic performance of the proposed system. Li [10, 11] proposed a splice connection and studied its performance in full-scale corner-supported modular buildings. The proposed connection was sufficient to transfer the vertical load and had a satisfactory tolerance for initial imperfections. Choi [12] adopted a bolted connection with access hole opening at the end of column in nonlinear static analyses of modular structures. It was found that the modeling of overlapped elements and the rotational behavior of connections can influence structure's lateral stiffness.

However, these connections mentioned above have some problems in the application. The most common problem is the lack of construction space, which makes it difficult to apply inter-module connections in locations with complex structures [13]. The use of welded and concrete in connections cannot give full play to the detachability of modular steel buildings. Using too many bolts in the inter-module connections will weaken the section of the members and cause the connections to be sensitive to installation errors.

In order to solve the above problems, this paper proposed an inter-module connection with a bolt and shear key fitting, which is very convenient and practical. The proposed connection separates the vertical load-bearing members from the horizontal load-bearing members. The bolts transmit the vertical loads, and the shear keys transmit the horizontal loads. The separation of load-bearing components simplifies the design and analysis of the connection. The bolt is located inside the module, not directly on the members, which allows the connection work to be completed inside the module and avoids the weakening of the members. The design of bolt holes and internal voids make the proposed connection have a high tolerance to installation errors. Therefore, the proposed connection can be used in various locations.

Studying the tensile performance of inter-module connections is very important to keep the structural integrity of modular buildings and is also beneficial to the application in high-rise modular buildings [14, 15]. In the event of members or modules being severely damaged by accidental actions, loads will be redistributed, and inter-module connections are supposed to provide an alternative load path to maintain the stability of the remaining structure. Different from the general working state, some inter-module connections may be subject to tension rather than compression. Therefore, in order to ensure that the inter-module connection can firmly tie the adjacent modules together, in addition to the shear performance, the tensile performance of the inter-module connection also needs to be studied. As shown in Fig. 1, the wind load will cause great tension in the inter-module connection at the bottom of the high-rise modular building when the structure's own weight is insufficient. If the tension exceeds the tensile capacity of the inter-module connection, the corners of the adjacent modules will break away, and the progressive collapse of the overall structure can even happen. In summary, it is very necessary to study the tensile performance of the inter-module connection.

This paper proposed an inter-module connection with bolt and shear key fitting that is convenient for construction and has a clear force transmission path. The structure, construction method and various advantages of the connection were introduced, and its tensile performance was studied through a monotonic static test. This article proposed a finite element model to simulate the performance of the connection and conducted a parametric study to obtain the main bearing components and multiple failure modes. Combining experimental data and finite element analysis results, a reasonable theoretical design formula was proposed.

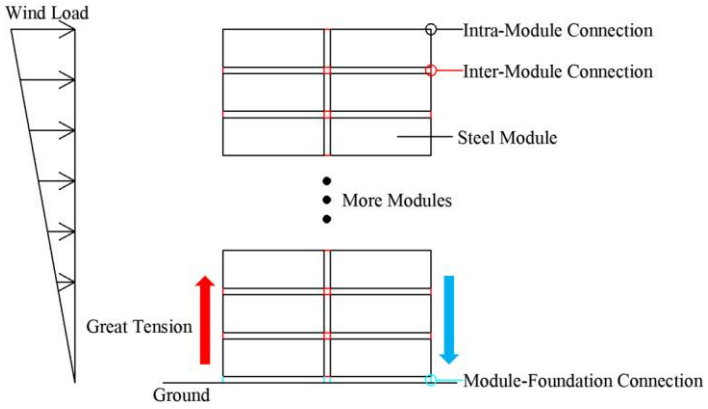

Fig. 1 Inter-module connections are under tension in some cases

2. Inter-module connection with bolt and shear key fitting

In order to facilitate design analysis and on-site installation, this paper proposed an inter-module connection with bolt and shear key fitting, in which the bolt bears most of the vertical action, and the shear key mainly bears the horizontal action [17]. Fig. 2(a) shows the construction details of the proposed connection at the corner, which is also the vertical connection of the proposed inter-module connection. The horizontal connection is achieved by sharing the same connecting plate. Its structure is simple, and the mechanism of force transmission is clear. However, the composition of vertical connection is more complex, and the internal force conditions at the vertical connection are more diverse, so this paper mainly studies the vertical connection.

The connection is composed of four parts: floor steel casting, connecting plate, ceiling steel casting and bolt. The connecting plate is located between two steel castings, and the outer contour of the connecting plate is consistent with steel casting. The shear key is welded on both sides of the connecting plate. The bolt connects two steel casting through the slotted hole on the triangular plate without contacting the connecting plate. Taking the ceiling steel casting as an example to introduce the details of the steel casting, as shown in Fig. 2(b), the ceiling steel casting consists of an L-shaped box (purple part) and a triangular plate (blue part). The L-shaped box is welded to the column and beam. The shear key hole is opened on the bottom plate (Plate P1). In addition, the two plates on the L-shaped box close to the triangular plate are called inner plates (Plate P2).

In engineering applications, after building the lower module on the flat ground, insert the shear key of the connecting plate into the ceiling steel casting's shear key hole of the lower module; then install the upper module, and the gap between the shear key and shear key hole can ensure that the shear key hole of floor steel casting is buckled with connecting plate's shear key; finally, the bolt's installation is completed in the reserved opening on the ceiling as shown in Fig. 2(a), connecting lower module's ceiling steel casting and upper module's floor steel casting.

Owing to its structure, the proposed connection has the following advantages in terms of mechanical performance and on-site construction: (1) The connection decomposes the vertical load-bearing and horizontal load-bearing components. The bolt bears most of the vertical action caused by tensile force and bending moment, while the shear key mainly bears the horizontal action caused by shear force. A clear and definite force transmission mechanism is convenient for connection analysis and design; (2) Compared with opening bolt holes at the beam end or column end, placing bolt on the triangular plate can avoid weakening members' sections and ensure the integrity of the beam and column; (3) During on-site construction, the main connection work is to install bolts after the module is positioned. The bolts are located inside the module rather than on the axis of the beam and column, overcoming the problem of insufficient construction space. Connection can be completed inside the module through the reserved opening, so the connection can be applied to various positions in the structure.

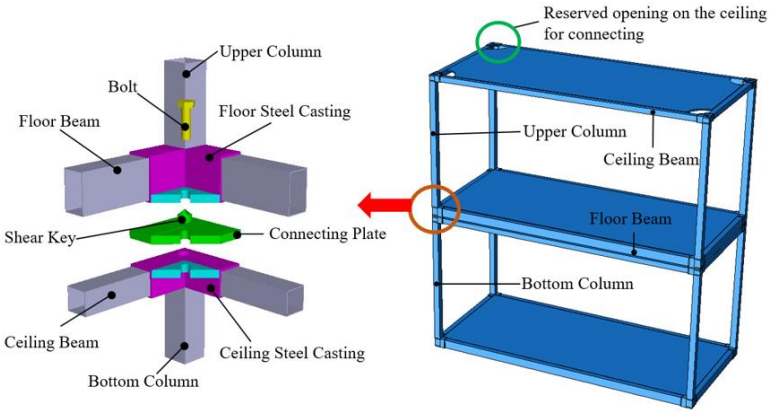

(a) Inter-module connection with bolt and shear key fitting

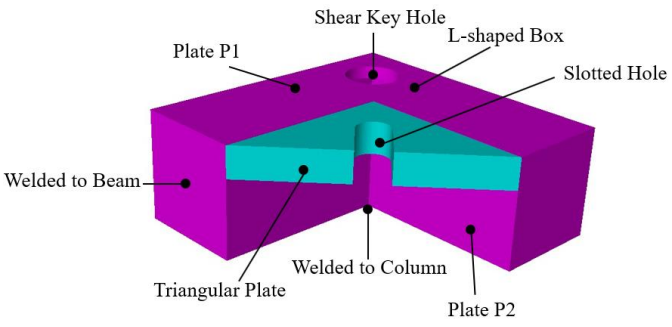

(b) Ceiling steel casting

Fig. 2 Details of the proposed connection

3. Experimental study

3.1. Materials and specimen

In the test, the 10.9-grade pressure-bearing high-strength bolts were used, and the material of members and steel casting was Q345B steel. As shown in Fig. 3, coupon tests were carried out according to the Chinese standard GB/T 228.1-2010 [16]. Three round rod specimens (Bolt1-3 and Steel1-3) were processed for the two materials. The tensile results are shown in Table 1, and the true stress-strain curve is shown in Fig. 4. Three stress-strain curves of Q345B steel basically coincide. While the curves of the bolts have certain differences, which are all within 10%.

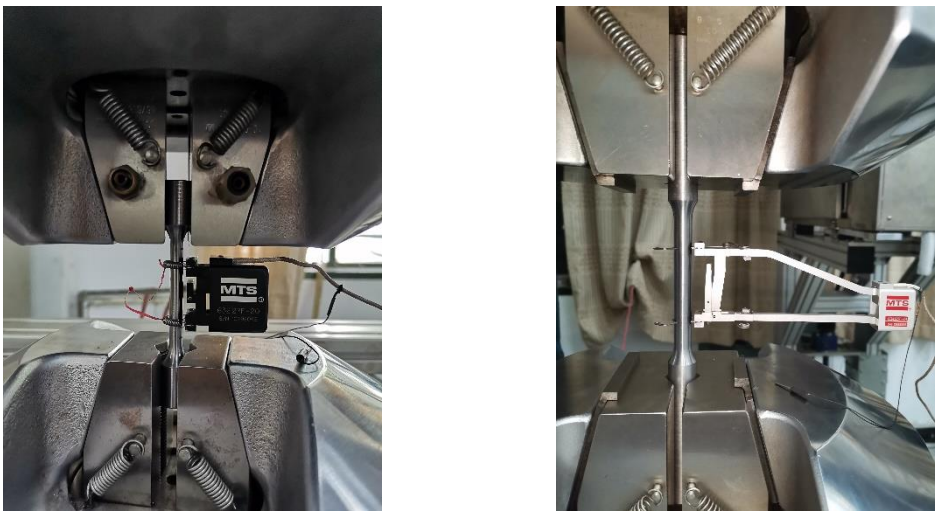

(a) Bolt specimen (b) Steel specimen

Fig. 3 Coupon tests

Table 1
Material properties

Material	Elastic Modulus (N/mm^2)	Yield Strength (N/mm^2)	Ultimate Strength (N/mm^2)	Ultimate Strain	Elongation (%)
Bolt	209766.70	1019.80	1163.67	0.04	11.30
Steel	206333.33	328.33	627.25	0.23	30.73

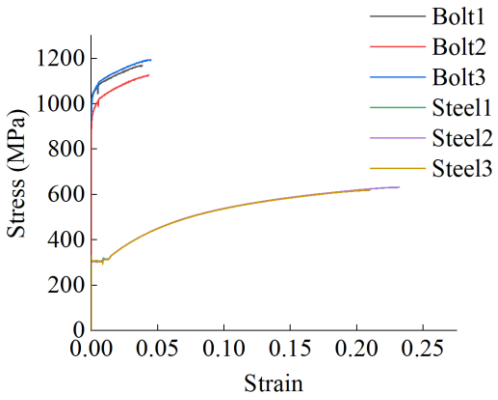

Fig. 4 Stress-strain curve of two materials

The tensile specimen in the test is shown in Fig. 5, including the top plate, upper column, connection, bottom column and bottom plate. The upper end of the upper column is welded to the top plate through stiffeners, and the lower end is welded to the connection. Similarly, the lower end of the bottom column is welded to the bottom plate through stiffeners, and the upper end is welded to the connection. The dimensions of the upper column, lower column, top plate and bottom plate are shown in Table 2. In order to facilitate production, steel castings were processed by welding.

Details of the connection's components are shown in Fig. 6. In the steel casting, the thickness of the bottom plate with the shear key hole was 25 mm (t_{bt}=25 mm), and that of the other plates was 18 mm (t_{st}=18 mm). The height of the floor steel casting was greater, and the dimensions of other parts were the same as the ceiling steel casting. In consideration of processing errors as well as facilitating construction, the diameter of the shear key hole was 4 mm larger than that of the shear key (d_{sk}=49 mm). The diameter of the bolt was 24 mm (d_b=24 mm).

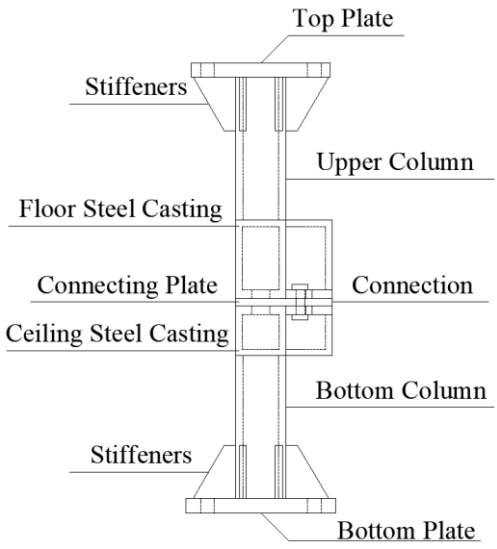

Fig. 5 Specimen

Table 2
Dimensions of the components in the tensile specimen

Member	Section Shape	Section Dimensions (mm)	Length or Thickness (mm)
Upper Column	Box	140×140×12	400
Bottom Column	Box	140×140×12	400
Top Plate	Rectangle	390×390	40
Bottom Plate	Rectangle	480×420	40

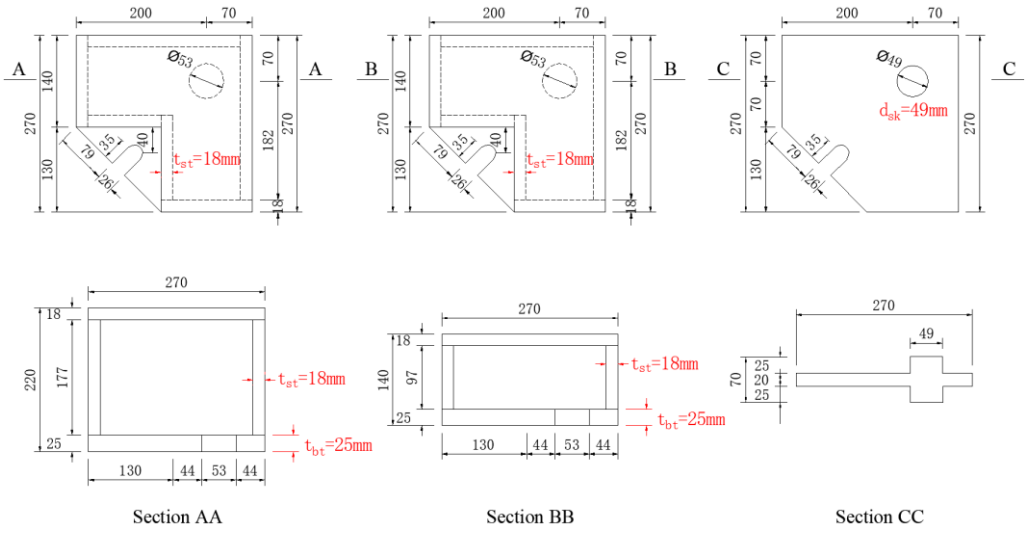

(a) Floor steel casting (b) Ceiling steel casting (c) Connecting plate

Fig. 6 Details of connection's components (unit in mm)

3.2. Experiment plan

The test setup is shown in Fig. 7. The test devices included a tensile specimen, rectangular reaction frame and 200T vertical actuator. The 200T vertical actuator was connected to the top of the specimen. The other end of the actuator is fixed on the reaction frame. The bottom plate of the specimen was connected to the reaction frame by four 36 mm-diameter bolts. The actuator applied a vertical load to the tensile specimen at a speed of 1 mm/min. And the loading will stop when the component is damaged or the load-displacement curve enters the descending section.

The measurement scheme of the experiment is shown in Fig. 8. Located at the four corners of the specimen, TD1~TD4 were vertical displacement meters used to measure the relative vertical displacement between the floor steel casting and the ceiling steel casting; TD5~TD8 were horizontal displacement meters, which were arranged symmetrically on the upper end of the floor steel casting and the lower end of the ceiling steel casting respectively to measure the horizontal displacement of the specimen. Strain gauges TS1~TS4 and TS7~TS10 were placed on the inner plate of the L-shaped box to observe the tensile strain on the inner plate; strain gauges TS5~TS6 and TS11~TS12 were placed on the triangular plate to measure the strain on the triangular plate; Strain gauge TS13 was placed on the outside of the bolt to measure the tensile strain on it.

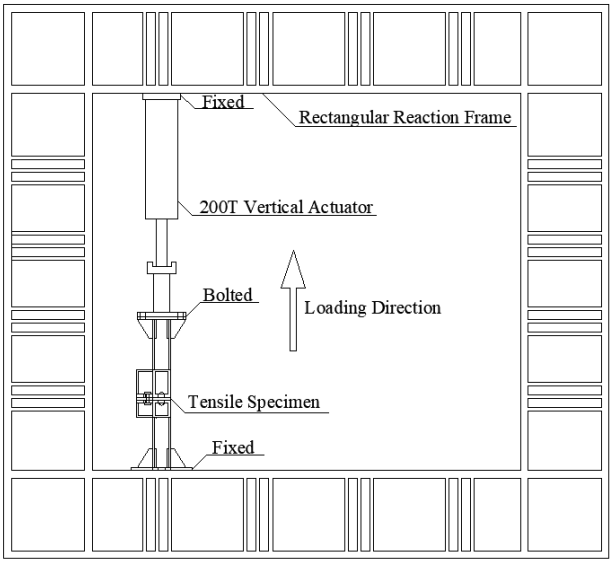

Fig. 7 Test setup

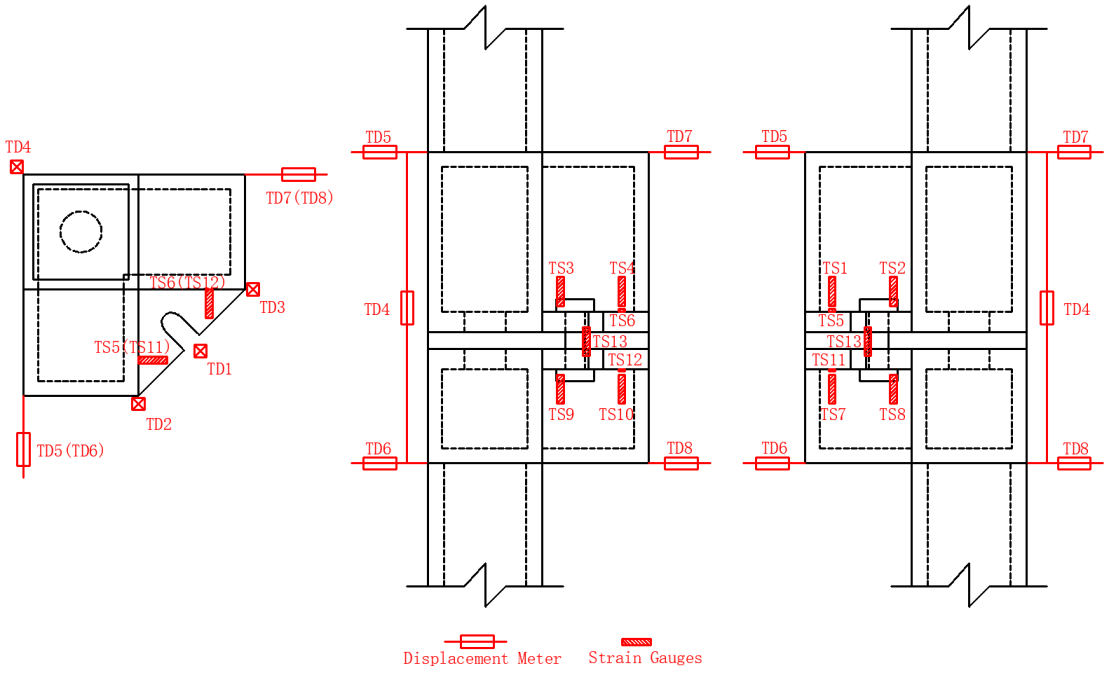

Fig. 8 Measurement scheme

3.3. Experiment results and discussion

The phenomena in the test are shown in Table 3 and Fig. 9. The failure mode of the specimen was bolt fracture, and the fracture position was in the threaded section. The load-displacement curve measured by the horizontal displacement meter TD5 and TD7 is shown in Fig. 10(a). TD5 and TD7 were located on the upper end of the floor steel casting, whose horizontal displacement was small and basically symmetrical. When the load was greater than 210 kN, the horizontal displacement at TD5 and TD7 began to increase significantly. In contrast, the horizontal displacement was very small when the load was less than 210 kN. The load-strain relationship curve measured by the strain gauge TS13 on the outside of the bolt is shown in Fig. 10(b). The tensile strain on it didn't increase monotonically. When the load was less than 103 kN, the bending deformation of the bolt was small, and the tensile strain increased. When the load was greater than 103 kN and less than 210 kN, the floor steel casting tended to rotate around the bolt. The rotation axis passed the bolt, so the tensile strain measured by TS13 decreased. When the load was greater than 210 kN, the bending deformation of the bolt was obvious, and the tensile strain of the full section of the bolt increased greatly.

Combined with the measurement results of the horizontal displacement meters TD5 and TD7 on the floor steel casting and the strain gauge TS13 on the outside of the bolt, the following conclusions can be drawn: when the load was less than 210 kN, the floor steel casting was vertically deformed; when the load was greater than 210 kN, the bolt underwent significant bending deformation, and the floor steel casting began to rotate around the bolt area. However, in actual situations, due to the overall constraint of the module, the floor steel casting cannot rotate excessively. Because the vertical displacement due to rotation is the smallest at the bolt, the relative vertical displacement of the steel castings at the bolt Δ_b is used to characterize the vertical displacement of the connection Δ_t. The Δ_b includes the deformation of the bolt and steel castings. Assuming that the steel casting rotated as a rigid body, the relative vertical displacement of the steel castings at the bolt Δ_b can be given by

$$\Delta_t = \Delta_b = td4 - \frac{td4 - td1}{l_{14}} \cdot l_{b1} \quad (1)$$

where, *tdi* is the displacement measured by displacement meter TDi, l_{b1} is the distance between the bolt and the displacement meter TD1, and l_{14} is the distance between the displacement meter TD1 and TD4.

Table 3
Phenomena in the experiment

Load (kN)	Δ_t (mm)	Phenomena	Figure
30.00	0.19	A gap of uneven width appeared between the floor steel casting and the connecting plate.	Fig 9 (a)
410.00	3.27	The floor steel casting was separated from the connecting plate; there was no obvious gap between the ceiling steel casting and the connecting plate.	Fig 9 (a)
397.60	5.54	A gap of uniform width appeared between the ceiling steel casting and the connecting plate.	Fig 9 (b)
380.60	6.28	The bolts were broken; the steel casting had no obvious cracks and deformations.	Fig 9 (c) Fig 9 (d)

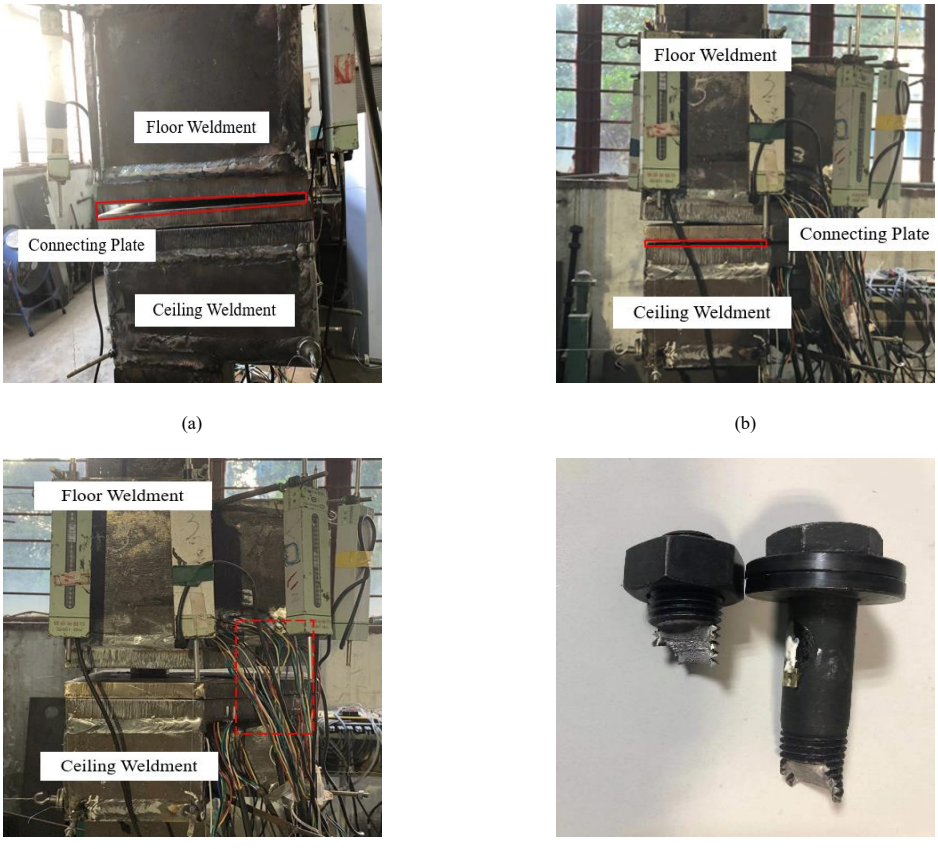

Fig. 9 Deforming state and failure behaviors in the test

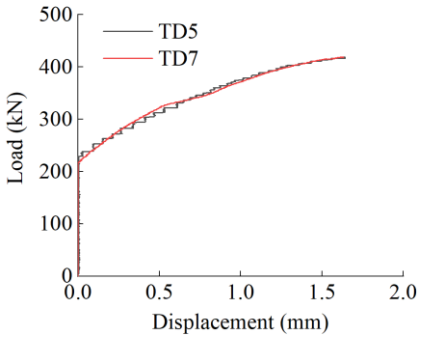

(a) Horizontal displacement

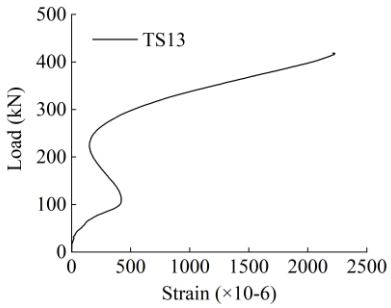

(b) Tensile strain on the outside of the bolt

Fig. 10 Data curves measured by displacement meters and strain gauges

The load-displacement curve is shown in Fig. 11. The section OA of the curve is in the stage of closing the gaps, which existed inside the specimen as well as between the specimen and the reaction frame, so the tensile stiffness K_1 is relatively small. For section AB, the gaps between the components were compacted, and the stiffness remained at a relatively large value K_2. In section BC, the tensile stiffness gradually decreased until the bolt broke, reaching the ultimate bearing capacity P_{tu}=418.8 kN. For the section OA and AB, the following formula is used to calculate the equivalent initial tensile stiffness of the specimen K_{t0}=170.49 kN/mm.

$$K_{t0} = \frac{\Delta P_{OA} \cdot K_1 + \Delta P_{AB} \cdot K_2}{\Delta P_1 + \Delta P_2} \quad (2)$$

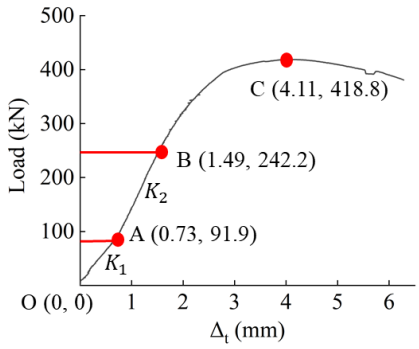

Fig. 11 Load-displacement curve of the specimen

In the test, the ultimate failure mode of the specimen was the yielding of the bolt, which was a ductile failure. This is the desired mode of failure. However, large strain values were measured on the plates of the steel casting. Therefore, in the design process, it is necessary to ensure that the steel casting is still in an elastic state when the bolt yields. In the process of data processing, considering that the connections are difficult to rotate due to the constraints inside and between the modules, the influence of the rotation of the connection under tension was minimized as much as possible. Finally, the load-displacement curve and related performance parameters of the connection under the tensile force were obtained.

4. Numerical study

4.1. Finite element model

In order to better understand the tensile performance of the bolt-shear key connection, ABAQUS was used to establish a finite element model. The dimensions and material properties of the components in the finite element model were the same as those in the experiment. In the model, the thread of the bolt was not considered. The gap between the shear key and the shear key hole, as well as the gap between the bolt and the slotted hole, was set. To ensure the accuracy of the simulation results and the normal operation of the contact, all elements of the model adopt the eight-node linear hexahedral reduction element C3D8R. The meshing result is shown in Fig. 12.

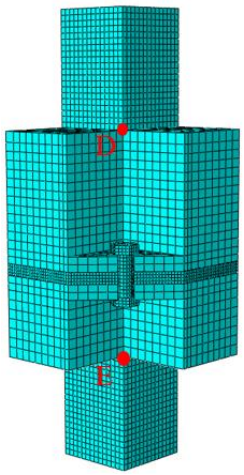

Fig. 12 Mesh of the finite element model

The members in the finite element model included the upper and bottom column, steel casting and the connecting plate. There were contacts between the steel casting and the connecting plate, between the shear key and the hole, and between the bolt and the triangular plate. The tangential behavior of contact was defined as surface contact with a friction coefficient of 0.15 [18]. And the normal behavior was defined as "hard" contact that allows separation. The relationship between columns and steel casting was simulated by tie. The fixed constraint was set at the bottom end of the bottom column, and the vertical upward displacement load was applied to the top end of the upper column.

4.2. Comparison of finite element and experiment

The load-displacement curve obtained by finite element calculation is shown in Fig. 13. Corresponding to the test, the displacement Δ_t was taken as the relative vertical displacement between the two points B and D on the steel casting near the bolt's connection area in Fig. 12. The tensile capacity and initial tensile strength obtained by the finite element analysis and experiment are shown in Table 4, and the difference between the two is relatively small. Because the bolts were broken in the threaded section and there were gaps in the experiment, the capacity and initial stiffness of the test are smaller. When the finite element model reached the ultimate capacity, the von mises stress contour plot of the connection is shown in Fig. 14. In the stress contour plot, the floor steel casting separated from the connecting plate; the bolt yielded under tension, and the stress on the inside of the bolt developed faster than the outside. The phenomenon in the finite element analysis was consistent with the experiment. According to the stress distribution of the finite element model, it can be found that the main bearing components in the tensile test are bolt, triangle plates and inner plates of steel casting.

Table 4
Comparison between experimental and numerical results

Item	Tensile Stiffness (kN/mm)	Tensile Capacity (kN)
Experimental	170.49	418.80
Numerical	185.60	436.71
Abs(error) (%)	5.93	4.28

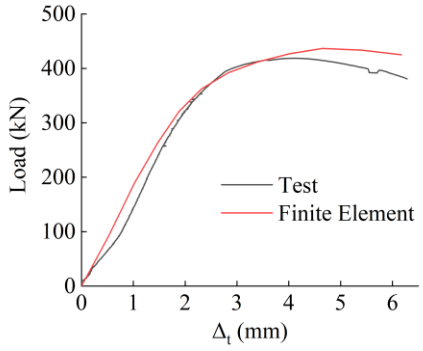

Fig. 13 Load-displacement curve of the finite element model

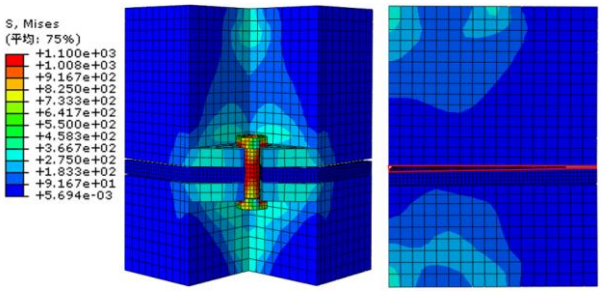

Fig. 14 Von mises stress contour plot of connection at ultimate load

4.3. Parametric study

Comparing the load-displacement curve and the experimental phenomenon, the finite element model proposed above can accurately simulate the tensile performance of the connection in the test. The proposed finite element model was used for parametric study. The parameters affecting the tensile performance of connection are: diameter of the bolt d_b, the thickness of the bottom plate of the steel casting t_{bt}, the thickness of the inner plate of the steel casting t_{st}, and diameter of the shear key d_{sk}, as shown in Fig. 6. In order to facilitate analysis and design, it is stipulated that the thickness of the other plates of the L-shaped box is the same except for the bottom plate. The thickness of the bottom plate of the L-shaped box is the same as that of the triangular plate. Through parametric study, the load-displacement curves of different dimensions' components are shown in Fig. 15, and tensile capacity's change with the dimensions of a component is shown in Fig. 16. The tensile capacity P_t is given by

$$P_t = min\left(P_{tu}, P_{t\Delta=0.02h_{cn}}\right) \tag{3}$$

where, P_{tu} is the ultimate capacity; $P_{t\Delta=0.02h_{cn}}$ is the load when displacement reached $0.02h_{cn}$; h_{cn} is the initial height of the connection.

For the parameter d_b: Shown in Fig. 15 (a), the tensile stiffness and tensile capacity of the connection increase with the increase of d_b. As shown in Fig. 16 (a), when d_b≤24 mm, the failure mode of the connection is that the bolt yields under tension; when d_b>24 mm, before the bolt yields, the steel casting has partially entered yielding, and large vertical displacement occurs. For the parameter t_{bt}: As shown in Fig. 15 (b) and Fig. 16 (b), when t_{bt}≥24 mm, the load-displacement curve changes little with the increase of t_{bt}; when t_{bt}<24 mm, the tensile stiffness of the connection is obviously reduced with the decrease of t_{bt}, and the tensile capacity is controlled by the displacement. For the parameter t_{st}: As shown in Fig. 15 (c) and Fig. 16 (c), when t_{st}≥16 mm, the tensile performance of the node does not change significantly as t_{st} increases; when t_{st}<16 mm, with the decrease of the thickness of the inner plate, the tensile capacity decreases significantly. For the parameter d_{sk}: As shown in Fig. 15 (d), the change of d_{sk} has almost no effect on the tensile performance of the connection. According to the parametric study, the main parameters that affect the tensile performance of the connection are the bolt diameter, the thickness of the bottom plate and the inner plates of the steel casting. In addition, when the bolt diameter is 24 mm, the minimum thickness of the steel casting plate is recommended to be: t_{bt}=24 mm, t_{st}=16 mm. Therefore, through parametric study, the minimum plate thickness corresponding to the bolt of a certain diameter can be obtained.

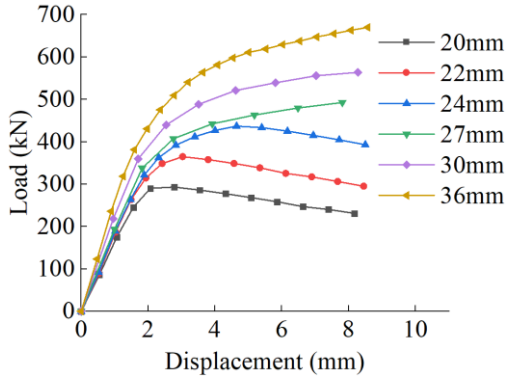

(a) diameter of bolt d_b

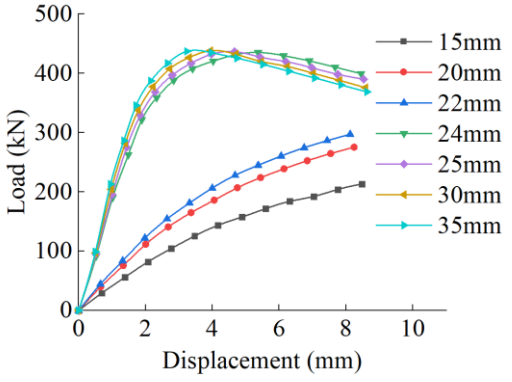

(b) thickness of the bottom plate t_{bt}

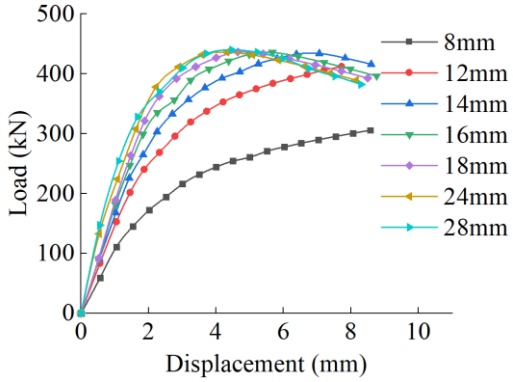

(c) thickness of the inner plate t_{st}

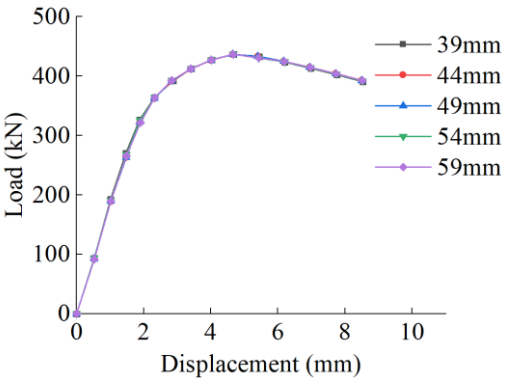

(d) diameter of the shear key d_{sk}

Fig. 15 Load-displacement curve of component's different dimensions

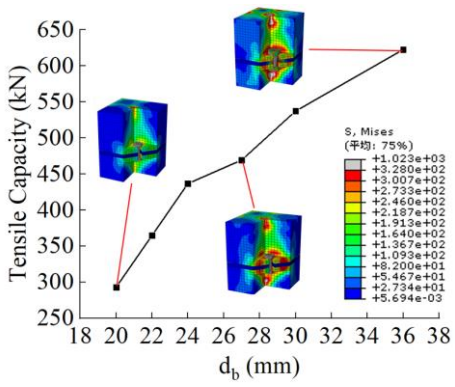

(a) diameter of bolt d_b

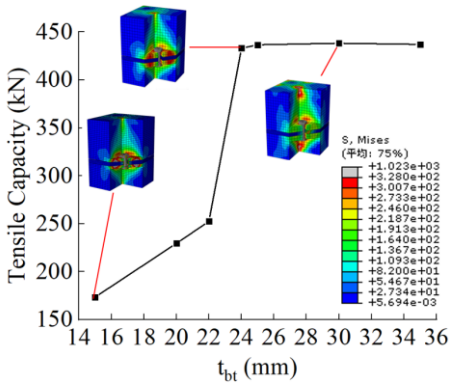

(b) thickness of the bottom plate t_{bt}

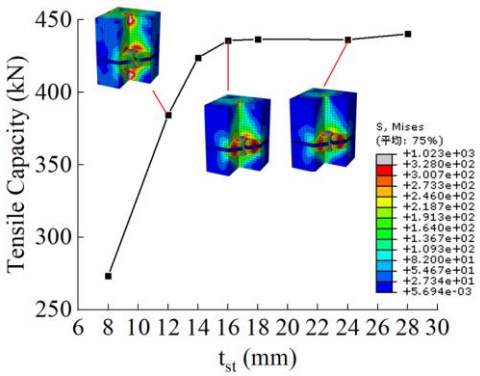

(c) thickness of the inner plate t_{st}

Fig. 16 Tensile capacity's change with the dimensions of the component

In this part, a finite element model that can well simulate the test well was proposed, whose effectiveness was verified by comparison with the experiment. Using the verified finite element model for parameter learning, it is further clarified that the main bearing components of the connection during tension are the bolt, the inner plates and the bottom plates of the steel casting. The shear key has almost no contribution to the vertical force transmission of the connection. Based on the bolt of a certain diameter determined by the vertical load between the modules, the recommended value of the minimum thickness of the steel casting plate can be obtained by parametric study.

5. Theoretical study

5.1. Theoretical analysis

According to the experimental research and finite element analysis, the parameters and components that mainly affect the tensile performance of the connection were obtained. Aiming at the failure mode of each bearing member, theoretical design formulas of tensile capacity related to the parameters were given below.

5.1.1. Failure mode 1: The bolt yields under tension

The bolt is not located on the axis of the column, so the bolt is subjected to the combined action of tensile force and bending moment, and the inner tensile strain develops faster. To be conservative, assume that the connection fails when the inner side of the bolt yields. The calculation formula of the tensile capacity P_{t1} is given by

$$P_{t1} = f_{yb}\left(\frac{1}{A_b} + \frac{l_{pb}}{W_b}\right)^{-1} \tag{4}$$

where, f_{yb} is the yield strength of the bolt; A_b is the cross-sectional area of the bolt; W_b is the flexural section coefficient of the bolt; and l_{pb} is the distance from the point of force to the bolt.

5.1.2. Failure mode 2: The L-shaped box yields under tension

As shown in Fig. 17, assuming that when the L-shaped box transmits tension, only the inner plate (red area) bears the force. Under the action of tensile force, it is assumed that the connection fails when the edge of the inner plate's section (blue line area) yields. According to the symmetry relationship, the formula for calculating the tensile capacity P_{t2} is given by

$$P_{t2} = f_{ys}\left(\frac{1}{A_{ip}} + \frac{l_{pc}}{W_{ip}}\right)^{-1} \tag{5}$$

where, f_{ys} is the yield strength of the steel casting; A_{ip} is the cross-sectional area of the inner plate; W_{ip} is the flexural section coefficient of the inner plate; and l_{pc} is the distance from the point of force to the centroid of the inner plate.

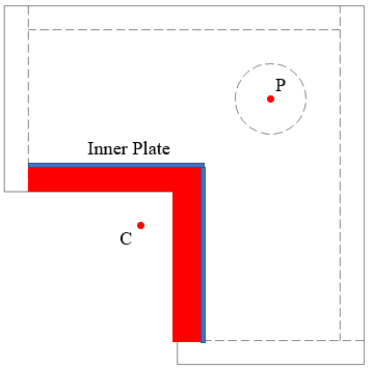

Fig. 17 The edge of the inner plate section yields

5.1.3. Failure mode 3: The triangular plate yields under tension

As shown in Fig. 18, according to the yield line theory and the stress distribution of the finite element model, there are three types of yield lines formed on the triangle plate under tension: line 1 and 3 are negative yield lines; line 2 are positive yield lines. According to the principle of virtual work, the calculation formula of internal virtual work W_{pl} is given by

$$W_1 = W_3 = m_p\left(l_{1x}\varphi_{1x} + l_{1y}\varphi_{1y}\right) = \frac{f_{ys}t_{bt}^2}{4}\frac{\sqrt{2}l_{st}}{2}\delta\frac{2\sqrt{2}}{l_{bt}} = \frac{\delta f_{ys}t_{bt}^2}{2} \tag{6}$$

$$W_2 = m_p l_2 \varphi_2 = \frac{f_{ys} t_{bt}^2}{4} l_2 \frac{2\sqrt{2}\delta}{l_{bt}} \tag{7}$$

$$W_{pl} = \sum W_i = \delta f_{ys} t_{bt}^2 \left(1 + \frac{d_d}{l_{bt}} - \frac{\sqrt{2} d_b}{4 l_{bt}}\right) \tag{8}$$

where, W_i is the virtual work done by the ith yield line; m_p is the yielding moment per unit length of the triangular plate; l_i is the length of the ith yield line; φ_i is the angle of the ith yield line; t_{bt} is the thickness of the triangular plate; l_{bt} is the side length of the triangular plate; d_d is the end distance from the bolt to the L-shaped box.

The external virtual work of the force is given by

$$W_b = P \frac{2 d_d \delta}{l_{bt}} \tag{9}$$

According to the equality of internal virtual work and external virtual work, the tensile capacity of the connection P_{t3} is given by

$$P_{t3} = \frac{f_{ys} t_{bt}^2}{2 d_d} \left(l_{bt} + d_d - \frac{\sqrt{2} d_b}{4}\right) \tag{10}$$

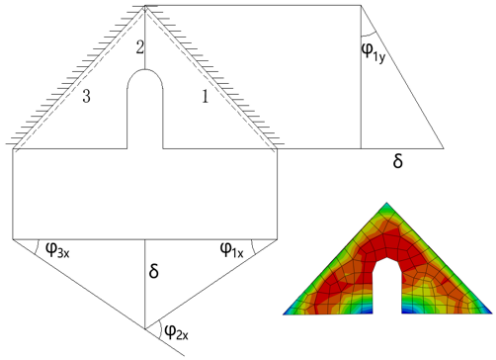

Fig. 18 Yield line distribution of triangular plate

By summarizing the above three failure modes, the tensile capacity of the connection P_t is given by

$$P_t = min(P_{t1}, P_{t2}, P_{t3})$$

$$= min\left(f_{yb}\left(\frac{1}{A_b} + \frac{l_{pb}}{W_b}\right)^{-1}, f_{ys}\left(\frac{1}{A_{ip}} + \frac{l_{pc}}{W_{ip}}\right)^{-1}, \frac{f_{ys} t_{st}^2}{2 d_d}\left(l_{st} + d_d - \frac{\sqrt{2} d_b}{4}\right)\right) \tag{11}$$

5.2. Comparison of the theoretical analysis against experimental results and parametric study

In engineering applications, we suggest that the failure mode of the connection under tensile force is the bolt yielding, which is convenient for the replacement and monitoring of the bolt. Therefore, the tensile capacity corresponding to other failure modes should be greater than that corresponding to the bolt yielding. After formula (4) is used to determine the bolt's diameter according to the tension requirements of the connection, the minimum thickness of the inner plates and bottom plate of the steel casting can be obtained by the above formula (5, 10). Assuming that the bolt diameter d_b=24 mm, the tensile capacity of the connection and the thickness of the steel casting can be calculated by the theoretical design formula. As shown in Table 5, the tensile capacity of the connection obtained by the numerical and theoretical analysis is basically consistent. Since the bolt broke in the threaded section in the experiment, the tensile capacity is relatively small. The comparison of the minimum thickness of the steel casting between the theoretical and numerical study is shown in Table 6. The minimum thickness of the steel casting calculated by the theoretical design formula is greater than that of the parametric study, and the difference between the two is not large. Results indicated that the theoretical calculation formula could reasonably design the bolt's diameter and the minimum thickness of the steel casting.

Table 5
Comparison of tensile capacity

Item	P_t (kN)	Abs(error) (%)
Experimental	418.80	
Numerical	436.71	4.28
Theoretical	434.44	3.73

Table 6
Comparison of the minimum thickness of plates between theoretical formula and parametric study

Item	P_t (kN)	t_{bt} (mm)	t_{st} (mm)
Numerical	436.71	24	16
Theoretical	434.44	26	18
Abs(error) (%)	0.52	8.33	12.50

Compared to complex parametric learning, more practical theoretical design formulas were proposed based on the conclusions of the experiment and finite element analysis. Through the theoretical design formula, the bolt diameter that can safely transmit the tension between the modules can be obtained, as well as the minimum thickness of the steel casting' plates corresponding to the bolt's diameter. The comparison with the parameter learning's results proved the practicability and rationality of the theoretical design formulas.

6. Conclusions

In order to reliably and conveniently connect modules of modular steel structure buildings, a novel bolt and shear key fitting was proposed for the inter-module connection, which has the advantages of easy installation, clear force transmission path and high tolerance to installation errors. This paper conducted both experimental and numerical studies on the tensile performance of the connection, and formula was proposed for predicting the tensile capacity of the connection. The following conclusions can be summarized:

(1) To facilitate design and analysis, the proposed inter-module connection decomposes the vertical load-bearing and horizontal load-bearing components, in which the bolt bears most of the vertical action, and the shear key mainly bears the horizontal action. The bolts are located inside the module, and on-site installation can be completed inside the module through the reserved opening. The slotted hole, as well as the gap between shear key and shear key hole, can provide high tolerance to installation errors.

(2) In the tensile test, the main bearing components included the bolt, the triangle plate and the inner plates of the steel casting, on which significant strain has been monitored. The ultimate failure mode of the specimen was the tensile yielding of the bolt. It is the expected failure mode because the bolt is easy to replace.

(3) By comparing the measured data and experimental phenomena, it is proved that the finite element model proposed can simulate the tensile performance of the connection in the test. Observing the stress distribution of the finite element model, it can be found that the main bearing component of the L-shaped box is the inner plate.

(4) Through parametric study, it is found that the tensile failure modes of the connection include bolt yielding, triangular plate yielding, and inner plate yielding. The size of the shear key has nothing to do with the tensile performance of the connection. According to the results of the parametric study, when the bolt's diameter is 24 mm, the recommended value of the inner plates' minimum thickness is 16 mm, and the recommended value of the bottom plate's minimum thickness is 24 mm.

(5) Combining experimental phenomena and numerical analysis, the theoretical design formula of the tensile capacity of the connection was obtained. According to the calculation of the theoretical design formula, when the bolt diameter is 24 mm, the minimum thickness of the inner plate of the steel casting is 18 mm, and the minimum thickness of the bottom plate is 26 mm, which is slightly larger than the result obtained by the parametric study. And the tensile capacity of the experiment is not much different from numerical and theoretical analysis. The theoretical formula can reasonably design the proposed inter-module connection.

Acknowledgements

The research work presented hereinabove was supported by the National Key Research and Development Program of China (Project No.2017YFC0703803-04) and the National Science Foundation for Young

Scientists of China (Grant No.51808068).

References

[1] F.J. Luo, C. Ding, A. Styles, Y. Bai, End Plate-Stiffener Connection for SHS Column and RHS Beam in Steel-Framed Building Modules, International Journal of Steel Structures, 19 (2019) 1353-1365.
[2] A.W. Lacey, W.S. Chen, H. Hao, K.M. Bi, Structural response of modular buildings - An overview, Journal of Building Engineering, 16 (2018) 45-56.
[3] R. Sanches, O. Mercan, B. Roberts, Experimental investigations of vertical post-tensioned connection for modular steel structures, Engineering Structures, 175 (2018) 776-789.
[4] Z.H. Chen, J.D. Liu, Y.J. Yu, Experimental study on interior connections in modular steel buildings, Engineering Structures, 147 (2017) 625-638.
[5] C.D. Annan, M.A. Youssef, M.H. El Naggar, Experimental evaluation of the seismic performance of modular steel-braced frames, Engineering Structures, 31 (2009) 1435-1446.
[6] C.D. Annan, M.A. Youssef, M.H. El Naggar, Seismic Overstrength in Braced Frames of Modular Steel Buildings, Journal of Earthquake Engineering, 13 (2009) 1-21.
[7] Z. Chen, H. Li, A. Chen, Y. Yu, H. Wang, Research on pretensioned modular frame test and simulations, Engineering Structures, 151 (2017) 774-787.
[8] Z.H. Chen, J. Wang, J.D. Liu, Z.Y. Cong, Tensile and shear performance of rotary inter-module connection for modular steel buildings, Journal of Constructional Steel Research, 175 (2020) 15.
[9] S. Lee, J. Park, E. Kwak, S. Shon, C. Kang, H. Choi, Verification of the Seismic Performance of a Rigidly Connected Modular System Depending on the Shape and Size of the Ceiling Bracket, Materials, 10 (2017).
[10] G.-Q. Li, K. Cao, Y. Lu, Column effective lengths in sway-permitted modular steel-frame buildings, Proceedings of the Institution of Civil Engineers-Structures and Buildings, 172 (2019) 30-41.
[11] Y.-F. Lyu, G.-Q. Li, K. Cao, S.-Y. Zhai, H. Li, C. Chen, Y.-Z. Wang, Behavior of splice connection during transfer of vertical load in full-scale corner-supported modular building, Engineering Structures, 230 (2021).
[12] Kyung-Suk Choi, Ho-Chan Lee, Hyung-Joon Kim, Influence of Analytical Models on the Seismic Response of Modular Structures, Journal of The Korea Institute for Structural Maintenance and Inspection, 20 (2016) 74-85.
[13] X.-M. Dai, L. Zong, Y. Ding, Z.-X. Li, Experimental study on seismic behavior of a novel plug-in self-lock joint for modular steel construction, Engineering Structures, 181 (2019) 143-164.
[14] P.M. Lawson, M.P. Byfield, S.O. Popo-Ola, P.J. Grubb, Robustness of light steel frames and modular construction, Structures & Buildings, 161 (2008) 3-16.
[15] R.M. Lawson, J. Richards, Modular design for high-rise buildings, Proceedings of the Institution of Civil Engineers-Structures and Buildings, 163 (2010) 151-164.
[16] GB/T 228.1-2010. Metallic materials-Tensile testing-Part 1: Method of test at room temperature, in, Standards Press of China, Beijing, 2010. (in Chinese)
[17] Guo-Qiang Li, Hong-Lei Chen,Chen Chen, Cast steel connections between modules. China Patent: ZL201810883013.6,December 4, 2020. (in Chinese)
[18] Tian-Hong Zheng, Theoretical and experimental study on friction model, in, Guizhou University, (2020) 59-61.

Advanced Steel Construction – Vol. 19 No. 2 (2023) 112–120
DOI:10.18057/IJASC.2023.19.2.3

EXPERIMENT STUDY ON THE INFLUENCES OF LENGTH ERRORS OF CABLES AND STRUTS ON SPATIAL CABLE-TRUSS STRUCTURE WITHOUT INNER RING CABLES

Jian Lu [1, 2], Su-Duo Xue [2, *] and Xiong-Yan Li [2]

[1] *School of Naval Architecture, Ocean and Civil Engineering, Shanghai Jiao Tong University, Shanghai 200240, China*
[2] *College of Civil and Architecture Engineering, Beijing University of Technolog, Beijing 100124, China*
** (Corresponding author: E-mail: sdxue@bjut.edu.cn)*

ABSTRACT

Spatial cable-truss structure without inner ring cables (SCSWIRC) belongs to tensile structure, which is composed of three kinds of cable, strut and stiff ring-beam, and its stiffness generates from the pre-stresses of cables. The manufacturing errors of the three kinds of components determine the final formed state and ultimate bearing capacity, so it is essential to study the influences of manufacturing errors of three kinds of components on the mechanical property of structure. The influences of manufacturing errors on SCSWIRC have been studied from four aspects that include elongation or shortening of cable and strut, different pre-stresses states, different cable-truss frames and external loads. The relations of manufacturing errors and four aspects have been studied based on finite element model and experimental model. The results show that the elongation and shortening of components has little influence on sensitive indexes of components when the elongation or shortening of components is the same. The manufacturing errors have the different influences on the mechanical property of structure under the different pre-stress states. The closer cable-truss frame is to the error position, the larger influence the error has on cable-truss frame. The external loads have not changed the basic mechanical property of SCSWIRC, but the external loads make upper chord cables easier to loose and make sensitive indexes change more greatly. The research contents reveal the influences of manufacturing errors on the mechanical property of SCSWIRC from the four aspects.

ARTICLE HISTORY

Received: 12 November 2021
Revised: 17 June 2022
Accepted: 19 June 2022

KEYWORDS

Tensile structure;
Spatial cable-truss structure without inner Ring cables;
Manufacturing errors;
Sensitive indexes;
Mechanical property

1. Introduction

Tensile structures are one important type of large-span spatial structures, which is generally composed of cables, struts and stiff ring-beam [1-2]. Tensile structures share these advantages of light weight, considerable-spanning ability, rapid construction speed and favorable appearance. Cable-truss tensile structures (CTTS) are one of the most comparative structural types, which share the same advantages as the tensile structures. Spatial cable-truss structure without inner ring cables (SCSWIRC) belongs to the kinds of CTTS, and it is a new kind of CTTS. At present, the main researches about SCSWIRC mainly focus on simulation analysis, theoretical research and model experiment [3]. There are still no any engineering cases in the world, so it is necessary to further study SCSTWRC.

At present, the form-finding analysis of SCSWIRC was studied and the improved force iteration method based on rational shape design was proposed to solve the form-finding problem of SCSWIRC [4]. The model experiment of SCSWIRC with a diameter of 17.15 m was carried out, and the experiment values agree with the simulation values that further reveal the static property of SCSWIRC [5]. Lu et al. [6] proposed the simplification method based on grid-jumped layout to simply SCSWIRC, and the simplification method can simplify structural system and save the project costs. The progressive collapse ability of SCSWIRC was studied by using LS-DYNA, which reveals the progressive collapse mechanism of SCSWIRC [7]. Lu et al. [8] studied the influences of film-covering on SCSWIRC, and the research results show that the film-covering effect is obvious. But there are hardly any references about construction control of SCSWIRC, and construction control determines the final forming state at the same time. The final forming state also further determines the mechanical property and ultimate bearing capacity, so it is necessary to study the construction control problem of SCSWIRC.

Some scholars have studied the construction control problem about other kinds of tensile structures. Tian et al. [9] proposed a method of solving the control criteria of cable length error based first-time and second-order moment reliability indexes. Gao et al. [10] used the orthogonal test design method to analyze the deviations of the experimental model and finite element model of rigid bracing cable dome. Deng et al. [11] introduced an uncomplicated sensitivity method to statistically evaluate the pretension deviation of tensile structures and revealed that different tensioning schemes take different effects on controlling the pretension deviations. A shape control framework which consisted of multi-objective search and reinforcement learning was experimentally validated on an active tensegrity structure by Adam and Smith [12-13]. Korkmaz et al. [14] investigated the active control performance of a tensegrity bride to assess the practicability of an active tensegrity structure in practice. Liang et al. [15] proposed an active control algorithm based on a nonlinear force method and the method was also used to prevent the failure of cable domes due to slackening of the ridge cables and excessive displacements of the central section of the cable dome. Sun et al. [16] proposed the small elastic modulus method to analyze the random error analysis of combining cable length and cable force, and the control index in practical engineering was ensured. Jin et al. [17] proposed the global sensitivity analysis method of parameters and then come to the conclusion that the cable cross-sectional area has the largest impact on the cable net structure of FAST (Five-hundred-meter aperture spherical radio telescope). Sun et al. [18] studied the influences of cable length errors and other parameters on cable force and then the deviation of cable length is the largest impact on the cable force. Shen et al. [19] systematically studied the independent error analysis and multiple error coupling analysis of cable-length error, active-cable tension error and outer-node coordinate of FAST based on the random error analysis method of normal distribution. Based on the above research contents, there are few scholars to study the influences of manufacturing errors on SCSWIRC.

In the paper, four aspects about manufacturing errors of components are studied based on experimental model and finite element model (FEM). Firstly, the influences of the elongation or shortening of cables on structures are studied based on manufacturing errors. Secondly, the influences of different pre-stresses states on structures are studied. Thirdly, the influences of manufacturing errors on different cable-truss frames are studied. Fourthly, the influences of manufacturing errors on structure under the external loads are studied. Finally, the conclusions of the paper are given at the end of the paper.

2. Design of experimental model

In order to study the influence of manufacturing errors on SCSWIRC, the experimental model of SCSWIRC with a span of 6 m is built. The experimental model is consisted of 10 planar cable-truss frames with winding and interwoven. Namely, the ring equivalent fractions are 10. The outer shapes of upper and lower chord cables conform to parabola shape and the equations of parabola are shown in Eq. (1). It can be known from Ref. [20] that the optimal rise-span ratios of upper and lower chord cables are 1/25 to 1/20 and 1/20 to 1/15, respectively. So, the rise-span ratios of upper and lower chord cables for the experimental model are selected as 1/24 and 1/16. Based on structural control parameters including Eq. (1), span, ring equivalent fractions and rise-span ratios, the coefficients of Eq. (1) are solved; Namely, A_1=-0.091778, B_1=0.075665, A_2=0.137668, B_2=-0.113497. The program of solving the nodal coordinates is compiled based on structural control parameters and Fortran Language. The FEM is built by the nodal coordinates, and then the integral FEM is built considering ring beam and supported column, shown in Fig. 1a. The size and element number of the half planar cable-truss frame is shown in Fig. 1b. The feasible pre-stress values are solved by using the method from Ref. [4], which is shown in Table 1.

$$\begin{cases} y_1 = A_1 x_1^2 + B_1 \\ y_2 = A_2 x_2^2 + B_2 \end{cases} \quad (1)$$

For Eq. (1), x_1 and x_2 stand for x-coordinate values, and y_1 and y_2 stand for y-coordinate values when cable-truss frames are in planar.

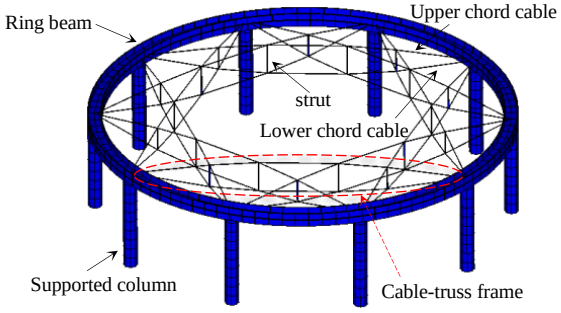

(a) Integral FEM of SCSWIRC

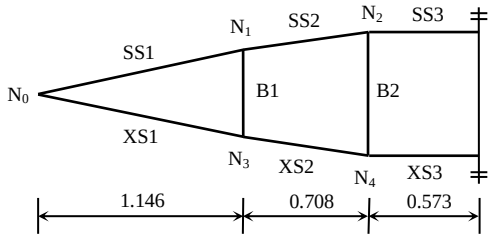

(b) Size of half planar cable-truss frame

Fig. 1 Integral FEM of SCSWIRC and Size of half planar cable-truss frame

Table 1
Feasible self-stress mode of FEM

Element number	Cable						Strut	
	SS1	SS2	SS3	XS1	XS2	XS3	B1	B2
Cable length/m	1.157	0.710	1.146	1.163	0.711	1.146	0.354	0.463
Non-stress cable length/m	1.153	0.709	1.142	1.161	0.709	1.144	-	-
Self-stress mode/kN	1.000	0.993	0.993	0.837	0.829	0.827	-0.139	-0.138

Table 2
Material properties of cable and strut

Element Type	Size	Area/mm^2	Elastic modulus/MPa	Broken force/kN
Cable	Φ6	21.487	1.21×10^5	36
Strut	P20×3	141.300	2.05×10^5	52.02

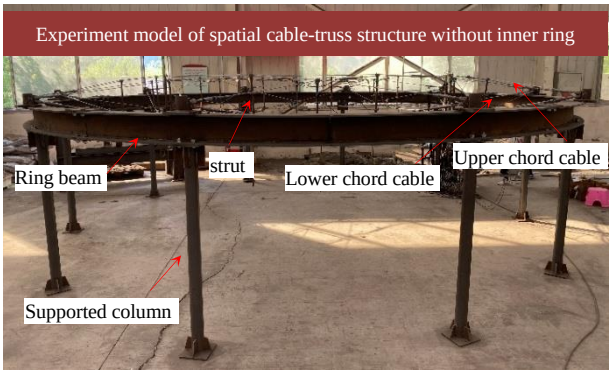

Fig. 2 Integral experiment model of SCSWIRC

Based on FEM, the integral experimental model is designed including main cable system structure, cable-strut joint, cable-beam joint, ring beam and supported column, shown in Fig. 2. The material properties of experimental model are gained by material test shown in Table 2. The real material properties are used in FEM in order to make the FEM and experimental model the same.

3. Influences of elongation or shortening of cable and strut on sensitive indexes of SCSWIRC

The cable length can be shortened or elongated in the manufacturing process. In numerical analysis, the elongation of cable and strut can be simulated by applying negative temperature (NT) to cable and strut, and the shortening of cable and strut can be simulated by applying positive temperature (PT) to cable and strut. But there are no relative references about how the elongation and shortening of cable and strut affect the internal forces of cable and strut.

The influences of elongation or shortening of cable and strut on internal forces of components are studied. The influence magnitude can be expressed as internal force variation (δ). In Fig. 1b, it is assumed that the initial cable force of SSi is σ_{ssi}, and the corresponding cable force is σ'_{ssi} when the variation of cable length SSi is $\triangle l$. The internal force variation of cable SSi can be expressed as

$$\delta_{ssi}=\sigma'_{ssi}-\sigma_{ssi} \quad (2)$$

For Eq. (2), SSi srands for the ith upper chord cable.
The sensitive indexes of cable and strut can be expressed as

$$\delta_{ssi}=(\sigma'_{ssi}-\sigma_{ssi})/(\triangle l) \quad (3)$$

Similarly, the sensitive indexes of other components can be gained by the same analysis method as Eq. (3).

The planar diagram and nodal number of SCSWIRC are shown in Fig. 3. The nodal numbers 1 to 10 are the boundary constraints and the nodal numbers 11 to 30 are the upper chord nodes and the nodal numbers 31 to 50 are the lower chord nodes. As the SCSWIRC is a centrosymmetric structure, the cable-truss frame 1-4 is selected as the research objective to study the influences of elongation and shortening of cable and strut on structure.

Based on the data in Table 1, the corresponding FEM and experimental model are built, respectively. In FEM, the elongation or shortening of cables and struts are simulated by applying positive or negative temperature to cables and struts. In the experimental models, the elongation or shortening of cables are completed by adjusting the threaded sleeves of the terminal or middle of cable and strut. The threaded sleeves are installed in the monitoring positions in advance, which are shown in Fig. 4a. The strain gauges are attached to the threaded sleeves to monitor the internal forces of cables. As the symmetry of cable-truss frame, the half cable-truss frame 1-4 is monitored shown in Fig. 4b.

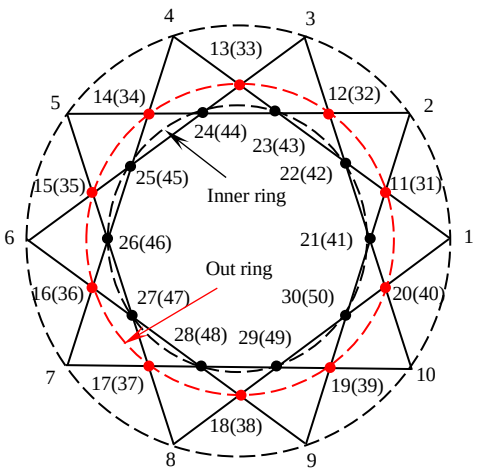

Fig. 3 Planar diagram and nodal number of SCSWIRC

(a) Threaded sleeves of cable and strut

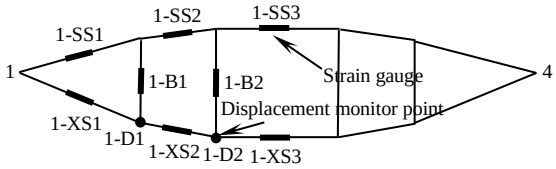

(b) The monitoring points of internal forces and displacements

Fig. 4 Threaded sleeves and monitoring points

When the cables and struts of cable-truss frame 1-4 are shorten or elongated by 3mm, the comparison results of sensitive indexes are solved by Eq. (3), shown in Fig. 5.

It can be known from Fig. 5 that the sensitivity indexes of cable and strut caused by negative temperature (NT) or positive temperature (PT) are the same. For the upper chord cables SS1 to SS3, the difference of sensitive indexes caused by negative temperature and positive temperature is in the range of 3.43 to 7.55%. For the upper chord cables XS1 to XS3, the difference of sensitive indexes caused by negative temperature and positive temperature is in the range of 3.84 to 6.31%. For the upper chord cables B1 to B2, the difference of sensitive indexes caused by negative temperature and positive temperature is in the range of 4.25 to 7.71%. The research results show that the negative or positive temperature has the same influences on the sensitive indexes of cable and strut in the linear elastic state. So one of two types of applying temperature to cable and strut can be selected in the solution process of sensitive problem.

4. Influences of manufacturing errors under different pre-stress states on internal forces of cable and strut

The influences of cable length errors under three different pre-stress levels on the internal forces of components are studied. The planar diagram and nodal number of SCSWIRC are shown in Fig. 3. As the SCSWIRC is a centrosymmetric structure, the cable-truss frame 1-4 is selected as the research objective. The three types of feasible pre-stress states are shown in Table 3. The P1, P2 and P3 stand for the feasible pre-stress levels 1 to 3, respectively.

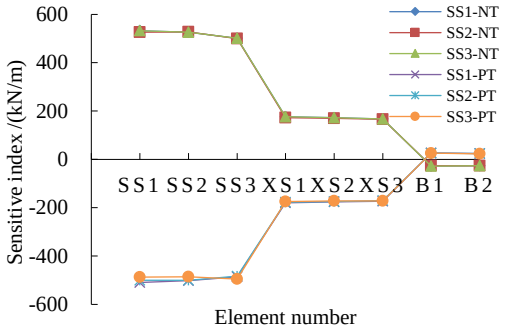

(a) Upper chord cable SS1 to SS3

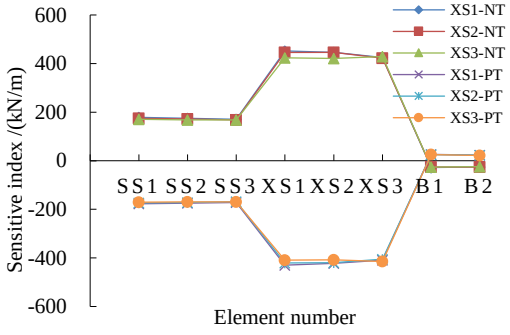

(b) Lower chord cable XS1 to XS3

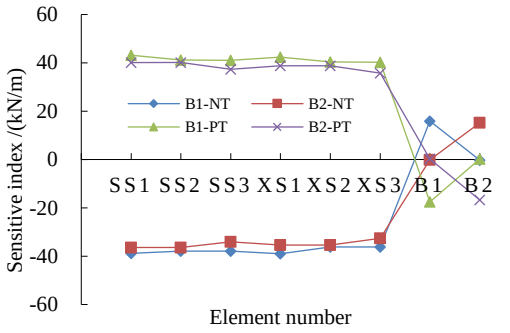

(b) Lower chord cable XS1 to XS3

Fig. 5 Influences of elongation and shortening of cable and strut on sensitive indexes of SCSWIRC

Table 3
Three types of feasible pre-stress states

Nodal number	Cable						Strut	
	SS1	SS2	SS3	XS1	XS2	XS3	B1	B2
Feasible pre-stress state 1 /kN	1.4616	1.452	1.4515	1.2596	1.2471	1.2449	-0.2067	-0.2053
Feasible pre-stress state 2 /kN	2.4565	2.4404	2.4394	2.0745	2.0537	2.0502	-0.3439	-0.3414
Feasible pre-stress state 3 /kN	3.4511	3.4285	3.4270	2.8897	2.8608	2.8559	-0.4810	-0.4776

Table 4
Relative variations of internal forces of cable (SS1) for FEM and experimental model

Element number	Relative variation between P2 and P1			Relative variation between P3 and P2			Relative variation between P3 and P1		
	Simulation values	Experiment values	Errors	Simulation values	Experiment values	Errors	Simulation values	Experiment values	Errors
XS3	-18.25	-17.43	4.48	-14.52	-15.32	5.55	26.15	24.87	4.90
XS2	-17.27	-18.32	6.05	-13.52	-13.23	2.13	24.89	22.94	7.84
XS1	-16.71	-18.01	7.80	-12.84	-11.93	7.08	24.07	23.43	2.64
SS3	4.66	4.98	7.01	3.07	2.89	5.72	-8.20	-8.72	6.32
SS2	5.88	5.53	5.95	4.23	4.45	5.27	-10.94	-11.73	7.23
SS1	6.13	6.34	3.41	4.47	4.18	6.49	-11.52	-10.76	6.54
B1	-1.13	-1.21	6.74	-0.37	-0.35	5.84	1.49	1.52	2.39
B2	-0.99	-0.92	6.66	-0.36	-0.34	4.27	1.33	1.34	1.14

Errors=abs (simulation values-experiment values)/simulations values

Based on the data in Table 1, the corresponding FEM and experimental model are built, respectively. It is assumed that the length of cable and strut is shortened by 3 mm. The variations of internal forces of cable and strut can be gained by Eq. (2). The variations of internal forces of cables and struts are shown in Fig. 6 and Fig. 7. As there are too many components, the SS1 is selected as the research objectives and the relative variations of internal forces of cable SS1 under three different pre-stress states are shown in Table 4.

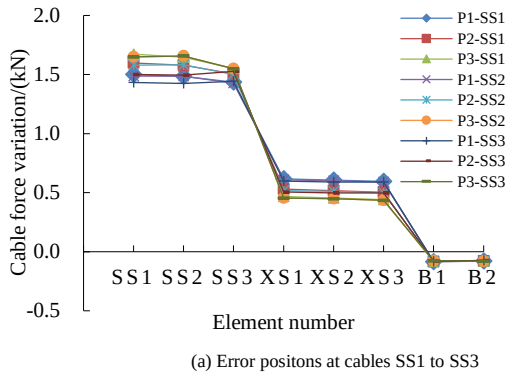

(a) Error positons at cables SS1 to SS3

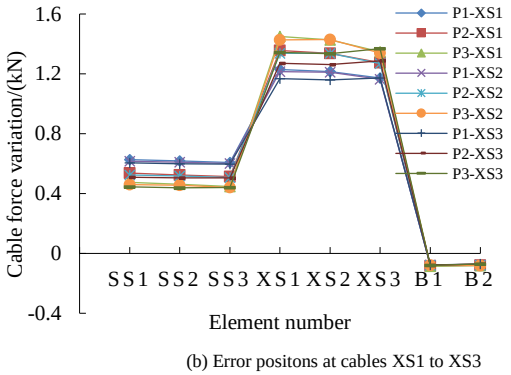

(b) Error positons at cables XS1 to XS3

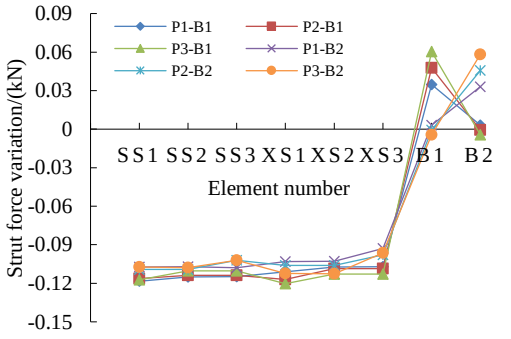

(c) Error positons at struts B1 to B2

Fig. 6 Variation of internal forces for FEM

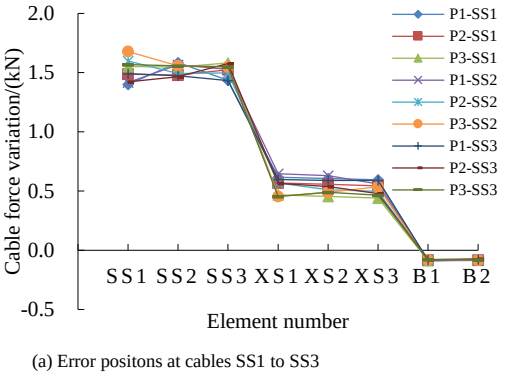

(a) Error positons at cables SS1 to SS3

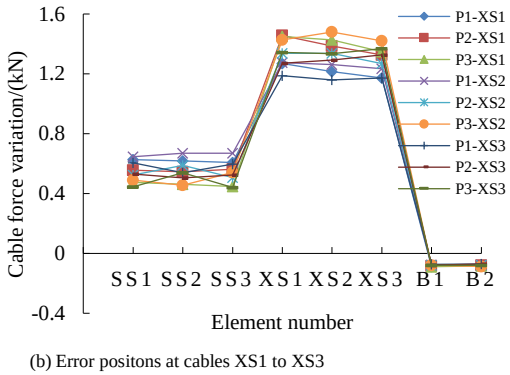

(b) Error positons at cables XS1 to XS3

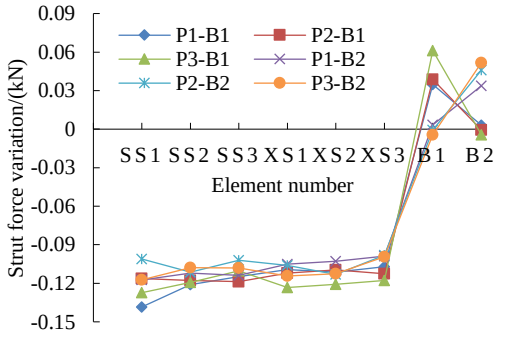

(c) Error positons at struts B1 to B2

Fig. 7 Variation of internal forces for experimental model

It can be seen from Fig. 6 and Fig. 7 that the simulation values agree with the experiment values. The most error between simulation values and experiment values is about 6%, which shows the correctness of experiment data. The variations of internal forces for all components under the three types of pre-stress states are different. The variations of internal forces of cables and struts gradually increase with internal force increase when the cable length errors are located at upper chord cables and struts, and the variations of internal forces of cables and struts gradually decrease with the increase of internal forces when the cable length errors are located at lower chord cables. The phenomenon shows that the influences of length errors of cable and strut on internal forces of components have certain influences. The larger the pre-stresses change, the larger the variations of internal forces are. It can also be seen from Table 4 that the simulation values agree with the experiment values and the most errors are within 8%. The relative variations of internal forces of cables and struts gradually increase with the increase of the difference of two kinds of pre-stress level. So the different kinds of pre-stress states should be considered in design.

5. The influences of length errors on the cable-truss frames at different positions

In order to study the influences of cable length errors on the cable-truss frames of different positions, four different types of cable-truss frames are designed. The four cable-truss frames include cable-truss frame 1-4, cable-truss frame 3-10, cable-truss frame 1-8 and cable-truss frame 7-10 in Fig. 3, respectively. According to the correlation of four types of cable-truss frames, the cable-truss frame 1-4 can be named as cable-truss frame itself (CTF1) and the cable-truss frame 3-10 can be named as near cable-truss frame (CTF2) and the cable-truss frame 1-8 can be named as interval cable-truss frame (CTF3) and the cable-truss frame 7-10 can be named as interval two cable-truss frame (CTF4), which is shown in Fig. 8. The sensitive indexes of cable is the Eq. (3). Similarly, the sensitive indexes of sturts can be gained by using the same way as Eq. (3).

The sensitive indexes of cables and struts for four types of cable-truss frames are gained based on the pre-stress state 2 in Table 3 when the errors of cables and struts are located at cable-truss itself. The solved sensitive indexes are shown in Fig. 9. The sign "SS1-CTF1" refers to the sensitive indexes of CTF1 (cable-truss frame itself) when the error is located at SS1, and other signs can be expressed by the same way.

It can be seen from Fig. 9 that length errors of cable and strut have great influence on the cable-truss frame itself (CTF1) and have little influence on the other three cable-truss frames (CTF2 to CTF4). When the cable length errors are located at SS1 to SS3, the most sensitive index of CTF1 is 532.50 kN/m and the most sensitive index of CTF2 to CTF4 is 49.97 kN/m. When the cable length errors are located at XS1 to XS3, the most sensitive index of CTF1 is 452.00 kN/m and the most sensitive index of CTF2 to CTF4 is 65.33 kN/m. When the cable length errors are located at B1 to B2, the most sensitive index of CTF1 is 39.00 kN/m and the most sensitive index of CTF2 to CTF4 is 5.47 kN/m. It can be seen from the analysis results that cable length errors have much greater influence on SCSWIRC than strut length error, so the strut length error can be

ignored in design and mechanical analysis. Meanwhile, the sensitive indexes of cables can be recognized as “sensitive component” and the sensitive indexes of struts can be recognized as “insensitive component”. The classification method helps to simplify the calculation process and distinguish the importance of components.

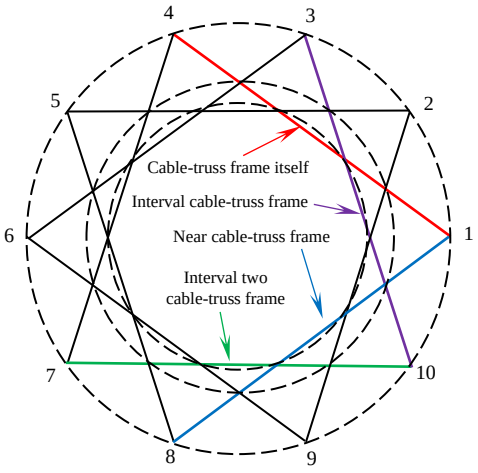

Fig. 8 Positions of four kinds of cable-truss frames

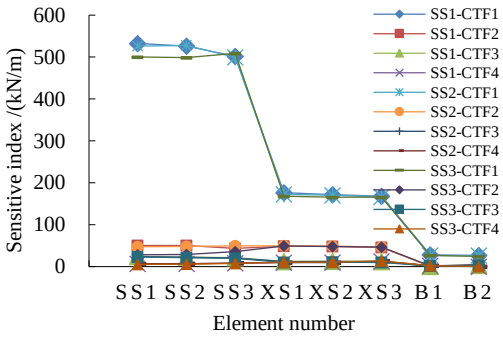

(a) Error position at cables SS1 to SS3

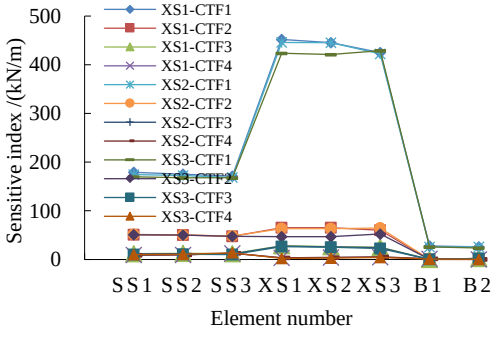

(b) Error position at cables XS1 to XS3

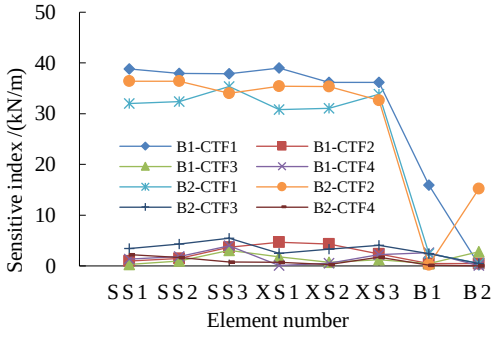

(c) Error position at struts B1 to B2

Fig. 9 Sensitive indexes when errors are located at cable-truss frame itself (CTF1)

6. Influence of manufacturing errors on the mechanical property of SCSWIRC under external loads

In order to further study the influence of manufacturing errors of components on the mechanical property of SCSWIRC under external loads, the sensitive analysis of all kinds of components are studied by numerical analysis and experiment research. The external loads can be divided into two types of full-span loads and half-span loads, shown in Fig. 10. The two types of loads are applied to the experimental model and FEM by the form of five loading levels. The external loads applied to the structure can be transformed into the equivalent nodal load, and the equivalent nodal load can be calculated by Ref. [1]. The equivalent nodal load can be expressed as F=[F_{N1}, F_{N2}]=[-0.429, -0.361] kN shown in Fig. 10, and the negative sign stands for the vertical direction. The five levels of loading can be written as 0.4F, 0.6F, 0.8F, 1.0F, 1.2F. In the experiment, the external loads are replaced with the iron block and the experimental models under the full-span load and half-span load are shown in Fig. 11. It can be known from Section 3 that manufacturing errors have great influence on cable-truss frame itself and have little influences on the other three kinds of cable-truss frames, so cable-truss frame itself is taken as the research objective. The monitoring points are shown in Fig. 4b. The length of cables and struts are shortened by 3 mm for FEM and experimental model, respectively.

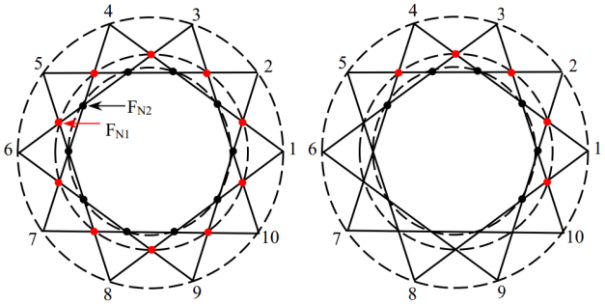

(a) Full-span load (b) Half-span load

Fig. 10 Planar layout diagram of full-span and half-span loads

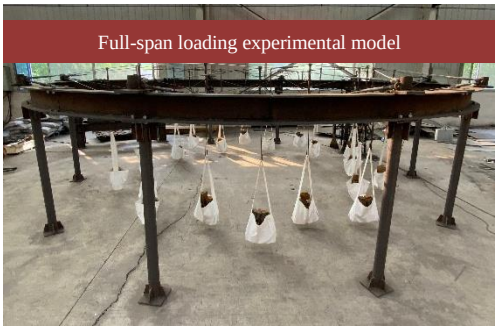

(a) Full-span loading experiment

(b) Half-span loading experiment

Fig. 11 Full-span and half-span loading experimental model

6.1. Cable length errors of upper chord cables

When manufacturing errors are located at SS1 to SS3, the solved sensitive indexes under full-span loads and half-span loads are shown in Fig. 12. The symbol “S” stands for “simulation value” and “E” stands for “experiment value”, the same below.

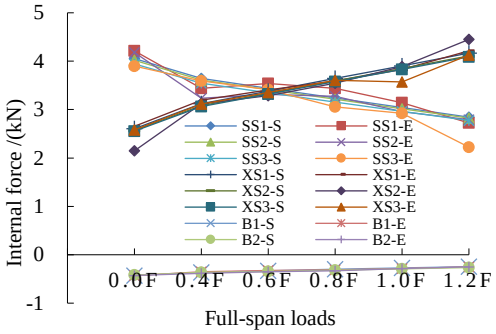

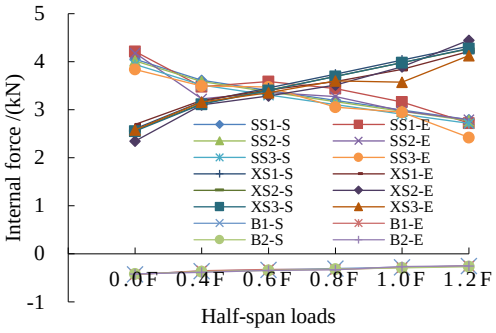

(a) Error position at SS1

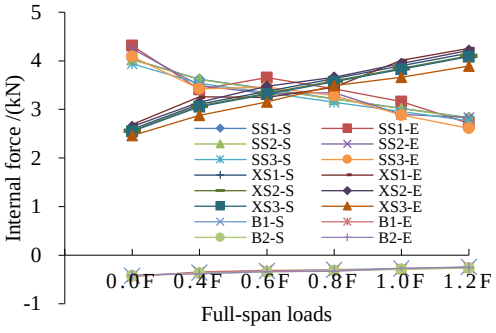

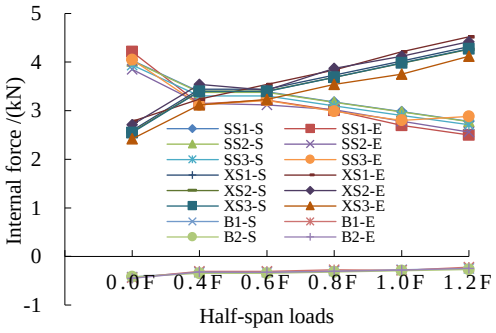

(b) Error position at SS2

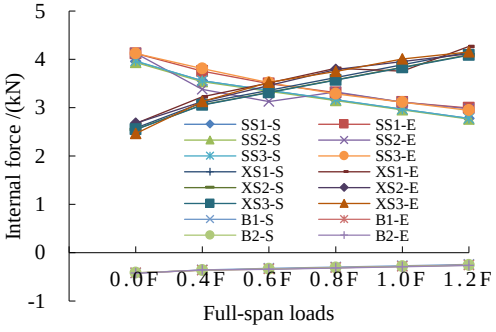

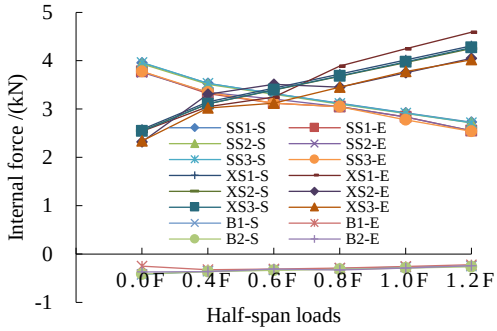

(c) Error position at SS3

Fig. 12 Internal forces under full-span and half-span loads when error positions are located SS1 to SS3

It can be seen from Fig. 12 that the experiment values agree with the simulation values when the errors are located at SS1~SS3 and the most errors are in the range of 2.34% to 6.25%. With the increase of full-span loads and half-span loads, the internal forces of SS1 to SS3 and B1 to B2 gradually decrease and the internal forces of XS1 to XS3 gradually increase, which shows that the external loads do not change the structural basic mechanical property when the components have the manufacturing errors. The internal forces of SS1 to SS3 under half-span loads are slightly less than those of SS1 to SS3 under full-span loads, and the internal forces of XS1 to XS3 under half-span loads are slightly greater than those of XS1 to XS3 under full-span loads. Namely, the internal forces of the upper and lower chord cables change significantly and the upper chord cables are easier to loose under the half-span loads and half-span load is more unfavorable to structures. Meanwhile, the internal forces of B1 to B2 gradually increase with external load increase, but the amplitude is slight. So the half-span loads have great influences on the internal forces of SCSWIRC. The change laws of upper and lower chord cables also show that cables belong to “sensitive component” and the struts belong to “insensitive component”, which conforms to the conclusions in Section 4. It can further be known from Eq. (3) that the sensitive indexes under half-span loads are slightly greater than those of full-span loads. Meanwhile, the main reasons of producing error include four aspects: (1) There are a certain differences between the FEM and experimental model; (2) The strain gauges are slightly drifting in measurements; (3) The measuring instrument will produce some errors; (4) The surrounding temperature has some influences on the experimental model.

6.2. Cable length errors of lower chord cables

When manufacturing errors are located at XS1 to XS3, the solved internal forces are shown in Fig. 13.

It can be seen from Fig. 13 that the experiment values agree with the simulation values when the errors are located at XS1 to XS3 and the most errors are in the range of 3.15% to 5.87%. With the increase of external loads, the internal forces of SS1 to SS3 and B1 to B2 linearly decrease and the internal forces of XS1 to XS3 linearly increase, which shows that the external loads do not change the basic mechanical property of structure when the components have the manufacturing errors. The internal forcecs of SS1 to SS3 under half-span loads are slightly less than those of SS1 to SS3 under full-span loads and the internal force of XS1 to XS3 under half-span loads are greater than those of XS1 to XS3 under full-span loads, which shows that upper chord cables are easier to loose and the half-span loads have greater influences on SCSWIRC. Meanwhile, the reasons of producing errors are similar to Section 5.1, so do not repeat it again.

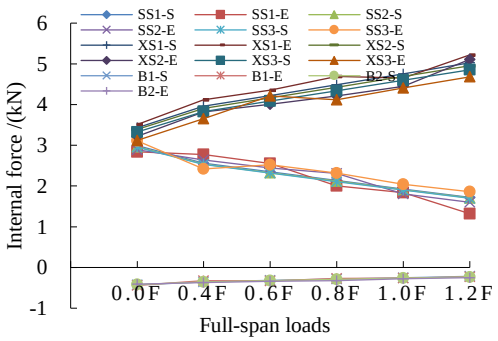

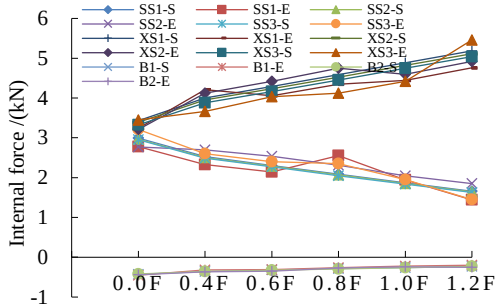

(a) Error position at XS1

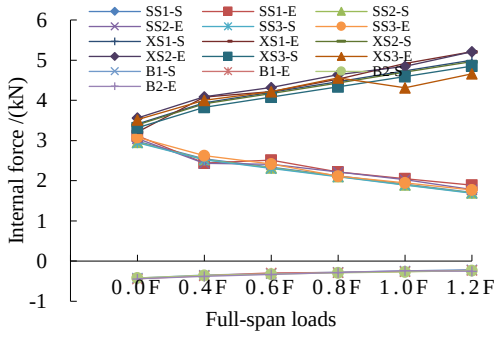

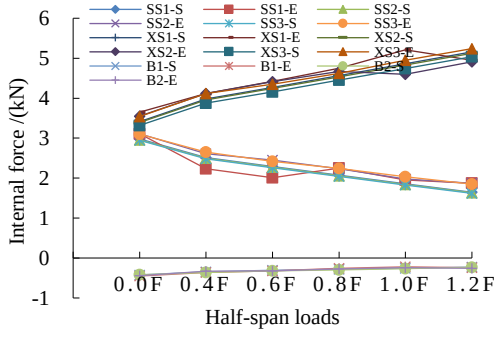

(b) Error position at XS2

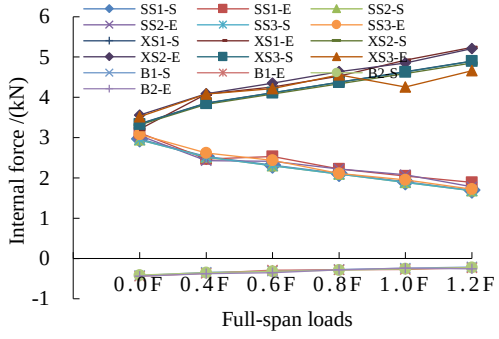

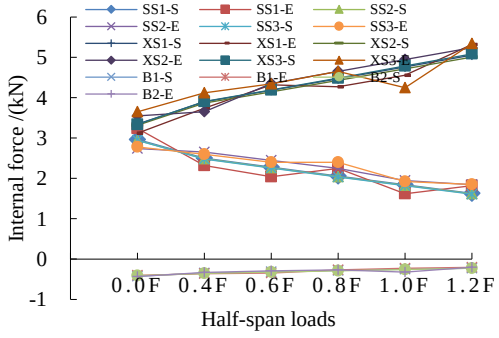

(c) Error position at XS3

Fig. 13 Internal forces of XS1~XS3 under full-span and half-span loads

6.3. Manufacturing errors of ring-beam and ear-plate

Although the installation and manufacturing errors of ring-beam and ear-plate are difficult to be simulated in Finite Element Software, the kind of errors will directly result in the elongation of upper and lower chord cables. So the installation and manufacturing errors of ring-beam and ear-plate can be equivalent to the errors of upper and lower chord cables. When the errors are located at ring-beam and ear-plate, the corresponding internal forces can be gained shown in Fig. 14.

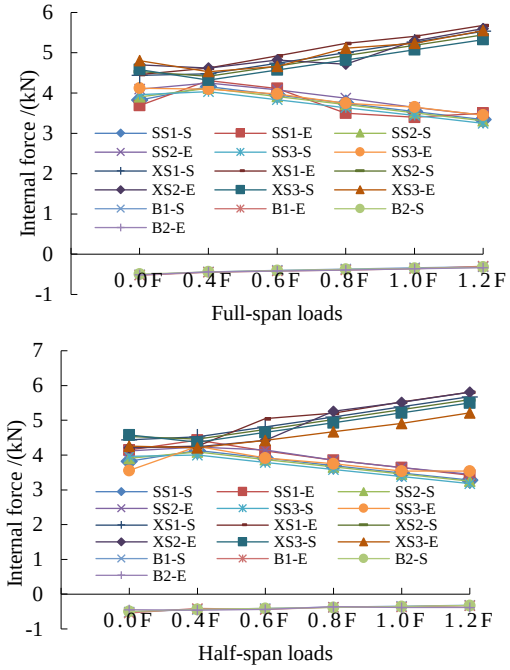

Fig. 14 Internal forces of ring-beam and ear-plate under full-span and half-span loads

It can be seen from Fig. 14 that the experiment values agree with the simulation values and the most errors are in the range of 2.65% to 7.21%. The reasons of producing errors are similar to Section 5.1 and Section 5.2. With the increase of external loads, the internal forces of upper chord cables linearly decrease and the internal forces of lower chord cables linearly increase, which shows that the external loads do not change the structural basic mechanical property when the components have the manufacturing errors. The variations of internal forces under half-span loads are larger than those of full-span loads. When error positions are located at ring-beam and ear-plate, the internal force variations under external loads are far greater than those of non-loads.

6.4. Manufacturing errors of struts

When the errors are located at ring-beam and ear-plate, the corresponding internal forces can be gained shown in Fig. 15.

It can be seen from Fig. 15 that the experiment values agree with the simulation values and the most errors are in the range of 1.79% to 5.47%. With the increase of external loads, the internal forces of upper chord cables gradually decrease and the internal forces of lower chord cables gradually increase, which shows that the external loads do not change the basic mechanical property of the structure when the components have the manufacturing errors. Meanwhile, the internal forces of B1 to B2 gradually increase with the increase of external loads, but the amplitude is slight. The change laws of upper and lower chord cables also show that cables belong to “sensitive component” and the struts belong to “insensitive component”, which conforms to the conclusions in Section 4. The internal force variations of upper and lower chord cables under half-span loads are greater than those of full-span loads, which shows that the half-span loads are unfavorable to the structure. The main reasons of producing errors are the same, so there are no more repeat again.

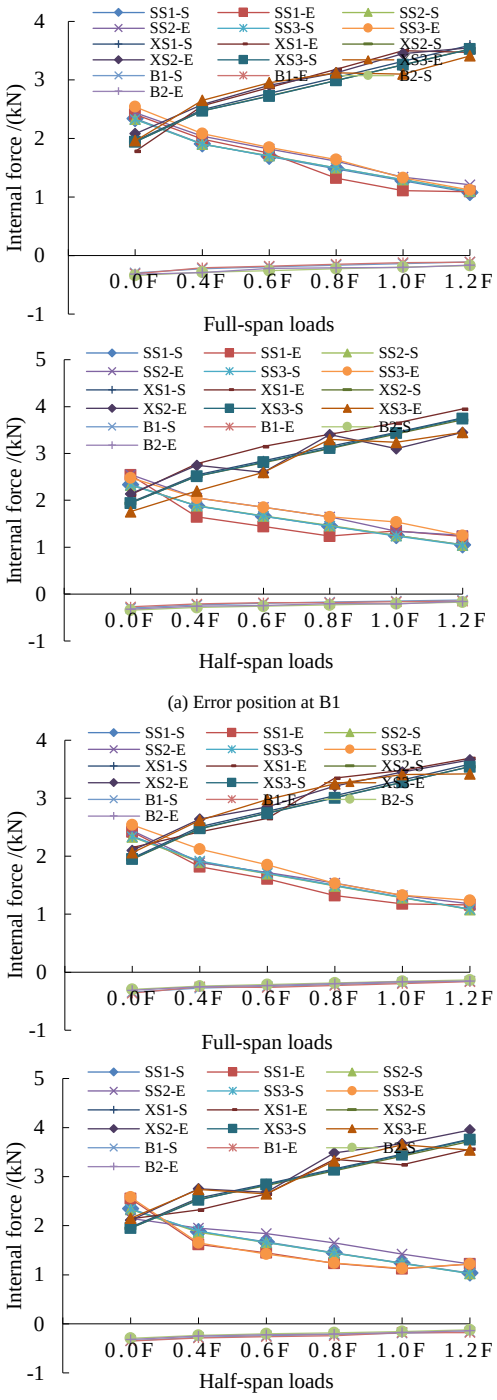

(a) Error position at B1

(b) Error position at B2

Fig. 15 Internal forces of B1 amd B2 under full-span and half-span loads

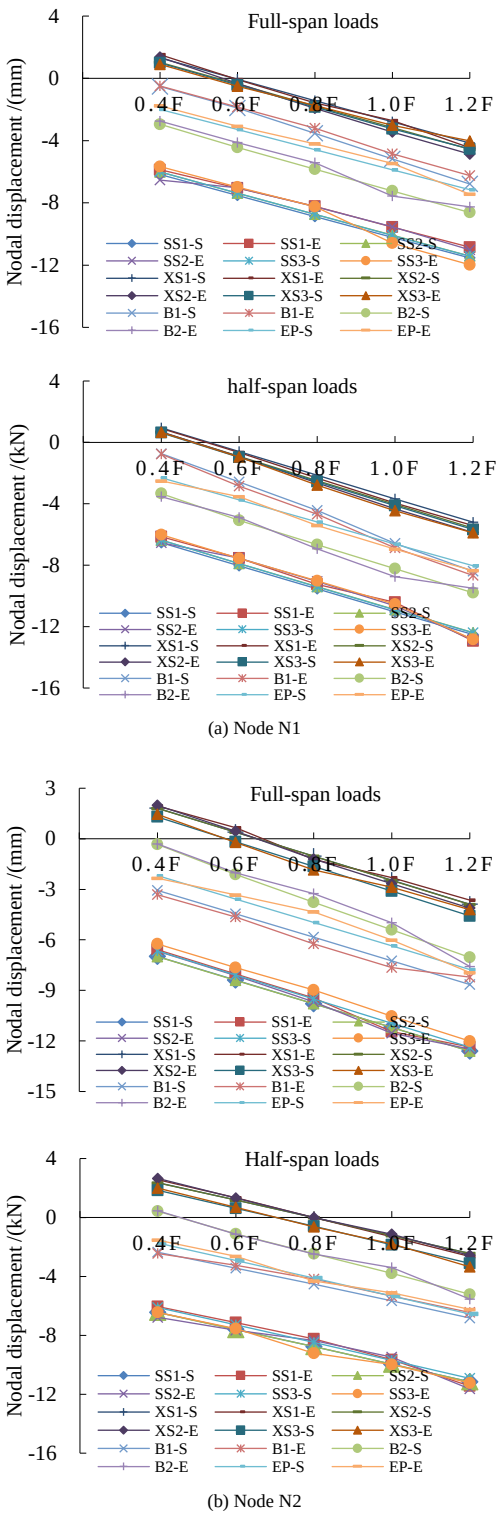

(a) Node N1

(b) Node N2

Fig. 16 Nodal displacements under full-span and half-span loads when errors are located at SS1 to SS3, XS1 to XS3, B1 to B2 and ear-plate

6.5. Influences of manufacturing errors on nodal displacements

When the error positions are located at SS1 to SS3, XS1 to XS3, B1 to B2 and ring-beam and ear-plate, the nodal displacements of N1 and N2 are gained under the external loads. The results are shown in Fig. 16.

It can be seen from Fig. 16 that the experiment values agree with the simulation values and the most errors are in the range of 2.25% to 6.37%. The nodal displacements gradually increase with the external loads. The nodal displacements under the external loads of 0.4F and 0.6F are the positive values when the error positions are located at lower chord cables (XS1 to XS3), which shows that the shortening of upper chord cables can make the SCSWIRC up toward. Similarly, the elongation of lower chord cables can make the SCSWIRC down. Meanwhile, the nodal displacements under half-span loads are greater than those of full-span loads, which shows that the half-span loads are unfavorable to the structure.

7. Conclusions

Based on ACCTS, the influences of manufacturing errors on structural mechanical property are studied from four aspects. The main conclusions as follows:

(1) The elongation or shortening of cable and strut has little influences on the sensitive indexes of cable and strut in the linear elastic state.

(2) The manufacturing errors have the different influences on the mechanical property of structure under the different pre-stress states, so the rational pre-stress level should be selected in practical engineering cases.

(3) The component errors have great influences on cable-truss frame itself and have little influences on the other cable-truss frames. Namely, the closer cable-truss frame is to the error position, the larger influence the error has on cable-truss frame.

(4) The external loads do not changed the basic mechanical property of structure, but the external loads make upper chord cables easier to loose and make sensitive indexes change more greatly. So the influences of external loads on structure should be considered in design.

Meanwhile, there are some problems in the paper. Such as, when cable-strut joints slip, there are no scholars to study the influences of joint slip on the manufacturing errors of structure. The author will continue to study how joint slip effects the structural mechanical property based on the manufacturing errors.

Acknowledgments

The authors would like to acknowledge the financial support of the National Natural Science Foundation of China (51778017).

References

[1] Guo J M, Jiang J Q. An algorithm for calculating the feasible pre-stress of cable-struts structure. Engineering Structures, 2016, 118(01): 228-239.
[2] Guo J M, Zhou D. Pretension simulation and experiment of a negative Gaussian curvature cable dome. Engineering Structures, 2016, 127: 737-747.
[3] Liu R J. Annular Crossed Cable-truss Structures: Numerical and Experimental Verification [D]. Brussels: Crazy Copy Press, 2017.
[4] Xue S D, Lu J, Li X Y, Liu R J. Improved force iteration method based on rational shape design solving self-stress modes of cable-truss tensile structure. Advanced Steel Construction, 2020, 16(02): 170~180.
[5] Xue S D, Liu R J, Li X Y, Marijke Mollaert. Concept proposal and feasibility verification of the annular crossed cable-truss structure. International Journal of Steel Structures, 2017, 17(04): 1549-1560.
[6] Lu J, Li X Y, Xue S D, Liu R J. Study on force mechanism of cable-truss frame and jumped layout of annular crossed cable-truss structrue. Advanced Steel Construction, 2021, 17(03): 243~252.
[7] Liu R J, Li X Y, Xue S D, Marijke Mollaert, Ye J H. Numerical and experimental research on annular crossed cable-truss structure under cable rupture. Earthquake Engineering and Engineering Vibration, 2017, 16(03): 557-569.
[8] Lu J, Xue S D, Li X Y, Liu R J. Study on membrane roof schemes of annular crossed cable-truss structure. International Journal of Space Structures, 2019, 34(3-4): 85-96.
[9] Tian G. Y, Guo Y L, Zhang B H, Wang K, Zhao S Y. Experiment on sensitivity to construction tolerance and research on tolerance control criteria in spoke structural roof Bao'an Stadium. Journal of Building Structures, 2011, 32(03):11-18.
[10] Gao Z Y, Xue S D, Wang T. Four-step tensioning construction method and experimental study for rigid bracing dome. International Journal of Steel Structures, 2015, 47(4): 1947-1958.
[11] Deng H, Zhang M R, Liu H C, Dong S L, Zhang Z H, Chen L Q. Numerical analysis of the pretension deviations of novel Crescent-shaped tensile canopy structural system. Engineering Structures, 2016, 119: 24−33.
[12] Adam B, Smith IF. Self-diagnosis and self-repair of an active tensegrity structure. Journal of Structural Engineering, 2007, 133(12):1752-1761.
[13] Adam B, Smith IFC. Active tensegrity: a control framework for an adaptive civil-engineering structure. Computers & Structures, 2008, 86(23-24):2215-2223.
[14] Korkmaz S, Ali NBH, Smith IFC. Configuration of control system for damage tolerance of a tensegrity bridge. Advanced Engineering Informatics, 2012, 26(1):145-155.
[15] Liang X T, Yuan X F, Dong S L. Active control experiments on a herringbone ribbed cable dome. Journal of Zhejiang University-Science A (Applied Physics & Engineering), 2018, 19(09): 704-718.
[16] Luo B, Sun Y, Guo Z X, Pan H T. Multiple random-error effect analysis of cable length and tension of cable-strut tensile structure. Advances in Structural Engineering, 2016, 19(8): 1289-1301.
[17] Jin X F, Fan F, Shen S Z. Parameter sensitivity analysis of the cable-net structure supporting the reflector of a large radio telescope-FAST. China Civil Engineering Journal, 2010, 43(02): 12-19.
[18] Kong X, Jiang P, Wang Q M. A study of influences of value variations of structural parameters on forces in cables in the net structure of cables of the FAST. Astronomical Research & Technology, 2015, 12(02): 159-165.
[19] Shen Y Z, Luo B, Xie G R, Guo Z X, Jiang P. Error sensitivity analysis and multiple error coupling analysis of FAST cable-net supporting structure. Journal of Mechanical Engineering, 2017, 53(17): 10-16.
[20] Shen S Z, Xu C B, and Zhao C. Suspension structure design [M]. China Architecture & Building Press, 17-19, 2006.

Advanced Steel Construction – Vol. 19 No. 2 (2023) 121–129
DOI:10.18057/IJASC.2023.19.2.4

ROTATIONAL RESISTANCE TEST OF A NEW ALUMINUM ALLOY PENETRATING (AAP) JOINT SYSTEM

Hui-Huan Ma [1, 2, 3], Chen-Yang Zhao [1, 2, 3, *], Yu-Qi Jiang [4, *], Guang-Tong Zhou [4] and Yu-Jin Wang [5]

[1] *School of Civil Engineering, Sun Yat-Sen University, Guangzhou, PR China*
[2] *Guangdong Key Laboratory of Oceanic Civil Engineering, PR China*
[3] *Key Laboratory of Building Fire Protection Engineering and Technology of MPS*
[4] *Harbin Institute of Technology, Harbin, 150090, China*
[5] *College of Ocean and Civil Engineering, Dalian Ocean Univ., Dalian 116023, China*
** (Corresponding author: E-mail: zhaochy28@mail.sysu.edu.cn; jiangyuqi@hit.edu.cn)*

ABSTRACT

Aluminum alloy penetrating (AAP) joint is an improved form of the Aluminum Alloy Temcor (AAT) joint system consisting of one penetrating member, four short members, gussets, bolts and a U-shaped connector. The rotational resistance performance of AAP joints is investigated by a static out-of-plane flexural test. The specific experimental parameters include the gusset thickness (6 mm and 12 mm) and shape (circular and X-shaped). The differences between penetrating and short members in AAP joints are analyzed, and the influence of thicknesses and shapes of gusset on rotational resistance behavior of the joints is analyzed. The establishment of the finite element model of the AAP joint system in this paper considers the effects of bolt pre-tightening force, installation gap and friction between contact surfaces. The M-Φ curves and damage patterns are obtained by numerical simulation. The detailed comparative analysis between AAP joint numerical simulation and test results verifies the accuracy of the numerical model.

ARTICLE HISTORY

Received: 8 January 2022
Revised: 29 June 2022
Accepted: 29 June 2022

KEYWORDS

Aluminum alloy penetrating (AAP) joint;
Semi-rigid joint;
Single-layer reticulated shell;
Rotational resistance test;
Numerical simulation

1. Introduction

The technology for producing aluminum alloy originated from the aerospace industry. In European and American countries, aluminum alloy buildings first appeared in the 1940s. It has been used widely and rapidly due to the unique advantages of aluminum alloy material [1]. China began to study aluminum alloy for construction in the 1990s and gradually applied it in building structures such as street overpasses, chemical storage tanks and stadium roofs [2]. The advantages of lightweight, corrosion resistance, and high strength make aluminum alloy an irreplaceable building material [3]. Aluminum alloy is particularly suitable for building structures exposed to corrosive environments for a long time. It has excellent prospects for development in large-span spatial structures with increasingly complex and diverse shapes [4]. There are already thousands of aluminum alloy space structures [5], of which the single-layer latticed shell structures account for the most siginificant proportion.

Single-layer free-form structures are increasingly being used in the roof structures of large-scale stadiums because they are more aesthetically pleasing and have more varied structural shapes. Therefore, the forms of aluminium alloy also need to adapt to this changing trend. The aluminium alloy joints used in space structures should have the load-bearing capacity and stiffness that meet the design requirements and have the characteristics of fast construction and high installation accuracy [6, 7]. Research and development of new types of aluminium alloy joints have been carried out, both nationally and internationally. Hoang et al. [8,9]conducted tests and numerical investigations on the self-piercing riveted joints. Matteis et al. [10,11] studied the performance of T-stub joints using finite element analysis and provided proposals for relevant amendments to the code for aluminium alloy construction. The design suggestions for welded connections [12] and cast aluminum joints [13] was also given by systematic study. The most widely used joint in China is the AAT joint system connecting H-section members. A lot of research have been done on the mechanical properties of AAT joints, including teats and numerical simulations under normal and high-temperature conditions. Ma [14, 15] developed an aluminum hollow prism-plate joint and investigated its moment resistance behavior subjected to moments and axial forces. Liu [16, 17] carried out a numerical analysis on semi-rigidly aluminum reticulated shells considering skin effect. Xiong [18~22] Research on the semi-rigid performance of aluminum gusset joints and single-layer reticulated shells under different loads and temperatures. Current research on aluminum reticulated shells are limited. However, a series of studies of the stability of steel latticed shells has been conducted. Fan [23-25] studied the elastoplastic stability of the reticulated shells by considering geometric and material nonlinearity. Through the comparison of buckling load, the plastic influence coefficients of various types of reticulated shells were summarized. The influence of random variables such as angles and amplitudes of initial curvature on the ultimate load of the reticulated shell was investigated, and an improved tolerance modal method was proposed, which could effectively calculate the minimum bearing load with initial curvature. Moreover, series of studies have been done on the semi-rigid joints in steel framing structures and space structures [26-29]. Hiyama [30] conducted load tests and numerical simulations on the aluminum alloy reticulated shell models composed of tubular members and spherical joints to discuss the buckling response. On this basis, a method for estimating the buckling strength of aluminum reticulated shells was proposed. Xiong [31] conducted an 8-meter aluminum spherical reticulated shell experiment and studied its buckling behavior and distribution of internal force. The numerical simulation method was used to analyze the effetcs of joint bending behavior on the buckling behavior of single-layer latticed shells.

In this paper, an improved form of the AAT joint system was proposed. The Aluminum alloy penetrating (AAP) joint consisted of one penetrating member, four short members, gussets, bolts and a U-shaped connector. The rotational resistance performance of AAP joints was investigated by static out-of-plane flexural test. The specific experimental parameters included the gusset thicknesses and shapes. The difference between the penetrating members and the short members in the AAP joints was concluded by analyzing the moment (M)-rotation (Φ) curves and damage patterns and the effects of gusset shapes and thicknesses on the joint performance was studied. An AAP joint simulation analysis model corresponding to the experiment was established. The detailed comparison analysis between the simulation and test results verified the accuracy of the finite element model.

2. Aluminum alloy penetrating (AAP) joint system

In aluminium alloy structures, the members are commonly connected by mechanical methods due to poor weldability, with the AAT aluminium alloy joint shown in Fig. 1 being the most common. In China, AAT joint system is used in more than 95% of the aluminium alloy single-layer latticed shell structures. The Shanghai Chenshan Botanical Garden completed in 2010 adopted the AAT joints to connect aluminium H-section members. However, in the joint region, the webs of the members of AAT joints are disconnected, which causes defects such as poor shear resistance and unclear load transmission paths.

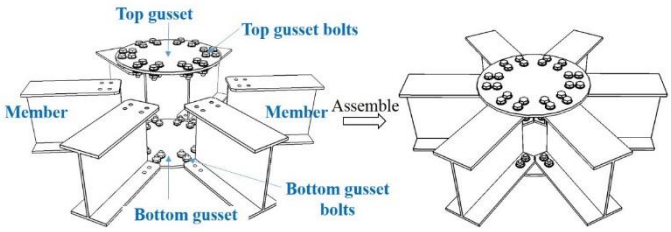

Fig. 1 Construction of AAT joint

To improve the mechanical properties of AAT joints, an improved form, AAP joint system, was proposed. The AAP joint system is composed of penetrating members, short members, U-shaped connectors, gussets and bolts, as shown in Fig. 2. The addition of the U-shaped connectors in the joint region allows the penetrating members to be joined to the short members as a single unit. At the same time, the presence of penetrating members solves the problem of discontinuous webs to some extent. This modification is effective at improving the shear resistance performance and stiffness of the joint.

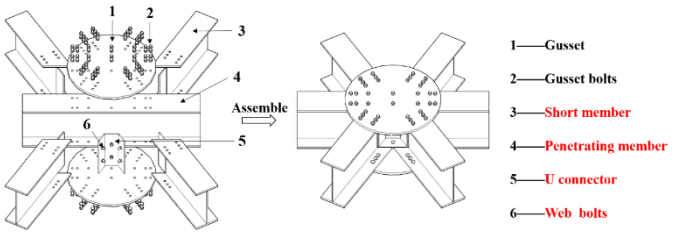

Fig. 2 Construction of AAP joint

3. Static tests of the AAP joints under bending moment

The rotational resistance behavior of the AAP joints was researched by means of an out-of-plane flexural test. The actual bearing capacity and damage patterns were obtained in order to verify the joint performance and ensure the safety and reliability of the structure. The test data such as damage patterns and M-Φ relationships of the specimens were obtained. The effects of gusset shapes and thicknesses on the moment bearing capacity and damage patterns of the joints was studied, as well as the stress distribution and force transmission mechanism.

3.1. Test loading and measuring devices

The purpose of the AAP joint test was to investigate the rotation resistance performance under the out-of-plane bending loads. Therefore, the five members of the joint needed to be pinned with a reaction force frame to achieve a bending moment.

Fig. 3 was the whole test device, including specimens, supports, reaction frame and loading and measuring instruments. A 200-ton hydraulic jack was used as the loading device. The force sensor was put between the distribution beam and the hydraulic jack. The distributive beam was a welded steel beam consisting of 6 H-section limbs which were equal in length. If the load was applied in the center of the distributive beam, it ensured that the concentrated vertical force would be separated, and the six component forces would be applied on each member equally.

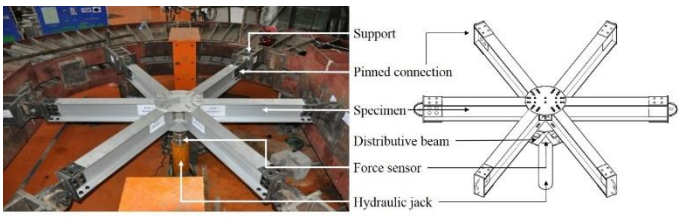

(a) Loading device

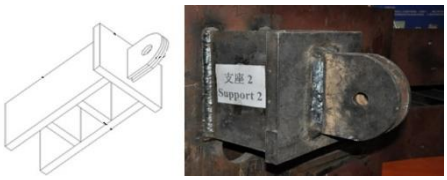

(b) Details of supports

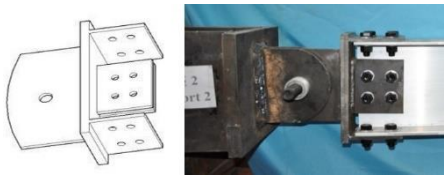

(c) Details of pinned connections

Fig. 3 Test devices

A force-controlled loading scheme was adopted. A hydraulic push-pull jack of which the loading speed could be controlled was used as the loading device. The loading speed during formal loading was controlled at 5 kN/min. The loading process was divided into two periods. In the first period, pre-loading, a small load was applied to the specimens to check whether the test device was working properly and making each part in close and stable contact. During the formal loading, a force-controlled loading scheme was used until the joint was broken. During each stage of the test, the load-holding time was not less than 10 minutes. When the load was loaded to the later stage, the load-displacement curve showed a horizontal section and a falling section. When the joint bearing capacity dropped to 80% of its maximum value during loading, the test was terminated. The data that were measured during the test include:

(i) Vertical load was measured by the force sensor;

(ii) Vertical displacements of the test specimens were measured by LVDTs, of which the arrangement and number were shown in Fig. 4(a). Three LVDTs were approximately equidistantly arranged on each member, and a dial indicator was arranged at the end of each of the six supports to measure the displacements.

(iii) Strain was collected by the tester and strain gauges. So as to monitor the stress changes of the components near the joint area, the gauges were placed near the bolt-holes, the webs and U-shaped connector where easy to yield during the loading. Fig. 4(b) was the position of strain gauges.

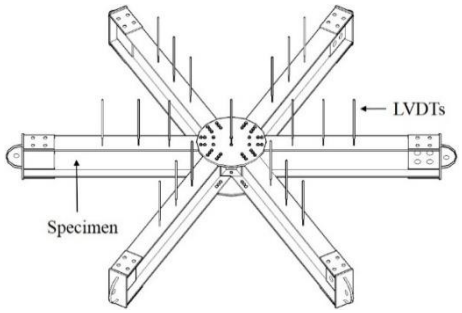

(a) Arrangement of LVDTs

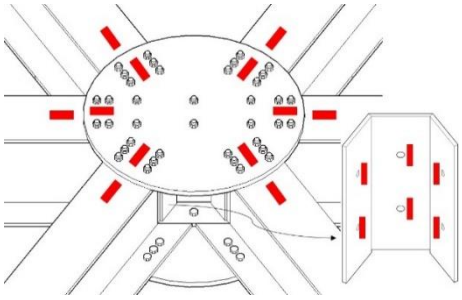

(b) Position of strain gauges

Fig. 4 Test measure device

3.2. Information of specimens

Table 1 listed the specific parameter settings of the AAP joint test, which

mainly investigated the effects of the gusset thicknesses and shapes on the moment bearing capacity and stiffness of AAP joints. Therefore, under the condition that the connection between the rod and the node is consistent, three gussets are designed as shown in Fig. 5: 6 mm circular gusset, 12 mm circular gusset and 12 mm X-shaped gusset, which reduced the material of the gusset in low-stress areas based on the original circular joint gusset.

Table 1
Parameter settings of specimens

Group number	Specimen number	Specimens	Gusset shape	Gusset thickness
Z1	2	Z1-A, Z1-B	Circular	6 mm
Z2	2	Z2-A, Z2-B	Circular	12 mm
Z3	2	Z3-A, Z3-B	X-shaped	12 mm

(a) Z1

(b) Z2

(c) Z3

Fig. 5 Three types of specimens

The gussets and H-section members were both 6061-T6 aluminum alloy. The sizes of specimens showed in Fig. 6. 6061 aluminum alloy had excellent machinability and corrosion resistance. Aluminum alloy 6061-T6 was widely used in building structures because of its excellent characteristics. The U-shaped connectors and the bolts were stainless steel. The bolt-holes on all the components were precision-machined using a CNC bed with high accuracy. Each component was connected by Huck bolts which were made of stainless steel. Six bolt-holes were designed on the top and bottom flanges of each short member, while the penetrating member was designed with six bolt-holes on each side of the flanges. In order to prevent the bolt spacing in the middle part from being too large, a set of two bolt-holes were set at the center of the meshing member. Meanwhile, two bolt-holes were designed in the web of each H-section member. Each U-shaped connector was bolted with three webs of members. The diameter of bolt and bolt-hole were 9.66 mm and 10 mm.

3.3. Material property tests

In order to understand and study more accurately the material properties of the joint specimens and prepare for the later numerical simulation research, the material properties of the main material of the joint (6061-T6 aluminum alloy) were tested. Specimens of material were sampled from the 6 mm gussets, 12 mm gussets and flanges and webs of H-section aluminum members, respectively, according to the national standard GB/T228.1-2010 [32]. The specific time dimension is shown in Fig. 7. The material properties curves obtained from different 6061-T6 aluminum alloy specimens are shown in Fig. 9 and Table 2.

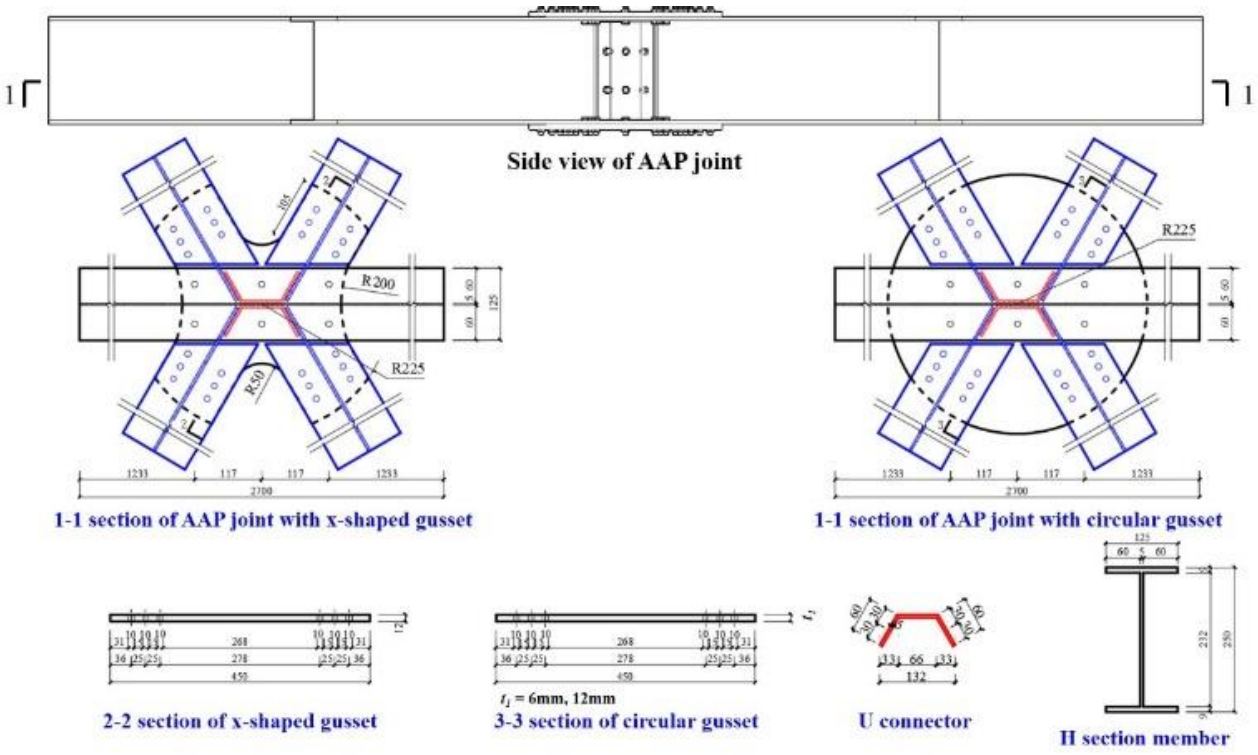

Fig. 6 Sizes of specimens

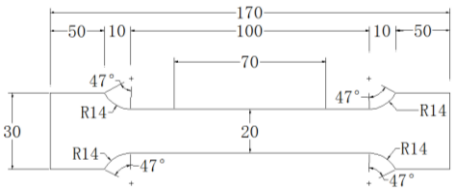

(a) 6 mm gusset

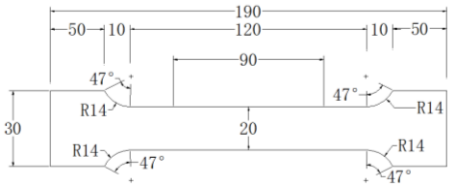

(b) 12 mm gusset

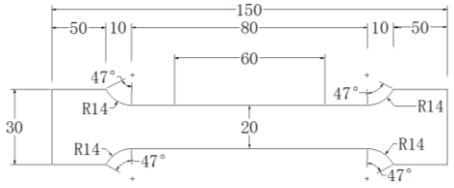

(c) Web of member

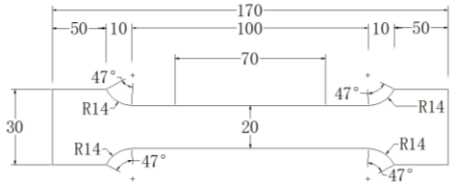

(d) Flange of member

Fig. 7 Dimensions of specimens of aluminum material property tests

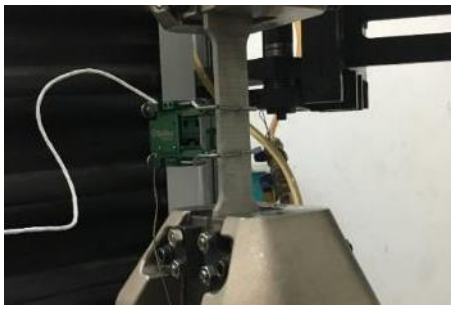

(a) Test device

(b) Specimens before and after tests

Fig. 8 Photographs of material property test

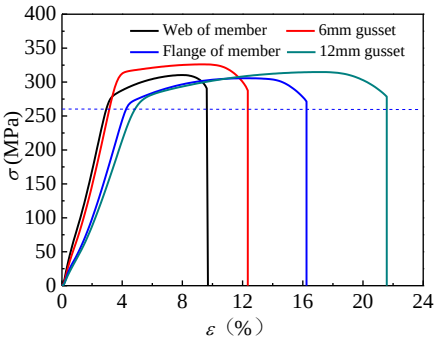

Fig. 9 σ-ε curves obtained from tests

Table 2
Results of material test

Specimen	$f_{0.2}$ (MPa)	f_u (MPa)	E (N/mm^2)
6 mm gusset	319.5	325.5	7.0×10^5
12 mm gusset	308.5	314.4	6.9×10^5
Web of member	301.7	310.3	7.0×10^5
Flange of member	298.5	305.5	6.9×10^5

4. Analysis of test results

4.1. Analysis of moment(M)–rotation(Φ) curves of AAP joint

The test is divided into three groups, with two members in each group, a total of 6 members. Due to small errors in the assembly of the joints, the welding progress of the distribution beams and the installation of the joints, there is a small difference in the stress among the five members. Within the allowable range of errors, the joint stress state can be approximated as the ideal pure bending failure state.

The *M*-*Φ* curves reflected the rotational resistance behavior of the joint. The moment and rotation of this test are calculated from the test data by equation (1) to (3).

$$M = P/6 \times L \tag{1}$$

$$\Phi = \arctan\left(\Delta/L_{ij}\right) \tag{2}$$

$$\Delta = l_i - l_j \quad (i,j = 1,2,3) \tag{3}$$

The M of the joint is the bending moment formed by the load transmitting from each member to the joint area, and the unit is kN•m. P is the concentrated force applied by the jack to the joint, which is measured by the force sensor. As shown in Fig. 10, L is the distance from the center position of the bolt-hole of pinned connections to the contact position between the distributive beam and the joint, specifically 1.115 m. The rotation of the joint, Φ, is defined as the change value of the central axis of the joint under load and no-load, and the unit is rad. Because the deformation of the member can be ignored in this test, Φ is represented by the rotation of the member around the center of the pinned support, Φ_m. Δ is the displacement difference between the two LVDYs after eliminating the bearing displacement, and L_{ij} represents the distance between the two LVDYs in the horizontal direction.

In this paper, some following key parameters of the *M*-*Φ* curves are defined which divide the curves into 3 phases, as shown in Fig. 11. The first phase, the *OA* phase, is the elastic phase which corresponds to the initial moment M_i and initial stiffness K_i of the joint. The second phase, the *AB* phase, is the elastic-plastic phase. In this phase, the moment of point *B* is the bending moment capacity M_{sup}, and the stiffness of this point is yield stiffness K_u. The third phase, the *BC* phase, is the plastic stage, in which the joint area enters the full section yield.

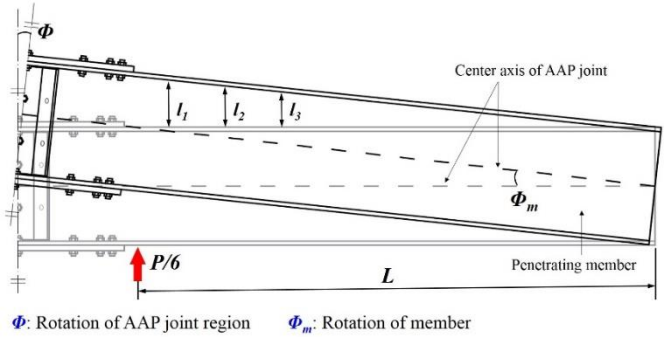

Fig. 10 Schematic diagram of calculation method of moment and rotation of AAP joint

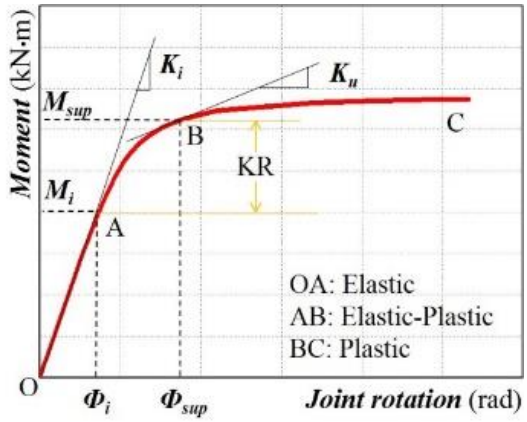

Fig. 11 Key parameters of the moment-rotation curve

4.2. Comparison of penetrating members and short members

The most significant difference between the new AAP and AAT joint is whether the web of the member is continuous or not within the joint area. This section discusses the *M-Φ* curves and damage patterns of the penetrating members and short members under different experimental variables.

Fig. 12 is a comparison diagram of the *M-Φ* curves of penetrating members and short members. Table 3 compares the key parameters of specimens. As shown in the figure, when the thickness of the gusset was 6 mm and the shape was circular, at the initial linear elastic stage, as the joint applied load increased, the rotation value of the penetrating members was always shorter than the short members. The two types of members basically entered the elastic-plastic phase at about 56 kN•m. When the bending moment reached the yielding moment, the rotation of the penetrating member was significantly larger than the short member. At this moment, the penetrating members were torn and then the moment of short members also reached the maximum. After this, the load capacity of the joint reduced, but the joint displacement still increased, and the joint was destroyed. When a pure bending moment was transmitted from the member to the joint area, in the case of 6 mm gusset thickness, due to the smaller gusset thickness, the joint overall stiffness was lower, and the gussets were first torn then destroyed. Compared with short members, penetrating members were more tightly connected to gussets in the joint area. Therefore, the rigidity of the penetrating members was larger than that of the short members, and the penetrating members also preceded the short members when they were damaged.

The difference of force state between the penetrating members and the short members of the joint caused the penetrating members to be the first to fail. When the thickness of the gusset was 12 mm, the values of K_i, M_i, and M_{sup} of the penetrating members and short ones were almost the same in the case of the two gusset shapes. The damage patterns of the joints manifested as simultaneous tears of the penetrating members and short members, and the tearing path appeared to be torn from the tension side of flanges to the webs. Therefore, it could be seen that the force and damage patterns of the two- most areas of the gussets did not member types are consistent. The reason is that when the gusset thickness was larger, the joint overall stiffness was larger. When the joints reached the yielding moment, most areas of the gussets did not buckle. In this case, the gussets were tightly connected to the penetrating members and the short members. The load was transmitted to the gussets by the two types of members, so there is almost no difference in the *M-Φ* curves of the penetrating members and the short members.

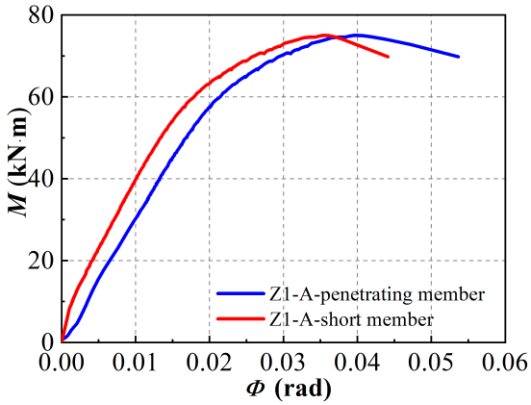

(a) Z1-A

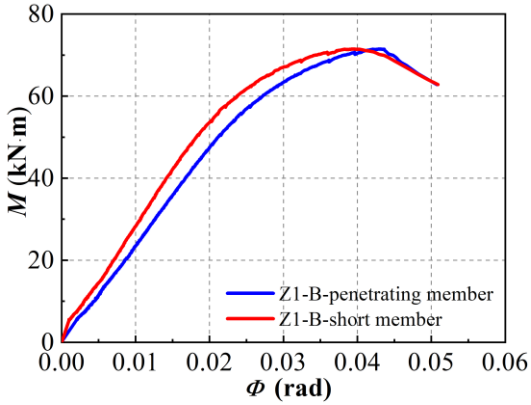

(b) Z1-B

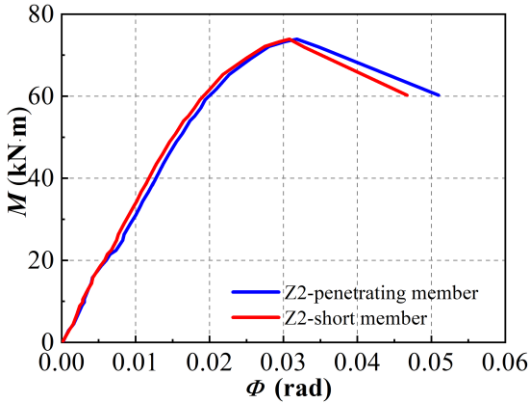

(c) Z2

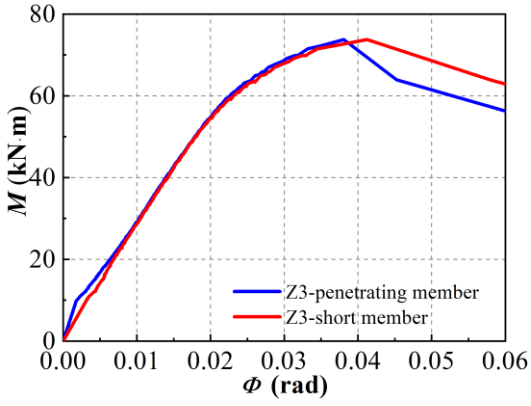

(d) Z3

Fig. 12 Comparison of penetrating members and short members

Table 3
Comparison of key parameters of penetrating members and short members

Group number	Member type	K_i (kN•m/rad)	M_i (kN•m)	M_{sup} (kN•m)
Z1-A	Penetrating	3172.3	56.3	75.04
	Short	2770.9	55.6	75.04
Z1-B	Penetrating	3163.6	53.1	71.42
	Short	2766.3	56.2	71.42
Z2	Penetrating	3182.2	55.2	73.76
	Short	3177.5	55.2	73.76
Z3	Penetrating	3185.6	50.1	67.20
	Short	3180.5	50.1	67.20

4.3. Influence of gusset thicknesses on rotational resistance performance of the AAP joint

The specimens, Z1-A and Z1-B, were circular gusset AAP joints with a gusset thickness of 6 mm. At the beginning of the loading process, the center displacements of the joints increased linearly with the applied load. As the joint gradually entered the plastic stage, the displacement increased rapidly, and the load growth slowed down until it reached the external load of 427.8 kN. After a few minutes, the load began to decrease. When the load dropped to 100 kN•m, loading progress was stopped, and the test data were saved. Fig. 13 is the comparison of the same specimen before and after deformation. It was found that the ultimate bearing capacity and damage patterns of Z1-A and Z1-B were basically consistent. Gussets of both joints buckled significantly, and the gussets tore at the bolt-hole. In addition, it was assumed that the peering members of the joints appeared tear failure and local buckling of the webs, and the damage patterns were shown in Fig. 14 (a).

The specimens, Z2-A and Z2-B, were circular gusset AAP joints with a thickness of 12 mm. During the loading process, the joint displacement also increased with the increasing load. When the average bending moment increased to 442 kN•m, a loud noise erupted. Then, the joint deformed violently, and the load no longer increased and began to drop sharply until the load dropped to 100 kN•m. The final situation after loading is shown in Fig. 14 (b). At that time, due to the larger thickness of the aluminum top and bottom gussets, the gussets had slight bending deformation but no obvious buckling deformation. The members near the joint area had significant tear damage, and the webs near the U-shaped connector also buckled. Comparing the damage patterns of Z1 and Z2, it was found that when the thickness of the gusset was 12 mm, the damage patterns were the buckling of member webs near the joint area and the tear of the flanges. When the thickness of the gusset was 6 mm, except for the damage patterns described above, the joint damage patterns also accompanied the tearing of the joint gussets and the buckling of the gussets.

(a) Before loading

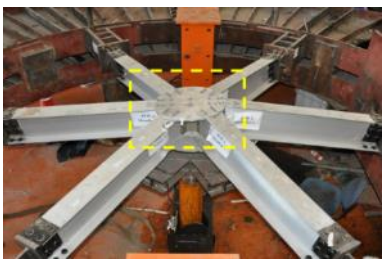

(b) After loading

Fig. 13 Comparison of specimens before and after loading

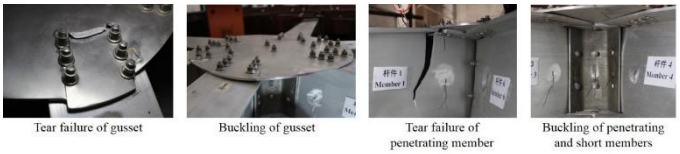

(a) Damage patterns of Group Z1

(b) Damage patterns of Group Z2

Fig. 14 Damage patterns of specimens with different gusset thicknesses

Fig. 15 compared the moment-rotation curves of 12 mm and 6 mm circular gusset AAP joint. In this paper, the *M-Φ* curves included two types: penetrating members and short members. Analyzing the two sets of curves, the following characteristic parameters were obtained, as shown in Table 4.

Further analysis of the data characteristics obtained from the *M-Φ* curves could find that the gusset thicknesses increased by 6 mm, the ultimate bending moment increased by 3%, the K_i of the penetrating member did not change much, and the K_i of the short member increased by 14%. If the thickness of joint gussets was enlarged, short members could work better with joint gussets. Under the same bending moment condition, the displacement and deformation were reduced. Comparing the damage patterns of two gusset thicknesses, local buckling and failure of the joint gussets occurred in the 6 mm circular gusset joint. This was because the screws contacted the holes successively, followed by the misalignment of the bolts and plates in the late loading stage. When the contacts were tight, the bolt entered the fastened state. The load was transmitted to the plate through the pressure of the bolt-hole walls. When the thicknesses of the gussets were thin, gussets buckled and were torn. When the thicknesses were large, the degree of bending deformation was reduced, and the failure was manifested as the fracture failure of members.

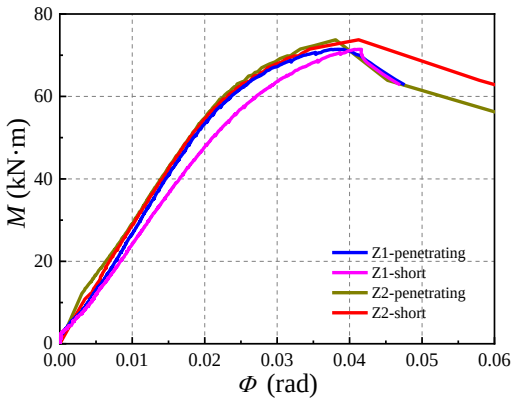

Fig. 15 *M-Φ* curves of specimens of Group Z1 and Z2

Table 4
Characteristic parameters of specimens with different gusset thicknesses

Group number	Member type	K_i (kN•m/rad)	M_i (kN•m)	M_{sup} (kN•m)
Z1	Penetrating	3163.6	53.1	71.42
	Short	2766.3	56.2	71.42
Z2	Penetrating	3182.2	55.2	73.76
	Short	3177.5	55.2	73.76

4.4. Influence of gusset shapes on rotational resistance performance of the AAP joint

The specimens, Z3-A and Z3-B, were based on circular gussets of the same size. Using the X-shaped gussets reduced the material of aluminum alloy gussets. When the joint was loaded to 428 kN, a crisp sound occurred, and the

load began to decline. The loading progress stopped at 100 kN. The experiment found that the overall stiffness of the joints in Group Z3 was greater. The X-shaped and circular gussets underwent slight buckling. The test photos in Fig. 16 showed that the main damage patterns were still the tearing failure of the members and the buckling of the webs.

(a) Damage patterns of Group Z2

(b) Damage patterns of Group Z3

Fig. 16 Damage patterns of specimens with different gusset shapes

There were many redundant areas on the circular gusset that did not cover the members. In fact, these areas had less force when the joints were damaged by the load. Therefore, based on the circular gusset, the proportion of the redundant areas was reduced. The use of aluminum alloy material was saved, and the use of excessive bolts on the penetrating members was also reduced. This section compared the difference between the AAP joint composed of X-shaped gussets and the previous circular gussets. The *M-Φ* curves of the penetrating members and the short members of joints with two gusset shapes were compared in the same figure, as shown in Fig. 17. Table 5 listed some basic characteristics of joints analyzed from the curves.

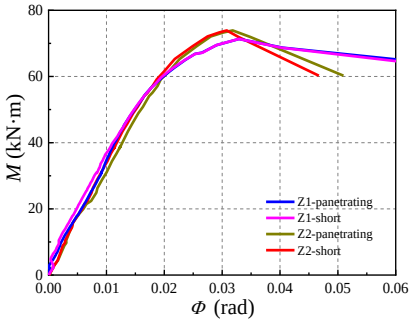

Fig. 17 *M-Φ* curves of specimens with different gusset thicknesses

Table 5
Characteristic parameters of specimens with different gusset shapes

Group number	Member type	K_i (kN•m/rad)	M_i (kN•m)	M_{sup} (kN•m)
Z2	Penetrating	3182.2	55.2	73.76
	Short	3177.5	55.2	73.76
Z3	Penetrating	3185.6	50.1	67.20
	Short	3180.5	50.1	67.20

Further analysis of the characteristics of the joint *M-Φ* curves found that after the area of X-shaped gussets was reduced, there was not much difference in rotational resistance between the penetrating members and the short members, but the ultimate bending moment of Group 3 decreased by 9%. The elastic segment of the joint was reduced, and its elastic limit bending moment was reduced by 10%, which indicated that reducing the gusset area and the number of bolts did not impact too much in the initial stage of the elastic phase. The difference of the joint stiffness and the rigidity between the circular and X-shaped gusset joints was very small at this stage, but as the bending moment load continued to increase, the joints with the X-shaped gussets relatively more quickly entered the elastic-plastic stage. Under the same load, the displacement of the X-shaped gusset joint was larger because in this form, the integrity of the joint decreases. As the load continued to increase, the joint stiffness decreased rapidly, the joint reached its maximum bending moment at 67.20 kN•m, and the joints were damaged.

5. Numerical simulation analysis of rotational resistance performance of AAP joint

Both the connection methods and the component sizes major factors affecting the rotational resistance behavior of AAP joints. The economic cost and time cost of experimental research are very high. Therefore, it is efficient and suitable to research the mechanical performance of the joint by the FEA method. In this chapter, an FEA joint model corresponding to the test size was established to examine the accuracy of the numerical model. The parametric analysis provided reliable and effective joint numerical method.

5.1. Numerical simulation models

Fig. 18 was the FEA model of the AAP joint system. The geometry of each component of the model was identical with that of the specimen. The boundary conditions were pinned constrains, and the locations of the loading point were identical with those in the test. The finite element adopted a simplified loading method to improve the calculation efficiency. The load was applied to each member via a rigid distributive beam in the test. In the simulation, the distributive beam was removed, and the load was directly applied to the same position. The nonlinearity of geometry and material were considered in this FEA model. The material properties of bolts are listed in Table 6. The material properties of aluminum members and gussets are the test results in Section 3.3.

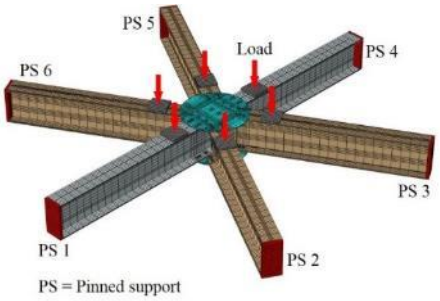

Fig. 18 Meshing of the AAP joint model

Table 6
Material properties of the finite element model

Material	Elastic modulus E (MPa)	Yield strength $f_{0.2}$ (MPa)	Density ρ (kg/m^3)	Poisson's ratio v
Stainless steel	200000	450	7800	0.3

5.2. Comparison of numerical simulation and test results

The *M-Φ* curves were of the AAP joints obtained from tests and FEA were shown in Fig. 19, and the Mises stress nephogram at the failure of the joints were shown in Fig. 20. Table 7 listed the main characteristic parameters. It could be seen that the error between the results obtained from tests and numerical simulation was about 4%, so the FEA model in the paper could simulate the rotational resistance performance of the AAP joints.

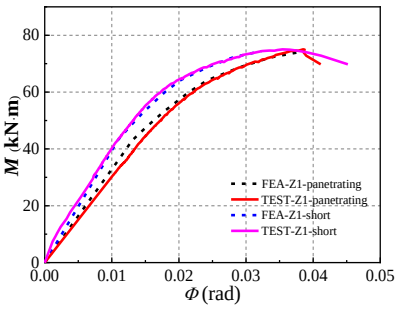

(a) Z1

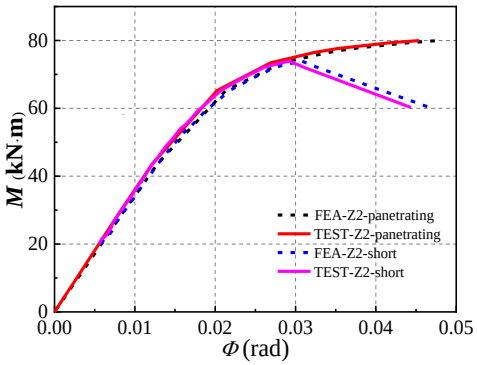

(b) Z2

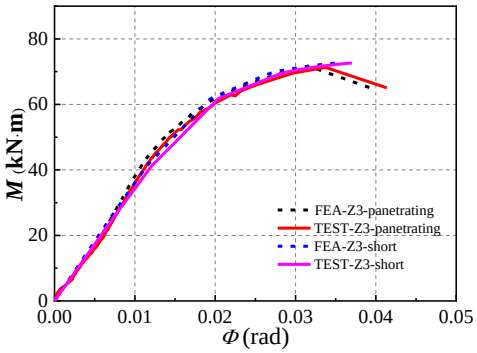

(b) Z3

Fig. 19 Comparison of test and simulation results

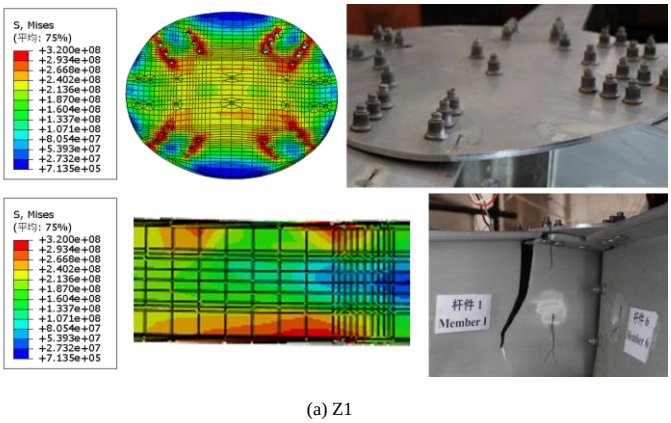

(a) Z1

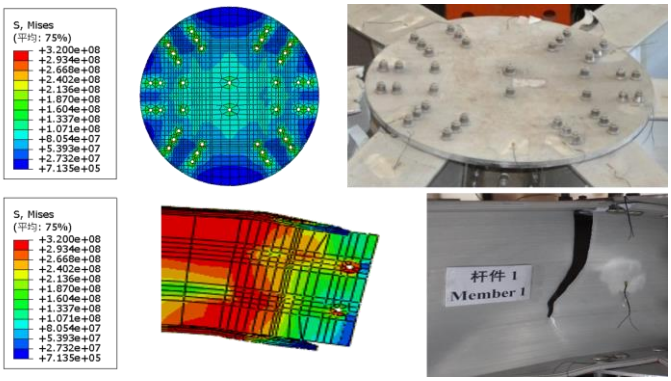

(b) Z2

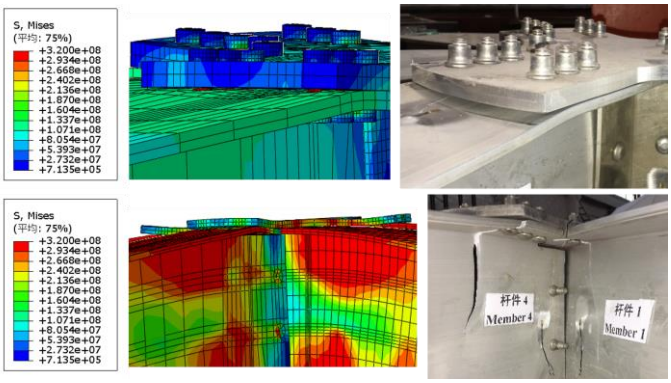

(b) Z3

Fig. 20 Damage patterns obtained from test and simulation

Table 7
Comparison of the test and simulation results

Group number	K_i (kN•m/rad)			M_{sup} (kN•m)		
	$K_{i,FEA}$	$K_{i,test}$	Error	$M_{sup,FEA}$	$M_{sup,test}$	Error
Z1	3158.5	3163.6	0.2%	72.5	71.4	1.5%
Z2	3175.5	3182.2	0.2%	75.2	73.8	2.0%
Z3	3190.5	3183.5	0.2%	74.3	72.2	3.0%

6. Conclusions

As the aluminum structure was developing rapidly, an improved joint, the AAP joint system, was proposed, which included additional penetrating members and U-shaped connectors compared to the Temcor joint. The rotational resistance behavior of the AAP joints was investigated by tests and numerical simulations. The obtained conclusions were as follows:

(1) Flexural tests of AAP joints was conducted to investigate the effects of different parameters. The *M*-*Φ* curves and damage patterns were acquired. The behaviors of the penetrating and short members in the AAP joints were compared, and rotational resistance of AAP joints with different thicknesses and shapes of gussets was analyzed. The *M*-*Φ* curves were defined which were divided into elastic, elastic-plastic and plastic stages.

(2) The difference between the behavior of the penetrating members and the short members was related to the thicknesses of the gussets. When the thickness of the gussets was 12 mm, the *M*-*Φ* relationships and damage patterns of penetrating and short members were not much different. The damage pattern mainly manifested in the tearing failure of the member and local buckling of the plate. When the thickness of the gusset was 6 mm, and the stiffness of the joint area was relatively smaller. At this time, the tearing damage of the penetrating members occurred before the short members.

(3) The thicknesses of the gusset had an effect on the rotational resistance of the AAP joint. Comparing the 12 mm circular gusset joints with the 6 mm, the initial bending stiffness of the short members increased by 14%, and the Msup of the 12 mm gusset improved by 3%. Only the 6 mm gussets showed tear and buckling failure.

(4) The shapes of the gussets had little effect on the rotational resistance of the AAP joints. When the area of the gussets reduced, the yield moment Msup of the joint reduced by 9% and the initial bending moment Mi reduced by 10%. The initial rotation stiffness Ki of circular and X-shaped gusset was similar, and the damage patterns of the joint showed as tearing failure of members and local buckling of the webs.

(5) A finite element model was established, and the rotational resistance behavior of the AAP joints was numerically simulated. The finite element results and test resultswere compared. The results proved that under bending moment, the damage patterns and *M*-*Φ* relationships obtained from the two research methods were in good agreement.

Acknowledgements

This research is supported by The National Science Fund for Distinguished Young Scholars (Grant No. 51525802) and The National Science Fund for Distinguished Young Scholars (Grant No. 52008072).

References

[1] Doyle, W. M, Aluminum alloys: structure and properties. Metal Science 35.11(1976): 408.
[2] Dwight, John, Aluminium design and construction. Spon Press (1999).
[3] Srivatsan, T. S., Review of: "aluminum structures: a guide to their specifications and design" by J. Randolph Kissell and Robert L. Ferry. Advanced Manufacturing Processes.
[4] Mazzolani, Frederico M., Aluminium Structural Design. Springer Vienna, 2003.
[5] Mazzolani, M. Federico, Structural Applications of Aluminium in Civil Engineering. Structural Engineering International 16.4(2006):280-285.
[6] Mukhopadhyay, A. K., Selection and Design Principles of Wrought Aluminium Alloys for Structural Applications. Materials Science Forum 710(2012):50-65.
[7] Y. Jiang, H. Ma, G. Zhou, F. Fan, Parametric and Comparison Study of a New and Traditional Aluminum Alloy Joint Systems, Advanced Steel Construction 17(1) (2021): 50-58.
[8] N. H. Hoang, A. G. Hanssen, M. Langseth, R. Porcaro, Structural behaviour of aluminium self-piercing riveted joints: an experimental and numerical investigation, Int. J. Solids Struct. 49(2012) 3211–3223.
[9] L.Han, M.Thornton, M. Shergold, A comparison of the mechanical behaviour of self-piercing riveted and resistance spot welded aluminium sheets for the automotive industry. Materials and Design. 31 (2010), 1457–1467.
[10] G.D. Matteis, A. Mandara, F.M. Mazzolani, T-stub aluminium joints: influence of beha vioural parameters, Comput. Struct. 78 (2000) 311–327.
[11] G.D. Matteis, M.T. Naqash, G. Brando, Effective length of aluminium T-stub connections by parametric analysis, Eng. Struct. 41 (2012) 548–561.
[12] T.K. Chan, R.F.D.P. Goff, Welded aluminium alloy connections: test results and BS8118, Thin-Walled Struct. 36 (2000) 265–287.
[13] Y.Q. Wang, C. Luo, Y.J. Shi, Design and research of cast aluminum joint in aluminum alloy spatial structures. International Conference on Electric Technology & Civil Engineering. IEEE, 2011.
[14] Huihuan Ma, Lingwei Yu, Feng Fan, Zhiwei Yu, Mechanical performance of an improved semi-rigid joint system under bending and axial forces for aluminum single-layer reticulated shells. Thin-Walled Struct. 142(2019) 332-339.
[15] Huihuan Ma, Yuqi Jiang, Chengrui Li, Zhiwei Yu, Feng Fan, Performance analysis and comparison study of two aluminum alloy joint systems under out-of-plane and in-plane loading. An experimental and numerical investigation. Eng. Struct. 214(2020) 110643.
[16] H. Liu, Z. Chen, S. Xu, Y. Bu, Structural behavior of aluminum reticulated shell structures considering semi-rigid and skin effect, Struct. Eng. Mech. 54(2015) 121–133.
[17] H. Liu, Y. Ding, Z. Chen, Static stability behavior of aluminum alloy single-layer spherical latticed shell structure with Temcor joints, Thin-Walled Struct. 120(2017) 355-365.
[18] Z. Xiong, X.N. Guo, Y.F. Luo, S.J. Zhu, Elasto-plastic stability of single-layer reticulated shells with aluminium alloy gusset joints, Thin-Walled Struct. 115(2017) 163-175.
[19] X.N. Guo, X. Zhe, Y.F. Luo, L.Q. Qiu, J. Liu, Experimental investigation on the semi-rigid behaviour of aluminium alloy gusset joints. Thin-Walled Struct. 87(2015), 30-40.
[20] Z. Xiong, X.N. Guo, Y.F. Luo, H. Xu, Numerical analysis of aluminium alloy gusset joints subjected to bending moment and axial force. Eng. Struct. 152(2017) 1-13.
[21] X.N. Guo, S.J. Zhu, X. Liu, L.L. Liu, Experimental study on hysteretic behavior of aluminum alloy gusset joints. Thin-Walled Struct. 131(2018) 883-901.
[22] X.N. Guo, S.J. Zhu, X. Liu, K. Wang. Study on out-of-plane flexural behavior of aluminum alloy gusset joints at elevated temperatures. Thin-Walled Struct. 123(2018) 452-466.
[23] F. Fan, Z.G. Cao, S.Z. Shen, Elasto-plastic stability of single-layer reticulated shells, Thin-Walled Struct. 48 (2010) 827–836.
[24] F. Fan, J.C. Yan, Z.G. Cao, Elasto-plastic stability of single-layer reticulated domes with initial curvature of members, Thin-Walled Struct. 60 (2012) 239–246.
[25] H.H. Ma, F. Fan, J. Zhong, et al., Stability analysis of single-layer elliptical paraboloid latticed shells with semi-rigid joints, Thin-Walled Struct. 72 (2013) 827128–827138.
[26] M. Taheripour, F. Hatami, R. Raoufi, Numerical Study of Two Novel Connections with Short End I or H Stub in Steel Structures, Advanced Steel Construction 18(1) (2022): 495-505.
[27] J. Dong, H. Liu, Z. Zhao, Buckling Behavior of a Wheel Coupler High-Formwork Support System Based on Semi-Rigid Connection Joints, Advanced Steel Construction 18(1) (2022): 425-435.
[28] W. Mashrah, Z. Chen, H. Liu, M. Amer, Experimental, Numerical, And Theoretical Study on Static Behaviour of Novel Steel Dovetail Joint Subjected to Axial Tensile Load, Advanced Steel Construction 18(1) (2022): 453-464.
[29] H. Ma, Y. Ma, F. Fan, Y. Zhang, Seismic Performance of Single-Layer Spherical Reticulated Shells Considering Joint Stiffness and Bearing Capacity, Advanced Steel Construction 18(2) (2022): 604-616.
[30] Y. Hiyama, H. Takashima, T. Iijima, et al., Buckling behaviour of aluminium ball jointed single layered reticular domes, Int. J. Space Struct. 15 (2) (2000) 81–94.
[31] Z. Xiong, X.N. Guo, Y.F. Luo, S.J. Zhu, Y.P. Liu, Experimental and numerical studies on single-layer reticulated shells with aluminium alloy gusset joints, Thin-Walled Struct. 118(2017) 124-136.
[32] GB/T228.1-2010, Metallic materials—Tensile testing—Part 1: Method of a test at room temperature, Beiging, China Construction Industry Press (2010).

Advanced Steel Construction – Vol. 19 No. 2 (2023) 130–142
DOI:10.18057/IJASC.2023.19.2.5

MOMENT-ROTATION MODEL OF EXTERNAL COVER PLATE JOINTS BETWEEN STEEL BEAMS AND CONCRETE-FILLED SQUARE STEEL TUBULAR COLUMNS WITH INNER I-SHAPED CFRP PROFILE

Guo-Chang Li [1], Ming-Hao Shen [1,*], Da-Cang Ji [1], Han-Bin Ge [2] and Xu Liu [1]

[1] *School of Civil Engineering, Shenyang Jianzhu University, Shenyang, Liaoning 110168, China*
[2] *Department of Civil Engineering, Meijo University, Nagoya, Aichi 468-8502, Japan*
** (Corresponding author: E-mail: shenminghao96@163.com)*

ABSTRACT

As a new type of beam-column joint, external cover plate joints can be used in concrete-filled square steel tubular (CFSST) structures. To accurately analyze the mechanical characteristics of this novel joint during structural design, it is necessary to investigate the moment-rotation relationships. Based on the analysis of the force-transferring mechanism, the formulas to decide the initial rotation stiffness and ultimate bending moment are founded by using the component analysis method, while the finite element analysis results are also utilized to verify these formulas. Considering the advantages and disadvantages of the existing typical moment-rotation models, a new representation for calculating the moment-rotation curve of the external cover plate joints is proposed using the ultimate bending moment and initial rotation stiffness as two basic parameters. The research reveals that the moment-rotation model proposed in this paper is able to take all loading stages of this joint into account, which facilitates the analysis of yield and ultimate loads. In addition, this model is smooth and continuous at the piecewise points to avoid numerical problems that may be caused in the calculation. Comparing the moment-rotation curves obtained by the calculation model and finite element simulation, the results show good consistency, demonstrating that the moment-rotation model presented in this paper is applicable to the analysis and design of the external cover plate joints.

ARTICLE HISTORY

Received: 13 May 2022
Revised: 11 July 2022
Accepted: 20 July 2022

KEYWORDS

Concrete-filled square steel tubular;
External cover plate joint;
I-shaped CFRP profile;
Initial rotational stiffness;
Ultimate bending moment;
Component method;
Moment-rotation model

1. Introduction

Concrete-filled steel tubular (CFST) members have seen increased use in actual engineering over the last few years for their high strength and ductility [1]. To further improve the mechanical properties of the structures and reduce the section size of the columns, the author's team proposed to put an I-shaped CFRP profile in the CFST member, taking full advantage of three materials, namely concrete, steel, and CFRP profile [2-4]. According to the seismic design principle, the structures should remain stable under seismic loads. During the process of resisting the earthquake, the joints between columns and beams should provide sufficiently large strength and stiffness to survive the structures under the earthquake. Therefore, the structural form and mechanical properties of the joints have always been the focus of many scholars. Among the main forms of beam-column joints, the joints with external diaphragms have the advantages of clear force transmission, good plasticity, high bearing capacity, and strong energy dissipation capacity [5-8]. Because of its own structural characteristics, this joint enables the plastic hinge to occur first in the beam section, allowing the beam to dissipate energy during the seismic event and thus ensure the column does not lose its load-bearing capacity [9,10]. However, due to a large amount of on-site construction work and high requirements for weld quality, the external diaphragm joints are rarely used. To solve the problem of low usage of the external diaphragm joints, our team proposed an external cover plate joint suitable for connecting concrete-filled square steel tubular (CFSST) columns and I-shaped steel beams. The proposed joint not only reduces the amount of on-site construction work but also solves the problem of matching the size of the external diaphragm with the column section in the traditional external diaphragm joints. Moreover, this joint has the same benefits of clear and reliable force transmission as the traditional external diaphragm joints.

All joints applied in practical engineering exhibit varying degrees of semi-rigid characteristics. However, in structural design, beam-column joints are usually simply regarded as completely rigid or hinged, so that only the moment resistance of joints is calculated, the rotational stiffness, which plays a crucial role in the stress distribution and deformation of the structure, is ignored [11,12]. Therefore, a thorough understanding of the rotational stiffness is necessary for accurate structural analysis. The moment-rotation relationship enables us to consider the rotation of the joints in structural analysis, so as to accurately analyze the story displacement of the structure [13]. Although an approximately accurate moment-rotation relationship captured from experiments or finite element simulations is available, they require high economic or time costs. Therefore, the insufficiency of experiments and simulations is generally filled by founding theoretical models. In recent years, several influential moment-rotation curve models have been proposed by numerous scholars. Ding et al. [14] put forward an improved bilinear model, which was practical to use in design because the mechanical behavior of a beam-column joint can be predicted by only two parameters. Wu et al. [15] proposed a three-parameter exponential function in which a shape-coefficient was introduced to adjust the overall shape of the curve. Yee et al. [16] presented a four-parameter exponential function that predicted the ultimate state of joints by introducing the strain hardening stiffness. Frye et al. [17] proposed a polynomial model by fitting multiple sets of experimental data with the least squares method. Colson [18] and Kishi [19] proposed power function models to obtain the ultimate bending moment of joints by solving asymptotes. To achieve a more precise mathematical model, Ang et al. [20] recommended a four-parameter power function model based on the Ramberg-Osgood function. The existing moment-rotation models can generally be classified into two types: piecewise function models and single nonlinear function models. The piecewise function model is prone to abrupt changes at the breakpoints, which may lead to numerical problems such as computational non-convergence in the subsequent analysis. In contrast, the single nonlinear function model has no clear definition for all loading stages of joints.

In this study, we analyzed the force-transferring mechanism of the proposed joint through numerical simulations. Additionally, the component method is introduced to analyze the external cover plate joint. To accomplish this objective, the force-transferring mechanism of the basic components is identified and clarified. Then, the calculation formulas for ultimate flexural capacity and initial rotation stiffness are derived utilizing the principle of the component method. Finally, considering the advantages and disadvantages of the typical moment-rotation models, according to the ultimate flexural capacity and initial rotation stiffness as two primary factors, a novel mathematical representation is presented to determine the moment-rotation relationship. The research results obtained in this paper can improve the design theory of this type of joint and provide a research basis for its application to concrete-filled square steel tubular structures.

2. Connection details and finite element model

In this section, we presented the specific details of the external cover plate joint and discussed the method of building a fine finite element model using the nonlinear analysis software ABAQUS.

2.1. Connection details

To solve the problem with the low usage of external diaphragm joints, our research group has proposed the external cover plate joint. The main components of this joint are cover plates, angle steels, and high-strength bolts. Compared with the traditional external diaphragm joint, this novel joint solves

the installation inconvenience caused by the deviation between the opening size of external diaphragms and the section size of columns, achieving the detachable connection and thus meeting the requirements of the fabricated building. Fig. 1(a) presents the overall schematic of the joint.

Every part of the joint can be prefabricated in the factory. The cover plate can be pre-welded to the upper flange of the beam before on-site assembly. Also, the angle steels are connected to the steel tube by fillet welds in advance. When assembling on-site, the cover plates and lower angle steels are connected by high-strength bolts in advance as temporary support for subsequent assembly, and the upper angle steel plays a positioning role. After the beam and column are lapped, the cover plates are connected with the upper angle steel by high-strength bolts. Finally, the welding work between the cover plate and the lower flange of the beam as well as the welding work between the beam web and the square steel tube are carried out. It is worth noting that all cover plates and steel tube are not welded. The assembly process is shown in Fig. 1(b).

The sizes of the base model (JZ-1) for finite element model analysis are as follows: The section size of the composite column is 250 × 250 mm^2, the wall thickness is 10mm, and the height is 3000mm; The beam is made of 300 × 150 × 6.5 × 9 mm I-steel, and the length is 1500 mm; The section size of angle steel is L90 × 10 mm, and the length is 770 mm; The cover plate size is 430 × 260 × 10 mm. According to the relevant design references [21-23], the sizes of the joint were checked, and the joint met the design principle of "strong column and weak beam, strong connection and weak members". Grade 10.9 M20 high-strength bolts are adopted for all connecting bolts. Each component's material strength of the joint is shown in Table 1. The specific size of the finite element model is shown in Fig. 2.

Table 1
Material strength

Materials	Steel tube	Concrete	Beam	Angle steel	Cover plate
Strength	Q460	C60	Q355	Q355	Q355

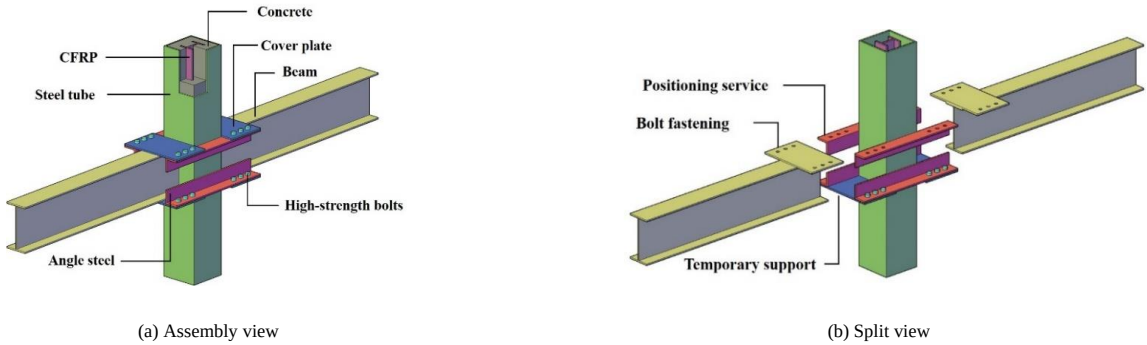

(a) Assembly view (b) Split view

Fig. 1 External cover plate connection overview

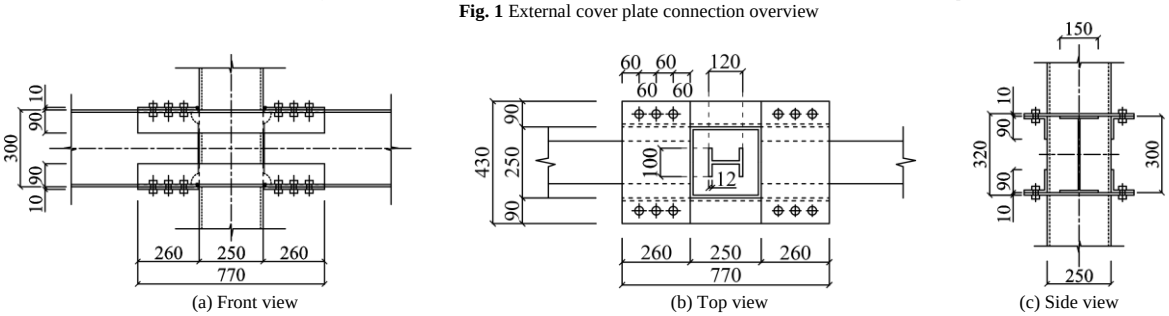

(a) Front view (b) Top view (c) Side view

Fig. 2 Details of the specimens

2.2. Refined finite element model

2.2.1. Material constitutive model

Considering the confinement effect of the square steel tube, the constitutive relation of infilled concrete proposed by Han [24] is adopted in this paper, with the range of application being f_{cu} = 30~120 MPa, f_y = 200~700 Mpa. A trilinear model considering the strengthening stage and the descending stage was used for the constitutive relation of steel. The I-shaped CFRP profile was made of internal unidirectional carbon fiber and external bi-directional carbon fiber by the pultrusion process, so it could be regarded as a three-layer orthogonal anisotropic material. A subroutine based on a secondary development in ABAQUS was utilized to define the CFRP material characteristics, and the Tsai-Wu failure criterion was used to discriminate whether its elements were damaged.

2.2.2. Contact analysis model

A frictional contact with a friction coefficient of 0.6 was used in the tangential direction for producing the contact surface between the square steel tube and the infilled concrete. Hard contact was used to mimic the contact behavior in the normal direction. The same settings were also applied to the contact surfaces between the cover plates, angle steels and high-strength bolts, except the tangential friction coefficient was 0.45. Tie restraint was used at the contact surface between the I-shaped CFRP profile and the concrete because the experimental results in [25,26] showed no relative sliding between the CFRP profile and concrete after loading. The cover plates and beam flanges were not welded with the steel tube, so the contact relationship between each of them and the steel tube was simulated by the "friction" and "hard" contacts with a friction coefficient of 0.45. Fillet welds were adopted for the connection between the angle steels/beam webs and the steel tube, so the tie constraints were applied between angle steels, beam webs and the steel tube. Similarly, the fillet welds were adopted between the cover plates and the beam flanges, because the contact relationship between them was taken as the tie constraint.

2.2.3. The boundary conditions and meshing

Fig. 3 shows the boundary conditions and meshing of the numerically simulated model. To avoid the occurrence of out-of-plane instability, the constraints of the lateral support on the beam were simulated by limiting the degrees of freedom along the Y-direction in the end section of the beam. Only the degree of freedom in the Z-direction on the top of the column was not restrained and applying an axial load (N_0) with an axial load ratio of 0.3 to the top of the column. Fixed restraint was used at the bottom of the column.

The I-shaped CFRP profile was modeled by the SC8R (continuous shell element), and a sweeping mesh method was adopted with the sweeping paths following the thickness direction of the flange and web respectively. Besides, concrete, steel tube, cover plates, angle steels, and beams were modeled by the C3D8R (eight-node reduced integral solid element). The meshing method used the structural mesh method. In addition, the panel area and the beam section connected to the cover plate were divided more intensively in the meshing.

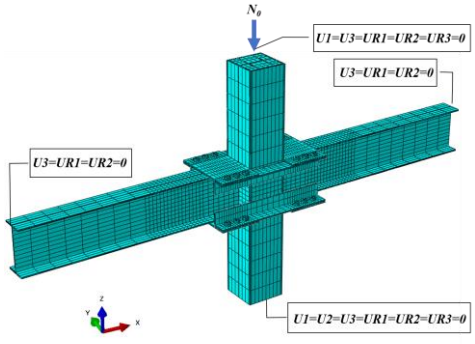

Fig. 3 Boundary conditions and meshing

2.2.4. Accuracy verification of finite element model

To assess the validity of the modeling approach, a few specimens from the current references [27,28] were simulated using the aforementioned finite element modeling technique. Fig . 4 compared the experimental and finite element simulation findings. It can be seen that the simulation results closely match the curves provided in the references. In summary, the finite element modeling method presented in this paper is precise and can be applied for subsequent analysis.

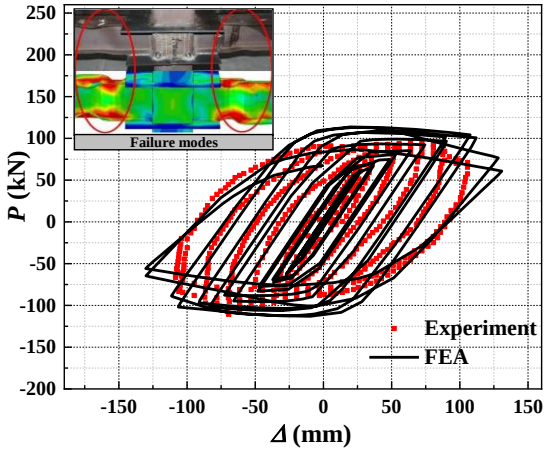

(a) Comparison with the hysteresis curves in [27]

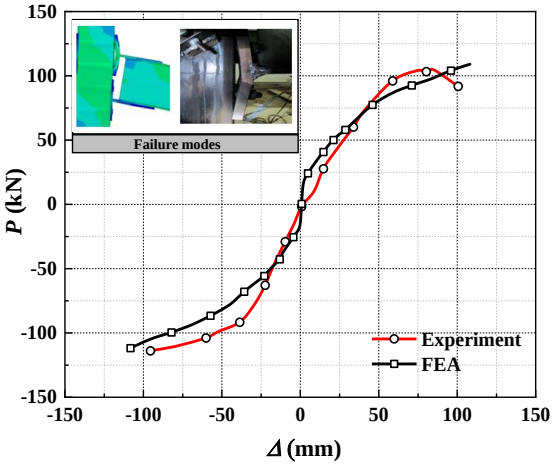

(b) Comparison with the skeleton curves in [28]

Fig. 4 Verification of finite element modeling method

3. Transfer mechanism analysis

In this study, it is considered that the bending moment applied to the beam can be decomposed into a set of horizontal loads on the beam flanges and the vertical load on the beam web, which is transferred to the panel zone of the combined column through the connectors. Therefore, based on the analysis of the distribution of horizontal and vertical stresses on the steel beam, cover plate, angle steel, and steel tube, this section discusses the force transmission mechanism of such composite joints.

In addition, since the stress distribution on each member does not change significantly from the beginning of loading to the peak load stage and only the stress value changes, the analysis can reveal the transmission mechanism of the joint by selecting a specific moment in the loading process.

3.1. Horizontal stress distribution

3.1.1. Horizontal stress distribution of steel beam

Fig. 5(a) reveals that, aside from the beam flange, the bending moment at the beam end can be resolved into a set of horizontal loads of equal magnitude and opposite directions acting on the beam web. When the shear force is exerted on the beam section, a distinct area of tension and compression forms at the beam web.

In ABAQUS, the path analysis approach was utilized to examine the horizontal stress distribution in the beam flange and web section. According to Fig. 6(a), point B is the position of the cross-section where the stress mutation occurs on the beam flange, and point A is the location of the cross-section where the beam flange is connected to the cover plate. It is observed that the curve at point B has a mutation, and the mutation position is about x = 300 mm. Compared with the upper flange of the steel beam, the position where the stress mutation of the lower flange is more obvious, indicating that the plastic deformation of the lower flange is more significant. The flange of the steel beam began to connect with the cover plate at point A, and the stress began to decrease rapidly after passing point A, indicating that the horizontal stress passed through the beam flange to the cover plate. In addition, the horizontal stress at the beam web starts to decline before reaching point A, indicating that the tensile and compressive forces at the web of the steel beam are first introduced into the beam flange and then transferred to the cover plate.

3.1.2. Horizontal stress distribution of cover plate

In Fig. 5(b), the transmission path of principal stress at the cover plate shows that the stress on the cover plate mainly comes from the flange of the steel beam and continues to be transmitted to the bolt holes along the 45° oblique direction.

Since the stress distribution of the cover plate is almost the same when it is in tension and compression, only the tensile stress distribution in different sections of the cover plate was analyzed, as shown in Fig. 6(b). It can be seen that the tensile stress in section ‘1-1’ is the largest between the area of x = 140 mm and 290 mm, which is because the beam flange is connected with the edge of the cover plate, and the tensile stress on the beam flange is transferred to the cover plate from this region. According to the figure, as the section position shifts from ‘1-1’ to ‘6-6’, the location of the maximum tensile stress shifts outward from x = 215.2 mm to 139.9 mm, indicating that the tensile stress on the cover is mainly transferred to the bolt holes in the oblique direction. Due to the stress concentration at the bolt hole, the stress values of the curve at x = 45 mm and x = 385 mm has a certain degree of mutation. Through the comparative analysis of sections ‘3-3’, ‘4-4’, ‘5-5’ and ‘6-6’, it is found that the tensile stress has been reduced to a greater extent in turn, with the tensile stress value in section ‘6-6’ close to 0 at x = 90 mm to 340 mm, indicating that most of the tensile stress is not transmitted through the cover plate into the column wall, but through the cover plate to the bolt hole, and from the bolt to the angle steel. By analyzing the tensile stress values in the six sections in the figure, a significant decrease in the tensile stress values of sections ‘4-4’ and ‘5-5’ is observed, indicating that most of the tensile stress is transmitted to the bolts in the second and third rows. In addition, there are negative values of tensile stress in sections ‘4-4’, ‘5-5’ and ‘6-6’, which are caused by the friction between the surface of the nuts and the surface of the cover plates.

3.1.3. Horizontal stress distribution of angle steel

From the transmission path of the principal stress at the angle steel in Fig. 5(c), the stress transmitted from the cover plate continues to be transmitted mainly along the horizontal limb of the angle steel and finally to the steel tube.

According to the Fig. 6(c), the distribution of tensile stress on the horizontal and vertical limbs of the angle steel was analyzed respectively. Comparing the changes in stress value on the horizontal limb sections ‘1-1’ to ‘4-4’ of the angle steel, it can be seen that the closer the position of the section is to the column wall, the lower the maximum stress value of that section. In addition, the location where the stress value appears to decrease is between x = 214.3 mm and 233.4 mm. In contrast, there is a significant increase in stress in section ‘5-5’ of the angle steel’s vertical limb in this region, indicating that most of the tensile stress on the horizontal limb is transferred to the vertical limb of the angle steel. At the location where the angle steel is connected to the steel tube, i.e., x = 260 mm, there is a substantial decrease in the stress on sections ‘4-4’ and ‘5-5’, indicating that most of the tensile stress on the angle steel is eventually transferred to the wall of the steel tube.

3.1.4. Horizontal stress distribution of steel tube

From the transmission path of the principal stress in Fig. 5(d), it can be verified that most of the horizontal stress on the angle steel is introduced into the corner of the steel tube wall.

Fig. 6(d) displays the stress distribution on the composite column's steel tube. It is observed that the stress at the steel tube wall increases gradually in the range of x = 0 mm to 12 mm, indicating that most of the tensile stress on the angle steel is transferred to the steel tube in this region. Notably, the compressive stress developed on the steel tube wall in sections ‘3-3’ and ‘4-4’ is due to The angle steel being subjected to vertical shear force from the beam end thus producing bending moments near the steel tube. Similar to the bending moment at the beam end, this bending moment is also transformed into a set of forces of equal magnitude and opposite direction applied to the cross-section of the angle steel.

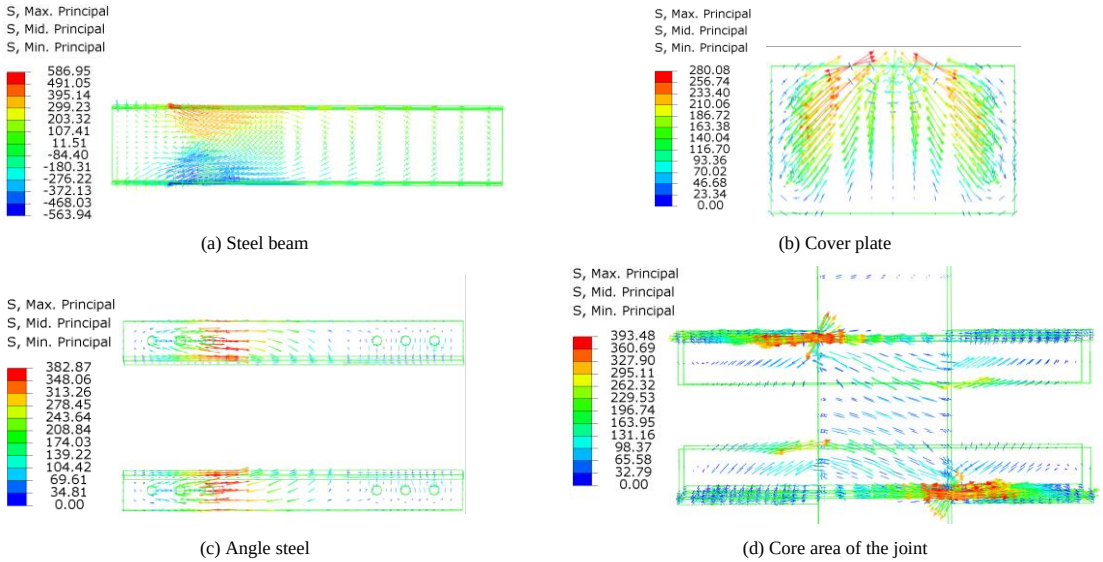

(a) Steel beam (b) Cover plate

(c) Angle steel (d) Core area of the joint

Fig. 5 The transmission path of principal stress on each component of the joint

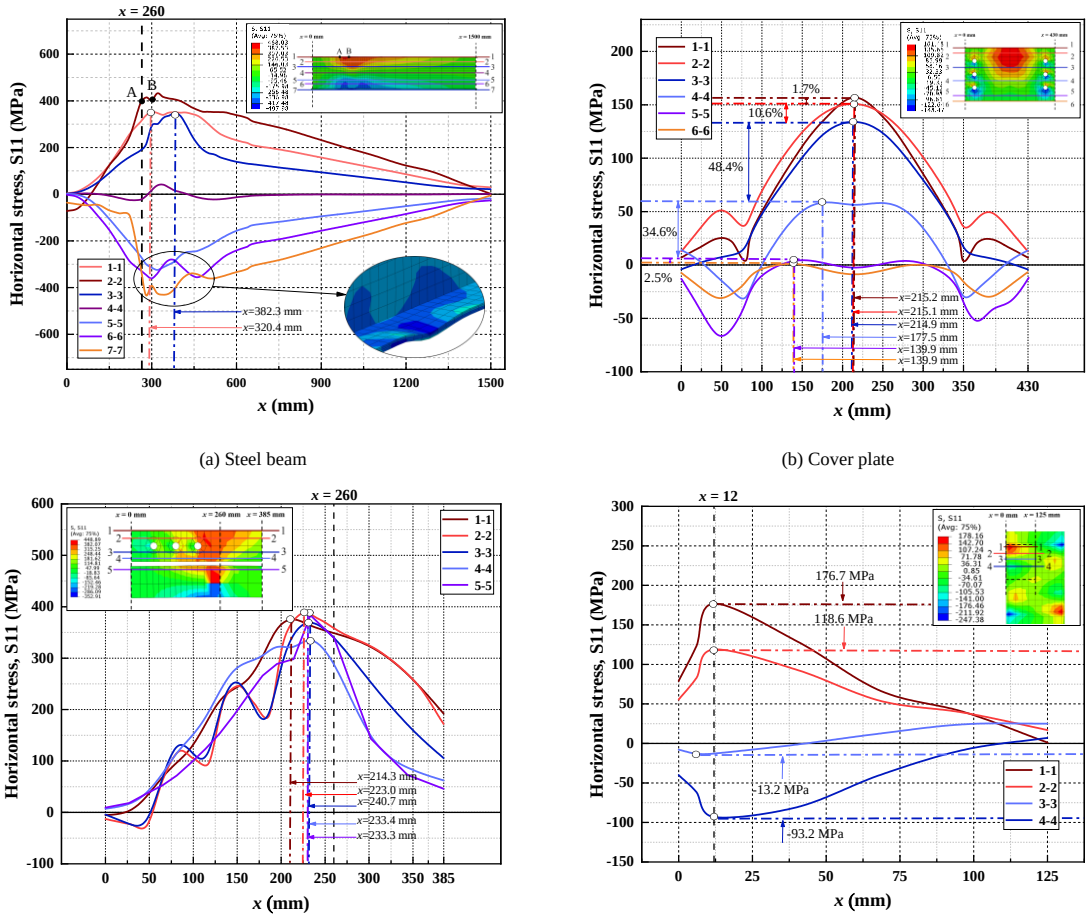

(a) Steel beam (b) Cover plate

(c) Angle steel (d) Steel tube web

Fig. 6 Horizontal stress distribution on each component of the joint

3.2. Vertical shear stress distribution

3.2.1. Vertical shear stress distribution of steel beam

The vertical stress in different sections of the steel beam was extracted using the path analysis method as shown in Fig. 7(a). There is a more obvious rise at x = 700 mm to 1500 mm in section '3-3' compared to the other sections in the figure, indicating that the shear stress at the end of the beam is delivered inward from the center of the beam web. The vertical stress of sections '2-2' and '4-4' increases in the range of x = 260 mm to 450 mm. However, the vertical stress of sections '1-1' and '5-5' only increases in the range of x = 0 mm to 260 mm, and the increase is remarkable, indicating that the shear stress began to spread to the upper and lower sides of the web at about x = 450 mm, and rapidly transferred to the upper and lower edges of the web at x = 260 mm.

3.2.2. Vertical shear stress distribution of cover plate

The vertical stress at different sections on the cover plate was analyzed as shown in Fig. 7(b). Section '1-1' shows a large vertical stress at x = 215 mm with a value of 17.2 MPa, indicating that a part of the vertical shear stress on the beam web is transferred to the centerline of the cover plate. On the other hand, section '2-2' shows a significant decrease in the vertical stress value at x = 215 mm, indicating that most of the vertical stress on the cover plate is not transferred along the centerline of the cover plate, but to the sides. It is worth noting that there is a large increase in the vertical stress at x = 80 mm to 175 mm and x = 290 mm to 350 mm for all sections, which is due to the vertical

limbs of the angle steel acting as vertical supports and providing larger reaction forces, indicating that most of the vertical shear stress on the cover plate is transferred to the vertical limbs of the angle steel. Sections '2-2', '3-3' and '4-4') show larger vertical stress at x = 45 mm and x = 395 mm, which is caused by the nut restraining the edge of the cover plate from buckling, indicating that a portion of the vertical shear stress on the cover plate is also transferred to the horizontal limbs of the angle steel through the bolts.

3.2.3. Vertical shear stress distribution of angle steel

Fig. 7(c) shows the distribution of vertical stress at different sections of the angle steel. Large vertical stress appears at x = 65 mm, x = 130 mm, and x = 195 mm for sections '1-1', '2-2' and '3-3' of the horizontal limb of the angle steel, indicating that part of the shear stress is transferred to the horizontal limb of the cover plate through the bolts. On the contrary, sections '4-4' and '5-5' show a gradual increase in vertical stress in the range of x = 0 mm to 195 mm, and the vertical stress value in section '5-5' is much higher than in other sections, indicating that most of the shear stress is transmitted into the vertical limb of the angle steel. In the range of x = 200 mm to 260 mm, the vertical stress values of sections '1-1', '2-2' and '3-3' show a substantial decrease, whereas the vertical stress values of sections '4-4' and '5-5' show a greater degree of elevation, demonstrating that the shear stress on the angle steel is transferred to the position close to the column section. Because of the restraining effect of the steel tube web on the angle steel, the maximum value of vertical stress occurs in sections '4-4' and '5-5' both at x = 360 mm, indicating that the shear stress on the sections of the angle steel is transmitted into the steel tube web.

3.2.4. Vertical shear stress distribution of steel tube

The shear stress distribution on different sections of the steel tube wall is shown in Fig. 7(d). The vertical stress values at y = 112.5 mm and y = 412.5 mm for section '1-1' are 495.6 MPa and 158.4 MPa respectively, indicating that a part of the vertical stress on the beam web is directly transferred to the steel tube wall. About 70% of the vertical shear stress is transmitted to the steel tube along the web on the compressed side of the steel beam. The vertical shear stress of sections '2-2' and '3-3' at y = 112.5 mm is increased by 6.7 % and 9.1 % respectively, with a minor increase in stress values. In contrast, the vertical stress values at y = 412.5 mm in both sections show a significant change, indicating that there is also a portion of vertical shear stress transmitted into the corner of the steel tube wall through the angle steel, and mainly through the angle steel on the tensile side.

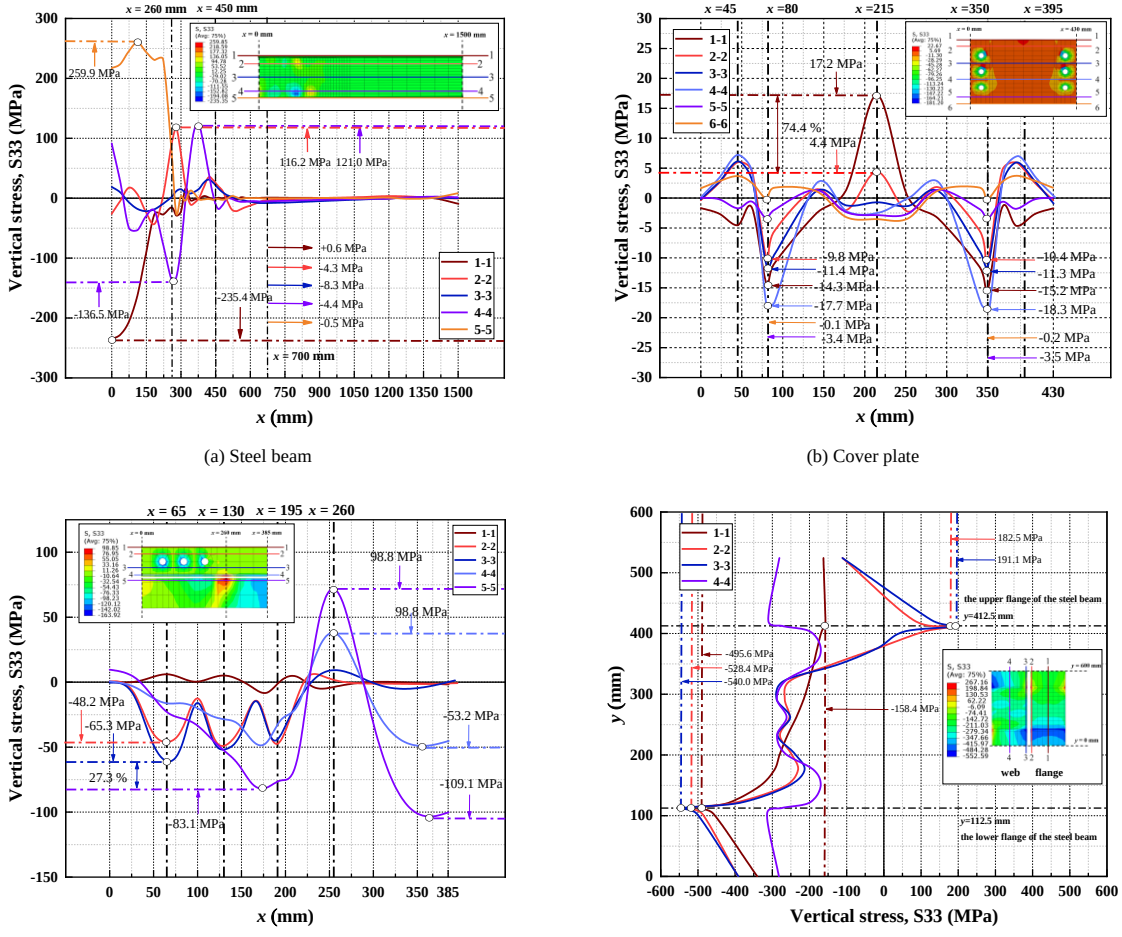

(a) Steel beam (b) Cover plate

(c) Angle steel (d) Steel tube

Fig. 7 Vertical stress distribution on each component of the joint

3.3. Stress distribution in the panel zone of the combined column

Considering the previous analysis, it is clear that the horizontal force acting on the beam flange and the vertical shear force acting on the beam web is eventually introduced into the column wall through the components of the joint. As a result, the horizontal forces and vertical shear force from the beam end are transformed into shear force after being transferred into the panel zone of the combined column. Fig. 8 shows the stress distribution within the core area of the joint is shown in Fig. 8. It has been noted that the steel tube web, the infilled concrete, and the I-shaped CFRP profile web all take the shear force within the joint's core area. Among them, the shear force shared by the steel tube web is significantly greater than the shear force shared by the concrete and CFRP profiles.

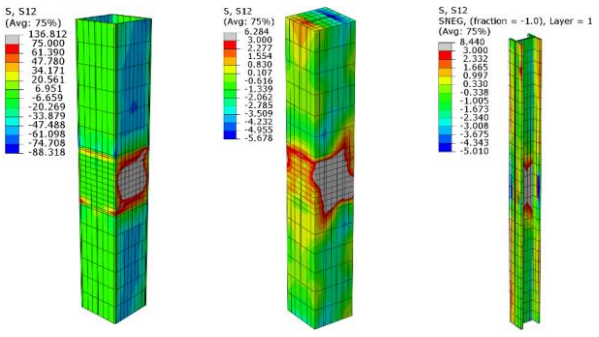

(a) Square steel tube (b) Infilled concrete (c) I-shaped CFRP profile

Fig. 8 Shear stress distribution in the panel zone

3.4. Transmission path of the joint

In summary, the transmission paths of the horizontal and shear forces on the beam are shown in Table 2. In addition, a single diagram to demonstrate the transmission path schematic of the external cover plate joint is shown in Fig. 9. In this diagram, *M* represents the bending moment supplied to the beam section, *N* represents the compressive load transferred along the beam flange, *T* represents the tensile load sent along the beam flange, and *V* represents the shear force transmitted along the beam web.

Table 2
The transmission path of the joint

Horizontal force	Beam flange → Cover plate → Angle steel → Steel tube
Vertical shear force	Beam web → Steel tube
	Beam web → Cover plate → Angle steel → Steel tube

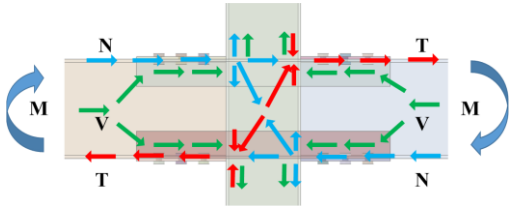

Fig. 9 Schematic diagram of the transmission path

4. Initial rotational stiffness analysis

The component analysis is a method currently used by the Eurocode to determine the initial rotational stiffness of beam-column joints. According to the concept of the component method, any joint can be divided into three different parts: tensile, compressive, and shear regions. Each region has several load-bearing components to bear the corresponding load. According to the analysis of the load transfer mechanism in Section 3, it is clear that the transmission mechanism of this joint is simple, and all components are planar components, so this new combined joint can be analyzed by applying the principle of the component method.

A crucial factor in describing the moment-rotation curve is the initial rotational stiffness. To obtain its precise formula, we simplified the basic components of the joint to spring elements based on the principles of component analysis. First, we calculated the stiffness of each spring element, and then we combined all spring elements into a simplified spring model. Finally, the initial rotational stiffness of the entire joint was calculated.

4.1. The basic components of the joint

The joint can be divided into tensile, compressive and shear regions under loading, and each part consists of several components. These components can simplify the two-dimensional force model of the joint under bending moment to the one-dimensional force model under tension and compression for calculation.

By analyzing the load transfer mechanism of the joint, the tensile (compressive) components are mainly the steel tube web, cover plate, angle steel, steel beam flange, and steel beam web; the shear components are mainly the steel tube web, concrete and I-shaped CFRP profile web.

4.2. Simplified spring model

The following can be assumed in light of the finite element analysis's findings: (1) Each member is in an elastic condition, and there is only minor deformation; (2) Each component satisfies the plane section assumption; (3) The center of rotation is centered between the flanges on either side of the beam.

The connecting portion of the entire joint is simulated by five pairs of springs, namely the cover plate, angle steel, beam flange, beam web, and the steel tube web in bending. The core area of the joint is simulated by three springs, namely the steel tube web in shear, the concrete in shear and the I-shaped CFRP profile web in shear. By dividing the tensile and compressive stress regions at the beam web (Fig. 10), the joint is simplified to a set of springs, and thus the rotation resulting from the bending deformation of the steel beam web is considered.

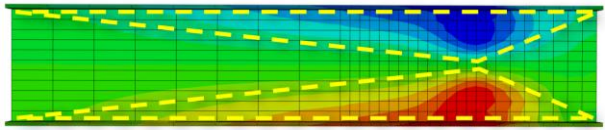

Fig. 10 Division of stress region

In calculating the rotation caused by the lateral deformation of the column section subjected to shear, the shear deformation of each component in the composite column can be considered the same due to the cooperative working characteristic of the column. Therefore, the steel tube web, concrete and I-shaped CFRP profile web can be modeled as three parallel shear springs. In summary, the joint is simplified to the spring element model in Fig. 11(a). After unifying the springs with the same force state, an equivalent spring element model can be obtained (Fig. 11(b)).

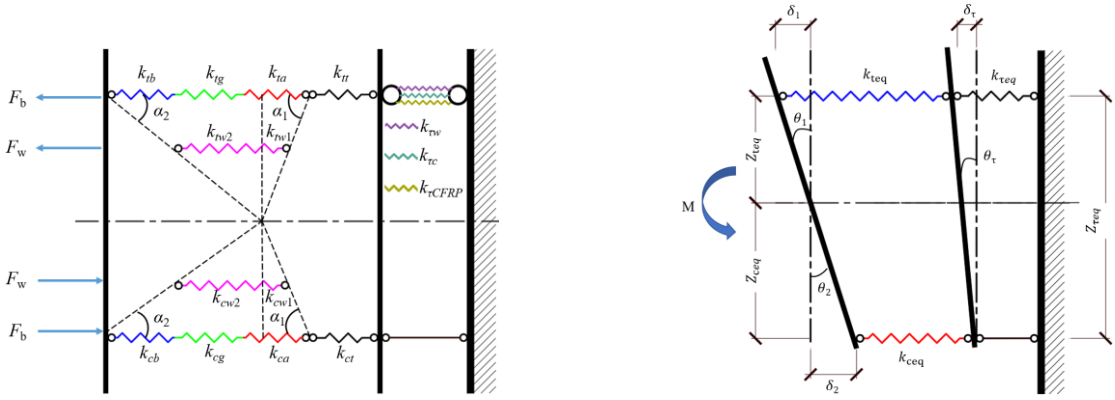

(a) Spring element model (b) Equivalent spring element model

Fig. 11 Calculation model for initial stiffness

In Fig. 11, k_{tb} and k_{cb} stand for the stiffness of beam flange under tension and compression respectively. k_{tg} and k_{cg} represent the stiffness of the cover plate under tension and compression. k_{ta} and k_{ca} are the stiffness of angle steel under tension and compression. k_{tt} and k_{ct} are the stiffness of steel tube web under tension and compression. k_{tw} for the tensile stiffness of the steel beam web, which is divided into two portions, k_{tw1} and k_{tw2}. k_{cw} stands for the compressive stiffness of the steel beam web, including k_{cw1} and k_{cw2}. $k_{\tau w}$ stand for the shear stiffness of the steel tube web, $k_{\tau c}$ represents the shear stiffness of the concrete, and $k_{\tau CFRP}$ means the shear stiffness of the I-shaped CFRP profile web. k_{teq}, k_{ceq} and $k_{\tau eq}$ denote the equivalent stiffness of the joint under tension, compression and shear respectively. δ_1 stands for tension-related deformation, δ_2 for compression-related deformation, and δ_τ for shear-related deformation. θ_1 is the rotation caused by tensile deformation, θ_2 is the rotation caused by compressive deformation, and θ_τ is the rotation caused by shear deformation. Z_{teq} represents the equivalent distance between the centroid of the tension spring element and the beam centre, Z_{ceq} stands for the equivalent distance between the centroid of the compression spring element and the beam centre, and $Z_{\tau eq}$ for the equivalent height of shear section.

Corresponding to Fig. 11, the following equations are established according to the force equivalence and bending distance equivalence:

$$k_{teq}Z_{teq}\theta_1 = k_{tg}Z_{tg}\theta_1 + k_{tb}Z_{tb}\theta_1 + k_{tw1}Z_{tw}\theta_1 + k_{tw2}Z_{tw}\theta_1 + k_{ta}Z_{ta}\theta_1 + k_{tt}Z_{tt}\theta_1 \quad (1)$$

$$k_{teq}Z_{teq}^2\theta_1 = k_{tg}Z_{tg}^2\theta_1 + k_{tb}Z_{tb}^2\theta_1 + k_{tw1}Z_{tw}^2\theta_1 + k_{tw2}Z_{tw}^2\theta_1 + k_{ta}Z_{ta}^2\theta_1 + k_{tt}Z_{tt}^2\theta_1 \quad (2)$$

$$k_{ceq}Z_{ceq}\theta_2 = k_{cg}Z_{cg}\theta_2 + k_{cb}Z_{cb}\theta_2 + k_{cw1}Z_{cw}\theta_2 + k_{cw2}Z_{cw}\theta_2 + k_{ca}Z_{ca}\theta_2 + k_{ct}Z_{ct}\theta_2 \quad (3)$$

$$k_{ceq}Z_{ceq}^2\theta_2 = k_{cg}Z_{cg}^2\theta_2 + k_{cb}Z_{cb}^2\theta_2 + k_{cw1}Z_{cw}^2\theta_2 + k_{cw2}Z_{cw}^2\theta_2 + k_{ca}Z_{ca}^2\theta_2 + k_{ct}Z_{ct}^2\theta_2 \quad (4)$$

Combining Eqs. (1 to 4) yields:

$$Z_{teq} = \frac{k_{tg}Z_{tg}^2 + k_{tb}Z_{tb}^2 + k_{tw1}Z_{tw}^2 + k_{tw2}Z_{tw}^2 + k_{ta}Z_{ta}^2 + k_{tt}Z_{tt}^2}{k_{tg}Z_{tg} + k_{tb}Z_{tb} + k_{tw1}Z_{tw} + k_{tw2}Z_{tw} + k_{ta}Z_{ta} + k_{tt}Z_{tt}} \quad (5)$$

$$Z_{ceq} = \frac{k_{cg}Z_{cg}^2 + k_{cb}Z_{cb}^2 + k_{cw1}Z_{cw}^2 + k_{cw2}Z_{cw}^2 + k_{ca}Z_{ca}^2 + k_{ct}Z_{ct}^2}{k_{cg}Z_{cg} + k_{cb}Z_{cb} + k_{cw1}Z_{cw} + k_{cw2}Z_{cw} + k_{ca}Z_{ca} + k_{ct}Z_{ct}} \quad (6)$$

$$k_{teq} = \frac{(k_{tg}Z_{tg} + k_{tb}Z_{tb} + k_{tw1}Z_{tw} + k_{tw2}Z_{tw} + k_{ta}Z_{ta} + k_{tt}Z_{tt})^2}{k_{tg}Z_{tg}^2 + k_{tb}Z_{tb}^2 + k_{tw1}Z_{tw}^2 + k_{tw2}Z_{tw}^2 + k_{ta}Z_{ta}^2 + k_{tt}Z_{tt}^2} \quad (7)$$

$$k_{ceq} = \frac{(k_{cg}Z_{cg} + k_{cb}Z_{cb} + k_{cw1}Z_{cw} + k_{cw2}Z_{cw} + k_{ca}Z_{ca} + k_{ct}Z_{ct})^2}{k_{cg}Z_{cg}^2 + k_{cb}Z_{cb}^2 + k_{cw1}Z_{cw}^2 + k_{cw2}Z_{cw}^2 + k_{ca}Z_{ca}^2 + k_{ct}Z_{ct}^2} \quad (8)$$

where Z_{tg} and Z_{cg} are the distance between the centroid of the spring element of the cover plate and the beam center, Z_{tb} and Z_{cb} are the distance between the centroid of the spring element of the steel beam flange and the beam center, Z_{tw} and Z_{cw} are the distance between the centroid of the spring element of the steel beam web and the beam center, Z_{ta} and Z_{ca} are the distance between the centroid of the spring element of the angle steel and the beam center, and Z_{tt} and Z_{ct} are the distance between the centroid of the spring element of the steel tube web and the beam center.

Under pure bending, the calculation models of tensile and compressive stiffness are the same, the areas of joints under tension and compression are symmetrical, and the tensile stiffness is the same as the compressive stiffness. Thus, $Z_{teq}= Z_{ceq}$; $k_{teq}= k_{ceq}$.

The shear deformation δ_τ in the core zone of the joint is mainly contributed by the web of square steel tube ($\delta_{\tau w}$), the cross-section of the infilled concrete ($\delta_{\tau c}$) and the cross-section of the I-shaped CFRP profile web ($\delta_{\tau CFRP}$). The force and deformation of each shear spring satisfy the relationship as follows:

$$F_s = F_{\tau w} + F_{\tau c} + F_{\tau CFRP} \quad (9)$$

$$\delta_\tau = \delta_{\tau\omega} = \delta_{\tau c} = \delta_{\tau CFRP} \quad (10)$$

where F_s is the total shear assumed by the core zone of the joint, $F_{\tau w}$, $F_{\tau c}$ and $F_{\tau CFRP}$ are the shear force taken by the steel tube, the infilled concrete, and the I-shaped CFRP profile web, respectively.

The following equation is established according to the cooperative working characteristic of the column:

$$k_{\tau eq} = k_{\tau\omega} + k_{\tau c} + k_{\tau CFRP} \quad (11)$$

4.3. Calculation of the mechanical model of the plate

Fig. 12 shows the mechanical calculation model of the plate. Based on Hooke's law of a tension rod, the tensile stiffness of the rectangular plate (Fig. 12(a)) is calculated according to Eqs. (12 to 15); while the tensile stiffness of the triangular plate (Fig. 12(b)) is calculated by Eq. (16).

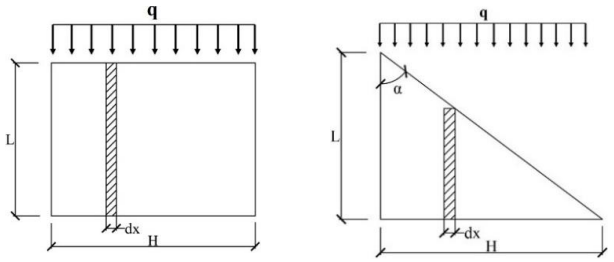

(a) Rectangular plate (b) Triangular plate

Fig. 12 Mechanical model of the panel

Adopting the calculation method in reference [29], the tensile stiffness in Eq. (15) of the rectangular plate can be derived according to Eqs. (12 to 14),

$$A = \int_0^H t dx = Ht \quad (12)$$

$$\Delta L = \frac{FL}{EA} = \frac{FL}{EHt} \quad (13)$$

$$k = \frac{F}{\Delta L} \quad (14)$$

$$k_R = \frac{EHt}{L} \quad (15)$$

similarly, the tensile stiffness of the triangular plate is calculated as:

$$k_T = Et \cdot \tan\alpha \quad (16)$$

In Eqs. (12 to 16), ΔL is the deformation of the panel induced by the force. F is the tensile force on the panel. A is the area of the panel. L and H are the lengths of the panel in the direction of force and vertically to the direction of force respectively. E and t stand for the elastic modulus and thickness of the panel respectively. k, k_R and k_T are the stiffness namely the general panel under tension, the rectangular panel under tension and the triangular panel under tension, respectively.

4.4. Calculation of the initial rotational stiffness

4.4.1. Calculation of the component stiffness under tension (compression)

Based on Fig. 12 and Eqs. (15 and 16), the stiffness of each spring element can be calculated as follows:

$$k_{tg} = \frac{E_g l_g t_g}{b_g} \quad (17)$$

$$k_{tb} = \frac{E_b b_f t_f}{l_b} \quad (18)$$

$$k_{tw1} = \frac{E_w t(h_b - 2t_f)}{2b_g} \quad (19)$$

$$k_{tw2} = \frac{E_w t(h_b - 2t_f)}{2(l_b - b_g)} \quad (20)$$

$$k_{ta} = \frac{E_a b_a t_a}{l_a} \quad (21)$$

$$k_{tt} = \frac{E_t(h_a + 2t_g)t_t}{2l_t} \tag{22}$$

In Eqs. (17 to 22), E_g, E_b, E_w, E_a and E_t are the elastic modulus of components namely cover plate, steel beam flange, steel beam web, angle steel and steel tube web, respectively. l_g, l_a, l_t and l_b are the lengths of the components namely cover plate, angle steel, square steel tube and steel beam, separately. The thickness of the cover plate, angle steel, square steel tube and steel beam flange applies t_g, t_a, t_t and t_f to represent in the above formulas. b_a and b_g are the width of the angle steel limb and cover plate along the beam. h_b represents the height the of steel beam section.

According to the structure of the external cover plate joint, the rotational distance between each spring element and the beam center is calculated as follows :

$$Z_{tg} = \frac{h_b + t_g}{2} \tag{23}$$

$$Z_{tb} = \frac{h_b - t_f}{2} \tag{24}$$

$$Z_{tw} = \frac{h_b - 2t_f}{3} \tag{25}$$

$$Z_{ta} = \frac{h_b - t_a}{2} \tag{26}$$

$$Z_{tt} = \frac{h_b + 2t_g}{4} \tag{27}$$

Substituting the stiffness and rotational distance of each component into Eqs. (5 to 8) yields k_{teq}, k_{ceq}, Z_{teq}, and Z_{ceq}.

4.4.2. Calculation of shear component stiffness

The above analysis shows that the shear force is mainly supported by the steel tube, concrete and CFRP profile web in the panel zone of the joint. In order to determine its stiffness in shear ($\delta_{cw,v}$), the panel zone of the joint can be viewed in Fig. 13 as a short column subjected to shear [16]. As a result, Eq. (28) can be used to determine the shear deformation of the column web under shear.

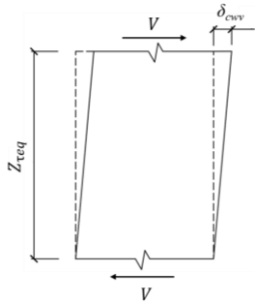

Fig. 13 Deformation of the column web under the shear force

$$\delta_{cw,v} = \frac{VZ_{teq}}{GA_{v,cw}} \tag{28}$$

where $A_{v,cw}$ stands for the shear cross-sectional area of the column web.

The shear force on the column web can be obtained from the horizontal force transmitted from the beam flange as in Eq. (29).

$$V = \beta F_{t,bf} \tag{29}$$

where β is the parameter related to the number of sheared edges. Since the object of this paper belongs to the beam-column joint of the middle column, and the bending moment applied on both sides of the joint has equal value and the same direction, β can be taken as 2 [30].

Utilizing the previous mentioned formula, the shear deformation of steel tube web ($\delta_{\tau w}$), the shear deformation of concrete ($\delta_{\tau c}$), and the shear deformation of I-shaped CFRP profile web ($\delta_{\tau CFRP}$) are derived as follows:

$$\delta_{\tau\omega} = 2(1+\nu)\frac{VZ_{teq}}{E_t A_{\tau w}} \tag{30}$$

$$\delta_{\tau c} = \frac{VZ_{teq}}{G_{\tau c}[(l_t - 2t_t)^2 - A_{CFRP}]} \tag{31}$$

$$\delta_{\tau w,CFRP} = \frac{VZ_{teq}}{G_{\tau CFRP}A_{\tau CFRP}} \tag{32}$$

In Eqs. (30 to 32), $G_{\tau c}$ and $G_{\tau CFRP}$ represent the shear modulus of concrete and I-shaped CFRP profile web, respectively. $A_{\tau w}$, $A_{\tau c}$, and $A_{\tau CFRP}$ are the shear cross-sectional area namely steel tube web, infilled concrete and I-shaped CFRP profile web. ν represents the Poisson's ratio.

Substituting the above parameters into Eq. (14) yields the stiffness of each shear component as follows:

$$k_{tw} = \frac{F_{tw}}{\delta_{\tau w}} = \frac{E_w l_t t_t}{2(1+\nu)\beta Z_{teq}} \tag{33}$$

$$k_{\tau c} = \frac{F_{\tau c}}{\delta_{\tau c}} = \frac{G_{\tau c}[(l_t - 2t_t)^2 - A_{CFRP}]}{\beta Z_{teq}} \tag{34}$$

$$k_{\tau w,CFRP} = \frac{F_{\tau CFRP}}{\delta_{\tau CFRP}} = \frac{G_{\tau w,CFRP}A_{\tau w,CFRP}}{\beta Z_{teq}} \tag{35}$$

From Eq. (10), the equivalent shear stiffness can be yielded as follows:

$$k_{teq} = \frac{E_w l_t t_t}{2(1+\nu)\beta Z_{teq}} + \frac{G_{\tau c}[(l_t - 2t_t)^2 - A_{CFRP}]}{\beta Z_{teq}} + \frac{G_{\tau w,CFRP}A_{\tau w,CFRP}}{\beta Z_{teq}} \tag{36}$$

where $Z_{\tau eq} = h_b + 2t_g$.

4.4.3. Calculation of initial rotational stiffness of the whole joint

The rotations caused by moment deformation and shear deformation under the application of external load are calculated as follows:

$$\delta_c = \frac{M}{Z_{eq}k_{ceq}} \tag{37}$$

$$\delta_t = \frac{M}{Z_{eq}k_{teq}} \tag{38}$$

$$\delta_\tau = \frac{M}{Z_{teq}k_{teq}} \tag{39}$$

The joint's overall rotation (θ) can be separated into the rotation (θ_M) caused by bending deformation and the rotation (θ_τ) brought on by shear deformation, so the rotation of the joint satisfies Eq. (40). The bending moment at the end of the beam is transformed into a set of the horizontal force of tension and compression at the upper and lower flanges, and the rotation caused by the bending moment can be separated into the rotation (θ_1) caused by tensile deformation and the rotation (θ_2) caused by compressive deformation of the component, as shown in Eq. (41).

$$\theta = \theta_M + \theta_\tau \tag{40}$$

$$\theta_M = \theta_1 + \theta_2 \tag{41}$$

Substituting Eqs. (37 to 39) into Eqs. (40 and 41), the rotation caused by the overall deformation of the joint can be yielded as follows:

$$\theta = \theta_M + \theta_\tau = \frac{\delta_t + \delta_c}{Z_{eq}} + \frac{\delta_\tau}{Z_{\tau eq}} = M[\frac{1}{Z_{eq}^2}(\frac{1}{k_{teq}} + \frac{1}{k_{ceq}}) + \frac{1}{Z_{\tau eq}^2 k_{\tau eq}}] \tag{42}$$

Finally, the initial rotational stiffness (K_i) can be calculated as follows :

$$K_i = \frac{M}{\theta} = \frac{1}{\frac{1}{Z_{eq}^2}(\frac{1}{k_{teq}} + \frac{1}{k_{ceq}}) + \frac{1}{Z_{\tau eq}^2 k_{\tau eq}}} = \frac{1}{\frac{2}{Z_{eq}^2 k_{teq}} + \frac{1}{Z_{\tau eq}^2 k_{\tau eq}}} \tag{43}$$

4.4.4. Verification of the calculation results for initial rotational stiffness

Currently, the initial rotational stiffness of the joint is defined mainly through two methods, as shown in Fig. 14. The first is the initial stiffness defined by the first-order derivative of the moment-rotation curve of the joint at the origin, as shown in Eq. (44).

$$K_0 = \left.\frac{dM}{d\theta}\right|_{\theta=0} \tag{44}$$

The second one is defined by the secant stiffness (K_s) of the line between the data point and the origin corresponding to a certain percentage of the characteristic load on the moment-rotation curve of the joint. Usually, K_0 will be higher than the actual stiffness of the joint when the load is larger, and the larger the load, the larger the deviation. Therefore, many scholars mostly use the secant stiffness (K_s) in the moment-rotation model to define the initial stiffness in practical applications. In this paper, the initial stiffness is taken with reference to the method of Han [24] for the stiffness of purely bending members, and the secant stiffness corresponding to 0.2 M_u on the moment-rotation curve is taken as the initial rotational stiffness of the joint, so α is taken as 0.2.

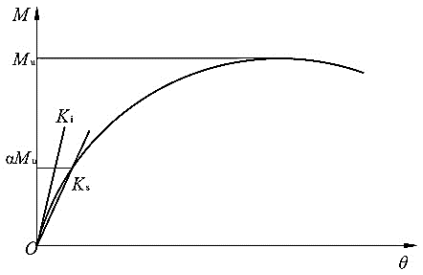

Fig. 14 Definition of initial stiffness

The finite element analysis of joints with various cover plate widths and thicknesses under monotonic static load is carried out by ABAQUS. Comparing the results of initial rotational stiffness calculated by the theoretical calculation model and finite element simulation in Table 3, it is clear that the mean of the ratio between theoretical calculation values and finite element analysis results is 0.91, and the standard deviation is 0.09. The above results demonstrate that the initial rotational stiffness calculated by the model agrees well with finite element analysis ones.

Table 3
Verification results of initial rotational stiffness

Model	Cover plate width /mm	Cover plate thickness /mm	Theoretical calculation result k_1/ kN·m·rad^{-1}	Finite element analysis k_2/ kN·m·rad^{-1}	k_1/ k_2
BK200	200	10	20743.86	25089.27	0.83
BK260	260	10	18617.68	23388.58	0.80
BK320	320	10	15347.74	15542.21	0.99
BH8	260	8	16150.10	15697.73	1.03
BH12	260	12	21626.79	24527.59	0.88
BH15	260	15	25496.74	27467.17	0.93
Average					0.91
Standard deviation					0.09

5. Calculation of ultimate bending moment

Because the joint's bending capacity is determined by the load-bearing ability of the failing component, which is typically the component with the lowest load-bearing capacity. In summary, it is necessary to analyze the possible failure modes of the external cover plate joint to calculate the flexural bearing capacity.

The possible failure modes of the joint are simulated by finite elements as shown in Fig. 15. The CFSST column is not damaged under lateral compression and shear in the core area. Therefore, the above two failure modes are not considered when calculating the ultimate bending moment of the joint to facilitate the practical engineering application, and only the following three possible failure modes are considered:

1) failure at the plastic hinge of beam section;
2) failure at the end of the cover plate connected to the steel tube;
3) failure at the angle steel section.

The ultimate capacity of various components of the joint under each of the above failure modes is calculated, thereby obtaining the ultimate flexural resistance of the joint.

It is worth noting that the finite element models used to analyze the failure modes all use the materials specified in Table 1. Therefore, the formula of ultimate bending moment obtained by the above method is only applicable to the joint using the materials in Table 1.

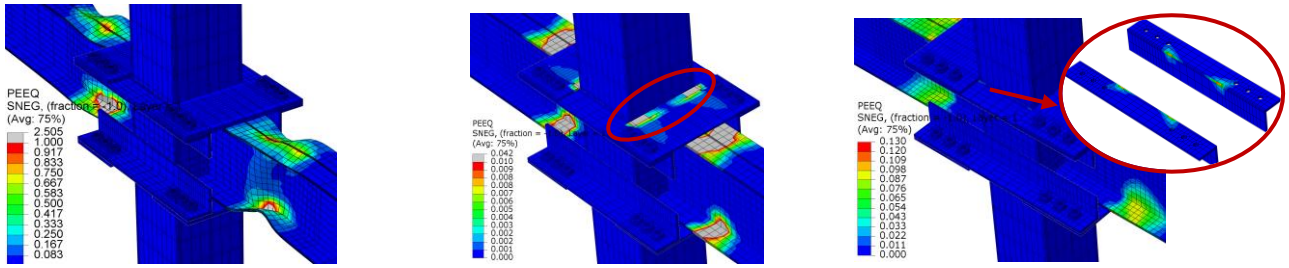

(a) Failure at the plastic hinge of beam section (b) Failure at the cover plate (c) Failure at the angle steel

Fig. 15 Failure models of the joint

5.1. Failure at the plastic hinge of beam section

Refering to Fig. 16, the plastic hinge of the beam section is assumed to be located approximately at the end of the cover plate. When the beam section appears a plastic hinge, the ultimate bending moment of the joint should be calculated by a similar triangular relationship considering the distance between the plastic hinge section and the column face.

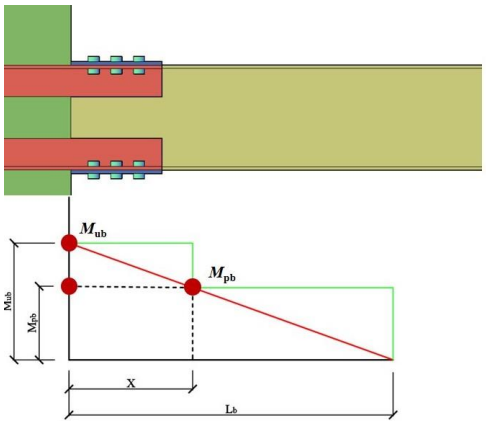

Fig. 16 Diagram of the bending capacity of the joint

Eqs. (45 and 46) can be used to determine the ultimate bending moment if damage happens to the steel beam's plastic hinge section as a result of the analysis above.

$$M_{ub} = \frac{M_{pb} L_b}{L_b - x} \tag{45}$$

$$M_{pb} = W_{pn} f_y \tag{46}$$

where M_{ub} stands for the ultimate bending moment of the joint, M_{pb} represents the ultimate bending moment of the section where the beam plastic hinge is located. In Eq. (45), L_b denotes the distance between the position of the load applied to the beam and the column wall, x is the distance of the plastic hinge position from the column wall. In Eq. (46), the plastic section modulus of the beam adopted W_{pn} to represent, and f_y is the yield strength of the steel.

The plastic resistance moment of the beam section is calculated as follows :

$$W_{pn} = 2S_n = 2\left[\frac{t_f b_f (h_b - t_f)}{2} + \frac{t_w (h_b - 2t_f)^2}{8}\right] \tag{47}$$

where S_n denotes the area moment from half of the beam section to the neutral axis of the plastic hinge, t_w is the thickness of the beam web, and b_f is the width of the beam flange.

The plastic ultimate bending moment of the steel beam is calculated according to the following formula：

$$M_{pb} = W_{pn} f_y = \left[t_f b_f (h_b - t_f) + \frac{t_w (h_b - 2t_f)^2}{4}\right] f_y \tag{48}$$

Substituting Eq. (48) into Eq. (45), the ultimate bending moment (M_{ub}) of the joint is obtained when the plastic hinge section of the steel beam is damaged.

5.2. Failure at the cover plate

Referring to the calculation method of the bending resistance of the through-diaphragm joint [31], the bending resistance of the joint mainly depends on the tensile capacity of the diaphragm, as shown in Fig. 17. The bending capacity of the joint can be obtained by multiplying the tensile capacity of the diaphragm by the center distance of the diaphragms. The formula for calculating the bending capacity is shown as follows:

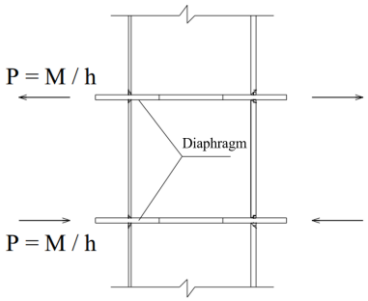

Fig. 17 Matsui calculation model

$$M = Ph = P(h_b - t_{bf}) \tag{49}$$

where P is the tensile capacity of the diaphragm, h is the center distance of the diaphragm, h_b denotes the height of the beam section, and t_{bf} represents the thickness of the beam flange.

Through the analysis of the horizontal force transmission mechanism in Section 3, it is known that the cover plate is subjected to the horizontal force transmitted by the flange of the steel beam. The tensile yielding capacity at the cross-section of the cover plate can be expressed as follows:

$$P_y^g = f_y^g A_g = f_y^g t_g l_g \tag{50}$$

In Eq. (50), P_y^g represents the yield capacity of the cover plate under tensile force, which can be derived by multiplying the yield strength of the steel applied for cover plate f_y^g by the cross-sectional area of the cover plate A_g. Where A_g can be obtained by multiplying the effective length of the cover plate l_g by the thickness of the cover plate t_g and then by f_y^g.

The ultimate tensile capacity of the cover plate can be obtained by substituting its yield strength with the ultimate strength of the steel plate used for the cover plate, and the ultimate bending capacity of the joint can be obtained by multiplying the ultimate tensile capacity of the cover plate by the center distance between the upper and lower cover plates as follows:

$$M_{ug} = P_u^g h_g = f_g^u t_g l_g h_g \tag{51}$$

where M_{ug} is the ultimate bending moment of the joint when the failure occurs at the cover plate, P_u^g is the tensile ultimate capacity of the cover plate and f_u^g denotes the ultimate strength of steel applied for cover plate.

5.3. Failure at the angle steel

From the analysis in Section 3, it is clear that the horizontal load on the cover plate is transferred to the angle steels on both sides through the bolts. Therefore, the angle steels on both sides should be considered for calculating the flexural bearing capacity of the joint. In addition, since the horizontal tension on the angle steel is transmitted not only through the horizontal limb, but also through the vertical limb, approximately the entire section of the angle steel can be considered in tension when calculating the tensile capacity of the angle steel.

In case of damage to the angle steel, the formula for determining the ultimate bending moment of the joint is provided by Eq. (52).

$$M_{ua} = 2P_u^a h_a = 2 f_u^a \left[t_a b_a + t_a (b_a - t_a)\right] h_a \tag{52}$$

where M_{ua} is the ultimate bending moment of the joint when the angle steel fails, P_u^a is the ultimate tensile capacity of the angle steel, h_a is the centroid distance between the upper and lower angle steels, f_u^a is the ultimate strength of steel for the angle steel, t_a is the thickness of the angle steel, and b_a is the width of the angle steel limb.

Through the above analysis, the ultimate bending moment under each failure mode can be obtained. Finally, the smallest ultimate bending moment is

selected as the ultimate flexural capacity of this joint, as follows:

$$M_u = \min\left\{M_{ub}; M_{ug}; M_{ua}\right\} \tag{53}$$

5.4. Verification of the calculation results for ultimate bending moment

To validate the correctness of the above method for determining the ultimate flexural capacity, adopting the proposed theoretical model and finite element simulation calculates all specimens in Table 4. From the comparison results between the above two methods, the average is 1.01, and the standard deviation is 0.02, illustrating that the ultimate flexural capacity calculated by the presented formula agrees well with the finite element simulation results, which can verify the accuracy of the formula for determining the ultimate bending moment proposed in this paper.

Table 4
Verification results of the ultimate bending moment

Model	Cover plate width /mm	Cover plate thickness /mm	Theoretical calculation result M_1/ kN·m	Finite element analysis M_2/ kN·m	M_1/M_2
BK200	200	10	230.3	233.7	0.99
BK260	260	10	241.4	235.8	1.02
BK320	320	10	253.7	245.1	1.04
BH8	260	8	230.1	231.9	0.99
BH12	260	12	241.5	236.3	1.02
BH15	260	15	241.5	236.6	1.02
Average					1.01
Standard deviation					0.02

6. Moment-rotation curve

6.1. Introduction of typical representations

The moment-rotation curve of the joint can reflect the rotation capacity and moment resistance of the joint. Therefore, exploring the mathematical expression function of the moment-rotation curve of the joint is helpful for the internal force analysis and design of the joint. At present, there are two main mathematical models for the moment-rotation curve of joints proposed by many scholars. One is the curve model defined by a piecewise function, and the other is the curve model defined by a single nonlinear function. The existing moment-rotation curve models take the moment resistance and initial rotational stiffness of the joints as the basic physical parameters. In addition, shape parameters are introduced in some curve models. In this paper, three typical curve models are introduced and compared.

6.1.1. Trilinear model

The trilinear model is regarded as the simplest model considering the mechanical behavior of the joints, which consists of the elastic, knee and ultimate components. The mathematical expression of the trilinear model in reference [13] can be expressed in Eq. (54), where $\theta_y = M_y / k_i$ is the yield rotation of the joint. To illustrate this model more clearly, the moment-rotation curves of the external cover plate joint calculated by the trilinear model are shown in Fig. 19. It is observed that the moment-rotation curves derived from the trilinear model have significant errors in the knee part compared with the finite element analysis results, which cannot accurately reflect the mechanical behavior of the joint. In addition, sharp points tend to appear at the breakpoints of the piecewise function, which may cause numerical problems such as computational non-convergence in the subsequent structural analysis.

$$M = \begin{cases} K_i\theta, & \theta \le \theta_y \\ M_y + \dfrac{K_i}{7}\left(\theta - \theta_y\right), & \theta_y < \theta \le 4.5\theta_y \\ 1.5M_y & \theta > 4.5\theta_y \end{cases} \tag{54}$$

6.1.2. Function model in Eurocode 3

As shown in Eq. (55), similar to the trilinear model, the moment-rotation model provided in Eurocode 3 is also defined by three parts, which also consists of the elastic, knee and ultimate parts [32]. However, compared with the trilinear model, the shape coefficient ζ is introduced in the knee part of this model to adjust the curve shape so that the calculation results of this model are more precise. The moment-rotation curves obtained by using the function model in Eurocode 3 are also shown in Fig. 19. Based on the results in the figure, the knee part of this model curve is more accurate than the trilinear model, but there are still obvious errors. In addition, this model only considers the continuity but not the smooth conditions at breakpoints, which may still cause numerical problems such as non-convergence in subsequent structural analysis.

$$M = \begin{cases} K_i\theta, & \theta \le \theta_y \\ (M_y^{\zeta} K_i \theta)^{\frac{1}{1+\zeta}}, & \theta_y < \theta \le 4.5\theta_y \\ 1.5M_y & \theta > 4.5\theta_y \end{cases} \tag{55}$$

6.1.3. Exponential function model

Zhao [33] proposed an exponential function model containing three main parameters, which includes shape coefficients c to adjust the curve shape. Compared with the four-parameter exponential model proposed by Yee [16], the complex process of introducing strain hardening stiffness to predict the ultimate state of joints is omitted. The model reduces the workload of calculating the moment-rotation curve while ensuring prediction accuracy. The mathematical expression of the exponential function model proposed by Zhao is shown in Eq. (56). For a clearer presentation of the model, Fig. 19 shows the moment-rotation curves of the external cover plate joint obtained by using the three-parameter exponential function model. Due to the fact that the moment-rotation curves are defined by a single nonlinear function, these curves are continuous and smooth. Therefore, numerical problems such as non-convergence can be avoided in subsequent structural analysis. However, this function model does not distinguish the elastic part of joints. As a result, when the shape coefficient is adjusted to make the curve model highly consistent with the elastic part in the finite element analysis results, the knee part in the curve model and the finite element simulation results show a significant error.

$$M = M_u[1 - e^{\frac{-(K_i + c\theta)\theta}{M_u}}] \tag{56}$$

6.2. Proposed model

The analysis of the typical moment-rotation curve models shows that although the piecewise function model defines the elastic and ultimate parts appropriately, the knee part is not accurate enough and prone to mutation at the piecewise points, resulting in numerical problems such as non-convergence of calculation. On the other hand, the single nonlinear function model can obtain a continuous and smooth curve but lacks a clear definition of the elastic part and the ultimate part, which brings difficulties to analyzing the yield and ultimate load of joints. Considering the advantages and disadvantages of the existing typical moment-rotation curve representations, an improved moment-rotation curve representation is proposed in this paper, and its mathematical function is expressed in Eq. (57). The ratio of yield bending moment and ultimate bending moment α is introduced in this model so that $\theta_y = \alpha M_u / k_i$ is the yield rotation of joints. The definition of the elastic part refers to the trilinear model and the function model in Eurocode 3. The knee part is improved based on the three-parameter exponential function model so that the knee part is tangential to the elastic part at the piecewise point. Although the model does not clearly define the ultimate part of the joint, the curve model is obtained by the ultimate bending moment M_u, and $M = M_u$ is the asymptotic line. Therefore, it is feasible to

analyze the ultimate load of the joint even if the ultimate part is not clearly defined. In addition, the knee part of the curve model is determined by the exponential function with shape coefficient *c*, so the limit state of the joint can be considered by adjusting the shape coefficient to control the speed of the curve approaching the asymptotic line. To sum up, the suggested function model has high accuracy in the knee part while considering all force stages and avoiding numerical problems such as the non-convergence of calculation at the piecewise point. The moment-rotation curve model suggested in this paper is shown in Fig. 18.

$$M=\begin{cases} K_i\theta, & \theta \le \theta_y \\ \alpha M_u+(1-\alpha)M_u\left[1-e^{\frac{-[K_i+c(\theta-\theta_y)](\theta-\theta_y)}{(1-\alpha)M_u}}\right] & \theta > \theta_y \end{cases} \tag{57}$$

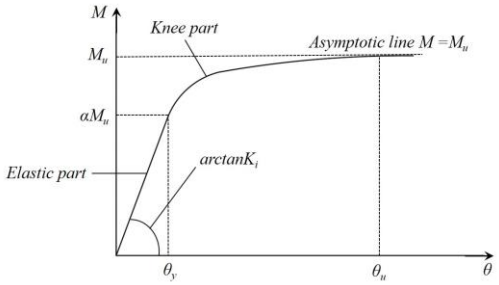

Fig. 18 The presented moment-rotation relationship model

The model recommended in this paper is utilized to calculate the moment-rotation curves of some beam-column joints with external cover plate in Table 2. In addition, the curves corresponding to the three typical models are presented in the same figure.The comparison of all curves is shown in Fig. 19. It is clear from this comparison that the curves calculated by the proposed model are well consistent with the finite element analysis results, which not only has the characteristics of high accuracy similar to a single nonlinear model in the knee part but also considers each force stage of the joint. In addition, the function model curve is continuous and smooth, which is convenient for subsequent structural analysis and calculation.

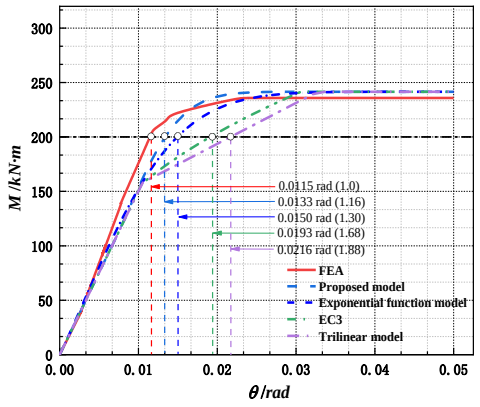

(a) BK260

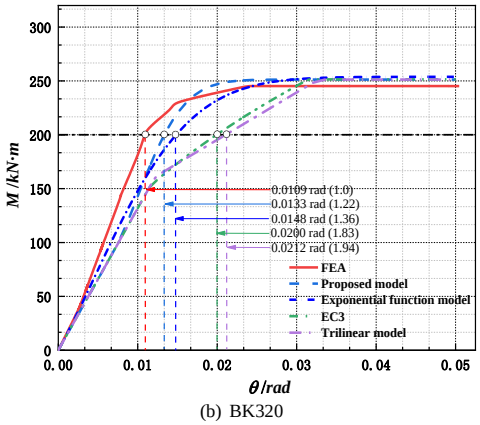

(b) BK320

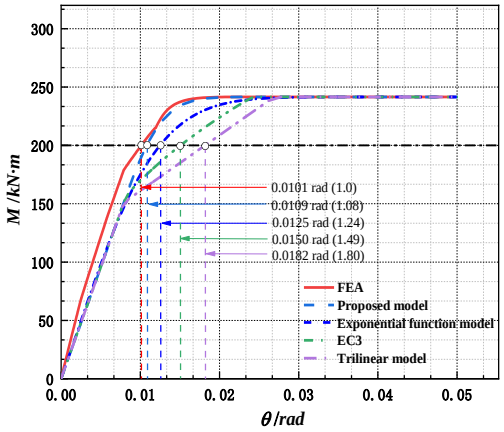

(c) BH15

Fig. 19 The moment-rotation curves determined by different models

7. Conclusions

In this paper, the force transmission mechanism of beam-column joints with the external cover plates was analyzed and the main force components of the joints were determined. The formulas for calculating the initial rotational stiffness and ultimate bending moment were supplied in accordance with the component analysis principle. On this basis, the moment-rotation curve model suitable for the external cover plate joint was proposed. From the study of this paper, The key findings may be summed up as follows:

(1) The equations for calculating the initial stiffness of this joint were established through the principle of the component method. The ratios between the predicted and actual findings from the numerical simulation had average and standard deviation values of 0.91 and 0.09, respectively, showing that the component analysis method can successfully predict the initial rotational stiffness of this joint.

(2) The various failure mechanisms of this joint were taken into consideration when developing the equations for the ultimate bending moment. The ratios between the predictions and the results of the numerical simulation had an average and standard deviation of 1.01 and 0.02, respectively, showing that the methods presented in this study can exactly determine the final moment resistance of this unique joint.

(3) The benefits of the previous piecewise and single nonlinear models are taken into consideration in the proposed model for the moment-roration relationship of beam-column joints. This model not only has a highly accurate knee part while considering each loading stage but also has smooth and continuous conditions at the piecewise points, which can avoid numerical problems such as non-convergence at the piecewise points in the subsequent analysis. Additionally, the moment-rotation curves derived by the suggested representation are in good agreement with the findings of the finite element analysis, showing that the suggested model is capable of properly projecting the mechanical behavior of the external cover plate joints.

Acknowledge

The authors sincerely acknowledge the financial support provided by the Key Project of the National Natural Science Foundation of China (No. 51938009) and the National Natural Science Foundation of China (No.51878419).

References

[1] Zhong S.T., The concrete-filled steel tubular structures, Beijing: Tsinghua University Press, 2003.
[2] Li G.C., Yu Y., Yang Z.J., Fang C., Ge H.B. and Liu Y.P., “Mechanical behavior of high-strength concrete filled high-strength steel tubular stub columns stiffened with encased I-shaped CFRP profile under axial compression”, Composite Structures, 275: 114504, 2021.
[3] Li G.C., Zhou B. and Pan J.H., “Finite element analysis on concrete-filled square steel tube short columns with inner CFRP profiles under axial compression”, Applied Mechanics and Materials, pp. 335-339, 2014.
[4] Feng X., Li G.C., Yang Z.J. and Cao W.Z., “Performance study on the mechanical behavior of a concrete-filled square steel tubular middle-long columns with inner I-shaped CFRP profiles under bi-axial eccentric loading”, Progress Steel Building Structures, 23(8):32-42+52, 2021. (in Chinese)
[5] Li W.Q., Chen Y.Y., Wang W., Xu Y.J. and Lv X.D., “Experimental study of external diaphragm joint connecting CHS column and H-shaped beam”, Advanced Steel Construction, 6(1): 578-588, 2010.
[6] Goswami R., Murty C.V.R., “Externally reinforced welded I-beam-to-box-column seismic connection”, Journal of Engineering Mechanics, 136(1), 23-30, 2010.
[7] Ye Q., Wang Y., Wang Z., Lin Y., Shu C. and Zhang F., “Experimental study of through diaphragm bolted joint between H-beam to CFST column”, Journal of Constructional Steel

Research, 182, 106647, 2021.
[8] Xu P.Z., Chen C., Yang L. and Zhu Y.G., “Finite element analysis on the seismic behavior of circular steel tubular column to H-shaped steel beam joint with cover-plate externally strengthened ring”, Progress in Steel Building Structures, 23(2): 14-21, 2021. (in Chinese)
[9] Cao S., Shu G., Lin K. and Qin Y., “Experimental seismic behaviour of bottom-through-diaphragm and top-ring connection to SST columns”, Journal of Constructional Steel Research, 150, 249-260, 2018.
[10] Wang W.D., Han L.H. and Uy B., “Experimental behaviour of steel reduced beam section to concrete-filled circular hollow section column connections”, Journal of Constructional Steel Research, 64(5), 493-504, 2008.
[11] Chen W.F., Torma S., Advanced Analysis in Steel Frames, Boca Raton: CRC Press, 1993.
[12] Masarira A., “The effect of joints on the stability behaviour of steel frame beams”, Journal of Constructional Steel Research, 58(10), 1375-1390, 2002.
[13] Faella C., Piluso V. and Rizzano G., Structural steel semirigid connections: Theory, Design and Software, Boca Raton, Florida: CRC Press LLC, 1999.
[14] Ding J.M., Shen Z.Y., “Influence of semi-rigid joint on internal force and displacement of steel frame structure”, Building Structure, 6, 8-12, 1991. (in Chinese)
[15] Wu F.H., Chen W.F., “A design model for semi-rigid connection”, Engineering Structures, 12(2), 88-97, 1990.
[16] Yee Y.L., Melchers R.E., “Moment-rotation curves for bolted connections”, Journal of Structural Engineering, 112(3), 615-635, 1986.
[17] Frye M., Morris G.A., “Analysis of flexibly connected steel frames”, Canadian Journal of Civi1 Engineering, 2(3), 280-291, 1975.
[18] Colson A., “Theoretical modeling of semirigid connections behavior”, Journal of Constructional Steel Research, 19(3), 213-224, 1991.
[19] Kishi N., Chen W.F., “Moment-rotation relation of semirigid connection with angles”, Journal of Structural Engineering, 116, 1813-1834, 1990.
[20] Ang K.M., Morris G.A., “Analysis of three-dimensional frames with flexible beam-column connections”, Canadian Journal of Civil Engineering, 11(2), 245-254, 1984.
[21] GB50017-2017, Steel Structure Design Standard. Beijing: China Construction Industry Press, 2017.
[22] GB50011-2010, Code for Seismic Design of Buildings. Beijing: China Construction Industry Press, 2016.
[23] JGJ99-2015, Technical Specification for High Rise Civil Steel Structures. Beijing: China Construction Industry Press, 2015.
[24] Han L.H., Concrete Filled Steel Tubular Structures: Theory and Practice. Beijing: Science Press, 2007.
[25] Li G.C., Zhan Z.C., Yang Z.J., Fang C. and Yang Y., “Behavior of concrete-filled square steel tubular stub columns stiffened with encased I-section CFRP profile under biaxial bending”, Journal of Constructional Steel Research, 169, 106065, 2020.
[26] Li G.C., Zhu Z.H., Sun X., Liu X.H. and Han Y.W., “Experimental research on concrete-filled square steel tubular slender columns with inner I-shaped CFRP under axial compression”, Journal of Building Structures, 38(S1), 226-232, 2017. (in Chinese)
[27] Zuo B., “Pseudo-static experimental study of H-shaped beams to cold-formed square steel tube columns connections with different outer diaphragm”, Qingdao Technological University, 2014. (in Chinese)
[28] Yuan Z.R., “The Research on the mechanical performance of the square concrete filled steel tube with T-stub connector”, Hunan University, 2013. (in Chinese)
[29] Liu H.C., Hao J.P., Xue Q. and Huang Y.Q., “Stress response and initial stiffness of side plate connections to WCFT columns”, Advanced Steel Construction, 17(3), 306-317, 2021.
[30] Zhao Q.W., Zhang S.M. and Jiang S.F., “Calculation model of initial rotational stiffness of steel beam-to-column bolted end-plate connections”, Engineering Mechanics, 26(6), 226-232, 2009. (in Chinese)
[31] Matsui C., “Strength and behavior of frames with concrete filled square steel tubular columns under earthquake loading”, Proceedings of the international specialty conference on concrete filled tubular structures, 104-111, 1985.
[32] EN1993-1-8, Eurocode 3: Design of Steel Structures - Part 1-8: Design of joints, 2010.
[33] Zhao J.H., Fan J.C. and Gao W.Q., “Moment-rotation analyses model of flush end-plate bolted connections between H-shape steel beams and rectangular CFST columns”, Engineering Mechanics, 38(6), 249-260, 2021. (in Chinese)

Advanced Steel Construction – Vol. 19 No. 2 (2023) 143–149
DOI:10.18057/IJASC.2023.19.2.6

HIGH PRECISION IDENTIFICATION METHOD OF MASS AND STIFFNESS MATRIX FOR SHEAR-TYPE FRAME TEST MODEL

Jin-Peng Tan [1, 2] and Dan-Guang Pan [1, *]

[1] *Department of Civil Engineering, University of Science and Technology Beijing, Beijing 100083, China*
[2] *Huachengboyuan Engineering Technology Group Co., Beijing 100052, China*
** (Corresponding author: E-mail: pdg@ustb.edu.cn)*

ABSTRACT

In the direct method of identifying the physical parameters of the shear-type frame structures through the frequencies and modes from the experimental modal analysis (EMA), the accuracy of the lumped mass depends on the initial mass, while the identified mass matrix and stiffness matrix are prone to generate some matrix elements without any physical meaning. In this paper, based on the natural frequencies and modes obtained from the EMA, an iterative constrained optimization solution for correcting mass matrix and a least squares solution for the lateral stiffness are proposed. The method takes the total mass of the test model as the constraint condition and develops an iterative correction method for the lumped mass, which is independent of the initial lumped mass. When the measured modes are exact, the iterative solution converges to the exact solution. On this basis, the least squares calculation equation of the lateral stiffness is established according to the natural frequencies and modes. Taking the numerical model of a 3-story steel frame structure as an example, the influence of errors of measured modes on the identification accuracy is investigated. Then, a 2-story steel frame test model is used to identify the mass matrix and stiffness matrix under three different counterweights. Numerical and experimental results show that the proposed method has good accuracy and stability, and the identified mass matrix and stiffness matrix have clear physical significance.

ARTICLE HISTORY

Received: 22 April 2022
Revised: 21 July 2022
Accepted: 27 July 2022

KEYWORDS

Shear-type frame;
Test model;
Physical parameter identification;
Mass matrix;
Stiffness matrix

1. Introduction

Shear-type steel frame structure is one of the most common engineering structures. In order to make the designed structure safer and more economical, a lot of theoretical research [1, 2] and experimental research [3, 4] have been carried out. When the stiffness of the beam is much greater than that of the column, this type of structure can be simplified into a lumped mass shear model. In the construction process of actual structures, there are usually geometric errors, material property errors and uncertainty of joint stiffness [5]. After careful consideration of the geometric similarity ratio of the experimental model, the size of the designed experimental model is typically small. As a result, the geometric error of the experimental model has a more significant impact on the mass and stiffness of the structure. In order to predict the response accurately for the analytical model under dynamic load or the damage in different test stages, it is necessary to identify the high precision mass matrix and stiffness matrix of the test model.

Depending on whether a priori model is required, the identification methods of mass and stiffness matrices can be classified as direct methods and indirect methods [6]. The indirect methods are to optimize the parameters of the analysis model to minimize the errors between the calculation results and the experimental results through the model updating method. The objective function of the optimization analysis significantly affects the results of the model updating. Since the frequencies and modes in practical engineering are the most easily obtained parameters, the objective function parameters are often constructed based on frequencies, modes and their derived variables [7-9]. Frequency response functions [10, 11] and time histories [12] contain more high frequency signals and are commonly used to construct objective functions. The iterative calculation of nonlinear equations is involved in the model updating, and the computational workload is considerably large. To improve the computational efficiency, based on sensitivity analysis [13], the nonlinear equations are linearized for the iterative calculation to accelerate the convergence, or artificial intelligence algorithms [14, 15] are used to compute the solution of the optimization equation. This method is suitable for complex large-scale structures and has a wider applicable range, but the computational workload is still significant. The direct methods are to calculate the mass and stiffness matrices of the system directly from the modal parameters or dynamic response time history of the structure without prior finite element model [16]. Among them, the physical parameter identification method based on modal parameters has been widely used because of its simplicity. Berman [17] established the Lagrange multiplier method for mass matrix correction with the minimum modified mass as the objective function. Baruch [18] also used the Lagrange multiplier method to obtain the correction of the mass matrix and stiffness matrix. Wei [19, 20] established methods to update the mass and stiffness matrices simultaneously and studied the interaction influence of mass and stiffness correction. Lee and Eun [21, 22] took the modified mass matrix and stiffness matrix as the objective function, modified the mass matrix and stiffness matrix at the same time and compared the accuracy of different methods to identify the stiffness matrix when the mass matrix was known. Qi [23] established the least squares solution of the lumped mass and lateral stiffness of a shear frame structure under the assumption that the mass and stiffness distribution of each layer is known. For the lumped-mass shear model, if the mass matrix of the system is known, then the stiffness matrix can be calculated directly by inverse analysis of the Jacobi matrix eigenproblem [24].

The direct method is easy to use and is usually suitable for structures with fewer degrees of freedom. Since the frame test model of the lumped mass shear model has fewer degrees of freedom, the mass matrix is diagonal, and the stiffness matrix is tridiagonal, it is more appropriate to use the direct method for calculation. The lumped mass shear model [25] of the frame structure is a simplified computational model obtained by using kinematic constraints. The diagonal matrix formed by the lumped mass is a simplification of the uniform mass matrix. Therefore, the exact value of the lumped mass is unknown. In addition, the calculated length of the column cannot be accurately estimated in the lateral stiffness calculation, which leads to a significant difference between the measured dynamic characteristics of the analytical model and the test model [26, 27]. When the mass matrix is unknown, the direct method to identify the physical parameters of the shear frame structure will face the following problems: (1) The accuracy of the direct method to identify the lumped mass is related to the initial solution, even if there is no modal error, the exact solution of the mass matrix still cannot be obtained. (2) The sparsity of the original matrix cannot be kept in the identified mass matrix and stiffness matrix, that is, the identified mass matrix and stiffness matrix may become full matrices and lose their physical meaning.

To address the above two problems, this paper proposes an iterative constrained optimization solution to correct the mass matrix so that the identified mass matrix is independent of the initial solution and converges to the accurate solution under the accurate mode. After the mass matrix is identified, the least squares solution of the lateral stiffness is also proposed. In this manner, the identified mass matrix and stiffness matrix are kept sparse, and each parameter meets the requirements of the calculation model and has a physical meaning. On this basis, the numerical simulation method was used to identify the mass matrix and stiffness matrix of a three-story frame structure. The influence of the initial mass and errors of measured modes on the identification results were analyzed. Then, the physical parameter identification of a two-story frame test model was studied. Finally, the accuracy and effectiveness of the proposed method are verified by comparing and analyzing the identification results of lumped mass and lateral stiffness of the model under different counterweights.

2. Iterative constrained optimization solution for correcting lumped mass

The *N*-layer shear frame structure shown in Fig. 1 can be simplified into a lumped mass shear model with *N* degrees of freedom. When the mass matrix is unknown, the initial lumped mass matrix is assumed to be:

$$\boldsymbol{M}_0 = diag[m_{i,0}] \tag{1}$$

in which $m_{i,0}$ is the lumped mass at the 0th iteration; $\boldsymbol{M}$ is $N\times N$ diagonal mass matrix.

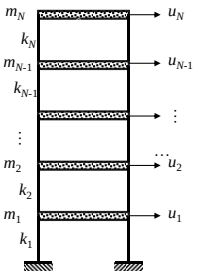

Fig. 1 Calculation model of shear-type frame structure

To identify the mass matrix of the model by the frequency domain method, the natural frequencies of the model and the corresponding modes $\omega_i, \boldsymbol{\phi}_i$ (i=1,2,…,N) are measured from the experimental model analysis. By using the iterative method to correct the mass matrix, the lumped mass matrix and the correction matrix of the (k-1)th iteration are denoted as $\boldsymbol{M}_{k-1}$ and $\Delta\boldsymbol{M}_{k-1}$ respectively, and the corrected mass matrix $\boldsymbol{M}_k$ can be therefore expressed as:

$$\boldsymbol{M}_k = \boldsymbol{M}_{k-1} + \Delta\boldsymbol{M}_{k-1} \tag{2}$$

Normalizing the measured modes gives:

$$\boldsymbol{\phi}_i^{\mathrm{T}}\boldsymbol{M}_k\boldsymbol{\phi}_i = 1 \tag{3}$$

Then

$$\boldsymbol{\phi}^{\mathrm{T}}\boldsymbol{M}_k\boldsymbol{\phi} = \boldsymbol{M}_{B,k} \tag{4}$$

in which $\boldsymbol{\phi}$ is the mode matrix made up of the N modes $\boldsymbol{\phi}_i$. If $\boldsymbol{M}_{B,k}$ is a unit matrix, the modes are orthogonal on $\boldsymbol{M}_k$, and there is no need to correct the mass matrix; otherwise, it needs to be corrected. Let the correction mass matrix $\Delta\boldsymbol{M}_k$ be a diagonal matrix $\Delta\boldsymbol{M}_k = diag[\Delta m_{i,k}]$ so that the corrected mass satisfies:

$$\boldsymbol{\phi}^T(\boldsymbol{M}_k + \Delta\boldsymbol{M}_k)\boldsymbol{\phi} = \boldsymbol{I} \tag{5}$$

where $\boldsymbol{I}$ is the unit matrix. Substituting Eq. (4) into Eq. (5) yields:

$$\boldsymbol{\phi}^{\mathrm{T}}\Delta\boldsymbol{M}_k\boldsymbol{\phi} = \boldsymbol{I} - \boldsymbol{M}_{B,k} \tag{6}$$

Expanding each upper triangular element in Eq. (6) yields:

$$\boldsymbol{\phi}_i^{\mathrm{T}}\Delta\boldsymbol{M}_k\boldsymbol{\phi}_j = \delta_{ij} - m_{Bij,k} \quad (j \geq i) \tag{7}$$

where δ_{ij} is the Kronecker symbol, when i=j, $\delta_{ij}=1$; when $i \neq j$, $\delta_{ij}=0$.

Expanding Eq. (7) gives:

$$\phi_{1i}\phi_{1j}\Delta m_{1,k} + \phi_{2i}\phi_{2j}\Delta m_{2,k} + \cdots + \phi_{Ni}\phi_{Nj}\Delta m_{N,k} = \delta_{ij} - m_{Bij,k} \tag{8}$$

For the Nth order mode, $N(N+1)/2$ equations can be obtained, and these equations can be arranged as a set of algebraic equations with $\Delta m_{i,k}$ ($i=1,2,\cdots,N$) as unknowns:

$$\boldsymbol{A}_k\{\Delta m\}_k = \boldsymbol{B}_k \tag{9}$$

in which, $\{\Delta m\}_k$ is a vector made up of main diagonal elements in $\Delta\boldsymbol{M}_k$. The number of equations contained in Eq. (9) is greater than the number of unknowns, and the least squares solution of $\{\Delta m\}_k$ can be expressed as:

$$\{\Delta m\}_k = \left(\boldsymbol{A}_k^T\boldsymbol{A}_k\right)^{-1}\boldsymbol{A}_k^T\boldsymbol{B}_k \tag{10}$$

For the frame structure, if the total mass m_a of the model is known, the sum of the lumped mass should be equal to m_a when the initial mass matrix is assigned; that is,

$$\sum_{i=1}^{N} m_{i,0} = m_a \tag{11}$$

When correcting the mass, the constraint condition is introduced:

$$\sum_{i=1}^{N} \Delta m_{i,k} = 0 \tag{12}$$

Using the Lagrange multiplier method, the optimal equation to solve the minimum value of Eq. (9) under the constraint of Eq. (12) can be expressed as:

$$\begin{aligned} f(\{\Delta m\}_k) = {} & \{\Delta m\}_k^T\boldsymbol{A}_k^T\boldsymbol{A}_k\{\Delta m\}_k - 2(\boldsymbol{A}_k^T\boldsymbol{B}_k)^T\{\Delta m\}_k \\ & + (\boldsymbol{A}_k^T\boldsymbol{B}_k)^T(\boldsymbol{A}_k^T\boldsymbol{B}_k) + \alpha\boldsymbol{A}_c^T\{\Delta m\}_k \end{aligned} \tag{13}$$

where α is the Lagrange multiplier; $\boldsymbol{A}_c = \{1 \quad 1 \quad \cdots \quad 1\}^T$ is a vector, whose elements are all unity. Taking the derivative of Eq. (13) with respect to $\{\Delta m\}_k$ and α respectively and setting the corresponding derivative to zero, the system of algebraic equations can be obtained:

$$\begin{bmatrix} 2\boldsymbol{A}_k^T\boldsymbol{A}_k & \boldsymbol{A}_c \\ \boldsymbol{A}_c^T & 0 \end{bmatrix}\begin{Bmatrix} \{\Delta m\}_k \\ \alpha \end{Bmatrix} = \begin{Bmatrix} 2\boldsymbol{A}_k^T\boldsymbol{B}_k \\ 0 \end{Bmatrix} \tag{14}$$

Solving Eq. (14) can get the kth iteration correction of lumped mass that satisfies the constraints.

Due to the errors of the measured modes, it is still impossible to accurately establish Eq. (5) through the correction of the mass matrix. However, the corrected mass can become smaller and smaller through iterative calculation. When the corrected mass is small enough, the iteration can be terminated. The conditions for the termination of the iteration can be expressed as:

$$\frac{\|\Delta\boldsymbol{M}_k\|}{\|\boldsymbol{M}_k\|} < e \tag{15}$$

in which, $\|\Delta\boldsymbol{M}_k\|$ and $\|\boldsymbol{M}_k\|$ are the second-order norms of $\Delta\boldsymbol{M}_k$ and $\boldsymbol{M}_k$ respectively; e is a predetermined tolerance and usually is set to 1×10^{-6}.

3. Least squares solution for lateral stiffness

After obtaining the corrected mass matrix $\boldsymbol{M}$, the jth mode satisfies the eigenvalue equation:

$$\boldsymbol{K}\boldsymbol{\phi}_j = \omega_j^2\boldsymbol{M}\boldsymbol{\phi}_j \tag{16}$$

where ω_j is the jth natural frequency; $\boldsymbol{K}$ is the stiffness matrix of the structure. When all natural frequencies and modes are known, the stiffness matrix can be expressed as:

$$\boldsymbol{K} = \boldsymbol{M}\boldsymbol{\phi}\ diag[\omega_j^2]\boldsymbol{\phi}^T\boldsymbol{M} \tag{17}$$

When the modal and mass matrices have errors, the stiffness matrix obtained by Eq. (17) is a full matrix, which leads to inconsistency between the stiffness matrix and the physical model. In order to make the identified stiffness matrix conform to the physical model, for the lumped-mass shear model, $\boldsymbol{K}$ has to be a tridiagonal matrix. When the numbering method of the degrees of freedom in Fig. 1 is adopted, the relationship between the stiffness matrix $\boldsymbol{K}$ and the lateral stiffness can be expressed as [24]:

$$\boldsymbol{K} = \boldsymbol{T}\boldsymbol{k}\boldsymbol{T}^T \tag{18}$$

where $\boldsymbol{k} = diag[k_i]$ is the diagonal matrix of lateral stiffness; k_i is the lateral stiffness of the ith layer; $\boldsymbol{T}$ is the stiffness transformation matrix:

$$\boldsymbol{T} = \begin{bmatrix} 1 & -1 & 0 & ... & 0 \\ 0 & 1 & -1 & ... & 0 \\ ... & ... & ... & ... & ... \\ 0 & ... & ... & 1 & -1 \\ 0 & ... & ... & 0 & 1 \end{bmatrix} \tag{19}$$

Eq. (18) denotes that the stiffness matrix is similar to the diagonal matrix of lateral stiffness for the lumped-mass shear model. After multiplying both sides of Eq. (16) by $\boldsymbol{\phi}_j^T$ on the left, using Eq. (18) and the modal orthogonality relation on the mass matrix, the following equations can be obtained:

$$\boldsymbol{\phi}_i^T \boldsymbol{T}\boldsymbol{k}\boldsymbol{T}^T \boldsymbol{\phi}_j = \lambda_i \delta_{ij} \tag{20}$$

Let

$$\boldsymbol{x}_i = \boldsymbol{T}^T \boldsymbol{\phi}_i \tag{21}$$

Expanding Eq. (20) gives:

$$x_{1i}x_{1j}k_1 + x_{2i}x_{2j}k_2 + \mathrm{L} + x_{Ni}x_{Nj}k_n = \delta_{ij}\lambda_i \tag{22}$$

After $N(N+1)/2$ numbers of Eq. (22) are taken from the upper triangular part of Eq. (20), these equations can be rewritten in matrix form:

$$\boldsymbol{X}\{k\} = \boldsymbol{Y} \tag{23}$$

in which $\{k\}$ is a vector composed of the main diagonal elements of $\boldsymbol{k}$. Then the least squares solution of $\{k\}$ is:

$$\{k\} = \left(\boldsymbol{X}^T\boldsymbol{X}\right)^{-1}\boldsymbol{X}^T\boldsymbol{Y} \tag{24}$$

From the calculation processes of Eq. (14) and Eq. (24), it can be seen that the prior information of the mass and stiffness of each layer is not required. The identified lumped mass and lateral stiffness is consistent with physical model. And the natural frequency and mode of the structure as well as the total mass are required to solve the lumped mass and lateral stiffness directly so that the calculation is relatively simple.

4. The algorithm workflow

To make the procedure of the algorithm clearer, the workflow of the proposed method is shown in Fig. 2. The algorithm is executed in six steps:

Step 1: Measure the natural frequencies of the model and the corresponding modes $\omega_i, \boldsymbol{\phi}_i$ (i=1,2,…,N).

Step 2: Assume initial lumped mass $m_{i,0}$(i=1,2,…,N) satisfy with Eq. (11), and set k=1.

Step 3: Normalize $\boldsymbol{\phi}_i$ (i=1,2,…,N) by Eq. (3).

Step 4: Assemble the matrix $\boldsymbol{A}_k$ and the vector $\boldsymbol{B}_k$, then obtain $\{\Delta m\}_k$ by Eq. (14), and set $\boldsymbol{M}_{k+1} = \boldsymbol{M}_k + \Delta\boldsymbol{M}_k$.

Step 5: If $\dfrac{\|\Delta\boldsymbol{M}_k\|}{\|\boldsymbol{M}_k\|} < e$, output the $\boldsymbol{M}_{k+1}$ as the solution and terminate the computation; otherwise, set k=k+1, and go back to Step 3.

Step 6: Assemble the matrix $\boldsymbol{X}$ and the vector $\boldsymbol{Y}$, then obtain $\{k\}$ by Eq. (24).

5. Validation of the proposed algorithm

The following 3-layer steel frame is an example to verify the accuracy and effectiveness of the proposed algorithm. The frame structure model, shown in Fig. 3, was analyzed by Clough and Penzien [25]. The exact mass of each layer is: m_1=10kg, m_2=7.5kg, m_3=5kg. The exact lateral stiffness of each layer is: k_1=1800N/m, k_2=1200N/s, k_3=600N/m.

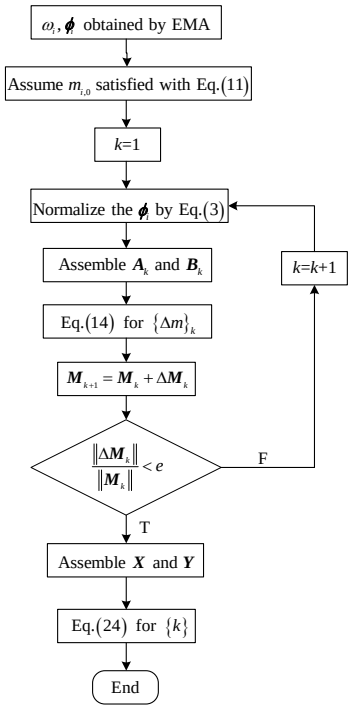

Fig. 2 Flowchart of the proposed method

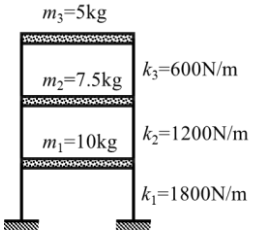

Fig. 3 3-layer steel frame structure model

5.1. Influences of the initial solution on the calculation result

The verification of accuracy and convergence of mass correction in Eq. (14) with the following two initial lumped mass are carried out:

Case 1: $\boldsymbol{M}_0 = diag[9.5 \quad 7.5 \quad 5.5]$

Case 2: $\boldsymbol{M}_0 = diag[7.5 \quad 7.5 \quad 7.5]$

Table 1 shows the lumped mass of each layer after the mass correction of the two cases. Qi [23] used the constrained least squares while Berman [17] used the Lagrange multiplier method for the lumped mass correction. Their results are also listed in the table for comparison.

It is observed that the results of the two cases by the proposed method are the same as the exact solution, while the calculation results by Qi [23] and Berman [17] are different from the exact solution. The relative error e_m of the identified lumped mass can be expressed as:

$$e_m = \frac{m^* - m}{m^*} \times 100\% \tag{25}$$

in which m and m* are the approximate and exact mass respectively.

The maximum relative errors of Case 1 and Case 2 obtained by Qi [23] are 4.72% and 23.28% respectively, and the maximum relative errors of the main diagonal elements of Case 1 and Case 2 obtained by Berman [17] are 3.54% and 17.74% respectively. This shows that the accuracy of the correction by these two methods is related to the initial solution. In these two methods, the smaller the difference between the initial solution and the exact solution, the higher the

accuracy of the correction result, and their identified total mass is unequal to the exact solution even if the total mass of the initial solution is consistent with the exact solution.

Table 1
The corrected lumped mass of 3-layer steel frame

Method	Case1	Case2
Present Study	$\begin{bmatrix} 10 & & \\ & 7.5 & \\ & & 5 \end{bmatrix}$	$\begin{bmatrix} 10 & & \\ & 7.5 & \\ & & 5 \end{bmatrix}$
Ref. [23]	$\begin{bmatrix} 9.911 & & \\ & 7.563 & \\ & & 5.236 \end{bmatrix}$	$\begin{bmatrix} 9.379 & & \\ & 7.525 & \\ & & 6.164 \end{bmatrix}$
Ref. [17]	$\begin{bmatrix} 10.016 & 0.226 & 0 \\ 0.226 & 7.597 & -0.004 \\ 0 & -0.004 & 5.177 \end{bmatrix}$	$\begin{bmatrix} 10.081 & 1.129 & 0 \\ 1.129 & 7.984 & 0.565 \\ 0 & 0.565 & 5.887 \end{bmatrix}$

On the contrary, in the proposed method, different initial mass would also converge to the exact solution, which demonstrates good calculation accuracy and stability. Fig. 4 shows the calculation errors obtained in the iterative process of the two cases. From the calculation results, the initial solution would only influence the number of iterative steps, 14 and 16 iteration steps for Case 1 and Case 2 respectively. However, it has no effect on the convergence result.

Table 2 shows the lateral stiffness of each layer obtained from Eq. (24) based on the identified lumped mass. The maximum relative errors of Case 1 and Case 2 stiffness obtained by Qi [23] are 1.50% and 5.75% respectively and by Berman [17] are 3.92% and 19.83% respectively. This result shows that the errors of the identified lateral stiffness by Qi and by Berman would increase with the increase of the error of the identified mass. In the proposed method, the identified lateral stiffness is the same as the exact solution.

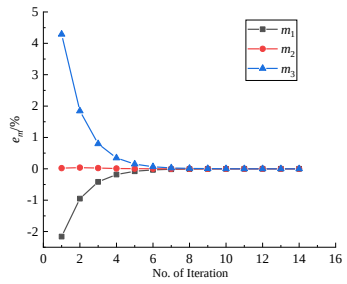

(a) Case 1

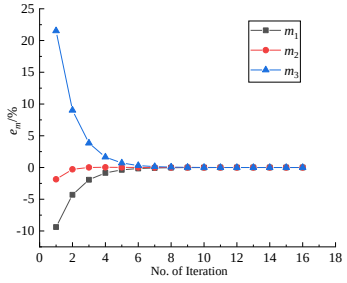

(b) Case 2

Fig. 4 Errors of identified lumped mass in the iterative process

5.2. The influence of the error of measured mode

Error is inevitable in experiment modal analysis (EMA) of engineering structures. Generally, the error of measured mode is much larger than that of measured frequency [6]. Therefore, in the following analysis, the influence of modal measurement error on the identification of the lumped mass and lateral stiffness is investigated, and the error of measured frequency is ignored. It is assumed that the relative error of measured modes is in a normal distribution:

Table 2
Identified lateral stiffness (kN/m)

k_i	Case1			Case2		
	Present study	Ref.[23]	Ref. [17]	Present study	Ref.[23]	Ref. [17]
k_1	1.800	1.824	1.819	1.800	1.884	1.888
k_2	1.200	1.193	1.153	1.200	1.131	0.962
k_3	0.600	0.609	0.609	0.600	0.633	0.640

$$\varepsilon \sim N(0,\sigma^2) \tag{26}$$

in which σ is the standard deviation. The mode with noise after considering the measurement error is:

$$\phi_{ij} = \phi_{ij}^{*}(1+\varepsilon) \tag{27}$$

in which ϕ_{ij}^{*} is the exact value of modal displacement.

In order to analyze the statistical results of the influence of measurement error on the identification of lumped mass and stiffness, 100 groups of random numbers are generated for each standard deviation. Fig. 5 is the box diagram of the lumped mass and stiffness under the standard deviation of 0.01, 0.02, 0.03, 0.04 and 0.05 respectively. Since the proposed method is independent of the initial mass, the convergence result of Case 1 initial mass distribution is the same as that of Case 2. It can be seen from the calculation results that although there is measurement error in the mode, the median value of the identified mass and stiffness are very close to the exact solution. The variance of identification results becomes greater with increasing error of the measured mode. Table 3 shows the errors of the mean value of the identified lumped mass and lateral stiffness under different variances. The numerical results show that the error of mean is less than 1% and is independent of the variation of measured mode.

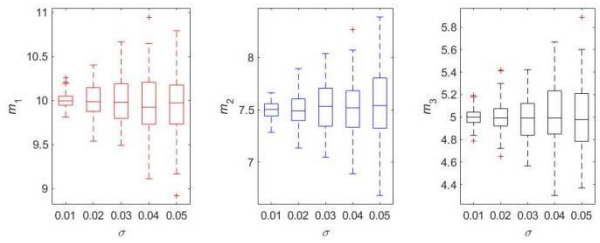

(a) Mass

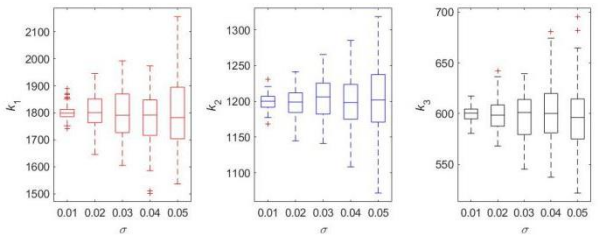

(b) Stiffness

Fig. 5 Box diagram for identifying mass and stiffness under different errors

Table 3
Errors of mean value of identified lumped mass and lateral stiffness (%)

σ	m_1	m_2	m_3	k_1	k_2	k_3
0.01	0.038	-0.055	0.008	0.060	-0.031	-0.022
0.02	-0.003	-0.008	0.017	0.307	-0.119	-0.147
0.03	-0.065	0.265	-0.267	-0.103	0.196	-0.316
0.04	-0.516	0.280	0.611	-0.786	-0.108	0.397
0.05	-0.303	0.595	-0.286	-0.093	0.257	-0.667

To further analyze the influence of the error of measured mode on the calculation results, the coefficients of variation (COV) of identified parameters

are defined:

$$\kappa = \frac{\sigma_{\xi}}{\overline{\xi}} \tag{28}$$

in which σ_{ξ} and $\overline{\xi}$ are the standard deviation and mean value of variable ξ (m_i and k_i, i=1, 2, 3) respectively. Fig. 6 shows the COV of the identified lumped mass and lateral stiffness under various variances of measured mode. The COV clearly increases with the increase of variance. However, the COV of the mass is almost the same as that of the stiffness. For example, when the standard deviation of mode is 5%, the COV of mass and stiffness are also approximately 5%, which shows that the error of identified lumped mass and lateral stiffness is almost the same as that of mode. The error of measured mode is not enlarged in the process of identifying lumped mass and lateral stiffness in turn, so the identification method has good stability.

6. Mass and stiffness identification of frame test model

To further verify the adaptability of the proposed method in the frame test model, a shear steel frame model is designed. The steel frame is a two-story two-span one-bay structure with layer height of 0.39m, a span of 500mm and a bay of 375mm. The designed section of the column is 4mm × 20mm, the beam is 4mm (width) × 15mm (height), and the floor slab is a 4mm thick steel plate. In order to avoid torsional vibration of the structure, diagonal braces with a cross-section of 4mm × 8mm are installed in the vertical vibration direction. The design weight of the model is 53.2kg. However, due to the thickness imperfection of the steel plates, the actual weight of the test model is 49.2kg. To analyze the lumped mass and lateral stiffness of two degrees of freedom formed by the frame model, three counterweight combinations are applied, as shown in Table 4, which are called Structure 1, Structure 2 and Structure 3 respectively. The photos of the tested steel frames are shown in Fig. 7. The EMA is carried out by the acceleration signal of the accelerometer under the excitation of a force hammer on the second floor. Then the eigensystem realization algorithm (ERA) [28] is used to identify the dynamic characteristics. The identified natural frequencies are shown in Table 5 and the mode shapes are shown in Fig. 8.

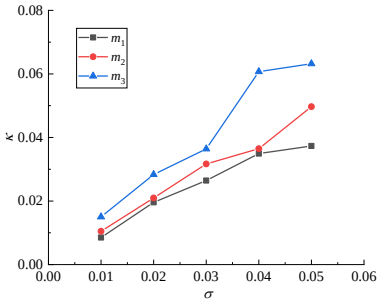

(a) Mass

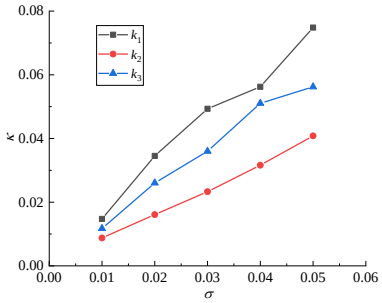

(b) Stiffness

Fig. 6 COV of the identified lumped mass and lateral stiffness

Table 4
Counterweight of structure (kg)

The Floor	Structure 1	Structure 2	Structure 3
1	13.5	27.5	41
2	8.6	22.6	36.1

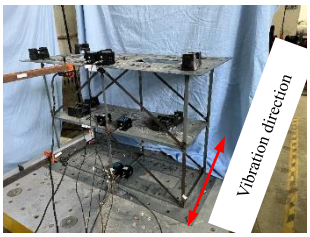

(a) Structure 1

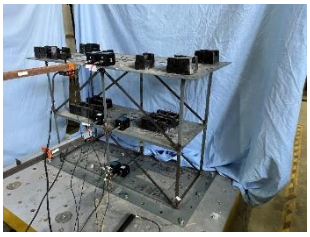

(b) Structure 2

(c) Structure 3

Fig. 7 Photos of tested steel frames

Table 5
Measured natural frequencies (Hz)

No. of Mode	Structure 1	Structure 2	Structure 3
1	2.990	2.380	2.030
2	7.934	6.331	5.420

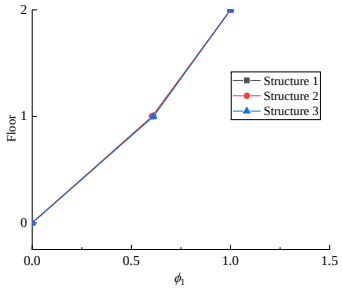

(a) The 1st mode

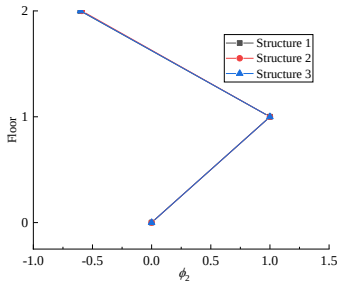

(b) The 2nd mode

Fig. 8 Modes of the structure

According to the measured mass of the frame structure, the total net mass of the two lumped mass of the test models is 31.33kg as the constraint condition. By the proposed method, the lumped mass and lateral stiffness of the three structures are identified, as shown in Table 6.

Table 6
The identified mass and stiffness of the 2-story steel frame

Floor	Structure 1			Structure 2			Structure 3		
	Mass (Kg)	Net mass (Kg)	Lateral stiffness (kN/m)	Mass (Kg)	Net mass (Kg)	Lateral stiffness (kN/m)	Mass (Kg)	Net mass (Kg)	Lateral stiffness (kN/m)
1	26.545	13.045	25.517	40.238	12.738	25.019	53.730	12.730	24.054
2	26.885	18.285	25.176	41.192	18.592	24.239	54.700	18.600	23.842

The net mass in Table 6 is the identified lumped mass minus the counterweight, which means the lumped mass of the test model. The maximum difference of the identified net mass of the three structures is 2.41%. The difference in the identification results of different counterweights is caused by random errors in the measured mode. The maximum difference of the identified lateral stiffness is 5.73%, which is slightly greater than that of the lumped mass. This is also caused by some random errors of the measured natural frequency. Based on the identified lumped mass and lateral stiffness, the analytical natural frequencies of the three structures are estimated by eigenvalue analysis, as shown in Table 7.

If the natural frequency obtained from the test is taken as the accurate solution, the relative error of the analytical natural frequencies can then be defined by:

$$e_{\omega} = \frac{\omega_j - \omega_j^*}{\omega_j^*} \times 100\% \tag{29}$$

in which ω_j and ω_j^* are the analytical and measured natural frequencies respectively. The relative error of the analytical natural frequency is shown in Table 8. The calculation result shows that the maximum error of analytical natural frequency is 1.72%, which shows good accuracy of the identified lumped mass and lateral stiffness.

Table 7
Analytical natural frequencies of the 2-story steel frame(Hz)

No. of Mode	Structure 1	Structure 2	Structure 3
1	3.030	2.421	2.065
2	7.932	6.329	5.418

Table 8
Relative errors (%) of analytical natural frequency of the 2-story steel frame

No. of Mode	Structure 1	Structure 2	Structure 3
1	1.338	1.723	1.724
2	-0.025	-0.032	-0.037

7. Conclusion

To identify the mass matrix and stiffness matrix of the shear-type frame test model, a high precision identification method is proposed to correct the lumped mass and lateral stiffness based on the natural frequencies and modes. According to the analytical and experimental results, the following conclusions can be drawn:

(1) For the shear-type frame structure, the lumped mass is a diagonal matrix, and the stiffness matrix can also be transformed into a diagonal matrix of lateral stiffness by the stiffness transformation matrix. The iterative constrained optimization solution of the mass matrix correction and the least squares solution of the lateral stiffness are established. Therefore, the identified mass matrix and stiffness matrix have clear physical significance.

(2) The identified mass matrix is independent of the initial mass and does not demand the prior mass distribution. When the measured modes are exact, the identified mass converges to the exact solution. When there are errors in the measured modes, the error of the identified lumped mass and lateral stiffness is almost the same as the modal error. The modal error does not enlarge in the process of identifying the lumped mass and lateral stiffness in turn, and the identification method has good stability.

(3) The maximum differences of identified lumped mass and lateral stiffness of steel frame test model with three different counterweights are 2.41% and 5.73% respectively. The maximum error between the analytical and experimental natural frequencies is 1.72%, which shows a good accuracy.

The identification method of stiffness coefficients in this paper is applicable to shear-type frame structures whose stiffness matrix is a tridiagonal matrix. In the future, more research is needed to identify the physical parameters of the bending-type structures.

References

[1] G. Q. Li, J. Z. Zhang, L. L. Li, et al., "Progressive collapse resistance of steel framed buildings under extreme events", Advanced Steel Construction, Vol. 17, pp. 318-330, 2021. Doi: 10.18057/IJASC.2021.17.3.10

[2] A. L. Zhang, G. H. Shangguan, Y. X. Zhang, et al., "Experimental study of resilient prefabricated steel frame with all-bolted beam-to-column connections", Advanced Steel Construction, Vol. 16, pp. 255-271, 2020. Doi: 10.18057/IJASC.2020.16.3.7

[3] J. P. Yang, P. Z. Li, Z. Lu., "Large-scale shaking table test on pile-soil-structure interaction on soft soils", The Structural Design of Tall and Special Buildings, Vol. 28, pp. 1679, 2019. Doi: 10.1002/tal.1679

[4] Q. Wang, J. T. Wang, F. Jin, et al., "Real-time dynamic hybrid testing for soil–structure interaction analysis", Soil Dynamics and Earthquake Engineering, Vol. 31, pp. 1690-1702, 2011. Doi: 10.1016/j.soildyn.2011.07.004

[5] K.S. Al-Jabri, S. M. Al-Alawi, A. H. Al-Saidy, et al., "An artificial neural network model for predicting the behaviour of semi-rigid joints in fire", Advanced Steel Construction, Vol. 5, pp. 452-464, 2009.

[6] J. E. Mottershead, M. I. Friswell., "Model updating in structural dynamics: A survey", Journal of Sound and Vibration, Vol. 167, pp. 347-375, 1993. Doi: 10.1006/jsvi.1993.1340

[7] X. Zhou, Y. Xia, S. Weng., "L1 regularization approach to structural damage detection using frequency data", Structural Health Monitoring, Vol. 14, pp. 571-582, 2015. Doi: 10.1177/1475921715604386

[8] W. X. Ren, H. B. Chen., "Finite element model updating in structural dynamics by using the response surface method", Engineering Structures, Vol. 32, pp. 2455-2465, 2010. Doi: 10.1016/j.engstruct.2010.04.019

[9] Y. F. Xu, W. D. Zhu, S. A. Smith., "Non-model-based damage identification of plates using principal, mean and Gaussian curvature mode shapes", Journal of Sound and Vibration, Vol. 400, pp. 626-659, 2021. Doi: 10.1016/j.jsv.2017.03.030

[10] A. K. Panda, S. V. Modak., "An FRF-based perturbation approach for stochastic updating of mass, stiffness and damping matrices", Mechanical Systems and Signal Processing, Vol. 166, pp. 108416, 2022. Doi: 10.1016/j.ymssp.2021.108416

[11] S. Pradhan, S. V. Modak., "A two-stage approach to updating of mass, stiffness and damping matrices", International Journal of Mechanics Sciences, Vol. 140, pp. 133-150, 2018. Doi: 10.1016/j.ijmecsci.2018.02.033

[12] X. G. Li, F. S. Liu., "A nonmode-shape-based model updating method for offshore structures using extracted components from measured accelerations", Applied Ocean Research, Vol. 121, pp. 103087, 2022. Doi: 10.1016/j.apor.2022.103087

[13] J. E. Mottershead, M. Link, M. I. Friswell., "The sensitivity method in finite element model updating: A tutorial", Mechanical Systems and Signal Processing, Vol. 25, pp. 2275-2296, 2011. Doi: 10.1016/j.ymssp.2010.10.012

[14] V. Alves, M. Oliveira, D. Ribeiro, et al., "Model-based damage identification of railway bridges using genetic algorithms", Engineering Failure Analysis, Vol. 118, pp. 104845, 2020. Doi: 10.1016/j.engfailanal.2020.104845

[15] H. Y. Gou, T. Q. Zhao, S. Q. Qin, et al., "In-situ testing and model updating of a long-span cable-stayed railway bridge with hybrid girders subjected to a running train", Engineering Structures, Vol. 253, pp. 113823, 2022. Doi: 10.1016/j.engstruct.2021.113823

[16] R. Ghanem, M. Shinozuka., "Structural system identification. I: Theory", Journal of Engineering Mechanics, Vol. 121, pp. 255-264, 1995. Doi: 10.1061/(ASCE)0733-9399(1995)121:2(255)

[17] A Berman., "Mass matrix correction using an incomplete set of measured modes", AIAA Journal, Vol. 17, pp. 1147-1148, 1979. Doi: 10.2514/3.61290

[18] P. Jack, T. P. Holman, M. Mott-Smith, et al., "Optimal correction of mass and stiffness matrices using measured modes", AIAA Journal, Vol. 20, pp. 1623-1626, 1982. Doi: 10.2514/3.7995

[19] F.S. Wei., "Analytical dynamic model improvement using vibration test data", AIAA Journal, Vol. 28, pp. 175-177, 1990. Doi: 10.2514/3.10371

[20] F.S. Wei., "Mass and stiffness interaction effects in analytical model modification", AIAA Journal. Vol. 28, pp. 1686-1688, 1990. Doi: 10.2514/3.25269

[21] E. T. Lee, H. C. Eun., "Correction of stiffness and mass matrices utilizing simulated measured modal data", Applied Mathematical Modelling, Vol. 33, pp. 2723-2729, 2009. Doi: 10.1016/j.apm.2008.08.010

[22] E. T. Lee, H. C. Eun., "Update of corrected stiffness and mass matrices based on measured dynamic modal data", Applied Mathematical Modelling, Vol. 33, pp. 2274-2281, 2009. Doi: 10.1016/j.apm.2008.06.004

[23] W. R. Qi., "Damping model and seismic response analysis of frame structures", University of Science and Technology Beijing, 2021. (in Chinese)

[24] G. L. Gladwell., "Inverse problems in vibration", Springer Netherlands, Waterloo, Ontario, Canada, 2005.

[25] R. W. Clough, J Penzien. "Dynamics of structures", 2nd Edition, Computers and structures, Inc., Berkeley, CA, USA, 1995.

[26] G. B. Wang, Y. Wang, H. T. Yu, et al., "Shaking table tests on seismic response of rocking frame structure considering foundation uplift", Chinese Journal of Geotechnical Engineering, Vol. 43, pp. 2064-2074, 2021. Doi:10.13374/j.issn1001-053x.2014.12.020 (in Chinese)
[27] D. G. PAN, L. L. Gao., G. H. Jin, et al., "Model test of dynamic characteristics of structure-soil-structure system", Journal of University of Science and Technology Beijing, Vol. 36, pp. 1720-1728, 2014. Doi: 10.13374/j.issn1001-053x.2014.12.020 (in Chinese)
[28] J. N. Juang, R. S. Pappa. "An eigensystem realization algorithm for modal parameter identification and model reduction". Journal of Guidance, Control, and Dynamics, vol. 8, pp. 620-627. 1985. Doi:10.2514/3.20031

Advanced Steel Construction – Vol. 19 No. 2 (2023) 150–156
DOI:10.18057/IJASC.2023.19.2.7

EXPERIMENTAL STUDY ON INTERACTION OF DISTORTIONAL AND GLOBAL BUCKLING OF STAINLESS STEEL LIPPED CHANNEL COLUMNS

Mei-Jing Liu [1], Jun-Feng Liu [2], Mei-He Chen [3, *], Guang-Ming Yu [4], Sheng-Gang Fan [5] and Cheng-Long Wan [3]

[1] *Department of Civil Engineering, Southeast University Chengxian College, Nanjing, China*
[2] *Three Gorges Renewables Yangjiang Power Co.,Ltd.,Yangjiang,Guangdong, China*
[3] *China Academy of Building Research, Beijing, China*
[4] *Institute of Science and Technology, China Three Gorges Corporation, Beijing, China*
[5] *Key Laboratory of Concrete and Prestressed Concrete Structures of Ministry of Education, School of Civil Engineering, Southeast University, Jiulonghu Campus, Nanjing, China*
** (Corresponding author: E-mail: mhechen@163.com)*

ABSTRACT

This paper presents an experimental program to investigate distortional and global interaction buckling of stainless steel lipped channel columns in compression. Appropriate cross-sections and lengths were chosen so as to observe distortional-overall interaction buckling. In total, 21 buckling tests were conducted. After a brief introduction to the choice of column specimen geometries, key experimental results have been presented and discussed. The tests aim to study and observe the effect of distortional-global interactive buckling, study member under pin-ended boundary conditions, and provide benchmarks for design. Column tests were carried out with 13 position transducers monitoring displacements at key locations. A 3-D laser scanner was used to measure the imperfection shapes and magnitudes of the columns before testing. Material tests have been performed to determine the mechanical properties of stainless steel. Distortional–global interactive buckling of all columns is shown to be a failure mode. The experimental results are also used to evaluate the Australian Standard AS/NZS, North American Specification AISI, as well as formulation proposed by Becque and Rasmussen's predictions, indicated that the Direct Strength Method (DSM) as described in AISI and AS/NZS for members undergoing distortional-overall interaction buckling are unconservative. Becque and Rasmussen's curve is much closer to the test points than DSM in AISI and AS/NZS.

ARTICLE HISTORY

Received: 8 August 2022
Revised: 16 December 2022
Accepted: 29 December 2022

KEYWORDS

Stainless steel;
Buckling mode interaction;
Lipped channel column;
Direct strength method;
Axial compression test

1. Introduction

Compared to carbon steel, stainless steel has attractive features in appearance, corrosion resistance, and fire resistance rating [1-3]. Stainless steel is also 100% recyclable and retains its good mechanical and physical properties after recycling [3]. Stainless steel is widely used in all walks of life and has attracted much attention. In addition, the boom in stainless steel production with continuous improvement in processing methods offers the possibility of more use in building structures.

As architects, designers and researchers are becoming aware of the good properties of stainless steel, many research projects have been conducted, including material properties [4-7], lipped channel columns [8-19], channel columns [20-23], I-section columns [24-29] and hollow section [30-35]. These research results have led to significant advances in design and application in the construction industry. However, tests performed on columns have mainly investigated failure by local, distortional, and global buckling. Currently, There needs to be more investigations on distortional-overall interaction buckling.

This paper aims to present an experimental program to study the distortional-overall interaction buckling in S30408 stainless steel lipped channels. Material tensile tests were first performed to investigate the mechanical properties of stainless steel. Then the imperfections were measured to obtain the imperfection distribution patterns and the maximum imperfection values of local, distortional and overall buckling. Axial compression tests on 21 columns were conducted to investigate the buckling damage characteristics of stainless steel columns. The test specimens are axially compressed while the columns are designed to undergo distortional-overall interaction buckling. The focus in this experimental program is to study the distortional-overall interaction buckling.

2. Material properties

Material property studies on stainless steel alloy materials are essential for designing appropriate sections and evaluating the strengths of the designed sections. Material tests have been carried out to study the mechanical behavior of stainless steel. Specimens were extracted from 1.5mm and 1.8mm columns using a laser cutter, as shown in Fig. 1.

The specimens were tested following the code of metallic materials-tensile testing [36]. The fractures of the tensile specimens after stretching were shown in Fig. 2, indicating that the specimens have a small necking range and a smooth fracture. The coupons were elongated after stretching, with good elongation of up to nearly 60%.

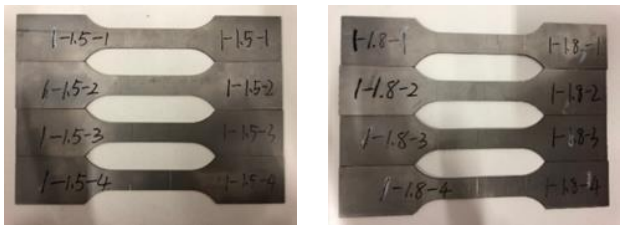

(a) 1.5mm coupons (b) 1.8mm coupons

Fig. 1 Tensile specimen

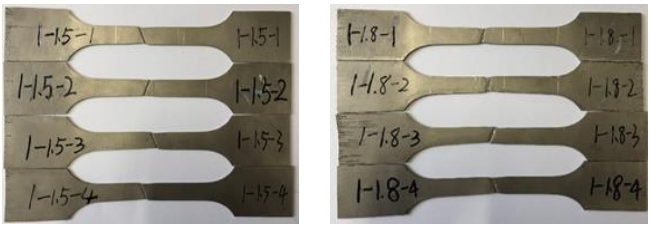

(a) 1.5mm coupons (b) 1.8mm coupons

Fig. 2 After tensile failure

Tensile results are listed in Table 1. In the table, E_0 is the material Young's modulus; $\sigma_{0.01}$ and $\sigma_{1.0}$ are the stresses corresponding to 0.01% and 1.0% residual deformation, respectively; $\sigma_{0.2}$ is the material 0.2% proof stress; σ_u is the peak material load; $\varepsilon_{t0.01}$, $\varepsilon_{t0.2}$, $\varepsilon_{t1.0}$ represent the strain corresponding to $\sigma_{0.01}$, $\sigma_{0.2}$, $\sigma_{1.0}$; ε_f is the elongation. The measured stress-strain relationships are shown in Fig. 3, indicating that stainless steel has a strong nonlinearity.

Table 1
Tensile properties

Specimen code	E_0 (MPa)	$\sigma_{0.01}$ (MPa)	$\sigma_{0.2}$ (MPa)	$\sigma_{1.0}$ (MPa)	σ_u (MPa)	$\varepsilon_{t0.01}$ (%)	$\varepsilon_{t0.2}$ (%)	$\varepsilon_{t1.0}$ (%)	ε_f (%)
F-1.5-1	192653	206.3	269.0	313.4	766.7	0.117	0.340	1.163	58.00
F-1.5-2	202049	242.2	272.3	309.9	767.3	0.130	0.335	1.153	63.00
F-1.5-3	215321	240.4	273.4	313.3	767.5	0.122	0.327	1.146	66.00
F-1.5-4	202148	230.3	270.4	312.9	763.2	0.124	0.334	1.155	64.00
Average	203042	229.8	271.3	312.4	766.2	0.123	0.334	1.154	62.75
F-1.8-1	206867	217.4	287.4	333.2	756.7	0.115	0.339	1.161	60.00
F-1.8-2	193045	220.1	281.5	325.4	758.0	0.124	0.346	1.169	58.00
F-1.8-3	202695	235.7	286.1	330.3	757.3	0.126	0.341	1.163	62.00
F-1.8-4	193299	245.9	285.4	328.4	770.0	0.137	0.348	1.170	60.00
Average	198977	229.8	285.1	329.3	760.5	0.126	0.344	1.166	60.00

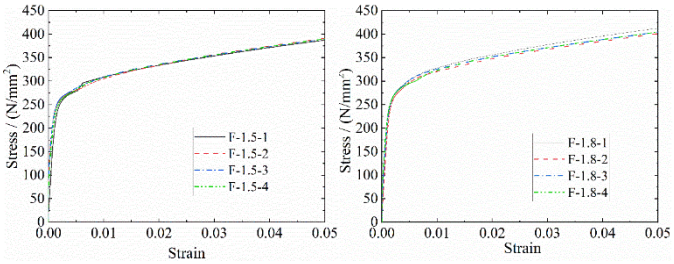

(a) 1.5mm (b) 1.8mm

Fig. 3 Measured Stress–strain relationships

3. Experimental investigation

3.1. Test setup

To investigate the distortional and overall interaction buckling of the channels. A total of 21 specimens hinged at both ends were conducted. The columns can rotate around the weak axis during the test. A test loading instrument (WDW-100) with high accuracy was used to conduct the test, as shown in Fig. 4. The single knife-edge bearing was used in the experiment, and the supports were lubricated, as shown in Fig. 5 (b). The complete experimental setup is illustrated in Fig. 5 (a). Four M16 bolts connected the support and the channel, and the end plates were connected with the support bottom plate as a whole to ensure that there was no relative sliding between the test column and the loading plate. A straight ruler was used to measure distortional buckling during the test, as shown in Fig. 5.

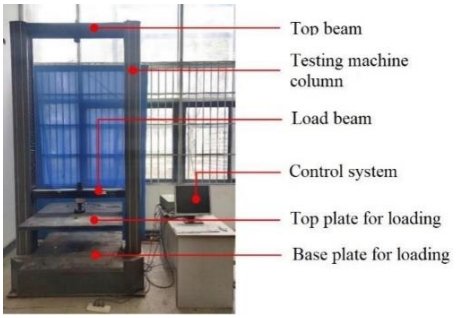

Fig. 4 Test loading instrument (WDW-100)

(a) Set-up (b) Specimen boundary conditions

Fig. 5 Test set-up

To study the cross-sectional stress variation with load at the middle of the column height during loading, 20 strain gauges were placed on each column, and the strain gauges were located on the inside and outside of the flanges, lips, and web. The numbers in parentheses in Fig. 6 are the numbers of the strain gauges inside the channels. The strain gauge data was obtained by the dynamic strain data acquisition instrument TDS-630, as shown in Fig. 7.

To obtain the axial displacements and lateral displacements of the channels, as well as the rotation angles of the support at both ends of the column, 13 LVDTs were installed on the specimens. The axial shortenings and the rotation angles of the columns can be obtained based on the results of LVDTs 6, 7, 8, 9, 10, 11, 12 and 13, and the lateral displacements can be calculated from the results of LVDTs 1, 2, 3, 4 and 5, as shown in Fig. 8.

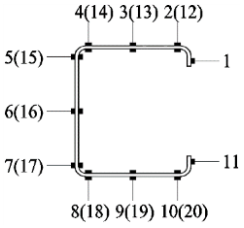

Fig. 6 Location of strain gauges **Fig. 7** TDS-630 Dynamic strain collector

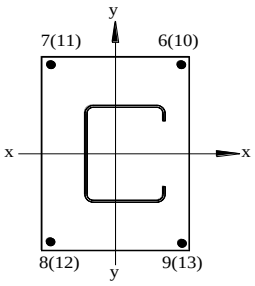

(a) Axial LVDTs at end plate

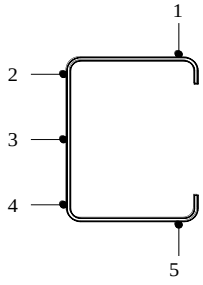

(b) Lateral LVDTs at column mid-height

Fig. 8 Location of LVDTs

Plates 20mm thick were welded at each end of the column to facilitate test loading and uniform force transfer. The dimensions of the plates are 240mm in

length and 160mm in width. All the finished test columns are shown in Fig. 9.

Fig. 9 Stainless steel column specimens

3.2. Specimen selection

The first step of the test is to design specimen dimensions, i.e., the cross-sectional sizes and the specimen lengths. The specimens were designed according to the CUFSM [37] buckling analysis results. The stainless steel columns were designed so that they have an interaction of distortional and global buckling modes. Fig. 10 shows a typical signature curve with two minimal value points: the local and distortional buckling half-wavelengths, respectively. The local buckling half-wavelength is smaller than the distortional buckling half-wavelength.

The column length is a key factor in determining what kind of buckling occurs in the column. First, the column should meet the requirements of $1.2P_{crd} < P_{crl}$ and $1.2P_{crg} < P_{crl}$, where P_{crd}, P_{crl} and P_{crg} are distortional, local and global buckling strength, respectively. Then $0.9P_{crd} < P_{crg} < 1.1P_{crd}$ should be satisfied. The specimen length should be greater than the distortional buckling half-wavelength. The global buckling of the specimen should be avoided, which means that the column length should be moderate.

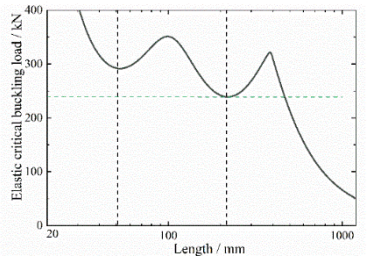

Fig. 10 Stainless steel column specimens

Table 2 lists the measured values of the columns, and the symbols are illustrated in Fig. 11. The column lengths here is the length of the stainless steel lipped channels, excluding the thickness of the end plates at both ends of the specimen.

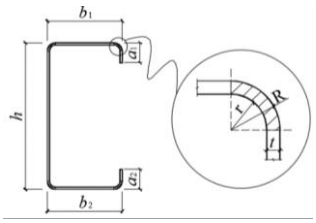

Fig. 11 Symbol definitions

3.3. Imperfection measurements

To improve the measurement accuracy, A 3-D laser scanner was used to measure the imperfection shapes and magnitudes of the columns prior to testing, as shown in Fig. 12 (a). The laser has an accuracy of 0.0001mm. The measurement process is as follows: firstly, mark points were attached to the test specimen, and then the 3-D laser scanner was used to scan the test column as a whole to obtain the data points, as shown in Fig. 12 (b).

Table 2
Measured dimensions (in mm)

Specimen code	Section code	h / mm	b_1 / mm	b_2 / mm	a_1 / mm	a_2 / mm	t / mm	Length / mm	r / mm
PP-1	C60×35×10×1.8	60.4	35.4	35.2	10.1	10.6	1.9	450.0	3.0
PP-2	C60×40×12×1.8	60.7	40.6	40.8	12.2	12.7	1.9	480.0	3.0
PP-3	C60×40×10×1.5	60.2	40.0	40.4	10.2	9.9	1.4	600.0	3.0
PP-4	C65×45×12×1.8	65.8	45.7	46.0	12.1	12.6	1.9	560.0	3.0
PP-5	C65×60×12×1.5	65.3	60.6	60.8	12.3	12.0	1.4	760.0	3.0
PP-6	C70×55×15×1.8	71.0	54.9	55.0	15.3	15.2	1.9	680.0	3.0
PP-7	C70×55×10×1.5	70.4	55.2	55.2	10.4	9.9	1.4	780.0	3.0
PP-8	C75×60×14×1.8	76.0	60.4	60.5	14.1	14.8	1.9	790.0	3.0
PP-9	C75×60×12×1.8	76.0	60.5	60.4	12.4	12.5	1.9	840.0	3.0
PP-10	C75×50×12×1.8	76.2	51.0	50.2	12.2	12.6	1.9	710.0	3.0
PP-11	C80×55×12×1.8	79.1	56.2	55.9	12.1	12.1	1.9	820.0	3.0
PP-12	C80×70×14×1.5	80.0	70.1	70.5	14.0	14.1	1.4	1000.0	3.0
PP-13	C80×65×12×1.5	80.2	65.1	65.1	12.1	12.2	1.4	1020.0	3.0
PP-14	C85×60×12×1.8	85.7	61.1	60.4	12.4	12.6	1.9	950.0	3.0
PP-15	C85×70×12×1.8	86.0	70.2	70.6	12.6	12.5	1.9	1050.0	3.0
PP-16	C85×70×15×1.8	85.0	70.8	70.1	15.6	15.8	1.9	1100.0	3.0
PP-17	C85×65×12×1.8	85.3	65.1	65.0	12.1	12.0	1.9	1080.0	3.0
PP-18-1	C88×60×12×1.8	88.2	60.7	60.4	12.4	12.7	1.9	960.0	3.0
PP-18-2	C88×60×12×1.8	88.5	60.9	60.3	12.4	13.0	1.9	960.0	3.0
PP-19-1	C96×68×12×1.8	96.6	68.5	69.0	12.3	11.9	1.9	1160.0	3.0
PP-19-2	C96×68×12×1.8	96.5	69.6	67.9	12.6	12.5	1.9	1160.0	3.0

Note: h is section height; b_1 and b_2 are upper and lower flange widths, separately; a_1 and a_2 are upper and lower lips widths, separately; t is thickness; l is column length; r is

Fig. 13 shows the imperfection distribution form of the PP-1 column. The imperfection distribution is not asymmetric and has a random nature. The imperfections were extracted along the lines in Fig. 14. Fig. 15 shows the measured imperfections of PP-1. Table 3 lists the maximum magnitude of

distortional, local and overall imperfections for the specimens. The overall initial imperfection amplitudes of the stainless steel columns are small, all less than one-thousandth of the column length, which can meet the requirements in the GB 50205-2001 [38]. The maximum imperfections amplitude of distortional and local buckling are 0.42mm and 0.40mm, respectively.

(a) 3-D laser scanner

(b) Measuring procedure

Fig. 12 Imperfection measurement

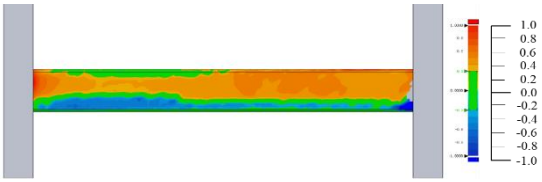

Fig. 13 Imperfection profile of PP-1

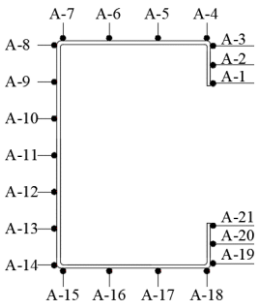

Fig. 14 Locations of the imperfection lines

Table 3
Maximum measured values of distortional, local and global buckling imperfections (in mm)

Specimen	Location	Local	Distortional	Global	Specimen	Location	Local	Distortional	Global
PP-1	Web	0.40	0.21	0.19	PP-11	Web	0.14	0.31	0.58
	Flange-up	0.32				Flange-up	0.26		
	Flange-down	0.29				Flange-down	0.11		
PP-2	Web	0.37	0.36	0.32	PP-12	Web	0.17	0.42	0.33
	Flange-up	0.13				Flange-up	0.11		
	Flange-down	0.36				Flange-down	0.24		
PP-3	Web	0.33	0.34	0.59	PP-13	Web	0.19	0.18	0.18
	Flange-up	0.19				Flange-up	0.25		
	Flange-down	0.19				Flange-down	0.29		
PP-4	Web	0.29	0.29	0.46	PP-14	Web	0.33	0.19	0.56
	Flange-up	0.29				Flange-up	0.40		
	Flange-down	0.21				Flange-down	0.29		
PP-5	Web	0.38	0.32	0.53	PP-15	Web	0.31	0.24	0.34
	Flange-up	0.33				Flange-up	0.17		
	Flange-down	0.39				Flange-down	0.31		
PP-6	Web	0.15	0.41	0.57	PP-16	Web	0.12	0.35	0.13
	Flange-up	0.29				Flange-up	0.18		
	Flange-down	0.31				Flange-down	0.19		
PP-7	Web	0.21	0.35	0.34	PP-17	Web	0.30	0.26	0.16
	Flange-up	0.37				Flange-up	0.23		
	Flange-down	0.32				Flange-down	0.28		
PP-8	Web	0.12	0.23	0.49	PP-18-1	Web	0.25	0.21	0.58
	Flange-up	0.16				Flange-up	0.33		
	Flange-down	0.15				Flange-down	0.34		
PP-9	Web	0.38	0.33	0.49	PP-18-2	Web	0.28	0.14	0.60
	Flange-up	0.24				Flange-up	0.23		
	Flange-down	0.35				Flange-down	0.21		
PP-10	Web	0.20	0.32	0.60	PP-19-1	Web	0.38	0.24	0.34
	Flange-up	0.38				Flange-up	0.26		
	Flange-down	0.16				Flange-down	0.34		

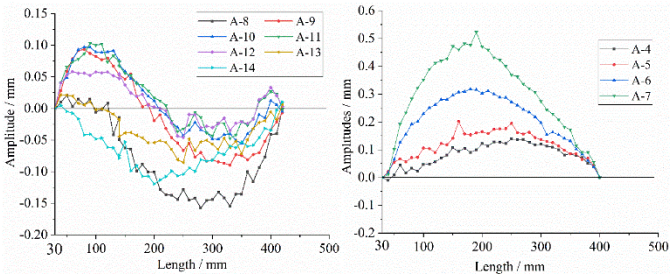

(a) A-8 ~ A-14 (b) A-4 ~ A-7

Fig. 15 Typical imperfection profile

4. Test results

4.1. Load-deformation curves

All experimental columns were expected to fail by distortional-overall interaction buckling. From the test observations, this hypothesis holds. Fig. 16 shows load–axial displacement relationships of the channels. The trends of the load-axial displacement relationships are basically the same. When the load is loaded, the axial displacement increases linearly with the increase of the load. As the load continues to increase, the stiffness of the specimen begins to decrease, and the load and displacement show a nonlinear relationship until the stiffness decreases to zero. The nonlinear part of the curve is relatively short, and the load soon reaches the peak load.

For PP-1 and PP-2, after the loads reach the peak loads, the load–axial displacements decrease slowly and no sudden damage occurs in the specimens. The reason why the specimens did not suffer sudden damage may be that the specimen lengths are relatively short and the boundary constraint plays a certain strengthening role. For other specimens, when the loads reach the peak loads, the load–axial displacement curves suddenly drop sharply, and the axial displacements suddenly increase. All specimens basically have no post-buckling strength.

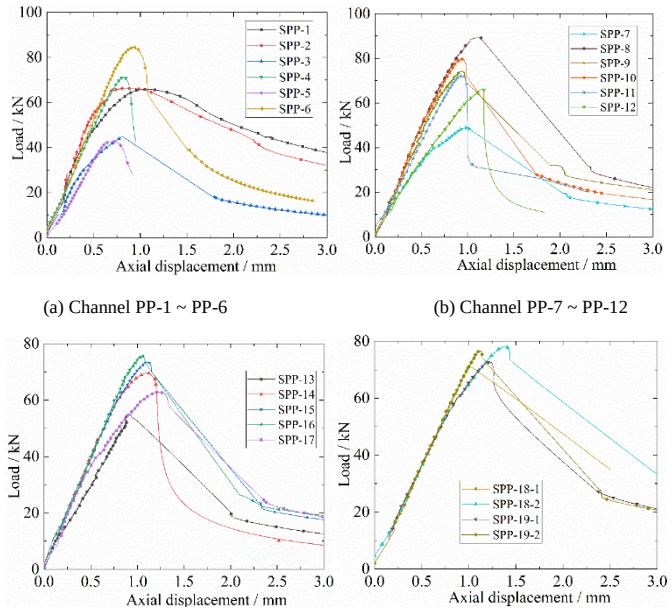

(a) Channel PP-1 ~ PP-6 (b) Channel PP-7 ~ PP-12

(c) Channel PP-1 ~ PP-6 (d) Channel PP-7 ~ PP-12

Fig. 16 Load vs. axial displacement curves

4.2. Load-rotation curves

During the experiment, the stainless steel columns were rotated around the weak axis of the section. According to the axial displacement values of the measuring points obtained by the axial LVDTs at end plates, the rotation angles can be calculated. Fig. 17 plots the load vs. the rotation of specimens PP-3, PP-6, PP-16, and PP-17. The diagrams in Fig. 17 show that the curves of both rotations of upper and lower supports are consistent, indicating that the upper and lower end plates have the same rotation angle, and the specimens were not twisted. This is consistent with the observed experimental phenomena.

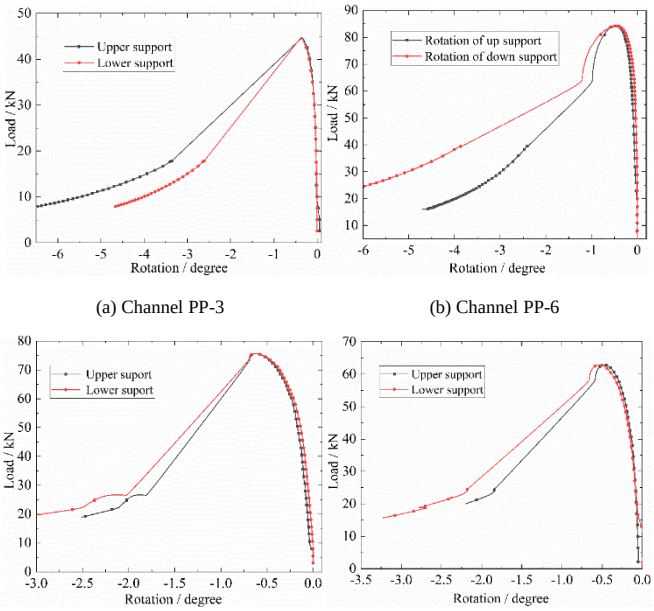

(a) Channel PP-3 (b) Channel PP-6

(c) Channel PP-16 (d) Channel PP-17

Fig. 17 Load vs. rotation curves

4.3. Load-lateral displacement relationships

The load-lateral displacement relationships of the PP-2, PP-6, PP-10, and PP-16 are shown in 18, indicating that the columns were not twisted, which is consistent with the conclusion identified in Fig. 17. Fig. 18 also shows that the lateral displacement of both LVDT 2 and 4 are earlier and larger than the lateral displacement of both LVDT 1 and 5, which indicates that the global buckling is earlier than distortional buckling.

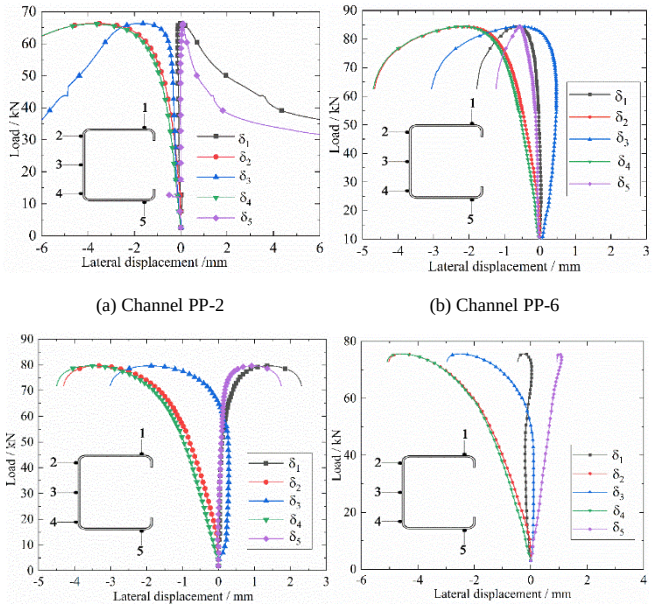

(a) Channel PP-2 (b) Channel PP-6

(c) Channel PP-10 (d) Channel PP-16

Fig. 18 Load vs. lateral displacement curves

4.4. Failure modes

All 21 columns were seen to show global buckling first, followed by eventual failure by distortional-global interaction buckling. No local buckling was visually seen in the designed channels. The peak strengths and buckling modes obtained from the test are detailed in Table 4. P_u is the ultimate capacity; D and G mean distortional and overall buckling, respectively; D+G means distortional-overall interactive buckling.

Observing the distortional buckling during the test is difficult, and the collected data can not reflect it in time. Moreover, distortional buckling has small post-buckling strength, and the specimen will reach the buckling damage soon after distortional buckling occurs. Therefore, to better observe the

distortional buckling, a ruler was used to measure the distance between the two lips, as shown in Fig. 19. If the distance between the two lips changes, the specimen can be judged to occur distortional buckling.

Fig. 14 Locations of the imperfection lines

Table 4
Measured ultimate strengths and failure modes

Specimen code	Section code	P_u (kN) / kN	Failure mode mode	Specimen code	Section code	P_u (kN) / kN	Failure mode mode
PP-1	C60×35×10×1.8	65.86	D+G	PP-12	C80×70×14×1.5	66.23	D+G
PP-2	C60×40×12×1.8	66.34	D+G	PP-13	C80×65×12×1.5	54.61	D+G
PP-3	C60×40×10×1.5	44.70	D+G	PP-14	C85×60×12×1.8	69.61	D+G
PP-4	C65×45×12×1.8	72.68	D+G	PP-15	C85×70×12×1.8	73.47	D+G
PP-5	C65×60×12×1.5	42.65	D+G	PP-16	C85×70×15×1.8	75.54	D+G
PP-6	C70×55×15×1.8	84.48	D+G	PP-17	C85×65×12×1.8	62.84	D+G
PP-7	C70×55×10×1.5	49.00	D+G	PP-18-1	C88×60×12×1.8	71.24	D+G
PP-8	C75×60×14×1.8	89.24	D+G	PP-18-2	C88×60×12×1.8	78.19	D+G
PP-9	C75×60×12×1.8	74.22	D+G	PP-19-1	C96×68×12×1.8	72.65	D+G
PP-10	C75×50×12×1.8	79.65	D+G	PP-19-2	C96×68×12×1.8	75.61	D+G
PP-11	C80×55×12×1.8	71.95	D+G				

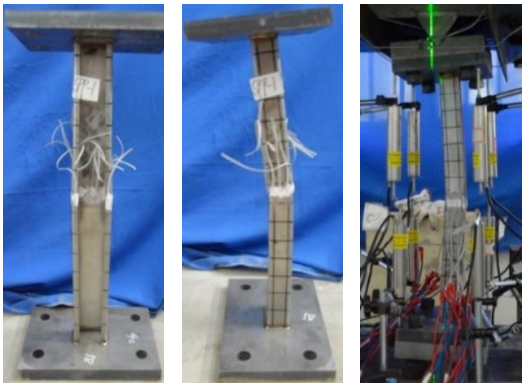

Fig. 20 Failure mode of PP-1

The failure modes of the above three types of specimens have the following common points: (1) after the test is loaded, no significant deformation was observed in all specimens in the early stage; (2) the overall buckling occurs before the distortional buckling; and (3) all the failure modes of the specimens show a certain degree of brittle failure, that is, when the ultimate strength is reached, the specimens suddenly fail and the bearing capacity drops sharply.

Fig. 21 The second category of failure mode

The member failure modes can be divided into three categories. In the first category, the specimen is bent toward the opening direction of the section as a whole, and the specimen with such failure is PP-1, as shown in Fig. 20. PP-1 is mainly dominated by global buckling.

In the second category, the specimens are bent toward the closed direction of the cross-section as a whole. The distortional buckling is outwardly convex. The specimens with this type are PP-3, PP-5, PP-6, PP- 7, PP-8, PP-9, PP-11, PP-13, PP-14, PP-18-1, PP-19-1 and PP-19-2, as shown in Fig. 21.

In the third category, the specimen is bent as a whole towards the closed direction of the section, and the distortional buckling is inwardly concave. The specimens with this type are PP-2, PP-4, PP-10, PP-12, PP-15, PP-16, PP-17 and PP-18-2, as shown in Fig. 22.

Fig. 22 The third type of failure mode

5. Comparison with predictions for design strength

No DSM for stainless steel lipped channels failed by distortional-overall interaction buckling in current specifications. However, the DSM for distortional buckling has been described in the AS/NZS [39] for carbon steel, AISI [40] for stainless steel, as well as the formulation established by Becque and Rasmussen [11] for stainless steel. To calculate the design strength of the lipped channel column failed by distortional-overall interaction buckling, the DSM for distortional buckling uses the member load (P_{ne}) instead of the yield load (P_y) for the definition of the distortional buckling slenderness (λ_d).

The test results are compared with the AS/NZS [39], AISI [40], as well as formulation proposed by Becque and Rasmussen's predictions [11], as shown in Fig. 23. DSM (AISI), DSM (AS/NZS) and DSM (Becque) in the figure indicate the results of bearing capacity calculations according to AISI, AS/NZS and Becque and Rasmussen calculation methods [11], respectively.

Most test data points are distributed under the DSM (AISI) curve and above the DSM (Becque) curve. The DSM (AS/NZS) curve does not have the same changing trend as the test results. DSM in AISI and AS/NZS for calculating the strength of the channels failing by distortional-overall interaction buckling was seen to be unconservative. DSM (Becque) curve is much closer to the test points than DSM in AISI and AS/NZS.

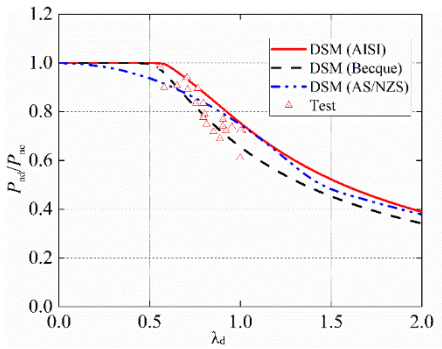

Fig. 21 The second type of failure mode

6. Conclusions

Axial compression tests on 21 columns were conducted to investigate the buckling damage characteristics of stainless steel columns. The focus of this experimental program is to study the distortional-overall interaction buckling. A 3-D laser scanner was used to measure the geometric imperfections. Material tensile tests were conducted to investigate the mechanical properties of stainless steel. Based on an analysis of the test results, the following general conclusions are made.

(1) All the test stainless steel lipped channel columns were successful in achieving interaction of distortional and global buckling about the minor axis.

(2) The member failure modes can be divided into three categories: 1) In the first category, the column is bent toward the opening direction of the section as a whole; 2) In the second category, the column is bent towards the closed direction of the cross section as a whole, and the distortional buckling is outwardly convex; 3) The third failure mode, the specimen is bent as a whole towards the closed direction of the section, and the distortional buckling is inwardly concave.

(3) The trends of the load-axial displacement relationships are the same. When the load is loaded, the axial displacements increase linearly with the load increases. As the load increases, the specimens' stiffness begin to decreases, and the load and displacement shows a nonlinear relationship until the stiffness decreases to zero. The nonlinear part of the curve are relatively short, and the load soon reaches the limit point.

(4) Both upper and lower support rotations are consistent, indicating that the stainless steel lipped channel cross sections were not twisted.

(5) Readings of both LVDT 2 and 4 are consistent, which indicates that the stainless steel lipped channel cross sections were not twisted. This is consistent with the conclusion identified in the load vs. rotation curves. The lateral displacements of both LVDT 2 and 4 are earlier and larger than the lateral displacements of both LVDT 1 and 5, which indicates that global buckling appears earlier than distortional buckling.

(6) DSM in AISI and AS/NZS for calculating the strength of stainless steel channels failing in distortional-overall interaction buckling are unconservative. The formulation proposed by Becque and Rasmussen is much closer to the test point than DSM in AISI and AS/NZS.

Acknowledgment

The authors would like to thank the financial support of the National Research Project Cultivation Fund of Southeast University Chengxian College (51878146) and National Natural Science Foundation of China (No. 52278153).

References

[1] Baddoo NR. Stainless steel in construction: A review of research, applications, challenges and opportunities. J. Constr. Steel Res. 2008; 64(11): 1199–1206.
[2] Gardner L. Stability and design of stainless steel structures – Review and outlook. Thin-Walled Struct. 2019; 141: 208–216.
[3] Sun Y., Su A., Jiang K., Liang Y. and Zhao O. Testing, numerical modelling and design of stainless steel welded I-sections under minor-axis combined loading. Engineering Structures, 2021, 243, 112513.
[4] Arrayago I, Real E, Gardner L. Description of stress–strain curves for stainless steel alloys [J]. Materials & Design, 2015(87): 540-552.
[5] Rasmussen K J R. Full-range stress–strain curves for stainless steel alloys [J]. Journal of Constructional Steel Research, 2003, 59(1): 47-61.
[6] Gardner L, Nethercot D A. Experiments on stainless steel hollow sections—Part 1: material and cross-sectional behaviour [J]. Journal of Constructional Steel Research, 2004, 60(9): 1291-1318.
[7] Tao Z, Rasmussen K J R. Stress-strain model for ferritic stainless steels [J]. Journal of Materials in Civil Engineering, 2016, 28(2): 1-5.
[8] Becque J, Rasmussen K J R. Experimental investigation of local-overall interaction buckling of stainless steel lipped channel columns [J]. Journal of Constructional Steel Research, 2009 (65): 1677-1684.
[9] Lecce M, Rasmussen K J R. Distortional buckling of cold-formed stainless steel sections: experimental investigation [J]. Journal of Structural Engineering, 2006, 132(4): 497-504.
[10] Kuwamura H. Local buckling of thin-walled stainless steel members [J]. Steel Structures, 2003(3): 191-201.
[11] Becque J, Lecce M, Rasmussen K J R. The direct strength method for stainless steel compression members [J]. Journal of Constructional Steel Research, 2008, 64(11): 1231-1238.
[12] Chen M , Fan S , Tao Y , et al. Design of the distortional buckling capacity of stainless steel lipped C-section columns[J]. Journal of Constructional Steel Research, 2018, 147(8.):116-131.
[13] Dobri J , Rossi B . Column Curves for Stainless Steel Lipped–Channel Sections[J]. Journal of Structural Engineering, 2020, 146(10):04020221.
[14] Fan S , Fang L , Zheng B , et al. Experimental study on bearing capacity of stainless steel lipped C section stub columns[J]. Thin-Walled Structures, 2014, 83(oct.):70-84.
[15] Barbara Rossi1; Jean-Pierre Jaspart; Kim J. R. Rasmussen. Combined Distortional and Overall Flexural-Torsional Buckling of Cold-Formed Stainless Steel Sections: Experimental Investigations[J]. Journal of Structural Engineering, 2010, 136(4): 354-360.
[16] Barbara Rossi1; Jean-Pierre Jaspart; Kim J. R. Rasmussen. Combined Distortional and Overall Flexural-Torsional Buckling of Cold-Formed Stainless Steel Sections: Design [J]. Journal of Structural Engineering, 2010, 136(4): 361-369.
[17] Chen M , Fan S , Li C , et al. Direct Strength Method for Stainless Steel Lipped Channel Columns Undergoing Local Buckling[J]. International Journal of Steel Structures, 2020:1-9.
[18] Lecce M, Rasmussen K J R. Distortional buckling of cold-formed stainless steel sections: Finite-element modeling and design [J]. Journal of Structural Engineering, 2006, 132(4): 505-514.
[19] Becque J, Rasmussen K J R. A numerical investigation of local–overall interaction buckling of stainless steel lipped channel columns [J]. Journal of Constructional Steel Research, 2009, 65(8): 1685-1693.
[20] Li S, Zhang L, Liang Y, and Zhao O. Experimental and numerical investigations of hot-rolled stainless steel channel section columns susceptible to flexural buckling [J]. Thin-Walled Struct. 164 (2021) 107791.
[21] S. Li, L. Zhang, O. Zhao, Global buckling and design of hot-rolled stainless steel channel section beam–columns [J]. Thin-Walled Struct. 170 (2022) 108433.
[22] S. Li, L. Zhang, O. Zhao, Testing, modelling and design of hot-rolled stainless steel channel sections under combined compression and minor-axis bending moment [J]. Thin-Walled Struct. 172 (2022) 108836.
[23 Liang Y, Zhao O, Long Y, et al. Experimental and numerical studies of laser-welded stainless steel channel sections under combined compression and major axis bending moment [J]. Thin-Walled Structures,2020, 157: 107035.
[24] Gardner L, Bu Y, Theofanous M. Laser-welded stainless steel I-sections: Residual stress measurements and column buckling tests - ScienceDirect[J]. Engineering Structures, 2016, 127(Nov.15):536-548.
[25] Yang L, Zhao M, Chan T M, et al. Flexural buckling of welded austenitic and duplex stainless steel I-section columns [J]. Journal of Constructional Steel Research, 2016, 122: 339-353.
[26] Becque J, Rasmussen K J R. Experimental investigation of the interaction of local and overall buckling of stainless steel I-columns [J]. Journal of Constructional Steel Research, 2009, 135(11): 1340-1348.
[27] Khate K, Patton M L, Marthong C. Structural behaviour of stainless steel stub column under axial compression: a FE study [J]. International Journal of Steel Structures, 2018, 18(5): 1723-40.
[28] Bredenkamp P J, Van Den Berg G J. The strength of stainless steel built-up I-section columns [J]. Journal of Constructional Steel Research, 1995 (34): 131-144.
[29] Anwar-Us-Saadat M, The continuous strength method for lateral-torsional buckling of stainless steel I-beams Ashraf M. [J]. Thin-Walled Structures, 2018(130): 148-60.
[30] Arrayago I , Real E . Experimental Study on Ferritic Stainless Steel RHS and SHS Cross-sectional Resistance Under Combined Loading[J]. Structures, 2015, 4:69-79.
[31] Liu Y, Young B. Buckling of stainless steel square hollow section compression members [J]. Journal of Constructional Steel Research, 2003, 59(2): 165-77.
[32] Theofanous M, Gardner L. Testing and numerical modelling of lean duplex stainless steel hollow section columns [J]. Engineering Structures, 2009, 31(12): 3047-58.
[33] Young B, Hartono W. Compression tests of stainless steel tubular members [J]. Journal of Structural Engineering, 2002, 128(6): 754-61.
[34] Young B, Liu Y. Experimental investigation of cold-formed stainless steel columns [J]. Journal of Structural Engineering, 2003, 129(2): 169-76.
[35] Rasmussen K J R, Hancock G J. Design of cold-formed stainless steel tubular members. I: columns [J]. Journal of Structural Engineering, 1993, 119(8): 2349-2367.
[36] National Standard of the People's Republic of China. Metallic materials-Tensile testing at ambient temperature [S]. Beijing: China Planning Press. 2010.
[37] B. Schafer. CUFSM software Version 5.0. Department of Civil Engineering, Johns Hopkins University, USA. (http://www.ce.jhu.edu/bschafer/cufsm/).
[38] National Standard of the People's Republic of China. Code for Acceptance of Construction Quality of Steel Structures (GB50205-2001) [S]. Beijing: China Planning Press. 2001.
[39] AS/NZS. Cold-formed stainless steel structures [S]. Australian/New Zealand-Standard, AS/NZS 4673:2001, Standards Australia, Sydney, Australia, 2001.
[40] North American Cold-Formed Steel Specification for the Design of Cold-Formed Steel structural Members [S]. American Iron and Steel Institute (AISI), Washington DC: 2016.

Advanced Steel Construction – Vol. 19 No. 2 (2023) 157–165
DOI: 10.18057/IJASC.2023.19.2.8

STUDY ON SEISMIC BEHAVIOR OF TRAPEZOIDAL CORRUGATED STEEL PLATE SHEAR WALL STRUCTURE WITH PEC COLUMN

Zhao-Sheng Huang [1, 2], Zhan-Zhong Yin [1, 3, *] and Bao-Yue Song [1]

[1] *School of Civil Engineering, Lanzhou University of Technology, Lanzhou 730050, China*
[2] *Gansu Institute of Architectural Design and Research, Lanzhou 730000, China*
[3] *Western Engineering Research Center of Disaster Mitigation in Civil Engineering of Ministry of Education, Lanzhou University of Technology, Lanzhou 730050, China*
** (Corresponding author: E-mail: yinzhanzhong@lut.cn)*

ABSTRACT

This paper has carried out experimental and numerical research on the hysteretic characteristics of a corrugated steel plate shear wall which has a partially encased composite (PEC) column (PEC-CSPSW). Two single layer PEC-CSPSW cycle tests were conducted. For the sake of simulating the experimental results, the writer made a numerical model and verified it. The capacity of energy dissipation and failure mode of the structure were studied. The results displayed the PEC-CSPSWs had excellent bearing capacity, ductility, and energy dissipation feature, and the bearing capacity declined gradully. The PEC composite column could heighten the frame column's stiffness, enhance the steel plate anchoring effect , and then give full play to its post-buckling strength. The effects of the thickness, wavelength, wave height of the corrugated steel plate, and the strength of concrete on the lateral force resistance were analyzed. The results indicated that, under the rational parameter design, the CSPSW proposed in this paper had a high bearing capacity and strong energy dissipation feature. Besides, it was an ideal lateral force resisting and energy dissipation member.

ARTICLE HISTORY

Received: 2 September 2022
Revised: 15 January 2023
Accepted: 20 January 2023

KEYWORDS

Partially encased composite column;
Corrugated steel plate shear wall;
Low-cycle reverse loading test;
Seismic performance;
Finite element method (FEM);
Parametric investigation

1. Introduction

As an effective component to resist lateral force, steel plate shear wall(SPSW) has been widely concerned and developed in the past few years. Non-stiffened steel plate walls resist horizontal loads through diagonal tension bands of steel plates, but thin SPSWs are prone to instability and thick SPSWs cost more. Corrugated steel plates, because of their special structure, have a very small compressive stiffness along the corrugation direction (wave propagation direction), and a much higher compressive stiffness perpendicular to the corrugation direction than steel plates with the same thickness. Meanwhile, thin corrugated steel plates have a larger buckling strength and out-of-plane stiffness. Therefore, introducing a corrugated steel plate into the SPSWs can make up for the shortcoming that the thin SPSWs is apt to lose stability and costs less than the thick SPSWs. A trapezoidal steel plate is used to form a double lateral force resisting structure with the surrounding frame to resist seismic force.When the corrugated ribs are arranged along the vertical direction, the higher cylinder stiffness along the corrugated ribs can effectively resist the vertical load caused by partial gravity. Therefore, the corrugated steel plate shear wall(CSPSW) can meet the current code requirements that the embedded plate will not buckle during construction and normal use. The research on resistance to the lateral force of the CSPSW structure has drew the interest of many scholars.

An experimental study on corrugated steel plates with 45 oblique folds was conducted by Berman and Bruneau [1]. The results of the test demonstrated that the folds in the steel plate could prominently enhance the stiffness and ductility of the members, and strengthen the structure energy dissipation capacity. Botross and Lan [2-3] both proposed the concept of a corrugated steel plate wall and carried out finite element method analysis and research, Their results showed that corrugated steel plate wall had great initial stiffness, brilliant hysteretic performance, and high energy dissipation capacity. Lu and Li [4] put forward a new type of buckling-restrained steel plate shear wall. They carried out loading tests which are monotonic and cyclic and focus on four groups of specimens with different aspect ratios, and completed the comparison test with ordinary SPSWs. Stajadinovic and Tipping [5] carried out hysteretic tests on 44 groups of light cold-formed corrugated steel plate walls, studied the seismic performance of light CSPSW, and proposed the recommended values of elementary parameters for the seismic design of light CSPSWs. LA Fülöp and I Hakola [6] proposed an analytical design method for light-gauge steel shear walls with thin sheet sheaths. Finite element simulations and experiments verified the effectiveness of this method. The comparison showed that it had good accuracy when evaluating strength, but the stiffness evaluation was not satisfactory.

Johnson et al. [7] studied the ultimate bearing capacity and shear elastic stiffness of corrugated steel web beams based on finite element analysis and experiment. Liu et al. [8]used the Galerkin method to derive the analytical formulas of the integral and interactive shear buckling stress of corrugated steel webs. A simplified formula of the shear buckling coefficient k_g of corrugated steel webs was given. Zhao et al. [9] showed through experiments that the corrugated steel plate shear wall structure had large initial stiffness, high bearing capacity, and minor out-of-plane deformation, which could enhance the pinching effect of the non-stiffened SPSW and made the hysteretic curve fuller. Dou et al. [10-11] studied the lateral bearing capacity and post-buckling performance of sinusoidal CSPSWs under unidirectional loads, and proposed a fitting formula to predict load-displacement curves.

Cao and Huang [12] discussed the hysteretic behavior of a double-layer single-span corrugated steel wall, and proposed its plate-frame interaction model under lateral load. In the above research, H-section steel columns were mostly used as the SPSWs's vertical edge members. However, under the additional influence of the steel plate tension field, the H-section steel columns were prone to premature local buckling, making the frame columns flexural and torsional unstable, and the effective anchorage of thin steel plate walls was lost, which was not conducive to the performance of SPSWs after buckling [13-15]. The partially encased composite (PEC) columns had a high bearing capacity, good ductility, fire resistance, seismic resistance, and convenient and economical manufacturing [16-20]. Therefore, some studies, introduced it into the non-reinforced SPSWs as a boundary element to provide reliable anchorage for the steel plate tension field expansion to solve the concave deformation and stability failure problems caused by the weak rigidity of the pure steel column [21-23]. Therefore, in this paper, the PEC column was applied in the CSPSWs by bolt connection, so that it became the edge member with a horizontal bearing capacity in the CSPSWs, provided strong anchoring force, and could bear high axial pressure, thus solving the concave deformation and stable damage of the pure steel column with weak rigidity and realizing the design philosophy of "strong frame and weak steel plate." The purpose was to explore the seismic performance of trapezoidal corrugated SPSWs with PEC columns. This paper made an experimental research on PEC-CSPSWs scale specimens. It analyzed the stiffness, energy dissipation performance, distribution and development of plastic deformation, and the structure failure mode. On the basis of verifying the finite element approach, the parameter research regarding to the height-thickness ratio of the steel plate, wavelength, and wave height of the corrugated plate, and the column concrete strength grade was carried out.

2. Experimental program

2.1. Specimen device and material characteristics

Two prefabricated PEC-CSPSWs specimens were used in this test, numbered PEC-CSPSW1 and PEC-CSPSW2 respectively. The PEC column

adopted double channel steel section, and the frame adopted H-shaped beam. The embedded trapezoidal corrugated plate was linked with the channel steel by friction type high-strength bolts, welded with the beam's lower flange, and the beam's web was connected with the column by bolts through the connecting plate welded on the flange of the column. In addition, φ 6 tensile steel bars were welded between channel steel flanges and concrete was poured to form specimens. At the test piece bottom, a 30mm thick steel plate was welded, which was connected to the reaction floor through the anchor rod. Through the material sample test, the steel material properties used in the sample were evaluated, as shown in Fig. 1. The sample design and specimen photos are shown in Fig. 2 and 3, respectively, and the geometric parameters of the corrugated plate can be detected from Fig. 4. The steel used in the test piece was Q235B, and the material test results are illustrated in Table 1. The concrete filled in the PEC column was C30, and the cubic compressive strength after 28 days was 31.5N/mm2. The Young's modulus of filled concrete was 3.2×104N/mm^2. Beam-column-infill plate connection adopted friction high-strength bolts with an ultimate strength of 1230MPa and a yield strength of 940MPa.

Fig. 1 Test of specimen material properties

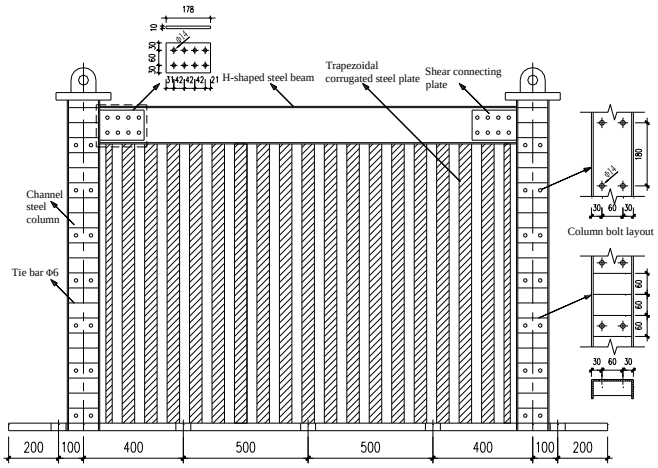

Fig. 2 Dimensions and details of specimens

Fig. 3 Pictures of PEC-CSPSW specimens

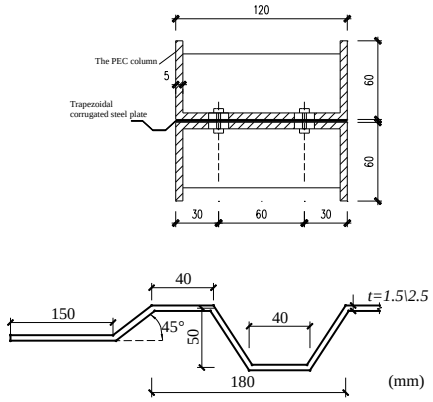

Fig. 4 Geometric parameters of vertical trapezoidal corrugated plate

Table 1
Material proprieties of steel

Item	f_y / MPa	f_u / MPa	E / MPa	δ / %
1	269.2	390.1	1.97	22.12
2	256.7	380.7	1.93	20.83
3	257.8	405.8	1.99	23.51
4	254.5	379.6	2.01	22.04
5	262.4	377.8	1.87	25.35
6	253.9	391.4	2.09	24.36
7	263.6	384.6	2.07	26.03
8	247.4	386.0	1.99	23.43
9	245.2	399.7	1.97	21.93
10	238.6	396.8	2.04	25.76
The average	254.9	389.2	1.99	23.53

f_y is yield stress; f_u is ultimate stress; E is the elastic modulus; δ is tensile elongation.

2.2. Loading protocol and instrument

The low-cycle repeated horizontal displacement loading method was adopted to test the mechanical performance of the specimen under earthquake action. Before the formal loading, pre-load was used to eliminate the pre-tightening force generated by the MTS loading end and loading beam end.

Constant amplitude cyclic loading with yield displacement Δ_y as multiple was adopted in the loading process. Each level was loaded for 3 times, first pushed and then pulled. When the sample is damaged or the load drops to 85% of the peak load, the test finished. Lateral supports with supports were arrayed on both sides of the intermediate part of the frame to prevent the specimen from buckling. [24].

The arrangement of measuring instruments is shown in Fig. 7. T-shaped resistance strain gauges were arranged on the main diagonal, and 1/3 diagonal of the embedded steel plate, the key parts of beams and columns, were also provided with a one-way resistance strain gage.A total of 104 strain collection points were laid out for each specimen, including 96 on steel and 8 on concrete. At the same time, a resistance displacement meter was arranged in the key parts of the plate to monitor the deformation of each position in the test.

2.3. Failure mode and damage procedure

The PEC-CSPSW1 specimen had no obvious phenomenon under the first two cyclic loads. When the load was pushed to 9mm(D=0.75%), the steel plate surface buckled slightly. At this time, there was no obvious phenomenon on the concrete surface, the deformation disappeared after unloading, and the plate was in the elastic stage. The buckling wave deformation became more obvious when the loading displacement was close to 15mm (D=1.25%). As the loading displacement increased, the buckling wavelength slowly increased, forming diagonal tensile bands from the upper left to the lower right, and the structure entered an elastic-plastic state. When the displacement was loaded to 21mm(D=1.75%), two oblique folds were formed in the center of the steel plate wall. Then, the bolt rod rubbed violently with the steel plate, producing a “squeaking” sound. When the loading displacement reached 33mm(D=2.75%), two large “X” shapes were formed by folding and crossing the front and back of the steel plates, and the steel plate at the center of the fold appeared convex corner, accompanied by the tearing of the steel plate. Most “X”-shaped tension bands had openings due to the tearing of steel plates at the center when loaded to 42mm(D=3.5%). Along with the reciprocating change of displacement, the degree of the opening increasingly grew, and the color of the steel around the opening became dark with burning marks. At this time, the yield area of steel plates increased slowly. The concrete surface in the PEC column was still intact when the load reached 45mm(D=3.75%), the yield range of the steel plate was not obviously increased, and the peak load in the load-displacement curve was not obviously decreased. The test stopped until the load reached 51mm(D=4.25%). Fig. 8 is the deformation diagram of the specimen.

Similar to PEC-CSPSW1, PEC-CSPSW2 was basically unchanged at the initial loading stage. When the displacement was loaded to 15mm (D=1.25%), the steel plate would buckle, and the deformation occured in the middle of the plate, which was about 50mm higher to the left than the buckling deformation position of specimen 1. After loading to 33mm(D=2.75%), the concrete surface of PEC column near the loading end has transverse cracks., and the area of steel plate folds increased. When loaded to 39mm(D=3.25%), the steel plate corner was torn, the steel plate yielded to a great extent, and the yield area increased slowly. As the load reached 42mm(D=3.5%),the steel plate tearing phenomenon became more obvious, the opening became larger, and the original cracks on the concrete surface became wider and longer. At this time, observing the load-displacement curve, the bearing capacity decreased little. With the load reaching 45 mm (D=3.75%), the corners of the “X”-shaped fold area basically showed openings, and the bearing capacity of the PEC column decreased greatly on account of different degrees of separation between flange and concrete, so the test was stopped. It is illustrated inFig. 9 the failure mode of specimen 2.

Under the horizontal load action, the two specimens achieved post-yield buckling, and both specimens were in the pure shear state before buckling, which fully developed plastic energy dissipation. After buckling, the tension band formed by buckling continued to uphold the load. Compared with the displacement requirements of the current code, it can be found that the edge frame of the structure kept elasticity under frequent earthquakes, and the steel plate consumed energy in buckling and shearing. Under rare earthquakes, the wallboard began to crack, but the structure had a certain loading capacity, and the loading capacity decreased slowly.

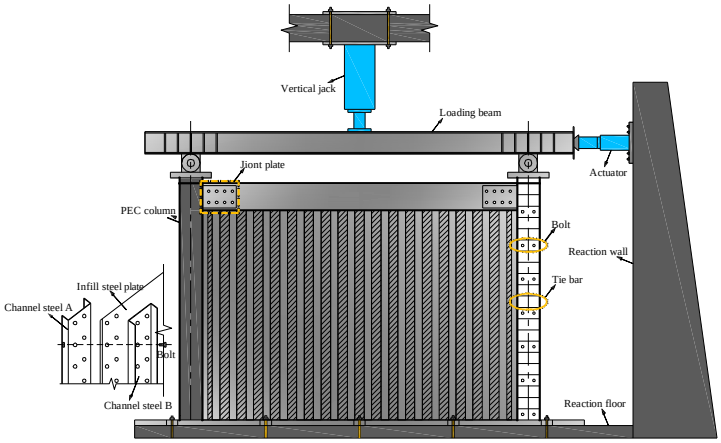

Fig. 5 Test setup

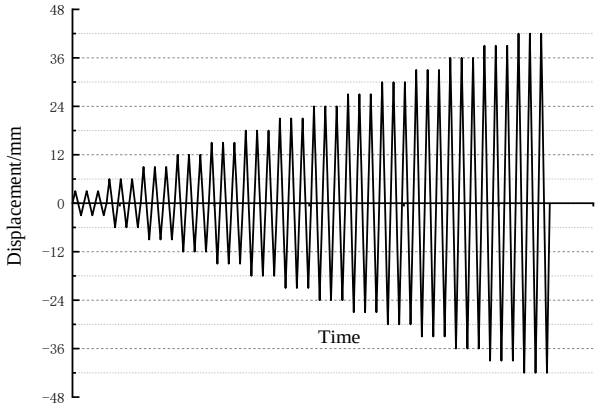

Fig. 6 Loading protocol

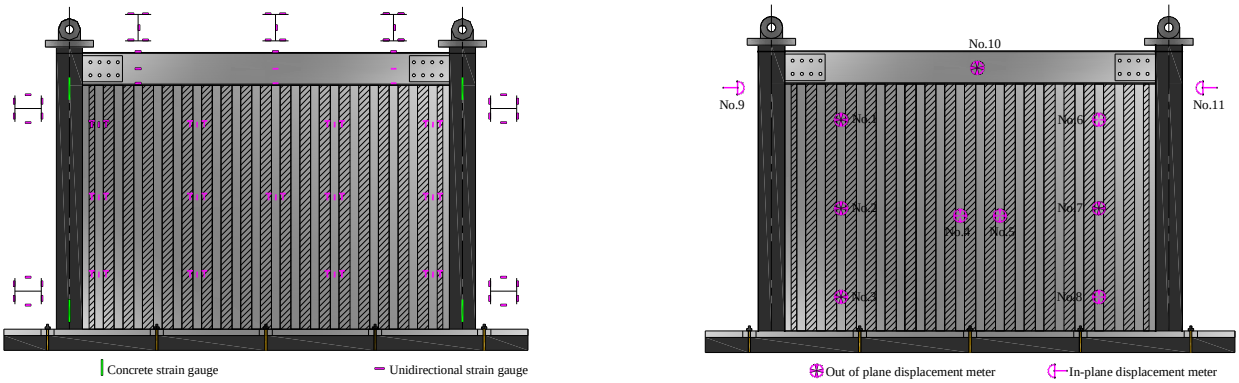

(a)Strain gauge layout

(b) Displacement gauge layout

Fig. 7 Layout of measuring instruments

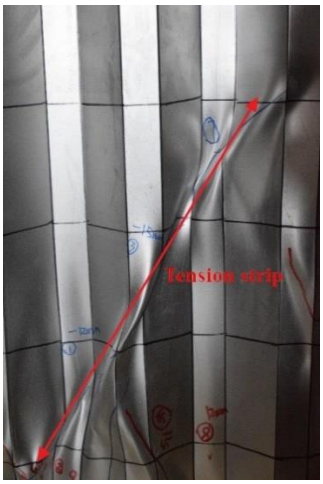

(a)Partial deformation when D=1.25%

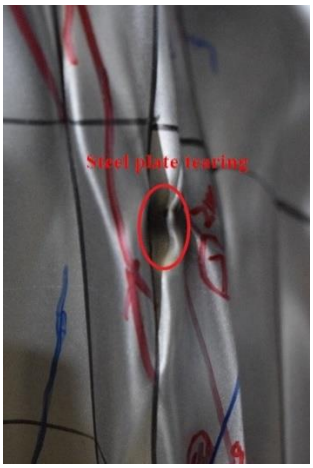

(b)Steel plate tear burn mark when D=3.5%

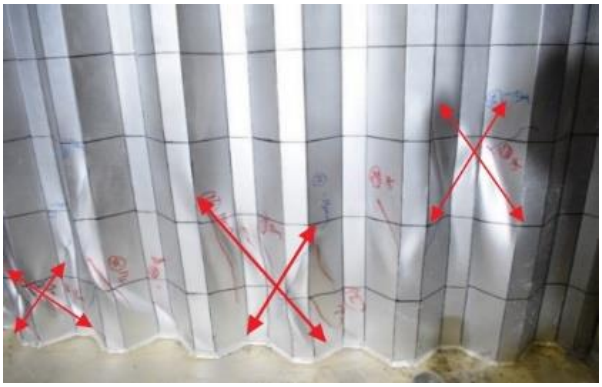

(c)Partial deformation when D=1.75%

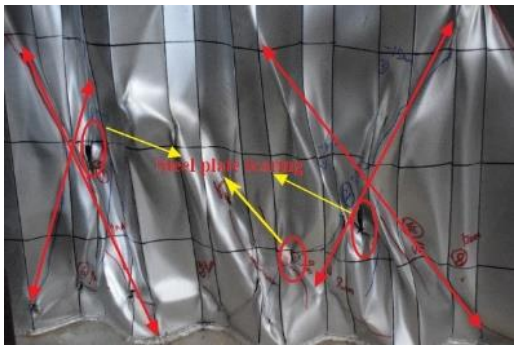

(d)The steel plate tears when D=3.5%

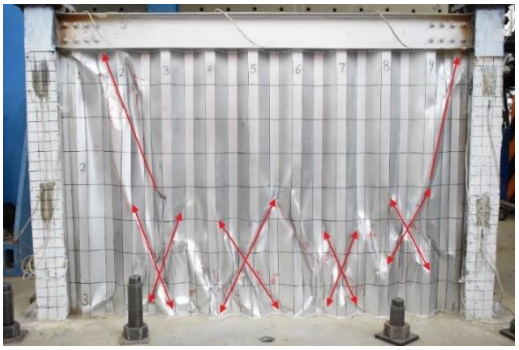

(e) Overall deformation when D=4.25%

Fig. 8 Failure mode of PEC-CSPSW1

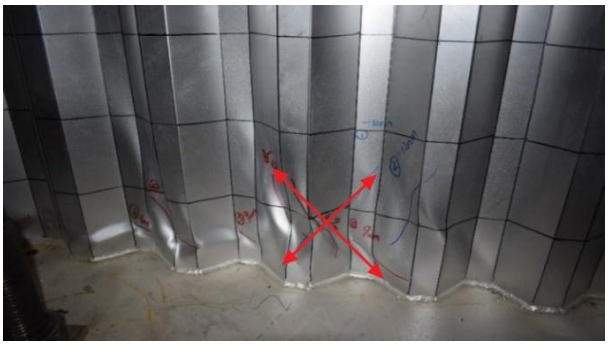

(a)Partial deformation when D=1.75%

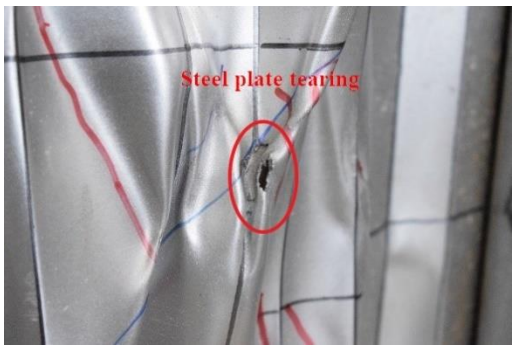

(b) The steel plate tears when D=3.25%

(c) The development of concrete cracks

Fig. 9 The failure mode of PEC-CSPSW2

2.4. Hysteretic behavior

The hysteretic curves of two specimens are diaplayed in Figure 10, both of which showed good working performance. The overall shape of the two specimens' hysteretic curves was cross-shaped, which was full and spindle-shaped at the initial loading stage. The shear resistance reached the maximum when the displacement was 10mm and 15mm, respectively, and then gradually began to decline, which is due to the stress state change from the overall shear resistance to the tension band shear resistance. As the displacement increased, the hysteretic loop area slowly increased, the shape gradually changed from spindle to bow, the

hysteretic curve reached a platform section, and the bearing capacity no longer decreased. As the plate began to tear, the pinch phenomenon became more and more obvious, and finally, it changed to a reverse S-shape. Specimens 1 had a smaller hysteretic area and lower yield capacity than specimens 2.

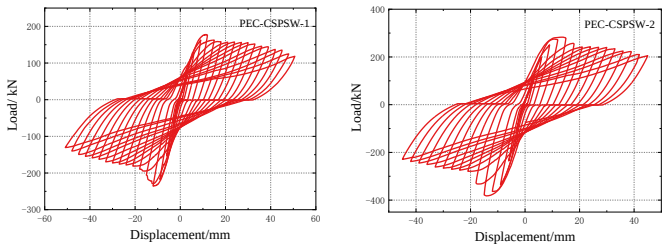

Fig. 10 Hysteretic curves of the specimen

2.5. Skeleton curves

The specimen's skeleton curve was symmetrical about the center of the coordinate origin. Furthermore, the value of the structure's initial stiffness was very large. The complete curve includes three stages: elasticity, strengthening, and plasticity. From the figure, we can find that on the elastic phase, the two specimens' skeleton curves rose linearly, and both of them had good initial stiffness. In the strengthening stage, it can be found that when reaching the yield load, the specimen's bearing capacity did not decrease immediately. This indicates that the specimens had preferable energy dissipation stability. When the specimen was on the plastic phase, the bearing capacity decreased, but the decreasing rate was relatively slow and still had a high bearing capacity.

Fig. 11 shows the comparison of skeleton curves. It shows that both specimens achieved post-buckling with relatively high initial bearing capacity. With the displacement increase, the skeleton curve showed a downward segment, but still had a fixed post-buckling bearing force. Among them, the performance of specimen 2 was more outstanding.

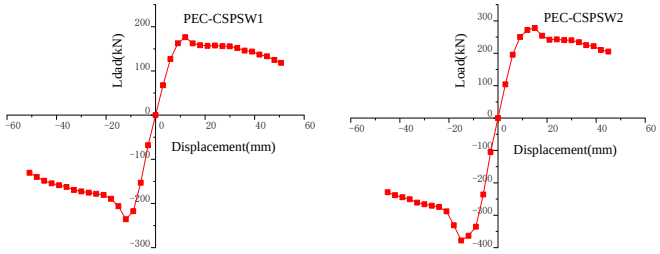

（a）PEC-CSPSW-1 （b）PEC-CSPSW-2

Fig. 11 Skeleton curves of the specimens

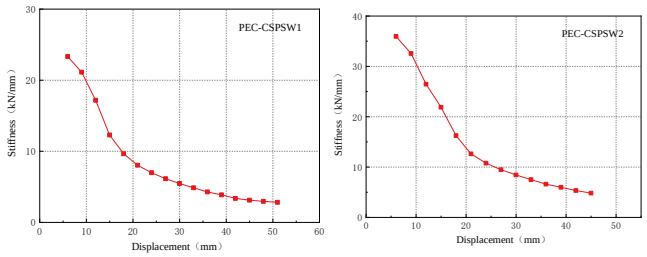

（a）PEC-CSPSW-1 （b）PEC-CSPSW-2

Fig. 12 Stiffness degradation curves of specimens

2.6. Stiffness degradation

Fig. 12 diaplays the specimens' stiffness degradation curve. It demonstrates that the stiffness degradation curves of PEC-CSPSW-1 and PEC- CSPSW-2 had the same general variation rule. As the displacement increased, the structure's global stiffness declined. The corrugated steel plates buckled with the loading displacement increase, the bearing capacity decreased greatly, and the stiffness degradation rate was high. On the middle and late phases of loading, the stiffness degradation rate slowed down, because, the surface of the corrugated steel plate has more tension bands, which could share the more lateral load, and the decline of bearing capacity was relatively stable.

2.7. Ductility and energy dissipation capacity

Table 2 lists the specimen's ductility coefficient. It demonstrates that the displacement ductility coefficient of PEC-CSPSW2 was higher than PEC-CSPSW1. The maximum peak load of PEC-CSPSW2 was 363.21kN when the displacement load was 15mm, which was 54.1% higher than that of PEC-CSPSW1. Results showed that the smaller the height-thickness ratio of the embedded trapezoidal corrugated steel plate, the greater the stiffness of the structure, meanwhile the bearing capacity of the structure is higher.

Table 2
Ductility of specimens

Item	$K_i(kN/mm)$	$P_y(kN)$	$P_m(kN)$	$P_u(kN)$	μ
PEC-CSPSW1	21.14	126.82	235.70	149.37	4.45
PEC-CSPSW2	32.57	195.44	363.21	228.97	5.56

K_i represents the initial stiffness; P_y represents yielding load; P_m represents peak load; P_u represents ultimate load; μ represents ductility coefficient.

The enveloping area of the hysteresis loop had the same energy dimension, which could reflect the energy consumption of the hysteresis loop. With larger area, more energy will be consumed. The energy consumption coefficient E was calculated as follows.

$$E = \frac{S_{ABC} + S_{CDA}}{S_{OBE} + S_{ODF}} \tag{1}$$

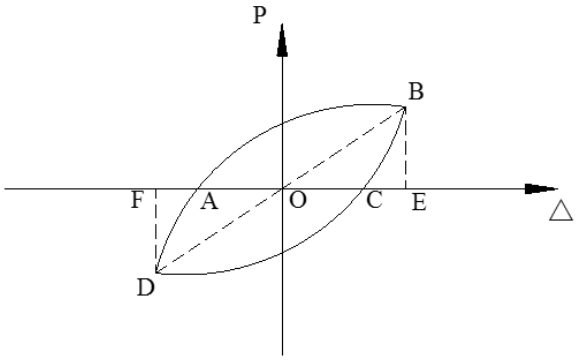

Fig. 13 The schematic diagram of the energy consumption coefficient

Table 3
The energy consumption coefficient

Item	PEC-CSPSW1	PEC-CSPSW2
E	2.25	2.76

Table 3 shows that, the two specimens' energy dissipation coefficient were greater than 2.0, and both of them had excellent energy dissipation ability. As the growth of the thickness of the corrugated steel plate, the overall stiffness of the structure accumulated, and the energy dissipation feature of the corrugated steel plate increased.

3. Finite element analysis of specimen

3.1. FEA model

FE software ABAQUS was adopted to simulate the model which adopted the same geometric size as the two specimens in the test. Columns, beams and wall plates were all made of linear reduced shell element (S4R) considering large deformation and small strain, and the core concrete was made of eight-node linear reduced hexahedral element (C3D8R).The contact relationship between concrete and channel steel was considered in the tangential and normal directions. Tangential friction was adopted, and the Coulomb friction coefficient of 0.3 was specified to reflect the bond and slip between channel steel and concrete. The normal direction adopted "hard contact". In addition, the out-of-plane freedom of the frame beam's flange was limited to simulate the out-of-plane constraint effect in the test. The model chart is displayed in Fig.14 and Fig.15.

The command "imperfections" was used in ABAQUS to include 3/1000b geometric defects extracted from buckling analysis in the model. To keep the

interface in contact, the initial defect values of the concrete and steel plate were the same. The elastic-linear hardening model and follow-up hardening rule were selected for steel, the hardening modulus , and Poisson's ratio in the elastic stage was 0.3. The constitutive relation of concrete was selected from the stress-strain expression of concrete proposed in reference [25], which considered the constraint effect of section steel. Table 4 shows the parameters of the concrete's plastic damage model.

Table 4
Plastic coefficients of concrete

$\alpha(°)$	e	σ_{b0}/σ_{c0}	K_c	γ
30°	0.1	1.16	2/3	0.0001

Therein, $\alpha(°)$ represents the dilation angle; e represents the eccentricity; σ_{b0} represents the initial equiaxial compressive yield stress; σ_{c0} represents the initial uniaxial compressive yield stress; K_c represents the second stress invariant ratio, and γ is the viscosity parameter.

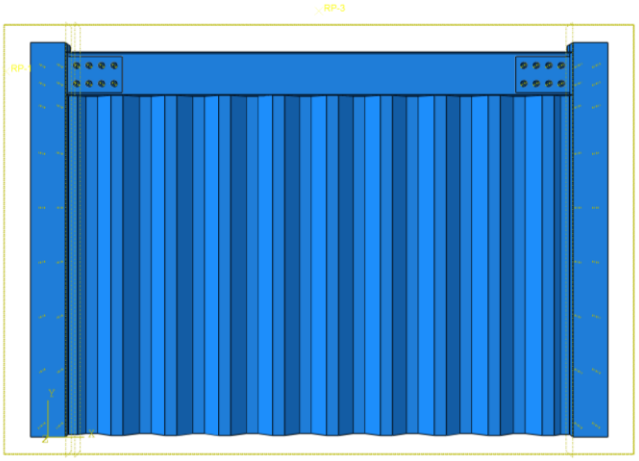

Fig. 14 The finite element model

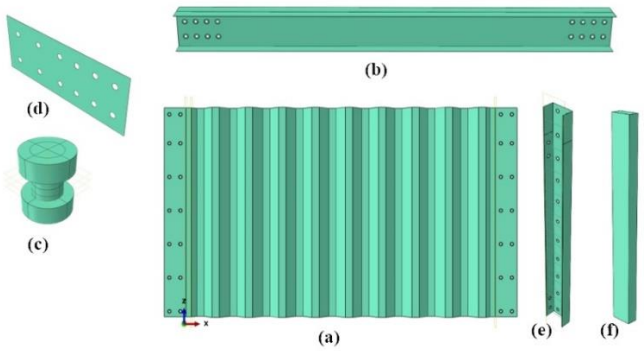

(a) corrugated plate;(b) beam; (c) bolt; (d) connection plate;
(e) steel column;(f) concrete;

Fig 15 The unit figure of the finite element model

3.2. FEA validation

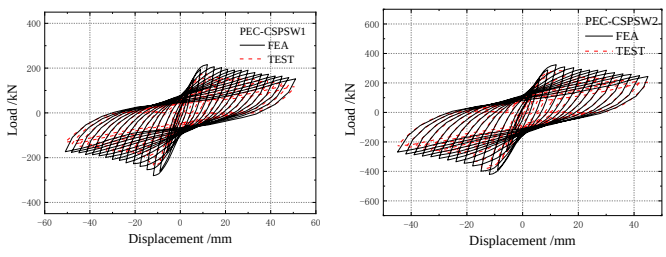

Fig. 16 Hysteretic curves of test and FEA results

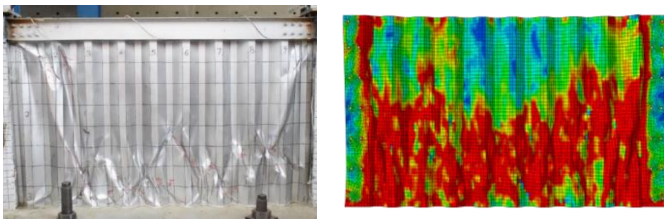

Fig. 17 Mises stress contrast nephogram of test and FEA results.

The study compares the experiment results of hysteretic curves and the FE model ,and it can be discovered that the specimen's initial stiffness was well predicted by the FEA method in Fig. 16. The two curves almost coincided when the displacement was small and also coincided well in the elastic-plastic stage. It was found that the specimen's stiffness, bearing capacity and hysteretic loop area calculated by the FEA method were slightly greater than the experimental results.This is because the influence of adverse conditions such as repeated bending and tearing of SPSWs and weld cracking was not considered in the finite element simulation. The hysteretic curve of the finite element model in the figure showed no obvious descending section after arriving at the peak load. In addition, the steel material constitutive model in the FEA model did not consider the material stiffness degradation and fracture caused by cyclic loading under the high stress state, and the hysteresis curve calculated by the finite element model was relatively full and the degree of "pinch" was relatively light. On the other hand, the residual stress accumulated during specimen processing and the inevitable existence of loading eccentricity in the loading process will reduce the test bearing capacity. But generally the finite element model well simulates the feature of SPSWs under cyclic loading, showing that the analysis method adopted in this paper was reliable.

Fig.17 demonstrates the Von Mises stress contrast nephogram for the experimental and FEA model at a lateral drift of 3.75%. It reveals that the yield distribution of plate in the test is primarily similar to the simulation results in the FEA, and the shear yield of steel plate is mostly concentrated in the lower region of steel plate and develops toward the ends of two columns. The yield area of the steel plate in test is minor than that of the finite element model, especially in the area near the edge column. This is because the edge frame has a better restraining effect on the corrugated steel plate in the FE simulation.

3.3. Parametric investigation

Based on the verified FEA method, to further research the impact of plate height-thickness ratio, wavelength, wave amplitude (Fig.18), and concrete strength grade on the lateral bearing capacity of PEC-CSPSWs, 26 finite element models were established in this paper. See Table 5 for the parameters of the models.

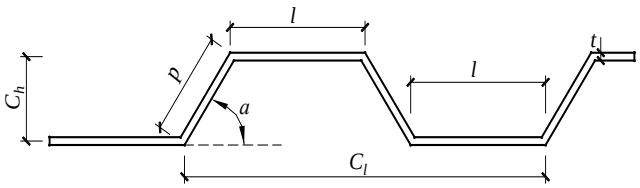

Fig. 18 Diagram of trapezoidal corrugated steel plate

Fig. 19 displays the skeleton curves of each group of specimens under cyclic loading. We can spot from the figure that the initial lateral stiffness of PEC-CSPSWs was roughly the same, and the skeleton curve showed an obvious S-shape, showing good lateral resistance. The structural bearing capacity increased slightly along with the growth of thickness and the corrugated steel plate wave amplitude. In addition, the initial stiffness of PEC-CSPSWs decreased gradually as the corrugated steel plate wavelength accumulated.

Fig. 20 displays the degradation curve of the secant stiffness of each specimen with loading displacement. Each model's stiffness degradation was obvious, and the change law was similar: the equivalent stiffness decreased gradually as the displacement increased, and the initial decline speed was faster. When the displacement was greater than 20mm, the decline speed slowed down and gradually became stable. After loading, the equivalent stiffness value of each specimen was the lowest, all about 5 kN/mm.

In Table 6, the energy dissipation coefficients of each model are listed. As the steel plate's thickness increased, the shape of the hysteresis loop became full, the energy dissipation coefficient increased, and the energy dissipation capacity

gradually increased. Models with different wavelengths and amplitudes had excellent energy dissipation performance, and their energy dissipation coefficients were similar, all around 4.0.

Fig. 21shows the Von-Mises stress distribution at the ultimate displacement of corrugated wallboard subjected to cyclic loading with different design parameters. Referring to Fig. 21(a)~(c), under cyclic loading, the value of the initial stiffness of the thin steel plate was smaller than that of the thick steel plate, the steel plate buckling occurred faster, and the distribution of "X" tensile bands was more. From Fig. 21(d)~(f), when the wavelength increased, the quantity of tensile bands decreased, and the stress on the steel plate surface increased. The reason for this is that with the growth of the steel plate wavelength, the number of ripples decreased, and the effective area for the steel plate to participate in the shear yield became smaller.This led to the steel plate early buckling and the bearing capacity decline. Fig. 21(g)~(i) shows that the number of tensile bands in the plate with a small wave amplitude was less, while the distribution of tensile bands in the plate with a large wave amplitude was more, basically covering the whole plate surface. This is because the out-of -plane stiffness of the steel plate which has small wave amplitude was small. Under reciprocating loading, a single "X" type tensile band was easier to form and the coverage area was increasingly large.

Table 5
Geometry parameters of PEC-CSPSW

Item	t/mm	λ	C_l /mm	C_h /mm	Column section/mm	C_g
P-CS1	1	1120	240	50	120×60×5	C30
P-CS2	1.5	747	240	50	120×60×5	C30
P-CS3	2	560	240	50	120×60×5	C30
P-CS4	2.5	448	240	50	120×60×5	C30
P-CS5	3	373	240	50	120×60×5	C30
P-CS6	3.5	320	240	50	120×60×5	C30
P-CS7	2	560	200	50	120×60×5	C30
P-CS8	2	560	220	50	120×60×5	C30
P-CS9	2	560	240	50	120×60×5	C30
P-CS10	2	560	260	50	120×60×5	C30
P-CS11	2	560	280	50	120×60×5	C30
P-CS12	2	560	300	50	120×60×5	C30
P-CS13	2	560	240	50	120×60×5	C30
P-CS14	2	560	240	60	120×60×5	C30
P-CS15	2	560	240	70	120×60×5	C30
P-CS16	2	560	240	80	120×60×5	C30
P-CS17	2	560	240	90	120×60×5	C30
P-CS18	2	560	240	100	120×60×5	C30
P-CS19	2	560	240	50	120×60×5	no-concrete
P-CS20	2	560	240	50	120×60×5	C25
P-CS21	2	560	240	50	120×60×5	C30
P-CS22	2	560	240	50	120×60×5	C40
P-CS23	2	560	240	50	120×60×5	C50
P-CS24	2	560	240	50	120×60×5	C60
P-CS25	2	560	240	50	120×60×5	C70
P-CS26	2	560	240	50	120×60×5	C80

Table 6
Energy consumption coefficient of models

Item	E	Item	E
P-CS1	3.54	P-CS14	3.99
P-CS2	3.20	P-CS15	4.07
P-CS3	3.96	P-CS16	4.02
P-CS4	4.10	P-CS17	4.03
P-CS5	4.12	P-CS18	3.85
P-CS6	4.93	P-CS19	3.84
P-CS7	4.07	P-CS20	3.99
P-CS8	3.96	P-CS21	3.90
P-CS9	3.96	P-CS22	3.77
P-CS10	3.89	P-CS23	3.73
P-CS11	3.85	P-CS24	3.63
P-CS12	3.57	P-CS25	3.64
P-CS13	3.96	P-CS26	3.65

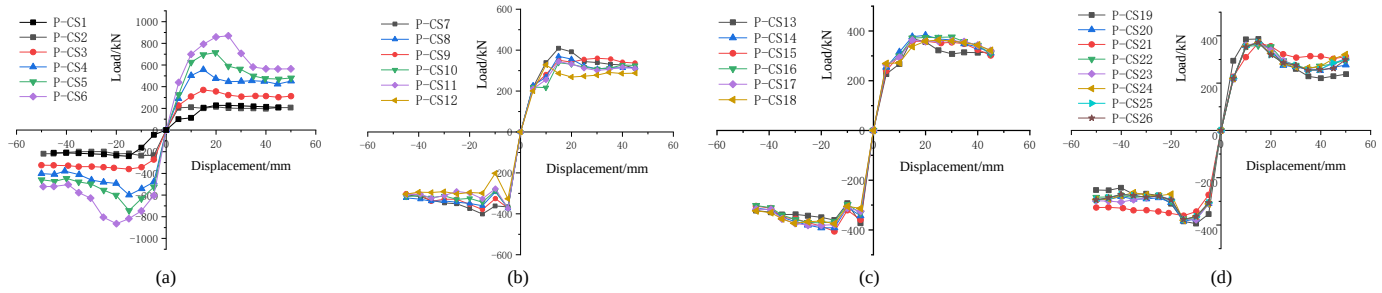

(a) (b) (c) (d)

Fig. 19 Skeleton curves of the model

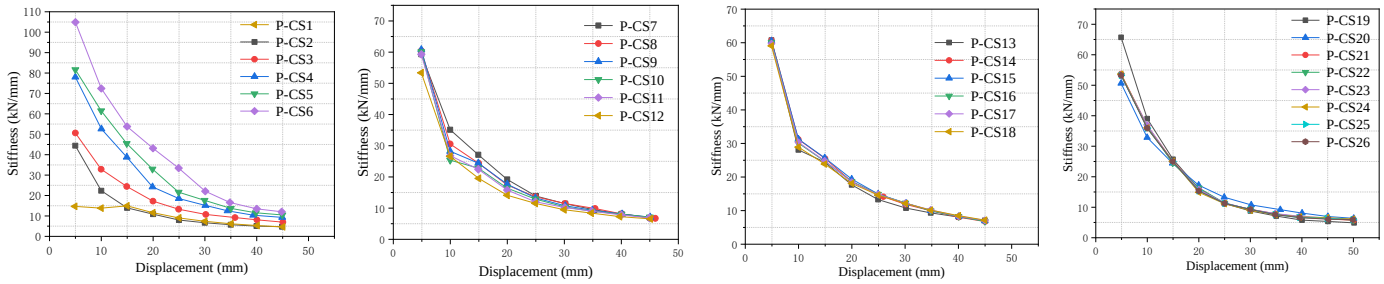

(a) (b) (c) (d)

Fig. 20 Stiffness degradation curves of models

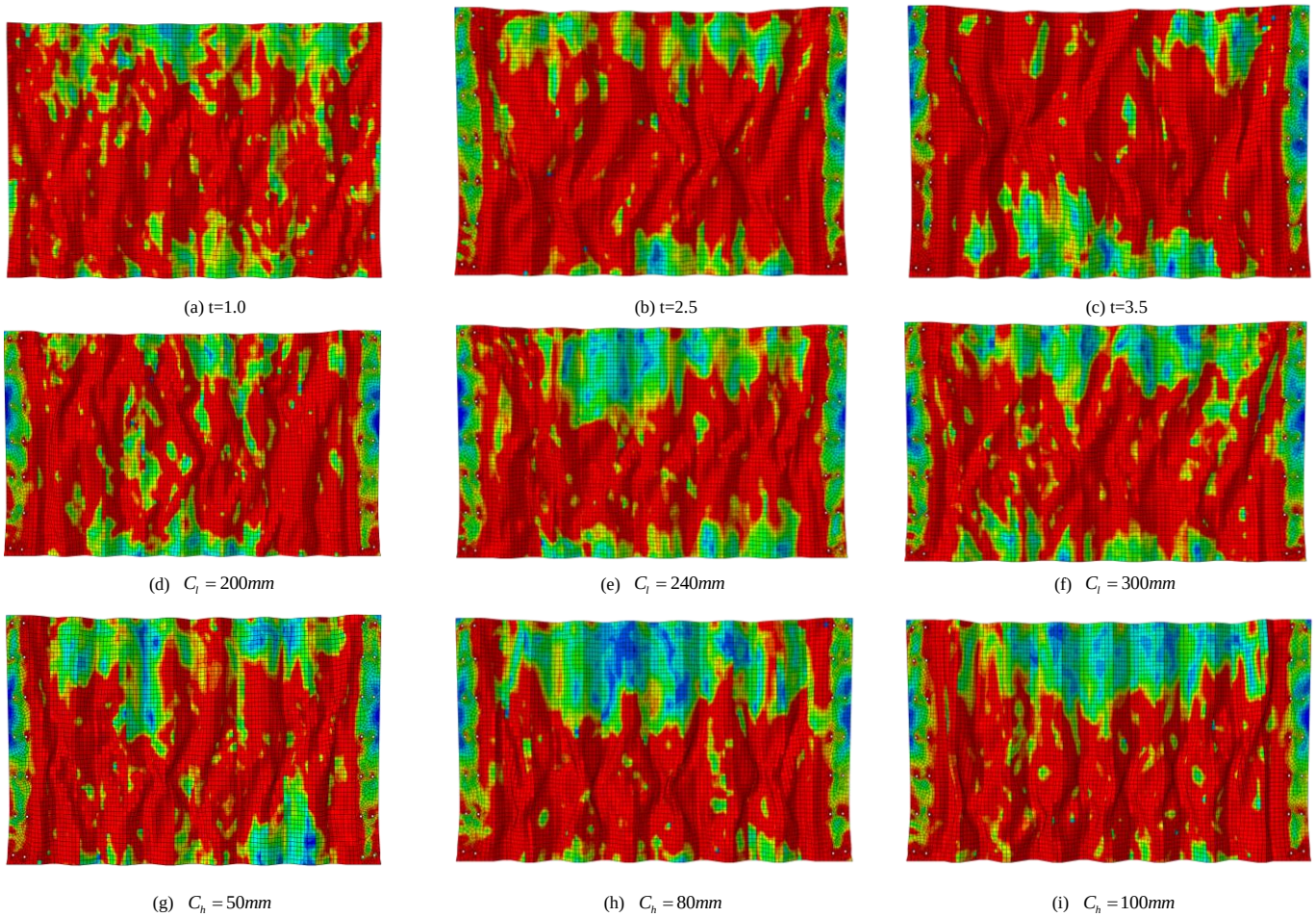

(a) t=1.0 (b) t=2.5 (c) t=3.5

(d) $C_l = 200mm$ (e) $C_l = 240mm$ (f) $C_l = 300mm$

(g) $C_h = 50mm$ (h) $C_h = 80mm$ (i) $C_h = 100mm$

Fig. 21 Von Mises stress distribution of the corrugated plate under cyclic loading

4. Conclusions

A new CSPSWs type was suggested in this paper, and two different types of specimens were designed. The seismic performance of the specimens was studied by a low-cycle reciprocating loading test, and reached the following conclusions:

(1) The trapezoidal CSPSWs with PEC columns connected by bolts had a high bearing capacity and lateral stiffness and had good hysteretic performance under cyclic loading. PEC column avoided the bending, torsion and buckling failure modes of pure steel column outside the plane, and formed the failure mode of “strong frame, weak wallboard, strong column and weak beam” in the plane. This structure could better meet the requirements of a double lateral force resistance design requirements; that is, the efficiency loss of the plate was before that of the boundary frame.

(2) The CSPSWs with PEC columns achieved post-yield buckling, and the

tension band formed after buckling continued to bear the load. The damaged parts of the specimens were concentrated in the middle of the wallboard, and the corner connection was not damaged. This indicates that the design of the fabricated connection structure proposed in this paper is reasonable and reliable.

(3) With the height-thickness ratio decrease of the corrugated steel plate, the ultimate bearing capacity of PEC-CSPSW increased and the initial lateral stiffness increased. The increase of wavelength and wave amplitude of the corrugated steel plate had little influence on the ultimate bearing capacity and initial lateral stiffness of PEC-CSPSW. In addition, the concrete addition enhanced the anchoring effect of side columns on the shear field of embedded steel plates, gave full play to the post-buckling strength of embedded steel plates, and obviously improved the bearing capacity and initial stiffness of the structure.

References

[1] Berman JW. and Bruneau M., "Experimental investigation of light-gauge steel plate shear walls", Journal of Structural Engineering, 131(2),259-267, 2005.

[2] Botros RBG. "Nonlinear finite element analysis of corrugated steel plate shear walls", Calgary，Alberta: University of Calgary, 62-109, 2006.

[3] Lan Y.J., "Research of resist lateral force structure-steel corrugated plate shear wall", MS Thesis, Xi'an University of Architecture and Technology,Xian,China, 2006. (in Chinese)

[4] Lu Y. and Li G.Q., "Slim buckling-restrained steel plate shear wall and simplified model", Advanced Steel Construction, 8(3),282-294, 2012.

[5] Stajadinovic B. and Tipping S., "Structural testing of corrugated sheet steel shear walls", Proceedings of the 9th International Specialty Conference on Cold-Formed Steel Structures St Louis, Missouri, USA: American Iron and Steel Institute, 425-439, 2008.

[6] L.A. Fülöp. and I. Hakola., "Design method for light-gauge steel shear walls sheathed with flat steel plates", Advanced Steel Construction, 3(3),628-651, 2007.

[7] Johnson RP., Cafolla J. and Bernard C., "Corrugated webs in plate girders for bridges", Structures and Buildings, 122(2),161, 1997.

[8] Liu S. M., Ding H. S., Taerwe L. and Corte W. D., "Modifications to the global and interactive shear buckling analysis methods of trapezoidal corrugated steel webs for bridges", Advanced Steel Construction, 15(4),349-363, 2019.

[9] Zhao Q.H, Sun J.H, Li Y.N. and Li Z.X., "Cyclic analyses of corrugated steel plate shear wall", The Structural Design of Tall and Special Buildings, 26(16), e1351, 2017.

[10] Dou C., Jiang Z.Q., Pi Y.L. and Guo Y L., "Elastic shear buckling of sinusoidally corrugated steel plate shear wall". Engineering Structures, 121,136-146, 2016.

[11] Dou C., Pi Y.L. and Gao. W., "Shear resistance and post-buckling behavior of corrugated panels in steel plate shear walls", Thin Walled Structures, 131, 816-826, 2018.

[12] Cao Q. and Huang J.Y., "Experimental study and numerical simulation of corrugated steel plate shear walls subjected to cyclic loads", Thin Walled Structures, 127,306-317, 2018.

[13] Yu J.G., Feng X.T.,Li B.,Hao J P. and Ge M.L., "Performance of steel plate shear walls with axially loaded vertical boundary elements", Thin-Walled Structure, 125(14), 152-163, 2018.

[14] Yu J.G. and Hao J.P., "Behaviour of semi-rigid steel frames with steel plate shear walls", Advanced Steel Construction, 12(2), 154-173, 2016.

[15] Chen Z.Y., Bian G.Q. and Huang Y., "Review on web buckling and hysteretic behavior of shear panel dampers", Advanced Steel Construction, 9(3),205-217, 2013.

[16] Piquer A. and Hernández-Figueirido D., "Protected steel columns vs partially encased columns: Fire resistance and economic considerations", Journal of Constructional Steel Research, 124,47-56, 2016.

[17] Song Y.C., Wang R.P. and Li J., "Local and post-local buckling behavior of welded steel shapes in partially encased composite columns", Thin-Walled Structures, 108(9), 93-108, 2016.

[18] Zhao G.T., Zhang Y.M., Cao F.B. and Zhou Y.H., "Experimental study on seismic performance of welded H-section steel partially encased columns with high strength concrete", Journal of Building Structures, 40(04), 116-122, 2019. (in Chinese)

[19] Chicoine T, Tremblay R, Massicotte B, Ricles J.M. and Lu L.W., "Behaviour and strength of partially encased composite columns with built up shapes", Journal of Structural Engineering, 128(3), 279-288, 2002.

[20] Feng J., Jin J., Xia J. and Fang Y.Z., "Experimental study on seismic performance of pec composite column-steel beam frame with welded t-stub strengthened connections", Advanced Steel Construction, 17(3), 264-272, 2021.

[21] Yin Z.Z., Li J.M. and Zhao S.P., "Experimental study of seismic behavior on steel plate shear wall with PEC columns", China Civil Engineering Journal, 51(S1), 139-144, 2018. (in Chinese)

[22] Yu J.G., Yu H.S., Feng X.T., Dang C.,Hou T.F. and Shen J., "Behaviour of steel plate shear walls with different types of partially-encased H-section columns", Journal of Constructional Steel Research, 170, 106123, 2020.

[23] Yin Z.Z., Zhang H. and Yang W.W., "Study on Seismic Performance and Damage Analysis of Steel Plate Shear Wall with Partially Encased Composite (PEC) Columns", Applied Sciences, 9(5), 907, 2019.

[24] JGJ/T 101-2015. Specification for Seismic Test of Buildings., China Architecture Industry Press, Beijing, China,2015.

[25] Han L.H. "Concrete-filled steel tube-theory and practice", 2nd ed. Beijing: Science Press, 2007:106. (in Chinese)

Acknowledgments

The financial supports from the National Natural Science Fund of China under grant No. 51968044 and research Project (JK2021-22，JK2022-06) of Gansu provincial department of housing and urban and rural construction are gratefully acknowledged.

Advanced Steel Construction – Vol. 19 No. 2 (2023) 166–176
DOI:10.18057/IJASC.2023.19.2.9

POST-FIRE BEHAVIOR OF CROSS-SHAPED STEEL REINFORCED CONCRETE COLUMNS: SIMULATION AND ANALYTICAL EXPRESSIONS

Tian-Gui Xu [1], Dun Liang [1], Sheng-Gang Fan [1, *] and Wei Li [2]

[1] *Key Laboratory of Concrete and Prestressed Concrete Structures of Ministry of Education, School of Civil Engineering, Southeast University, Jiulonghu Campus, Nanjing, China*
[2] *The IT Electronics Eleventh Design & Research Institute Scientific and Technological Engineering Corporation Limited, Shandong Branch, Jinan, China*
** (Corresponding Author: E-mail: 101010393@seu.edu.cn)*

ABSTRACT

In order to explore the behavior of cross-shaped steel reinforced concrete (SRC) columns after fire, the heat transfer analysis model and structural analysis model were established by ABAQUS software. The simulation results of the cross-shaped column were compared with the existing test results, in the aspect of the temperature distribution, time-temperature curve, failure mode, and load-displacement relationship after fire exposure. The results show that the simulation results agree well with the experimental results. The influence of critical parameters on residual bearing capacity coefficient k was discussed, which including constant heating duration, maximum heating temperature, concrete strength, yield strength of section steel, yield strength of rebars, limb thickness, effective column length, rebar diameter, and steel content. Finally, a simplified formula was proposed to calculate the residual bearing capacity of cross-shaped SRC columns after fire.

ARTICLE HISTORY

Received: 23 November 2022
Revised: 3 March 2023
Accepted: 9 March 2023

KEYWORDS

Steel reinforced concrete column;
Cross-shaped column;
After fire exposure;
Finite element analysis;
Residual bearing capacity calculation

1. Introduction

In recently, cross-shaped steel reinforced concrete (SRC) columns have been widely used in high-rise buildings. This structure possesses not only the characteristics of high bearing capacity, significant stiffness and flexible layout, but also more esthetical and higher space utilization than ordinary square column, as depicted in Fig.1. Unfortunately, high-rise building fires are not uncommon, posing a serious threat to people's safety. After exposed to fire, the strength and rigidity of the steel-concrete composite members are lost, so it is essential to re-evaluate the residual bearing capacity to take appropriate reinforcement measures to ensure that the structure can withstand the corresponding load [1-4] and continue to put into use. However, the core issue of repair assessment is how to determine the residual bearing capacity of the structure after fire, which has not been resolved yet.

Nowadays, the behavior of SRC columns at room temperature has been extensively investigated [5-8], leading to the development of various design codes, such as *Technical specification for steel reinforced concrete composite structures* (JGJ138-2001) [9] in 2001, *Technical specification of Steel-Reinforced Concrete Structures* (YB9082-2006) [10] in 2006 and *Code for design of composite structures* (JGJ138-2016) [11] in 2016 by China. At the same time, some scholars [12-13] have combined new materials with this structure, providing a new perspective for the application of SRC columns.

In general, SRC columns have a high proportion of steel components and thin layer of concrete cover, making them more vulnerable to damage than reinforced concrete columns when exposed to the same fire conditions. Some scholars have studied the fire-resistance of SRC columns at high temperature and made some achievements. Zheng and Han [14] carried out the fire resistance test of SRC columns and analyzed the effects of different parameters. It revealed that the fire resistance of SRC columns was significantly impacted by the section size and slenderness ratio. Han et al. [15-18] carried out the tests of square section SRC columns and beam-column joints at high temperature. The effect of stress distribution, explosion spalling of concrete, bonding between steel and concrete on its mechanical properties was analyzed. In these tests, SRC structure both show a good bearing capacity and ductility at high temperature. Young [19] investigated the behavior of axially restrained SRC columns at elevated temperatures. The fire resistance obtained from the finite element model was compared with the values in EC 4. The result showed that the EC4 was generally conservative for the axially restrained SRC columns. Ellobody [20] introduced the modeling process, and post-processing of circular section steel-concrete composite columns under fire, analyzed the influence of geometric defects, residual stress, material properties, and other parameters on the load-displacement relationship and fire resistance of composite columns to perfect the design criteria in the norm further.

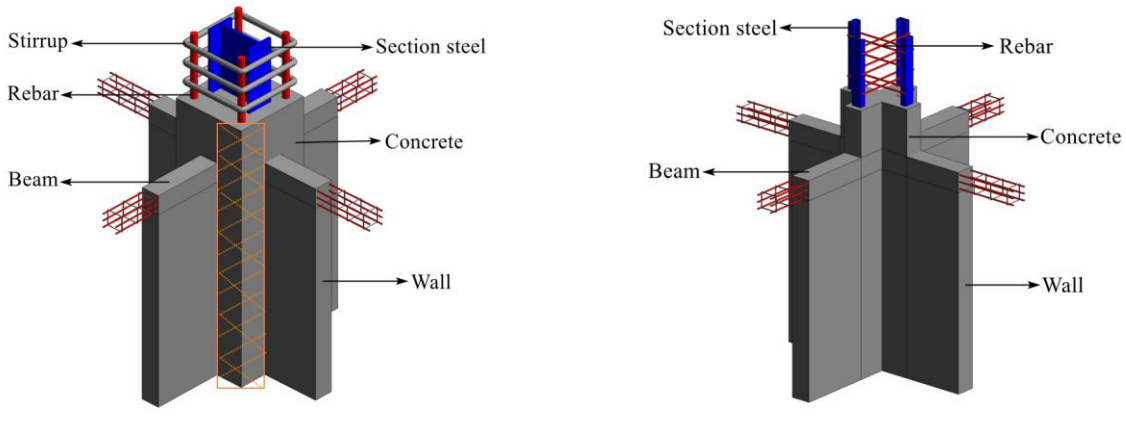

(a) (b)

Fig. 1 Steel Reinforced Concrete Columns: (a) Ordinary square column; (b) Cross-shaped column

Previous studies have shown that SRC columns have a good mechanical property at high temperatures, so this type of structure may still be put into use after exposure to fire. Therefore, the mechanical properties of SRC columns after exposure to high temperature have also attracted the attention of many experts and scholars. Zhang et al. [21], Meng et al. [22], Han et al. [23, 24], Chen et al. [25] and Liu et al. [26] investigated the behavior of square section steel-concrete composite columns after fire, revealed the relationship between temperature distribution and load-displacement. In addition, the effects of fire time, steel content, and other parameters that can influence the residual bearing capacity of columns were also considered. Yang et al. [27] carried out the compressive performance test of SRC short columns after exposure to high temper, and established the calculation formula of ultimate strength after fire. The proposed formula can better calculate the ultimate strength of short columns, but it has some limitations for the calculation of medium and long columns.

In summary, these research finds compensated for the deficiencies of existing studies, but the section type still was limited, mainly concentrate on square and circular, which cannot meet the needs of the research on special-shaped columns. There were few studies on the performance of SRC special-shaped columns after fire. The post-fire behavior of nine T-shaped SRC columns was studied by Wang et al. [28]. A formula for calculating the remain bearing capacity of T-shaped columns after high temperature was proposed. Liu et al. [29] completed the post-fire test of cross-shaped SRC columns. Due to the restriction of fire test cost and instrument, the parameter study of cross-shaped columns after exposure to high temperature was limited. However, in many aspects, such as maximum temperature, concrete strength, steel content, etc. will have unpredictable impact on the post-fire behavior of cross-shaped SRC columns. Accordingly, it is necessary to use the finite element method to analyze the performance of cross-shaped SRC columns after the fire.

In this paper, the ABAQUS [30] software was used to establish finite element models to analyze the fire effect of the cross-shaped SRC column. A series of systemic studies were carried out, including finite element simulation, parameter analysis and simplified design method, which can offer references for the repairing and strengthening of cross-shaped SRC columns after fire.

2. Test overview

2.1. Description of specimens

To further evaluate the post-fire behavior of cross-shaped SRC columns, the test data published by Liu et al. [29] was selected for comparison with the simulation results. Fig. 2 was the three-dimensional figure of the cross-shaped SRC columns with four 5 # section steel (50 mm × 37 mm × 4.5 mm × 7 mm, Cross-sectional area of section steel A_s= 692 mm^2). The rebar with a diameter of 8 mm was used as the web member to connect all the section steel. The high of column was 600 mm and limb thickness was 100 mm. In order to facilitate heating and loading, 200 mm high reinforced area were arranged at both ends of the column, as depicted in Fig. 3. The layout parameters details of cross-shaped columns are summarized in Table 1. Four temperature measuring points were arranged on the middle section of cross-shaped column, as illustrated in Fig. 4. These included measuring point 1 (the concave surface of the column), measuring point 2 (the center position), measuring point 3 (the inner margin of the steel web), and measuring point 4 (the convex surface), which were used to record the temperature-time history of the specimen. The specimen was heated at electric furnace, and kept different heating duration (60 min, 120 min and 180 min) at 600 ℃ as shown in Fig. 5.

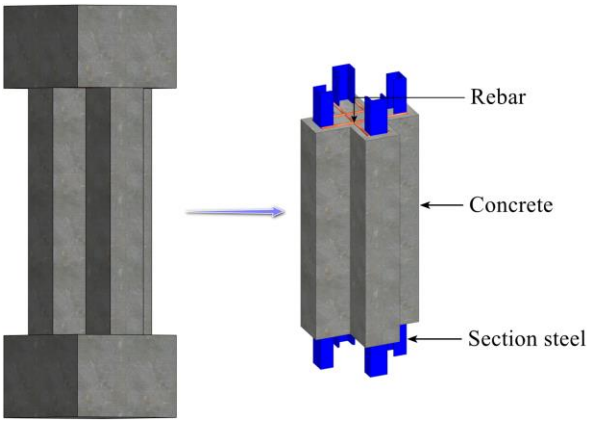

Fig. 2 Cross-shaped column three-dimensional figure

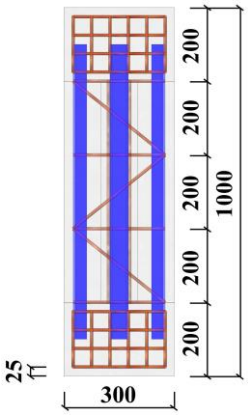

Fig. 3 Design drawing of steel skeleton

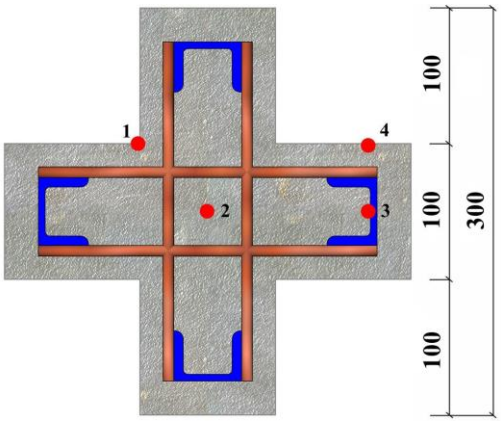

Fig. 4 Layout of measuring points

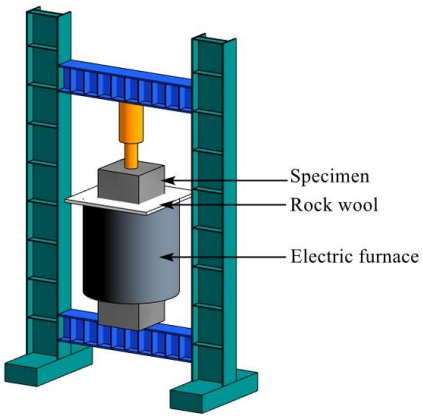

Fig. 5 Electric furnace for heating test

Table 1
Details of specimen parameters

Specimen	Constant heating duration (min)	Limb thickness (mm)	Effective length (mm)	Concrete strength (MPa)	Yield strength (Q235) (MPa)	Yield strength (HRB400) (MPa)
SRC-01	60	100	600	47.4	330	473
SRC-02	120	100	600	47.4	330	473
SRC-03	180	100	600	47.4	330	473

Table 2
The properties of concrete

Concrete coupon	Compressive strength (MPa)	Average compressive strength (MPa)	Young's modulus (GPa)	Average Young's modulus (GPa)
1	46.5		34.1	
2	48.5	47.4	34.7	34.4
3	47.2		34.6	

Table 3
The properties of steel

Steel type	Young's modulus (GPa)	Yielding strength (MPa)	Tensile strength (MPa)
5 # section steel	204	330	450
Rebar	205	473	615

2.2. Material properties

Liu et al. [29] conducted mechanical property tests on materials of concrete and steel. Table 2 summarizes the compressive strength and Young's modulus of concrete, while Table 3 provides the detailed test results of steel.

2.3. Test results

The experimental results carried out by Liu et al. [29] were summarized in this section. It was revealed that the temperature decreased with increasing depth of the measurement points and the thermal gradients reduced with increasing constant heating duration. The high temperature caused a reduction in the bond load between the concrete and section steel, leading to serious concrete falling off during the heating process, and all specimens exhibited shear failure mode under the load. Furthermore, the influence of heating duration on the bearing capacity of the specimen was studied. The results exhibited that both the cracking loads and ultimate loads decreased with increasing heating duration.

3. Finite element model

The thermal-mechanical coupling analysis of cross-shaped SRC columns under axial load after fire is complex. Two commonly used methods for this analysis are: the fully thermal-mechanical coupling method and the sequential thermal-mechanical coupling method. The former discussed the interplay between temperature development and stress, while the latter included the heat transfer stage and the structural analysis stage. Since the fully thermal-mechanical coupling method lacks computational efficiency and is difficult to converge when simulating complex structures, most scholars prefer the sequential thermal-mechanical coupling analysis method. The following four assumptions were set to simplify the simulation process: (1) the temperature distribution of steel is assumed to be uniform. (2) Ignore the thermal resistance among interfaces. (3) The deformation of steel and concrete is coordinated. (4) Ignore the concrete cover spalling.

3.1. Material constitutive

3.1.1. Thermal parameter

The thermal parameters of materials are the most basic data needed to simulate the temperature field, including density ρ, thermal conductivity λ_c, specific heat capacity C_c and Coefficient of thermal expansion α_c [31]. These thermal parameters will change with the increase in temperature. In recent years, scholars have proposed many methods to calculate the thermal performance of concrete and steel. The definitions of thermal parameters of steel and concrete were different in various countries fire resistance design codes. In the simulation test, the thermal parameters of steel and concrete were calculated by applying Eurocode 2 [32], Eurocode 3 [33] and Eurocode 4 [34].

3.1.2. Material properties of concrete

After fire, the various performance parameter of concrete is reduced greatly, and the stress-strain relationship also changes, as shown in Fig.6 (a). The influencing factors include not only the properties of aggregates and the strength of concrete, but also the external conditions such as heating rate, peak temperature, cooling method, etc. At present, many stress-strain relationship constitutive equations of concrete after exposure to fire have been derived by scholars. In this paper, the research results provided by Lu et al. [35] were adopted, and the constitutive equation was selected as follows.

$$y=\begin{cases}1-\varepsilon_{op}(T)\left(115(x-1)/(1+0.00504T)\right) & x\le 1\\ 2x-x^2 & x>1\end{cases} \tag{1}$$

where $x=\varepsilon_c/\varepsilon_{op}(T)$, $y=\sigma_c/\sigma_{op}(T)$ (2)

$$\sigma_{op}(T)=\sigma_o/\left(1+2.4(T-20)^6\times 10^{-17}\right) \tag{3}$$

$$\varepsilon_{op}(T)=\varepsilon_o\left(1+2.5\times 10^{-3}T\right) \tag{4}$$

where T is the highest temperature experienced; σ_c represents the stress of concrete and ε_c is the strain of concrete; σ_o and $\sigma_{op}(T)$ represent the peak stress of concrete at room temperature and after high-temperature, respectively; ε_o and $\varepsilon_{op}(T)$ represent the peak strain of concrete at room temperature and after high-temperature.

3.1.3. Material properties of steel

Compared with concrete, steel softens rapidly under fire. Steel strength declines significantly with the rise of temperature, while its lost strength will be substantially restored after cooling down. Fig.6 (b) indicates that the stress reduction of steel after the fire is minimal. Literature [36] pointed out that Poisson's ratio of steel is less affected by temperature. Therefore, this article assumes that the Poisson's ratio of steel remains unchanged after exposure to fire. The value of steel strength and elastic modulus in Eq. (5) adopts the suggestion of Wu [37], which are expressed as

$$\sigma_s=\begin{cases}E_{sr}(T)\varepsilon_s & \varepsilon_s\le\varepsilon_{yr}(T)\\ f_{yr}(T)+E_{sr}^{'}(T)\left(\varepsilon_s-\varepsilon_{yr}(T)\right) & \varepsilon_s>\varepsilon_{yr}(T)\end{cases} \tag{5}$$

$$f_{yr}(T)=\begin{cases}(100.19-0.01586T)\times 10^{-2}f_y & 20\ ℃<T<600\ ℃\\ (121.395-0.0512T)\times 10^{-2}f_y & 600\ ℃\le T<900\ ℃\end{cases} \tag{6}$$

$$E_{sr}(T)=(100.53-0.0265T)\times 10^{-2}E_s \qquad 20\ ℃<T\le 900\ ℃ \tag{7}$$

where σ_s and ε_s represent stress and strain of steel respectively; $\varepsilon_{yr}(T)$ represents the yield strain of steel after exposure to high-temperature; f_y and $f_y(T)$ are the yield strength of steel at ambient temperature and after high-temperature exposure, respectively; E_s and $E_{sr}(T)$ represent the elastic moduli of steel at ambient temperature and after high-temperature, respectively; $E_{sr}^{'}(T)$ represents the elastic modulus of the steel at the hardening stage after high-temperature, taking 1% of the elastic module of the specimen during the elastic phase.

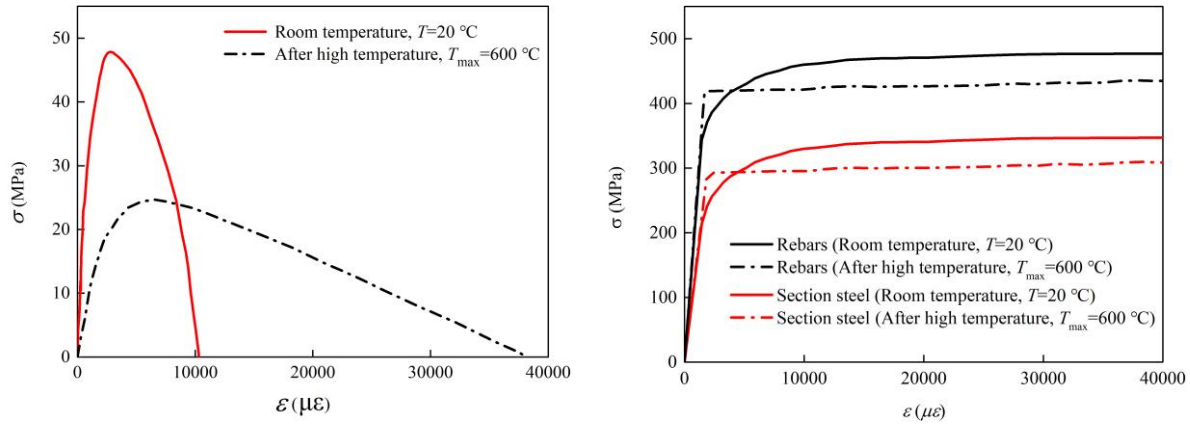

(a) (b)

Fig. 6 Stress-strain relationship of materials at different stages: (a) Concrete; (b) Steel

3.2. Heat transfer model

The temperature field modeling is a prerequisite for structural modeling. In the simulation test, the nonlinear heat transfer of cross-shaped columns was analyzed by using the finite element equation of energy conservation and the Fourier law of controlling heat conduction. Lie [38] revealed that the influence of rebars on heat transfer was small, so the role of rebars can be ignored in temperature field simulation. Note that the steels can be ignored in the temperature field analysis. When the temperature field was introduced into structural modeling, the steels can be added to the modeling and the temperature of the steels can be obtained by linear interpolation. Before the fire, the component was in the indoor environment, so the starting temperature of each point was 20 °C, the absolute zero was defined as -273 °C, and the Stefan-Boltzmann constant $\sigma = 5.67 \times 10^{-8}$ W / (m^2·K^4) was used.

The finite element mesh division needs to consider various conditions. As the element mesh is refined, the accuracy of the calculation results will be improved, but at the same time, the calculation efficiency will be reduced. Therefore, it is necessary to weigh various factors and conduct multiple tests to select the appropriate mesh division method. The maximum cell size of the grid density of the cross-shaped SRC columns was set as 20 mm in this test and the details of grid division as shown in Fig. 7.

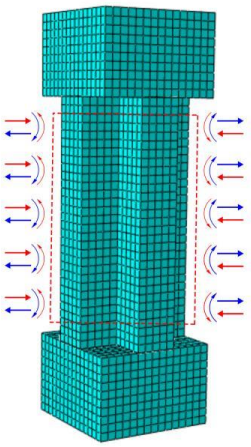

Fig. 7 Mesh model

The eight-node linear heat transfer hexahedral element DC3D8 was introduced to simulate concrete and section steel. The command "Tie" constraint was adopted between section steel and concrete, concrete and concrete without considering the influence of relative slip. The thermal convection and radiation boundary conditions were defined on the surface of the column according to Eurocode 4 [34]. The thermal radiation coefficient was defined as 0.7, and the convective heat transfer coefficient was defined as 25 W / (m^2·°C).

Fig. 8 shows the temperature distribution nephograms of cross-shaped columns at constant heating duration for 60 min, 120 min, and 180 min, respectively. It shows that the temperature of the column section decreases gradually from the outer surface to the center. The temperature near the section steel was basically similar. The temperature of the center of the column section was gradually increased with the rise of the constant heating duration.

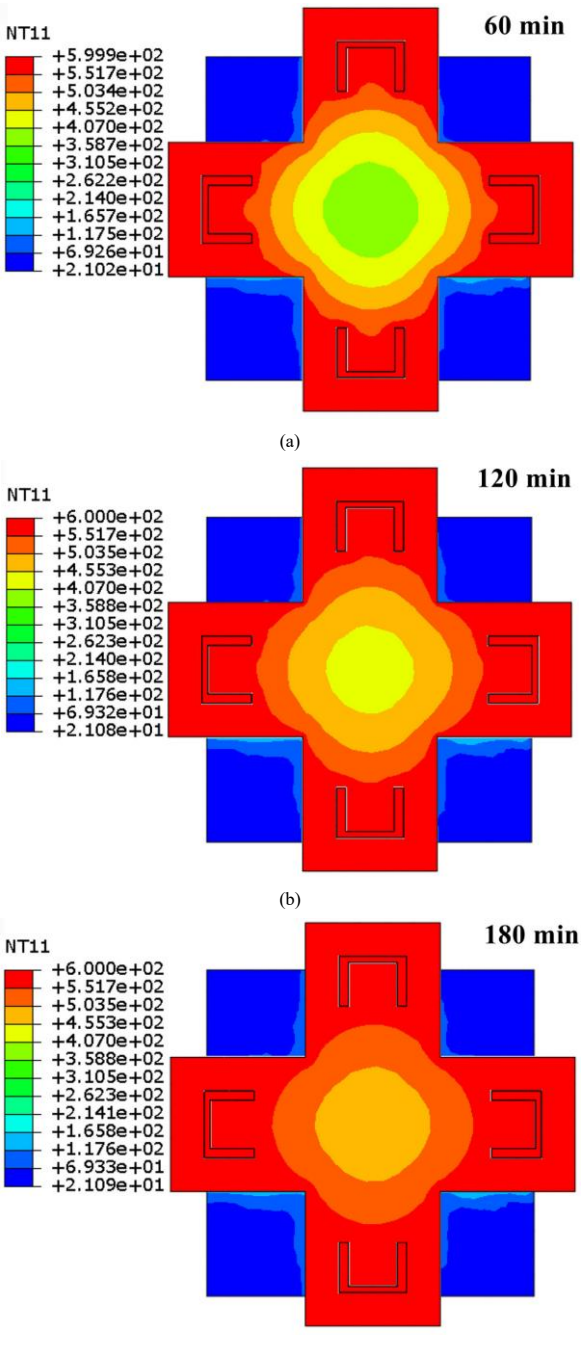

(a) (b) (c)

Fig. 8 The temperature field of different constant heating duration: (a) 60 min; (b) 120 min; (c) 180 min

3.3. Structural model

The thermal-mechanical coupling method was introduced to analyze the performance of cross-shaped SRC columns after fire. The secondary development of ABAQUS was carried out through Python, and the maximum temperature of each element node in the heat transfer process was extracted. Then the heat transfer analysis results were imported into the mechanical model to analyze the remain bearing capacity of the specimen after high temperature. It is necessary to keep the mesh division and node numbering consistent with the thermal field analysis model when establishing a mechanical finite element analysis model, so as to correctly read the temperature value of each node. Concrete and section steel were simulated by an eight-node three-dimensional solid linear shrinkage integral element (C3D8R), and rebars were affected by a three-dimensional truss linear element (T3D2).

The "Tie" constraint was assumed between section steel and concrete, and the "Embedded region" restriction was adopted between concrete and rebars. An external load was applied to the top connection point of the cross-shaped column by displacement. Since the initial geometric imperfection of cross-shaped columns was considered, the first elastic buckling mode of columns was multiplied by the amplification factor in the model, which is defined as L_s / 1000 [39], where L_s is effective column length.

The existing research [17] shows that the interface slip between concrete and section steel has a slight impact on the behavior of cross-shaped columns after fire, and thus was not taken into account in this paper.

4. Finite element verification

4.1. Temperature field analysis and verification

Fig. 9 shows the change of temperature-time histories of cross-shaped columns under different constant heating duration. The temperature rising trend of measuring point 2 was the slowest because of the longest conduction path of the cross-shaped column section. The rise in temperature of measuring point 4 was closest to the furnace temperature, which was caused by the direct exposure of the outer surface of the cross-shaped column to air. In the constant temperature stage, the difference in this temperature change trend was decreasing, because the concrete has a small heat transfer coefficient [29].

Fig. 9 demonstrates that the simulation can accurately predict the development of the time-temperature curve. At the start of heating process, the simulated temperature was similar to the result of the test. As temperature increased, the temperature rise trend of simulation and test was different. There are three main reasons: First, in the test process, when the concrete reaches about 100 °C, the water consumption energy will be evaporated, which retards the speed of the increase of temperature. Second, the contact between concrete and section steel is incomplete under fire, which produces certain thermal resistance in heat transfer [40], and the contact thermal resistance between concrete and section steel is ignored in heat transfer modeling. Third, concrete is essentially a discrete material, and concrete is usually regarded as a continuous medium in finite element simulation, resulting in the difference between the predicted temperatures and the measured results.

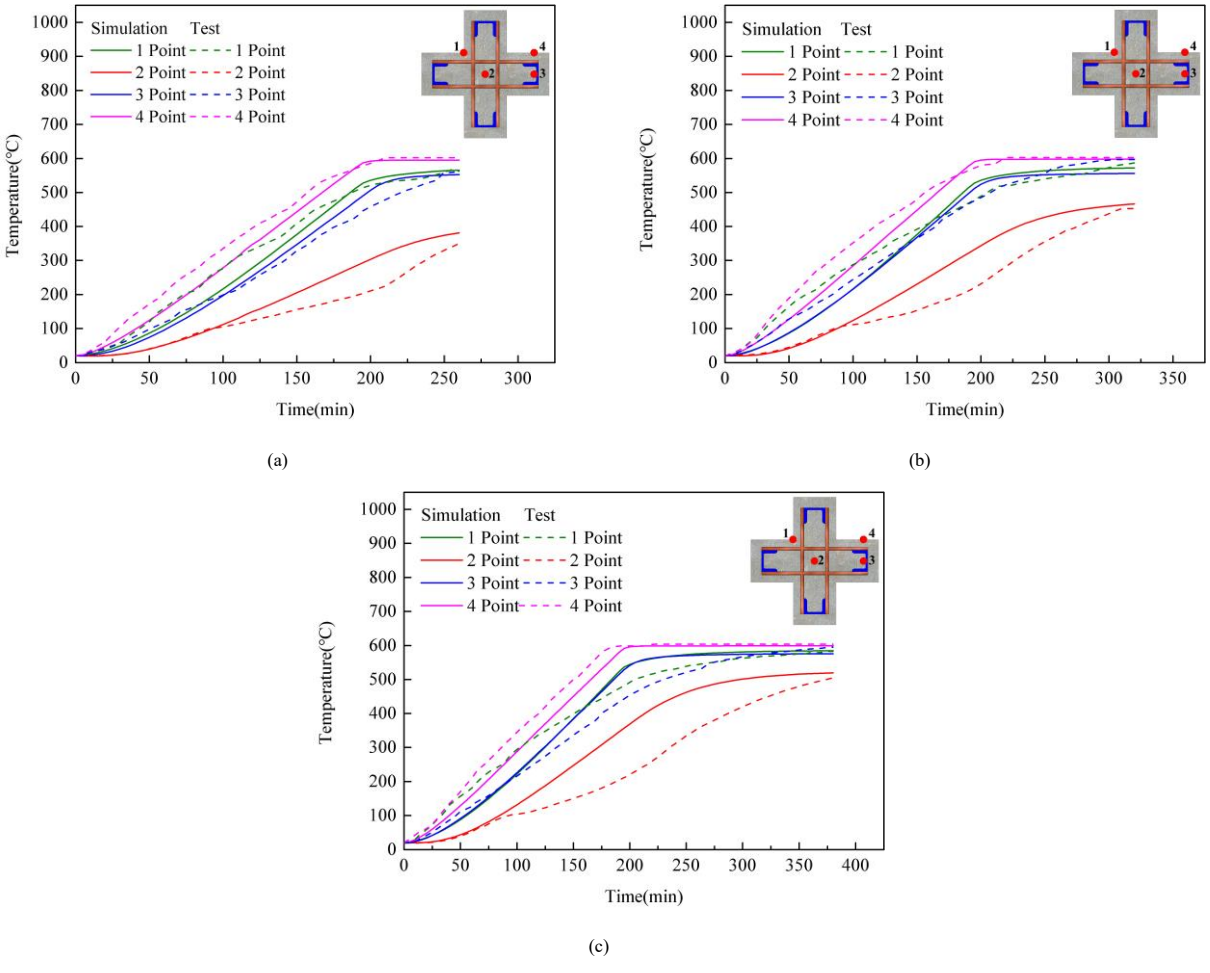

Fig. 9 Comparison of test and simulated temperature-time history: (a) Constant heating duration 60 min, (b) Constant heating duration 120 min, (c) Constant heating duration 180 min

4.2. Structural analysis and verification

Fig. 10 illustrates the failure modes between simulated and tested cross-shaped columns after fire. The simulated cloud picture shows the equivalent plastic strain of external concrete. The simulation results were found to be in agreement with the experimental results, and the simulation cloud picture of cross-shaped columns after fire shows a high lateral displacement in the middle. During the test, high-temperature heating caused the deterioration of concrete, resulting in the formation of vertical and oblique cracks under the load, mainly in the middle of the specimen. Therefore, the simulated strain distribution was basically consistent with the crack and shedding observed in the test.

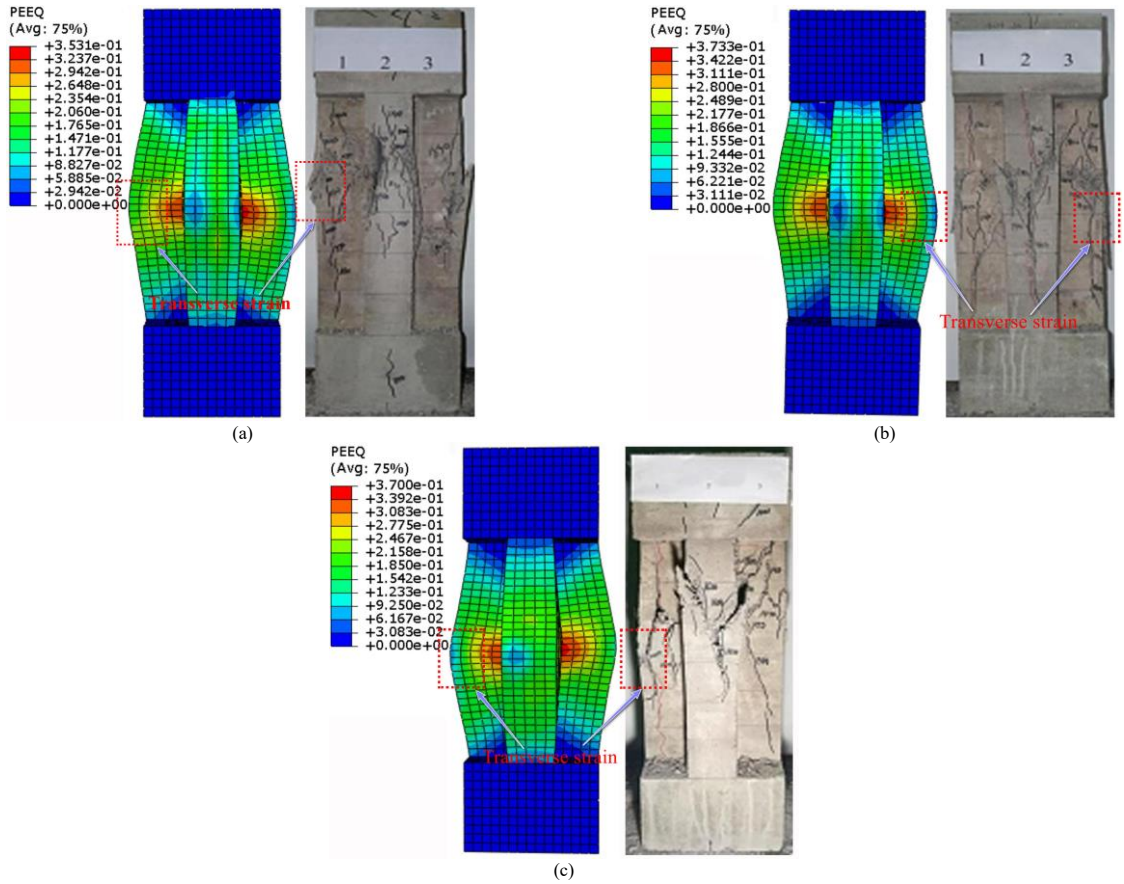

Fig. 10 Comparison of test results and simulated cloud picture: (a) SRC-01, (b) SRC-02, (c) SRC-03

The load-displacement curves of cross-shaped columns after fire is shown in Fig. 11. Under an axial load, the cross-shaped columns experienced the elastic stage, elastic-plastic stage, strengthening stage, descending stage, and residual stage. In the elastic stage, the deformation of concrete and section steel were coordinated, and no cracks appeared. In the elastic-plastic stage, concrete cracks appeared and expanded, section steel and rebars gradually yield. In the strengthening stage, the concrete was loose owing to the evaporation of free water in the internal pores of concrete after the fire. In the loading process, as the load increased, the loose concrete was gradually compacted, resulting in an increase in the stiffness of the column. In the descending stage, as the concrete protective layer continuously falls off, the bearing capacity of the column declines obviously. As displacement increases, the load drop tends to be gentle, and the residual bearing capacity was chiefly provided by concrete and section steel in the core zone in the residual stage. The load-displacement curves of the simulation and test of cross-shaped SRC columns is shown in Fig. 11. The finite element simulation of cross-shaped columns stiffness slightly overestimated the test value due to the lack of consideration of the influence of concrete spalling in the fire stage.

Table 4 compares the simulated and experimental results of the residual bearing capacity of cross-shaped SRC columns after fire. It shows that the average value and standard deviation of residual bearing capacity of cross-shaped columns were 1.016 and 0.007, respectively, indicating that the finite element model was effective.

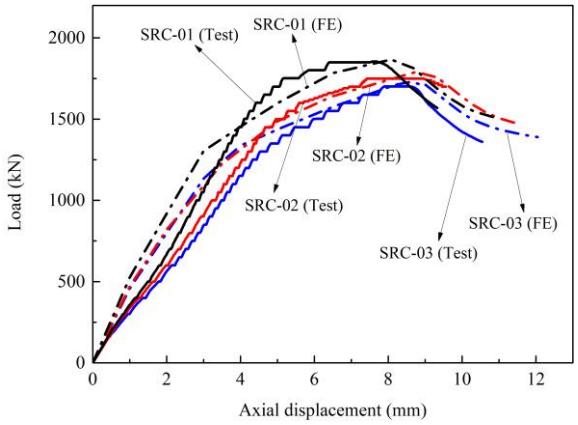

Fig. 11 Comparison between simulated and test values of load-displacement curves

Table 4
Comparison of residual bearing capacity between simulated and test values

Specimen	Constant heating duration (min)	Limb thickness (mm)	N_{FE} (kN)	N_{test} (kN)	N_{FE}/N_{test}
SRC-01	60	100	1863	1850	1.007
SRC-02	120	100	1790	1750	1.023
SRC-03	180	100	1732	1700	1.019
Mean value					1.016
Standard deviation					0.007

Note: N_{FE} represents the simulated value in kN, and N_{test} represents the test value in kN.

5. Effect of parameters on residual bearing capacity after fire

5.1. Parameter introduction

The critical parameters are set as shown in Table 5 for extended analysis, including constant temperature duration, maximum temperature, concrete strength, yield strength of section steel and rebars, limb thickness, effective column length, rebar diameter and steel content. Parameter values (Table 5) were selected according to Eurocode 4 [34] and practical engineering practices. These critical parameters were modeled using the same heating curve and boundary

conditions as the test.

Table 5
Parameters of the study

Parameter	Sign	Numerical value	Unit
Constant heating duration	t_c	60、120、180	min
Maximum temperature	T_m	600、700、800、900、1000	℃
Concrete strength	f_{cu}	20、30、40、50、60	MPa
Yield strength of section steel	f_y	215、235、345、390、420	Mpa
Yield strength of rebars	f_{yb}	335、400、500	Mpa
Limb thickness	L_e	100、150、200	mm
Effective column length	L_s	600、1000、1500、2000	mm
Rebar diameter	Φ	6、8、10	mm
Steel content	α	5.5、6.8、8.2	%

5.2. Definition of the residual bearing capacity coefficient

In order to estimate the residual bearing capacity of cross-shaped SRC columns after fire, the parameter k was introduced as the residual bearing capacity coefficient of cross-shaped SRC columns after fire, which is

$$N_u(t) = kN_u \tag{8}$$

where $N_u(t)$ represents the residual bearing capacity of cross-shaped SRC columns after fire; N_u represents the ultimate bearing capacity of cross-shaped SRC columns at ambient temperature.

5.3. Parametric analysis

The change of k value with the analysis parameters under different constant heating duration conditions is illustrated in Fig. 12. It shows that with the increase of constant heating duration, the residual bearing capacity of the cross-shaped SRC column decreases gradually, resulting in a significant decrease in the k value. Table 6 shows the range of k values corresponding to different analysis parameters under the conditions of constant heating duration of 60 min, 120 min, and 180 min (the difference between the maximum k value and the minimum k value). It can be seen from Table 6 that with the increase of constant heating duration, the range of k value was gradually reduced. In this paper, the average value of the range of k value was used as a reference, and divides the analysis parameters into two levels for description. Taking 15% of the range as the limit, greater than 15% was defined as the first-level parameter, and less than 15% was defined as the second-level parameter.

The first-level parameters include maximum temperature (T_m) and concrete strength (f_{cu}). Fig. 12 (a) displays that the k value declines with the rise of T_m, because the rise of T_m reduces the material behavior of the column. Besides, the downward trend of k value was also becoming more and more gentle, especially when the temperature rises from 900 °C to 1000 °C. This was because after T_m reaches 600 °C, the concrete protective layer has fallen off seriously. If the temperature continues to rise, the concrete will fall off less and less until it completely falls off.

Fig. 12 (b) shows that the value of k gets decreases as f_{cu} increases. The reason may be that the increase in concrete compressive strength leads to a decrease in internal porosity and a denser microstructure. Therefore, it becomes more difficult to release water vapor from the sample at high temperature, which leads to more serious degradation of material strength.

The second-level parameters include the yield strength of section steel (f_y) and rebar (f_{yb}), limb thickness (L_e), effective column length (L_s), rebar diameter (Φ), and steel content (α). From Fig. 12 (c) and Fig. 12 (d), it is evident that the value of k increases with the rise of steel yield strength. This is because the higher steel yield strength leads to an increase in the total plastic resistance of components. In addition, compared with the concrete strength (Fig.12 (b)), the increase of steel yield strength has slight influence on the k value, due to the steel strength has been dramatically restored during the cooling stage. The rise of f_{yb} has little impact on the value of k, and its range of less than 3% can be ignored.

Fig. 12 (e) shows that the k value increases with the increase of L_e. The reason was that the thermal inertia of concrete will increase with the rise of cross-section area, thereby reducing the temperature of the internal structure and improving the residual bearing capacity of columns.

Fig. 12 (f) displays that the k value declines with the rise of L_s, which was consistent with the research of buckling theory. In addition, the downward trend of the k value was more and more gentle, mainly because the increase of L may produce more residual deformation after exposure to fire, thereby increasing the second-order effect of load.

As can be seen in Fig. 12 (g) and 12 (h), the value of k increases with an increase in Φ or α. This was because higher Φ or α can improve the resistance to deformation of cross-shaped columns.

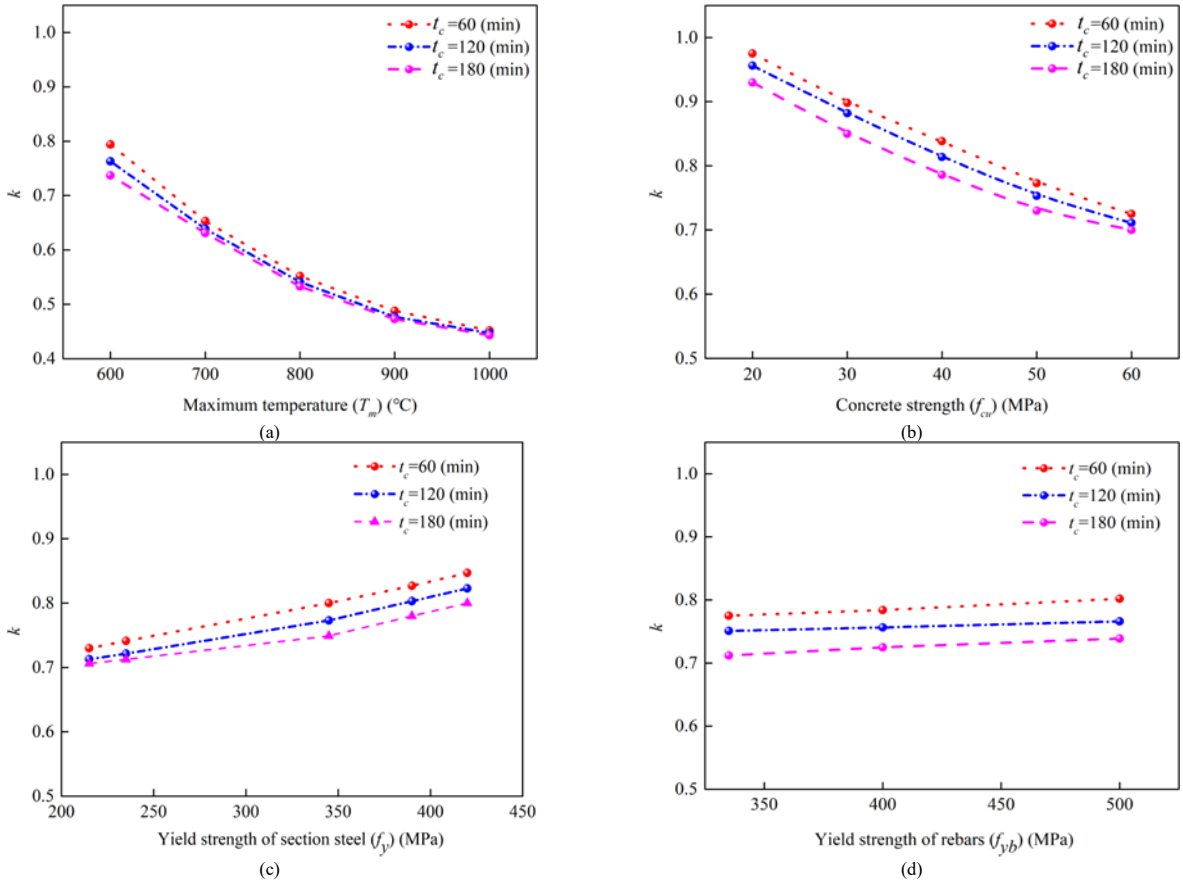

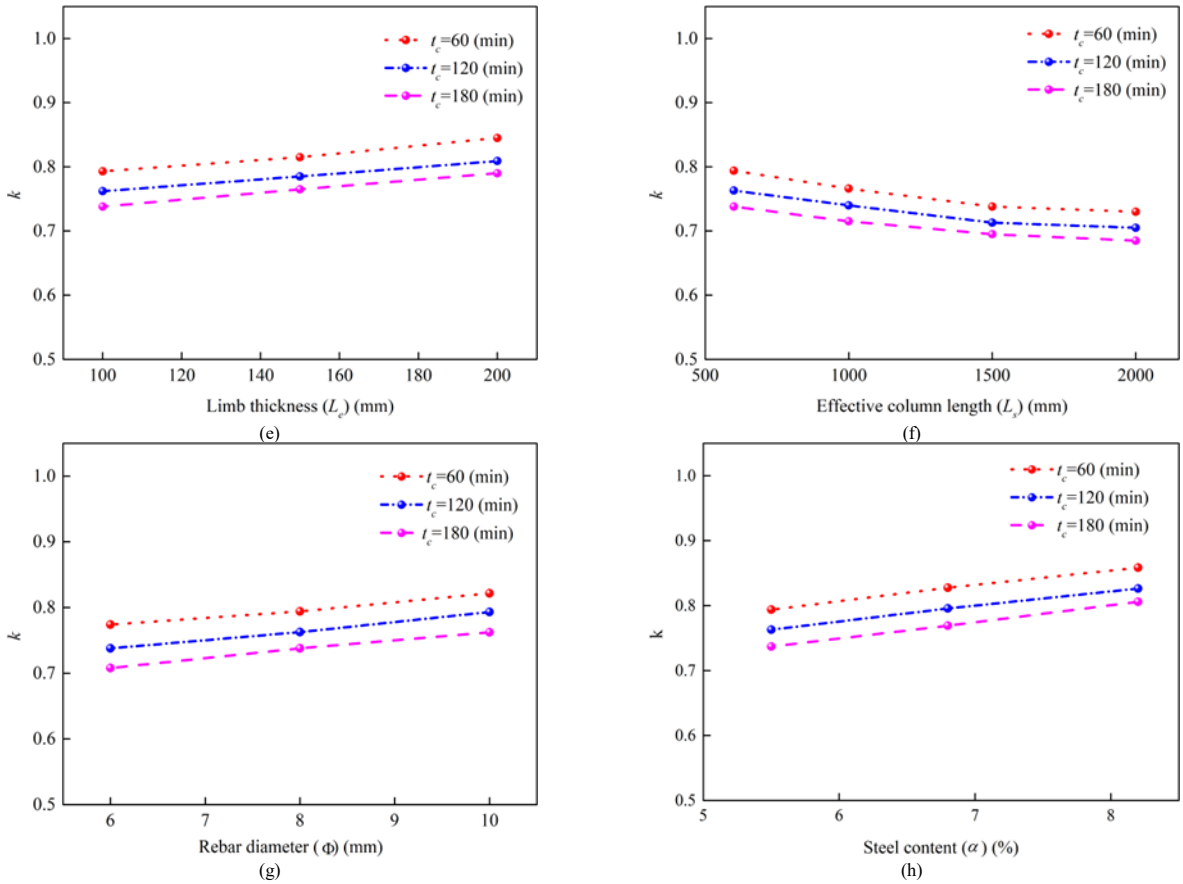

Fig. 12 Effect of parameters on the residual bearing capacity coefficient k: (a) Maximum temperature, (b) Concrete strength, (c) Yield strength of section steel, (d) Yield strength of rebars, (e) Limb thickness, (f) Effective column length, (g) Rebar diameter, (h) Steel content

Table 6
The variation of the range of k value with each analysis parameter under different constant heating durations

Parameter	Constant heating duration of 60 min	Constant heating duration of 120 min	Constant heating duration of 180 min	The mean value of the range of k
Maximum temperature	0.354	0.327	0.305	0.329
Concrete strength	0.250	0.245	0.233	0.243
Yield strength of section steel	0.117	0.110	0.074	0.100
Yield strength of rebars	0.027	0.015	0.027	0.023
Limb thickness	0.051	0.046	0.053	0.050
Effective column length	0.064	0.058	0.055	0.059
Rebar diameter	0.048	0.055	0.054	0.052
Steel content	0.064	0.063	0.069	0.065

6. Simplified design method

6.1. Temperature calculation formula

According to the simulation results, the temperature calculation formulas (20 ℃-1000 ℃) of each measuring point can be proposed respectively.

The temperature of measuring point 1 at the concave surface of cross-shaped columns can be calculated by the following formula:

$$T_{wc} = T_w + T_c \tag{9}$$

$$T_w = 1298.8 - 1470 \Big/ \left(1 + \exp\left((t_w - 211.7)/102.7\right)\right) \tag{10}$$

$$T_c = 40.3 - 16237.3 \Big/ \left(1 + \exp\left((t_c + 253)/41.8\right)\right) \tag{11}$$

$$T_m = 2131.1 - 37302 \Big/ \left(1 + \exp\left((T_w + 4461.2)/1577.8\right)\right) \tag{12}$$

where t_w and t_c is the heating time and constant heating duration, 20 min ≤ t_w ≤ 330 min, 10 min ≤ t_c ≤ 180 min. T_w and T_c are the temperatures of the heating section and constant temperature section, respectively, T_{wc} represents the measuring point temperature, T_m represents the ambient temperature around the column.

Measuring point 2 is situated in the middle of cross-shaped columns, and the temperature calculation formulas are as follows:

$$T_{wc} = T_w + T_c \tag{13}$$

$$T_w = 761.4 - 833.5 \Big/ \left(1 + \exp\left((t_w - 207.8)/86.8\right)\right) \tag{14}$$

$$T_c = 154.9 - 874.3 \Big/ \left(1 + \exp\left((t_c + 72)/47.3\right)\right) \tag{15}$$

$$T_m = 2211.3 - 19998.9 \Big/ \left(1 + \exp\left((T_w + 2158.1)/1017.9\right)\right) \tag{16}$$

Measuring point 3 is located in the inner edge of the steel web, which can be calculated by the following formula:

$$T_{wc} = T_w + T_c \tag{17}$$

$$T_w = 1386.7 - 1676 \Big/ \left(1 + \exp\left(\left(t_w - 208.65\right)/125.8\right)\right) \tag{18}$$

$$T_c = 45.15 - 29022.45 \Big/ \left(1 + \exp\left(\left(t_c + 127\right)/19.5\right)\right) \tag{19}$$

$$T_m = 3156 - 29141.5 \Big/ \left(1 + \exp\left(\left(T_w + 5150.3\right)/2418.6\right)\right) \tag{20}$$

The measuring point 4 is located on the convex surface of the cross column. The temperature of the concrete surface was nearly equal to the surrounding temperature during the heating stage, and remained relatively constant during the constant temperature stage. Therefore, the change of measuring point 4 temperature in the constant temperature stage can be ignored:

$$T_{wc} = T_w + T_c \tag{21}$$

$$T_w = 1542.6 - 2007.3 \Big/ \left(1 + \exp\left(\left(t_w - 186.5\right)/151.8\right)\right) \tag{22}$$

$$T_m = 7329.3 - 35192.5 \Big/ \left(1 + \exp\left(\left(T_w + 7647\right)/5703.6\right)\right) \tag{23}$$

6.2. Simplified calculation of ultimate bearing capacity at ambient temperature

In this paper, according to the method proposed by Eurocode 4 [34], and ignoring the constraint effect between section steel and concrete, the bearing capacity formula of cross-shaped SRC column at room temperature is derived as follows:

$$N_u = 0.9(\varphi_1 f_c A_c + 4\varphi_2 f_y A_s) \tag{24}$$

where φ_1 and φ_2 are the stability coefficients of cross-shaped columns, through the numerical fitting, φ_1 = 0.938, φ_2 = 0.931, f_c is the compressive strength of concrete at ambient temperature (f_c=0.79f_{cu}), f_y is the yield strength of steel at room temperature, A_c represents the cross-sectional area of the concrete cross-shaped column, and A_s is the cross-sectional area of single section steel.

6.3. Simplified calculation of the residual bearing capacity coefficient

The main parameters affecting the k value have been analyzed in the previous section. According to the numerical results in Fig. 12, the simplified formula of the k value is derived by the linear regression method:

$$k = \mu k_t k_{T_m} k_{f_{cu}} k_{f_y} k_{L_e} k_{L_s} k_\Phi k_\alpha \tag{25}$$

$$k_t = 0.8244\exp\left(-0.0006t\right) \qquad 30\ \text{min} \le t \le 180\ \text{min} \tag{26}$$

$$k_{T_m} = 1310.8T_m^{-1.16} \qquad 600\ ℃ \le T\ \le 1000\ ℃ \tag{27}$$

$$k_{f_{cu}} = 1.12\exp\left(-0.0072 f_{cu}\right) \qquad 20\ MPa \le f_{cu} \le 60\ MPa \tag{28}$$

$$k_{f_y} = 0.6261\exp\left(0.0007 f_y\right) \qquad 215\ MPa \le f_y \le 420\ MPa \tag{29}$$

$$k_{L_e} = 0.7448\exp\left(0.0006L_e\right) \qquad 100\ mm \le L_e \le 200\ mm \tag{30}$$

$$k_{L_s} = 1.2589L_s^{-0.072} \qquad 600\ mm \le L_s \le 2000\ mm \tag{31}$$

$$k_\Phi = 0.707\exp\left(0.0149\Phi\right) \qquad 6\ mm \le \Phi \le 10\ mm \tag{32}$$

$$k_\alpha = 1.4\alpha^{0.1957} \qquad 5.5\% \le \alpha \le 8.2\% \tag{33}$$

where k_t, k_{T_m}, $k_{f_{cu}}$, k_{f_y}, k_{L_e}, k_{L_s},k_Φ,k_α respectively represent the influence of constant temperature duration, maximum temperature, concrete strength, yield strength of section steel, cross-shaped columns section side length, effective column length, rebar diameter and steel content on the value of k. μ is stability factor, which takes 5.1.

6.4. Numerical comparison

Fig. 13 compares the time-temperature curve between the formula calculation results and the simulation results. It displays that those curves were very similar, which confirms the effectiveness of the temperature calculation method.

Fig. 14 displays the comparison between the k value calculated using the formula and the k value obtained from the simulation. The difference between the two values was within 10%, indicating that the formula-based method of calculating the k value was accurate within the given range.

Fig. 15 compares the calculated value of the formula in this paper with the calculated value of the formula proposed by Liu [29]. The calculation formula proposed in this paper can well envelope the test value of Liu. In addition, the calculation formula proposed in this paper is more applicable and has a wider parameter range than Liu's formula, as it does not require the temperature field distribution of the specimen to be determined before calculating the bearing capacity.

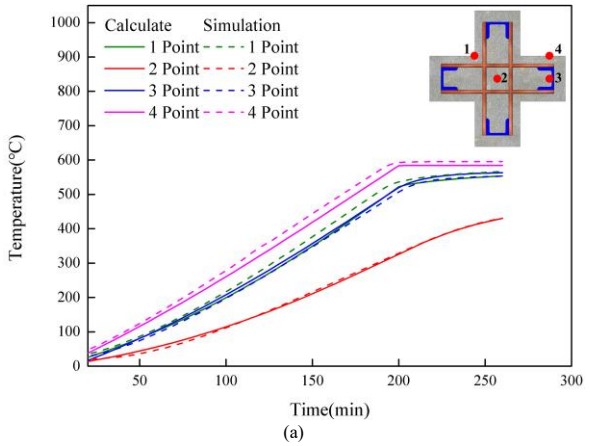

(a)

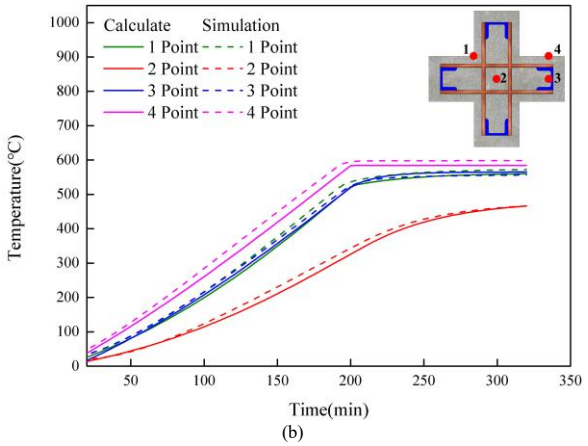

(b)

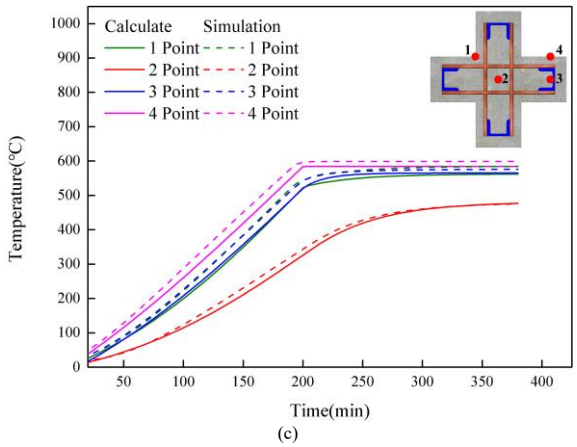

(c)

Fig. 13 Comparison of simulated and formula calculated temperature-time history: (a) Constant heating duration 60 min, (b) Constant heating duration 120 min, (c) Constant heating duration 180 min

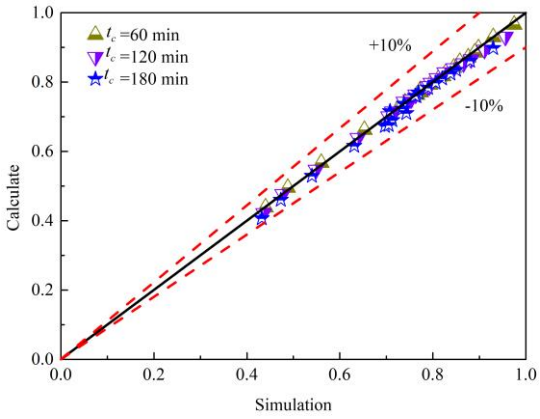

Fig. 14 Comparison of numerical analysis results and formula calculation results of *k* value

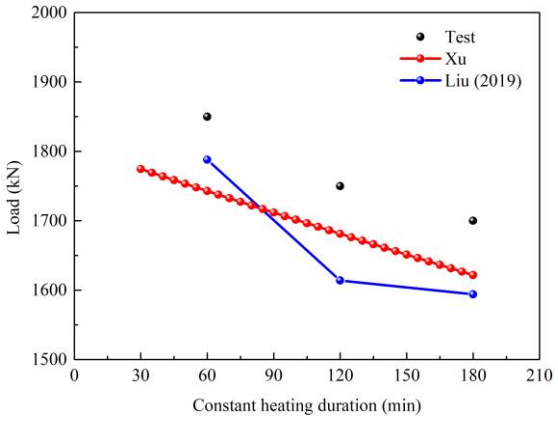

Fig. 15 Comparison of calculated load between different formulas

7. Conclusions

To further explore the post-fire behavior of cross-shaped SRC columns, a series of systemic studies were carried out in this paper, including test overview, finite element simulation, parameter analysis, and simplified design method. The following conclusions were obtained.

(1) The simulated equivalent plastic strain nephogram of the cross-shaped SRC column was compared with the actual failure diagram. The average value and standard deviation (1.016 and 0.007, respectively) of the residual bearing capacity of the cross-shaped SRC column after fire were calculated. It reveals that the finite element model is effective.

(2) The *k* value was gradually decreased with an increase in constant heating duration, maximum temperature, concrete strength, and effective column length. With the increase of yield strength of section steel, yield strength of rebar, limb thickness, rebar diameter, and steel content, the *k* value gradually increases.

(3) The concrete strength and the maximum temperature have the most significant influence on the *k* value. When the concrete strength is between 20 MPa and 60 MPa, the average value of the *k* value range is 24.3%. Similarly, when the maximum temperature is between 600 °C and 1000 °C, the average value of the *k* value range is 32.9%. The yield strength of reinforcement has the most negligible impact on the *k* value, where the range was less than 3%.

(4) The temperature calculation method of measuring points and the simplified calculation method of residual bearing capacity of the cross-shaped SRC column after fire were deduced. The calculation results were in good agreement with the finite element simulation results, which verifies the accuracy of the calculation method.

Declaration of competing interest

The authors state that they have no competing financial interests or personal relationships that could have influenced the work reported in this paper.

Acknowledgements

The authors are grateful for the financial support of The Open Fund of Shanghai Key Laboratory of Engineering Structure Safety (No. 2020-KF05) for sponsoring this research.

References

[1] Hou, L.F., Li, M., Liu, Y.C., “Numerical Simulation and Analysis of On-building High-rise Building Fires”, Procedia Engineering, 11, 127-134, 2011. DOI: 10.1016/j.proeng.2011.04.637

[2] Zhang, B.J., Wang, Y.Z., Li, G.Q., Qu, S., Fu, C.G., Xu, T.G., “Structural performance of steel reinforced concrete T-shaped columns exposure to high temperature”, Structures, 34, 716-728, 2021. DOI: 10.1016/j.istruc.2021.08.023

[3] Wang, Y.Z., Xu, T.G., Liu, Z.Q., Li, G.Q., Jiang, J., “Seismic behavior of steel reinforced concrete cross-shaped columns after exposure to high temperatures”. Engineering Structures, 230, 111723, 2021. DOI: 10.1016/j.engstruct.2020.111723

[4] Wang, Y.Z., Wang, X., Li, G.Q., Jiang, J., Xu, T.G., “Residual Strength of L-shaped Steel Reinforced Concrete Columns after Exposure to High Temperatures”, KSCE Journal of Civil Engineering, 25(4), 1369-1384, 2021. DOI: 10.1007/s12205-021-0658-9

[5] Cao X.L., Wu L.M., Li Z.M., “Behaviour of steel-reinforced concrete columns under combined torsion based on ABAQUS FEA”. Engineering Structures, 209, 109980, 2020. DOI: 10.1016/j.engstruct.2019.109980.

[6] Yang Y., Chen Y., Feng S.Q., “Study on behavior of partially prefabricated steel reinforced concrete stub T columns under axial compression”. Engineering Structures, 199, 109630, 2019. DOI: 10.1016/j.engstruct.2019.109630.

[7] Xiang S., Zeng L., Liu Y.H., Mo J.X., Ma L.L., Zhang J.C., Chen J., “Experimental study on the dynamic behavior of T-shaped steel reinforced concrete columns under impact loading”. Engineering Structures, 208, 110307, 2020. DOI: 10.1016/j. engstruct.2020.110307.

[8] Xue Y.C., Yang Y., Yu Y.L., “Shear strength model for steel reinforced concrete composite members: Short columns and deep beams”. Engineering Structures, 216, 110748, 2020. DOI: 10.1016/j.engstruct.2020.110748.

[9] JGJ138-2001. “Technical specification for steel reinforced concrete composite structures”, China Ministry of Construction, 2001. (in Chinese)

[10] YB9082-2006. “Technical specification of Steel-Reinforced Concrete Structures”, Nation Development and Reform Commission, 2006. (in Chinese)

[11] JGJ138-2016. “Code for design of composite structures”, China Ministry of Construction, 2016. (in Chinese)

[12] Dong H. Y., Zhu J., Cao W.L., Rao, Y.X., “Axial compressive behavior of mega steel-reinforced high-strength concrete columns with different steel sections”. Structures, 48, 1158-1174, 2023. DOI: 10.1016/j.istruc.2023.01.017.

[13] Lai B.L., Zhang. M.Y., Zheng X.F. Chen Z.P., Zheng, Y.Y., “Experimental Study on the Axial Compressive Behaviour of Steel Reinforced Concrete Composite Columns with Stay-in-Place ECC Jacket”. Journal of Building Engineering, 106174, 2023. DOI: 10.1016/j.jobe.2023.106174.

[14] Zheng, Y.Q., Han, L.H., “Calculations on the fire resistance of steel reinforced concrete (SRC)

columns", Fourth International Conference on Advances in Steel Structures, 2, 1017-1022, 2005. DOI: 10.1016/B978-008044637-0/50149-9

[15] Han, L.H., Tan, Q.H., Song, T.Y., "Fire Performance of Steel Reinforced Concrete (SRC) Structures", Procedia Engineering, 62, 46-55, 2013. DOI: 10.1016/j.proeng.2013.08.043

[16] Han, L.H., Tan, Q.H., Song, T.Y., "Fire Performance of Steel Reinforced Concrete Columns", Journal of structural Engineering, 141(4), 28-37, 2015. DOI: 10.1061/(ASCE)ST.1943-541X.0001081

[17] Han, L.H., Zheng, Y.Q., Tao, Z., "Fire performance of steel-reinforced concrete beam-column joints", Magazine of Concrete Research, 61(7), 499-518, 2009. DOI: 10.1680/macr.2008.61.7.499

[18] Song, T.Y., Han, L.H., Yu, H.X., "Temperature field analysis of SRC-column to SRC-beam joints subjected to simulated fire including cooling phase", Advances in Structural Engineering, 14(3), 353-366, 2013. DOI:10.1260/1369-4332.14.3.353

[19] Young, B., Ellobody, E., "Performance of axially restrained concrete encased steel composite columns at elevated temperatures", Engineering Structures, 33(1), 245-254, 2011. DOI: 10.1016/j.engstruct.2010.10.019

[20] Ellobody, E., "A consistent nonlinear approach for analyzing steel, cold-formed steel, stainless steel and composite columns at ambient and fire conditions", Thin-Walled Structures, 68,1-17, 2013. DOI: 10.1016/j.tws.2013.02.016

[21] Zhang, C., Wang, G.Y., Xue, S.D., Yu, H.X., "Experimental research on the behaviour of eccentrically loaded SRC columns subjected to the ISO-834 standard fire including a cooling phase", International Journal of Steel Structures, 16(2), 425-439, 2016. DOI: 10.1007/s13296-016-6014-0

[22] Meng, F.Q., Zhu, M.C., Mou, B., He, B.J., "Residual Strength of Steel-Reinforced Concrete-Filled Square Steel Tubular (SRCFST) Stub Columns After Exposure to ISO-834 Standard Fire", International Journal of Steel Structures, 19(3), 850-866, 2018. DOI:10.1007/s13296-018-0174-z

[23] Han, L.H., Zhou, K., Tan, Q.H., Song, T.Y., "Performance of steel reinforced concrete columns after exposure to fire: Numerical analysis and application", Engineering Structures, 211, 110421, 2020. DOI: 10.1016/j.engstruct.2020.110421

[24] Han, L.H., ASCE1, M., Zhou, K., Tan, Q.H., and Song, T.Y. "Performance of Steel-Reinforced Concrete Column after Exposure to Fire: FEA Model and Experiments", Journal of Structural Engineering, 142 (9), 55-67, 2016. DOI: 10.1061/(ASCE)ST.1943-541X.0001511

[25] Chen, Z.P., Liang, Y.H., Mo, L.L., and Ban, M.G., "Residual Properties and Axial Bearing Capacity of Steel Reinforced Recycled Aggregate Concrete Column Exposed to Elevated Temperatures", Frontiers in Materials, 7, 1-14, 2020. DOI: 10.3389/fmats.2020.00187

[26] Liu, F.Q., Yang, H., Yan, R., Wang, W., "Experimental and numerical study on behavior of square steel tube confined reinforced concrete stub columns after fire exposure", Thin-Walled Structures, 139, 105-125, 2019. DOI: 10.1016/j.tws.2019.02.037

[27] Yang, H., Yang, X., Mao, Z.H., "Compressive performance of steel-reinforced concrete columns after exposure to high temperature", Journal of Building Engineering, 59, 105120, 2022. DOI: 10.1016/j.jobe.2022.105120

[28] Wang, Y.Z., Gong J.L., Qu, S., Zhang B.J., Chen Y.T., "Mechanical properties of steel reinforced concrete T-shaped column after high temperature", Structures, 46, 852-867, 2022. DOI: 10.1016/j.istruc.2022.10.117

[29] Liu, Z.Q., Wang, Y.Z., Li, G.Q., Jiang, J., Fu, C.Q., "Mechanical behavior of cross-shaped steel reinforced concrete columns after exposure to high temperatures", Fire Safety Journal, 108, 102857, 2019. DOI: 10.1016/j.firesaf.2019.102857

[30] ABAQUS Standard Version 6.14 User's Manual, Volumes I-III Pawtucket, Dassault Systemes Simulia Corp, Rhode Island, USA, 2014.

[31] Hong, S.D., Varma, A.H., "Analytical modeling of the standard fire behavior of loaded CFT columns", Journal of Constructional Steel Research, 65(1), 54-69, 2009.

[32] EN l992-1-2, "Eurocode 2 Design of Concrete Structures", European Committee for Standardization, 2004.

[33] EN 1993-1-2, "Eurocode 3 Design of Steel Structures, Part 1.2: General Rules-Structural Fire Design", European Committee for Standardization, 2005.

[34] EN 1994-l-2, "Eurocode 4 Design of Composite Steel and Concrete Structures", European Committee for Standardization, 2005.

[35] Lu, Z.D., Zhu, B.L., Tan, W., "Study on reinforcement and repair of reinforced concrete beams after fire", Proceedings of the State Key Laboratory of Civil Engineering Disaster Prevention, 152-162, 1993. (in Chinese).

[36] Li, G.Q., Han, L.H., Lou, G.B., Jiang, S.C., "Fire design for steel and steel-concrete composite structures", Beijing: China Architecture and Building Press, 2006. (in Chinese).

[37] Wu, B., "Mechanical performance of reinforced concrete structures after exposure to fire", Beijing: Science Press, 2003. (in Chinese).

[38] Lie, T.T., "Fire resistance of circular steel columns filled with bar-reinforced concrete", Journal of Structural Engineering, 120(5), 1489-1509, 1994. DOI: 10.1061/(ASCE)0733-9445(1994)120:5(1489)

[39] Zhou, K., Han, L.H., "Modelling the behaviour of concrete-encased concrete-filled steel tube (CFST) columns subjected to full-range fire", Engineering Structures, 183, 265-280, 2019. DOI: 10.1016/j.engstruct.2018.12.100

[40] Ghojel, J., "Experimental and analytical technique for estimating interface thermal conductance in composite structural elements under simulated fire conditions", Experimental Thermal and Fluid Science, 28(4), 347-354, 2004. DOI: 10.1016/S0894-1777(03)00113-4

Advanced Steel Construction – Vol. 19 No. 2 (2023) 177–184
DOI: 10.18057/IJASC.2023.19.2.10

EXPERIMENTAL AND NUMERICAL ANALYSIS OF L-SHAPED COLUMN COMPOSED OF RECYCLED AGGREGATE CONCRETE-FILLED SQUARE STEEL TUBES UNDER ECCENTRIC COMPRESSION

Teng-Fei Ma [1, 2], Zhi-Hua Chen [1], Kashan Khan [1] and Yan-Sheng Du [1, *]

[1] *School of Civil Engineering, Tianjin University, Tianjin 300072, China*
[2] *Department of Civil Engineering, North China Institute of Aerospace Engineering, Langfang 065000, China*
** (Corresponding author: E-mail: duys@tju.edu.cn)*

ABSTRACT

The eccentric compression behaviors of L-shaped columns made of recycled aggregate concrete-filled square steel tubes (L-RACFST) with various replacement ratios of recycled coarse aggregate (RCA) are introduced in this paper. The experimental study demonstrates that the overall instability failure is the final failure mode of the L-RACFST columns and that the replacement ratio of RCA has little influence on the final failure mode of the specimens. When the RCA replacement ratio exceeds 40%, the specimens frequently move right into the failure stage. Recycled aggregate concrete (RAC) inside steel tubes can increase the load-carrying capacity and stiffness, preventing them from buckling inward compared to hollow steel tubes. The load-carrying capacity of the specimens gradually decreases as the replacement ratio of the RCA rises, and the ductility and stiffness deteriorate progressively. The bearing capacity declines more quickly, and the ductility coefficient and stiffness coefficient fall more slowly when the replacement ratio of RCA is higher than 40%. The bearing capacity of the specimens decreased by 29%, the ductility coefficient by 54%, and the stiffness coefficient by 60% as the replacement ratio of RCA increased from 0% to 100%. The specimen's ultimate strength decreases as the eccentricity rises. The numerical analysis results demonstrate that in the engineering design, the specimens' ultimate strength can be increased by strengthening the steel and raising the steel ratio; however, it is not advised to increase the connection plate's width to enhance the load-carrying capacity. The connection plate's primary function is to increase the stiffness of the steel surface and prevent local buckling, which has little bearing on improving the specimens' bearing capacity. It is advised that the replacement ratio of RCA in the L-RACFST columns should be less than 40% when considered with the research findings of reference [28].

ARTICLE HISTORY

Received: 31 August 2022
Revised: 9 February 2023
Accepted: 23 February 2023

KEYWORDS

Concrete-filled steel tube;
L-shaped column;
Recycled aggregate concrete;
Compression behaviour

1. Introduction

The use of steel structure homes has greatly accelerated the industrialization of building development in China. One of the most efficient ways to achieve building industrialization is to develop prefabricated construction. Recycled aggregate concrete (RAC), a green building material, can efficiently recognize the recyclability of waste concrete. With this method, resource recycling is feasible. Studies [1-4] show that RAC has low strength and significant creep shrinkage. Through experimental research, Wedding P A, Ridzuan A R M et al. [5–6] demonstrated that the strength of the RAC is decreased by 30% compared to natural concrete when the water and cement ratio is 0.35. The experiments conducted by Huda et al.[7] revealed that the mechanical properties of the RAC, such as the elastic modulus, strength, and Poisson ratio, decreased when compared to natural concrete. The impact of recycled coarse aggregates (RCA) of various ages on the resilience of RAC was investigated by Mahmood et al.[8].The findings indicate that when the replacement ratio of the RCA is less than 30%, its mechanical properties and durability are comparable to those of natural concrete. Shi et al. [9] .'s study of the mechanical properties and strength of the RAC with various RCA replacement ratios looked at the change law variation against time. The findings demonstrated that RAC with different RCA replacement ratios has lower density and strength than natural concrete.

According to some scholars, the RAC can be poured into steel tubes to produce recycled aggregate concrete-filled steel tubes (RACFST). Both the steel tube and the RAC are restrained. RAC and the benefits of steel tubes can both be utilized simultaneously [10–15]. Chen et al. [16] investigated the mechanical characteristics of the RAC-filled square steel tube columns using experimental research and numerical simulation. According to research findings, the bearing capacity slightly increases as the RCA replacement ratio rises. The failure mode of square steel tubes filled with RAC is comparable to that of square steel tubes filled with natural concrete. The compressive performance strength of steel tube columns filled with RAC under axial compression was investigated by Wang et al. [17]. The study's findings indicate that RACFST columns' compressive performance strength has decreased by less than 10%. In material tests, the strength reduction of the RACFST columns is less than that of the RAC samples. Tang et al. [18]'s study compared the seismic performance of steel tubes filled with natural concrete and those filled with RAC. This demonstrates that the seismic performance of the steel tube columns filled with RAC is comparable to that of the corresponding columns filled with natural concrete. The RAC-filled steel tube columns have a greater lateral bearing capacity and better ductility than the equivalent naturally concrete-filled steel tubular columns.

The home interior layout is restricted by the traditional square and rectangular section columns that protrude from the wall. A unique-shaped column made of square steel tubes filled with concrete (SCFST) can be concealed in a wall to increase the interior utilization space (Fig.1).

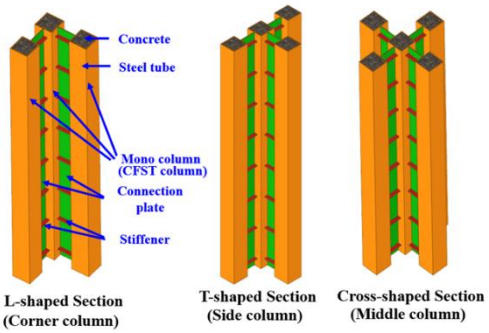

Fig. 1 The pecial-shaped column

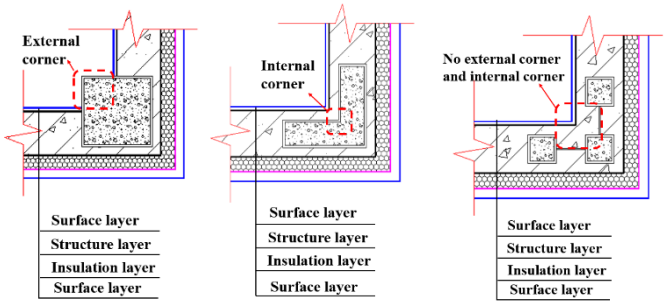

Fig. 2 The comparison of different types of columns

The L-shaped column comprises three square steel tubes filled with concrete that are joined together by stiffeners and connection plates. Connection plates' restricting impact on mono columns cannot be disregarded. The L-SCFST avoids internal corner folding compared to the L-shaped steel tube section column and does not lead to stress concentration (Fig.2).

Square concrete-filled steel tubular special-shaped (SCFST) column research has been conducted, but all of it is based on examining naturally concrete-filled square steel tubes. It was studied by Rong et al. [19–22] for its compressive properties under axial loads. The failure modes were also studied. The two types of failure that can occur in specimens with different slenderness ratios are strength failure and stability failure. The mechanical characteristics of hollow steel tubular special-shaped columns and SCFST columns were compared by Zhou et al. [23]. According to the study's findings, the SCFST's stiffness and bearing capacity are better than those of the hollow steel tube specimens. But its ductility was diminished. The eccentric mechanical behavior of the L-SCFST with various eccentricities was studied by Xu et al. [24]. The findings indicate that the specimen's bearing capacity decreases with increasing specimen eccentricity. The mechanical behavior of L-shaped columns made up of steel tubes filled with concrete that are connected by double vertical steel plates was investigated by Xiong et al. [25–27]. The findings demonstrate that the specimen transitions from a failure due to strength to an instability failure as the slenderness ratio increases under axial compression. The specimen's bearing capacity will significantly decrease as the eccentricity increases under the influence of the load.

The SCFST columns have great potential and can be used extensively in residential construction, whereas the RAC has not been employed to study behavior. The advantages of steel tubes and RAC can be fully utilized by recycled aggregate concrete-filled square steel tubes (RACFST); therefore, suggested in this paper. It can efficiently conserve indoor space, achieve resource recycling, encourage the transformation of buildings into low-carbon structures, and bring about the green development of buildings.

This study examined an L-shaped column of square steel tubes filled with recycled aggregate concrete (L-RACSFT). The L-RACFST columns, which are in a bidirectional bias state, are typically used as corner columns in engineering. The mechanical characteristics of the L-FACFST under eccentric compression are examined in this paper using various RCA displacement ratios. The effects of steel strength, steel ratio, eccentricity, and other factors on the mechanical properties of the L-RACFST columns are investigated through numerical simulation. The study's findings may serve as a theoretical basis for the L-RACFST columns' engineering design.

2. General situation of experiment

2.1. Specimens design and manufacture

The average building's story height in actual engineering is 3 m. The specimens created for this paper are limited by the test environment and are reduced by half scale, with the column height being taken as 1.5 m, the mono column's width being 100 mm, and its thickness being 3.75 mm. The connection plates have a 100 mm width and a 3.75 mm thickness. In Fig.3, the specimens' sizes are depicted. The specimens' ends' welding steel plates were measured as 20 mm. On the top steel plate, the load is applied. One hollow steel tube column was made as the comparison specimen to study how the RAC affected steel tubes. Table1 contains a list of the specimens' details. The L-RACFST columns' specifications also apply to hollow steel tube columns, except that no RAC is contained within them. The samples underwent a 28-day natural curing process. If the RAC sinks, it must be smoothed out with expanded mortar before welding the top cover plate.

Table 1
The specimens parameters

Specimens	Replacement ratio of RAC	Steel tube $h\times l\times t$ (mm)	Connection plate $l\times t$ (mm)	Eccentric distance(mm)
P40-0	0%	1500×100×3.75	100×3.75	40
P40-20	20%	1500×100×3.75	100×3.75	40
P40-40	40%	1500×100×3.75	100×3.75	40
P40-60	60%	1500×100×3.75	100×3.75	40
P40-80	80%	1500×100×3.75	100×3.75	40
P40-100	100%	1500×100×3.75	100×3.75	40
P40-K	--	1500×100×3.75	100×3.75	40

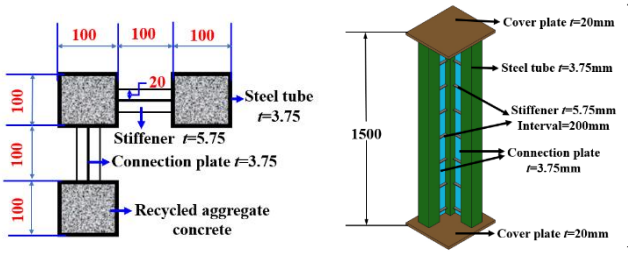

Fig. 3 Details of the L-shaped column (in mm)

2.2. Material properties

C30 natural concrete was used in this paper to form recycled aggregate concrete (RAC) using various ratios of recycled coarse aggregate (RCA) in place of natural coarse aggregate. Q235 is the strength grade of the steel, while to test the characteristics of RAC, concrete cubes were constructed.

Steel tubes, connection plates, and stiffeners were used as the sources for the samples of steel used to measure the properties of steel material. Additionally, the static test was used to determine the mechanical properties of the specimens subjected to the eccentric load discussed in this paper. Therefore, the RAC's strength and elastic modulus are primarily considered. This paper's material property test procedure follows the reference [28]. Three cubic blocks (100mm×100mm×100mm) and three prism blocks (150mm×150mm×300mm) for each RCA replacement ratio of RAC were tested to reduce the test error according to specification GB/T50081 [29]. The characteristics of RAC are listed in Table 2. Where $f_{c,cube}$ denotes the RAC's compressive strength in cubic units; $f_{c,prism,}$ shows RAC's compressive strength in prismatic units; and E_c represents the RAC's elasticity modulus. The strength and elastic modulus of the RAC gradually decline as the replacement ratio of the RCA rises. Table 3 provides a list of the steel's characteristics. Where $\boldsymbol{t}$ represents steel thickness, $\boldsymbol{f_y}$ denotes yield strength, $\boldsymbol{f_u}$ defines ultimate strength, and $\boldsymbol{E_s}$ indicates elastic modulus.

The reference[28] specifies the proportion of recycled concrete in the mix.

Table 2
The mechanical properties of RAC

Replacement ratio of RAC	$f_{c,cube}$(MPa)	$f_{c,prism}$(MPa)	E_c(MPa)
0%	33.36	26.7	32964
20%	29.00	25.8	23064
40%	17.59	14.0	13722
60%	13.30	12.2	14369
80%	11.94	10.0	10345
100%	8.99	8.4	9912

Table 3
The properties of the steel coupons

Material	t(mm)	f_y(MPa)	f_u(MPa)	E_s(MPa)
Steel tube	3.75	269	445	208,305
Connection plate	3.75	258	402	186,208
Stiffener	5.75	372	467	187,355

2.3. Loading point location

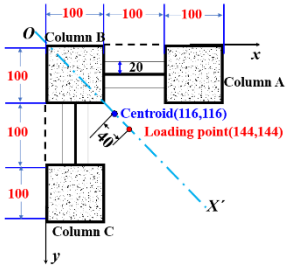

Fig. 4 Position diagram of the centroid and loading point(in mm)

The L-shaped columns, which have a bidirectional bias state, are typically used as corner columns. The ox's loading point was chosen for this study because it can recognize that the specimens are biased in both directions. The bearing capacity and ductility do not significantly decrease when the eccentricity is greater than 80 mm, according to the research findings of reference [24]. While studying the mechanical characteristics of the L-RACFST columns under various eccentricities, this paper uses the position with an eccentricity of 40 mm as the eccentric loading point and compares it to reference [28]. Fig. 4 depicts the loading point's position diagram. According to the source [28], the axial position of test specimens is calculated.

2.4. Experimental equipment and scheme

A 500T electro-hydraulic servo pressure test machine serves as the experimental apparatus. The L-RACFST column was placed on the pressure test machine's bottom plate and lined up its loading position with the machine's. While maintaining alignment between the pressure test machine's loading position and the special-shaped column's loading point, the L-RACFST column under the loading beam machine is prepared for loading. The L-shaped column has hinges at the top and bottom. The spherical hinge device, shown in Fig. 5, releases the restraint.

There are two stages to the loading process:

(1) Preloading: While ensuring the proper operation of the test machines, a preload of 100 kN was applied and maintained for 10 minutes. After that, the specimens were unloaded for formal loading.

(2) Formal loading: The method of gradual loading is used. A 200 kN force-controlled interval load was used and kept constant for 10 minutes before the specimens yielded. When the specimen yields, the loading is reduced by 100 kN in each successive step, and displacement control is applied.

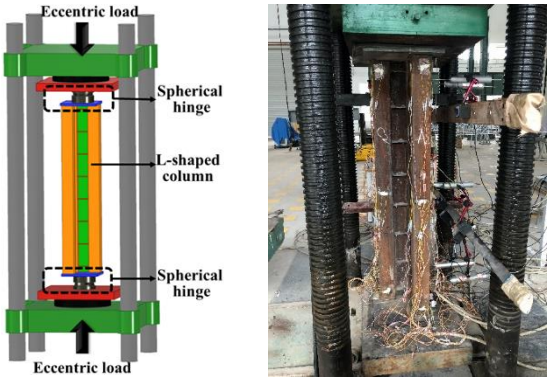

(a) Loading diagram (b) On-site photo

Fig. 5 Experimental equipment

2.5. Measurement arrangement

(1) Strain: The three mono columns were set up with strain gauges to measure the lateral and vertical strain of the steel tubes at the measurement points (see Fig. 6a).

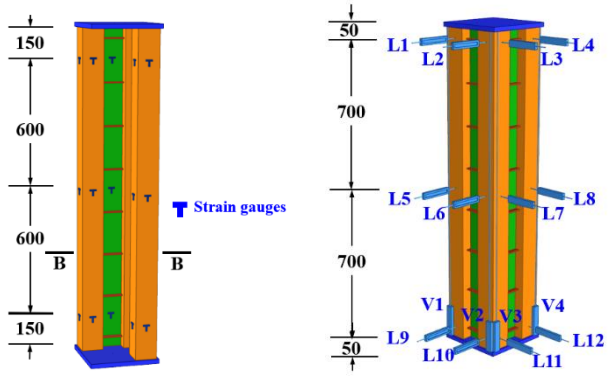

(a) Strain gauges (b) LVDT

Fig. 6 The layout of the measurement

(2) Displacement: Linear variable displacement transducers (LVDTs) are used to measure displacement. Twelve lateral LVDTs measured the specimens' lateral displacement at the column's top, middle, and bottom (L1-L12). Four vertical LVDTs (V1-V4) were used to measure the column's vertical displacement, as shown in Fig. 6(b).

3. Analysis of experimental phenomena and results analysis

3.1. Experimental phenomena

Similar experimental phenomena are observed in L-RACFST columns with various RCA replacement ratios. This suggests that the RCA's replacement ratio has little influence on experimental phenomena. The L-RACFST columns are bent and deformed with an angle to the weak axis. Both side mono columns (columns A and C) have distorted in a nearly symmetrical pattern. In general, column A and column C's deformation is greater than the corner mono column (column B). Local buckling of the specimens occurred within half of the top portion of the columns when the replacement ratio of RCA was 0% and 20%, respectively. Local buckling happened at the specimens' top or bottom when the RCA replacement ratio was greater than 40%. This is because the RAC filled in the steel tubes has low strength and high brittleness when the replacement ratio of RCA is greater than 40%. When the specimens are first loaded, the large cracks or compression will cause the RAC inside the steel tubes to quickly leave the work. Due to the lack of an effective RAC support inside, the top steel tubes would then buckle. However, the RAC filled inside the steel tubes has high strength and good ductility when the replacement ratio of RCA is between 0% and 20%. The steel tubes and the RAC filled inside of the steel tubes were stressed simultaneously during the initial stage of load application. The steel tubes are now holding the RAC in place to prevent it from being crushed. Meanwhile, the steel tubes' local buckling can be postponed by the RAC's efficient support for them. As the load grows, a portion of the RAC inside the steel tubes will separate from the work and become ineffective at supporting the steel tubes, which will cause localized buckling of the tubes. It is important to note that no local buckling on the surface joined to the connection plate, demonstrating that the stiffeners and connection plates increase the specimens' stiffness. During the test, it was discovered that some connecting plates were deformed along with the specimens' overall deformation, but this deformation had no impact on the specimens' overall deformation. The global instability failure of the L-RACFST columns is the last.

Local steel tube buckling is what ultimately causes hollow steel tubes to fail. This is due to the steel tubes' weak compression strength and the lack of an effective RAC support inside the hollow steel tubes. Thus, when the steel tubes experienced local buckling, the specimen could not support the load indefinitely, leading to ultimate failure. According to this, the RAC inside the steel tubes keeps them from buckling inward and improves the stiffness of the L-RACFST columns. Fig.7 depicts the L-RACFST columns' failure mode.

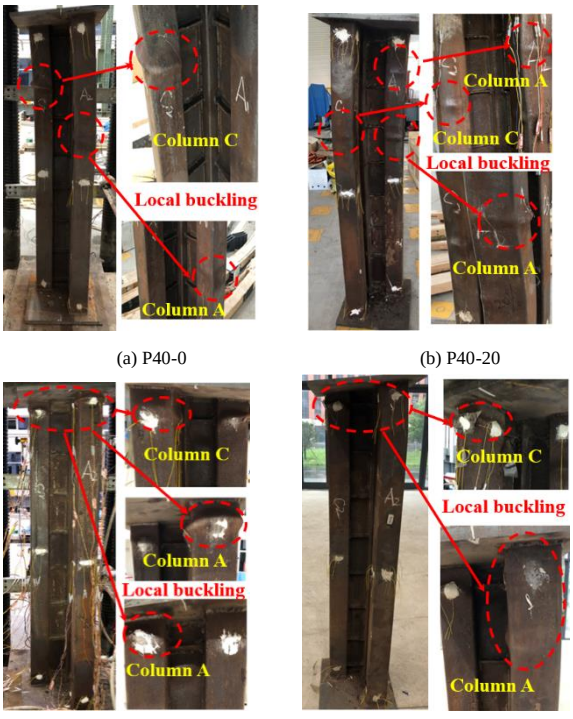

(a) P40-0 (b) P40-20

(c) P40-40 (d) P40-60

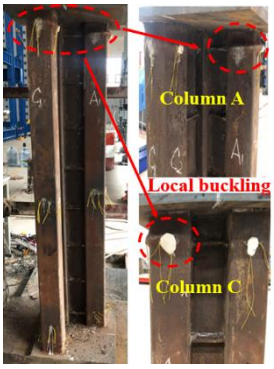

(e) P40-80

(f) P40-100

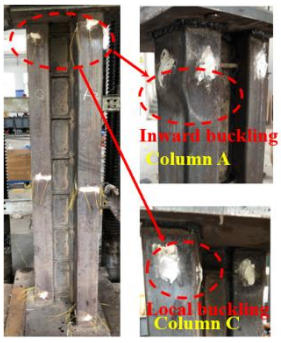

(g) P40-K

Fig. 7 Failure mode of the L-RACFST columns

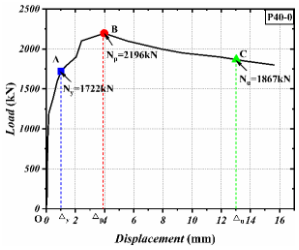

(a) P40-0

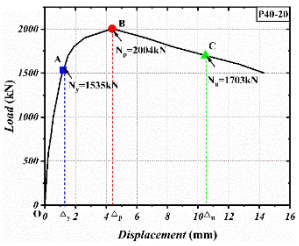

(b) P40-20

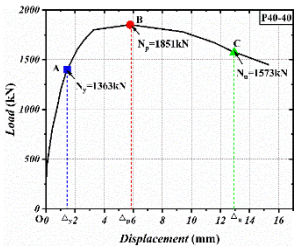

(c) P40-40

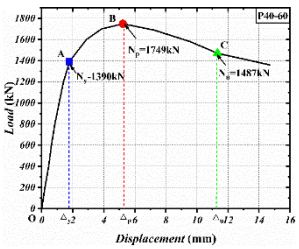

(d) P40-60

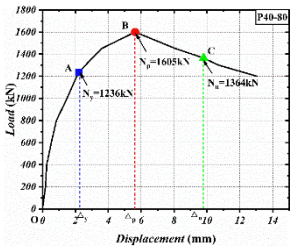

(e) P40-80

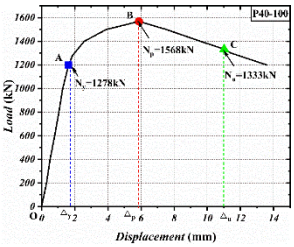

(f) P40-100

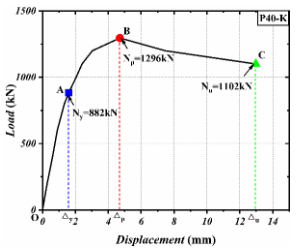

(g) P40-K

Fig. 8 Load-displacement curve

Fig. 8 displays the load-displacement curves. The yield load is denoted by A, the peak load point is pointed at B, and the ultimate load point is C. The "farthest point method" can determine the yield load point, which is the critical point between the elastic and elastic-plastic stages [30]. The test procedure can be divided into three stages, as shown by the curve: the elastic, elastoplastic, and plastic stages.

(1) Elastic state (OA section) is the region from the initial loading to the yield load. The load-vertical displacement curve exhibits linear behavior at this point. The RAC and steel tubes operate separately and without interactions. Vertical deformation is present in RAC and steel tubes alike. The connection plate does not restrain the steel tubes. In Fig. 9(a), the deformation diagram is displayed.

(2) Elastoplastic stage (AB section) extends from yielding to the peak load. The load-displacement curve exhibits a softening behavior at this point. The steel tubes and RAC interact; as the lateral deformation of the concrete increases, the steel tubes are constrained from buckling inward. The steel tubes also prevent the RAC from producing excessive deformation, which delays the crushing process. Numerous stress redistribution processes between steel tubes and RAC culminate in deformation coordination. The connection plate also restrains the steel tubes. In Fig. 9(b), the deformation diagram is displayed.

(3) Plastic stage (BC section) occurs when the load starts to decline after reaching its ultimate load. The load-displacement curve displays a descending branch at this point. Higher stress causes the RAC to deform significantly and become crushed. Depending on the RAC failure mode, there are various supporting effects on the steel tubes. As a result, the L-RACFST columns' plastic section is unique.

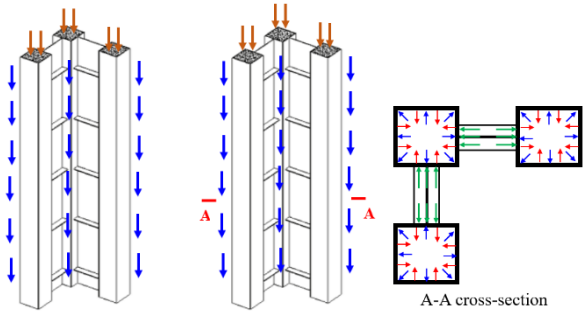

(a) Elastic stage (b) Elastoplastic stage

Fig. 9 Deformation diagram

The L-RACFST columns enter the failure stage immediately during the test when the replacement ratio of RCA is greater than 40%. It suggests that the ductility is deteriorating. The reason is that the strength and elastic modulus of the RAC gradually decrease as the replacement ratio of the RCA rises. As a result, as the load increases, the maximum load that the RAC inside the steel tubes can support gradually declines. Additionally, the steel tubes' ability to support a load for a shorter period decreases as RAC strength increases inside the steel tubes. The load-vertical displacement curve analysis's findings align with the phenomena observed in experiments.

3.2. Analysis of the experimental results

3.2.1. Bearing capacity

Table 4 displays the feature points of the load displacement data. The peak load gradually decreases as the replacement ratio of RCA rises. The reduction ratio of load of the L-RACFST columns compared to the specimen with a 0% RCA replacement ratio is shown in Table 5. Fig. 10 depicts the bearing capacity change curve with the replacement ratio change. The yield load and peak load decreased by 15.71% and 20.85%, respectively, as the replacement ratio of RCA increased from 0% to 40%. However, the RAC's cubic compressive strength fell by 47.27%. Peak load decreased by 28.60%, and yield load by 25.78% as the replacement ratio of RAC increased from 0% to 100%. However, the RAC's cubic compressive strength dropped by 73.05%. It is clear that RAC materials' strength reduction is much greater than the strength reduction of L-RACFST columns. This demonstrates that when RAC is injected into steel tubes, the steel tubes will restrain the RAC, allowing the benefits of both steel tubes and RAC to be utilized.

The yield load and peak load of the L-RACFST columns decrease more quickly when the RAC replacement ratio is higher than 40%, as seen from a comparison of the load value results.

Table 4
The load and displacement information of the specimens

Speci-mens	Yield point		Peak point		Ultimate point		*DI*	S_y
	Δ_y /mm	N_y /kN	Δ_p /mm	N_p /kN	Δ_u /mm	N_u /kN		
P40-0	1.01	1722	3.97	2196	13.03	1867	12.90	1705
P40-20	1.20	1535	4.39	2004	10.45	1703	8.71	1279
P40-40	1.35	1363	5.78	1851	12.95	1573	9.59	1010
P40-60	1.79	1390	5.23	1749	11.12	1487	6.21	777
P40-80	2.20	1236	5.63	1605	9.80	1364	4.45	562
P40-100	1.86	1278	5.88	1568	11.02	1333	5.92	687
P40-K	1.59	882	4.71	1296	12.97	1102	--	--

Table 5
The date of the specimens(comparison with P40-0)

Speci-mens	N_y /kN	Reduce proportion	Np /kN	Reduce proportion	N_u /kN	Reduce proportion
P40-0	1722	--	2196	--	1867	--
P40-20	1535	10.86%	2004	8.74%	1703	8.78%
P40-40	1363	20.85%	1851	15.71%	1573	15.75%
P40-60	1390	19.28%	1749	20.36%	1487	20.35%
P40-100	1278	25.78%	1568	28.60%	1333	28.60%
P40-K	882	48.78%	1296	40.98%	1102	40.97%

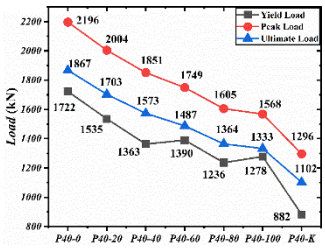

Fig. 10 Bearing capacity

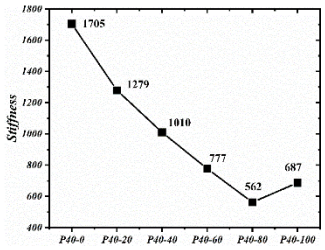

Fig. 11 Stiffness

3.2.2. stiffness

The ability of a material to resist elastic deformation when applied with force is referred to as stiffness. It represents the difficulty of elastomeric material deformation. The stiffness performance of the specimens in this paper is described using the secant stiffness (S_y) coefficient.

In Equation (1), where y is the vertical displacement of the specimens when the load reaches the yield load, the secant stiffness (S_y) of the yield point was used to characterize the stiffness of the L-RACSFT columns.

N_y is the specimens' yield load.

$$S_y = \frac{N_y}{\Delta_y} \tag{1}$$

Table 4 displays the S_y data. Fig. 11 depicts the stiffness coefficient-displacement ratio curve. The stiffness decreases by about 41% as the RCA replacement ratio rises from 0% to 40%. The stiffness decreases by about 60% as the RAC replacement ratio increases from 0% to 100%. The L-RACFST column's stiffness (RCA replacement ratio of 0%) is lower than the L-SFCST column's stiffness. The stiffness of the L-RACFST columns gradually decreases as the replacement ratio of RCA rises. This demonstrates that the specimens' resistance to elastic deformation is weaker the higher the replacement ratio of the RCA of the RAC. This is because the RAC's ductility in steel tubes decreases, and its exit from service accelerates with increasing RCA replacement ratios.

3.2.3. ductility

When a material exhibits ductility, it can fully exert its plastic deformation capacity while maintaining its bearing capacity even after it has reached its yield load. Evaluating the structure's seismic performance is very important. In this paper, the ductility performance of the specimens is described using the Secant Ductility Index (DI).

The secant ductility index (DI), which is defined as Equation (2), is used to characterize the ductility of the L-RACFST columns.

$$DI = \frac{\Delta_u}{\Delta_y} \tag{2}$$

where, Δ_u denotes axial shortening at the ultimate load. Δ_y represents vertical displacement at the yield load.

Fig. 12 displays the ductility index-displacement ratio curve. The L-RACFST columns are less ductile than the L-SFCST ones. The ductility decreases by about 54% as the replacement ratio of RCA rises from 0% to 100%. When the load reaches its peak during the test for the specimen with a 20% replacement ratio of RCA, the application speed of the load is not well controlled, leading to low ductility of the specimen, which is a test error.

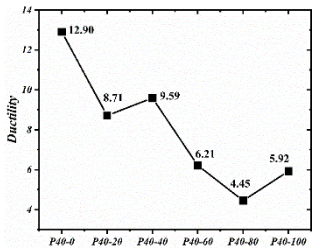

Fig. 12 Ductility

3.2.4. Strain analysis

The bottom or top of the mono column was where the specimens' maximum strain position occurred. This is essentially consistent with where each test specimen's maximum deformation occurred during the test procedure. Fig. 13 provides the lateral and longitudinal strain curves for each local measurement point of the specimens. The main test deformation points and the strain measurement points are both nearby. Analysis of the steel strain during the specimen's failure is possible. The steel is in the elastic stage at the initial loading stage, and the strain increased linearly with the eccentric load at that stage, according to the trend of the eccentric load-strain curve. Under an eccentric load, steel tubes underwent elastic deformation. The specimen started to experience significant deformation during the elastoplastic stage, and the steel's plasticity peaked. As a result, the eccentric load-strain curve's slope was reduced. Local yielding of the steel tube is earlier than specimen yielding when combined with specimen yielding load. The positions of the maximum lateral and longitudinal strains of the L-RACFST columns with various RCA replacement ratios are nearly identical, as shown in Fig. 13. Except for the specimens with a 60% RAC replacement ratio, the L-RACFST columns' maximum lateral and longitudinal strains all occurred at the same location. Even though there could have been some test errors, they also happened at the top of the specimen. The L-RACFST columns' maximum strain position matches the experimental phenomenon.

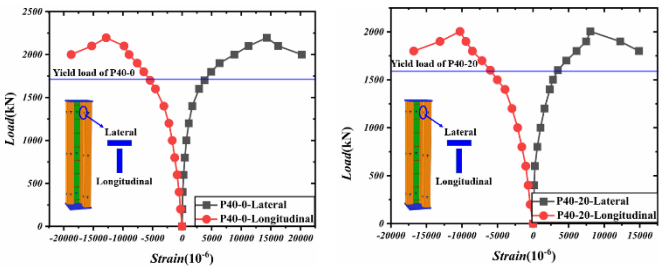

(a) P40-0 (b) P40-20

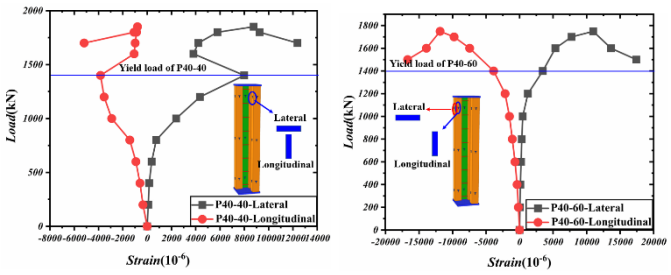

(c) P40-40 (d) P40-60

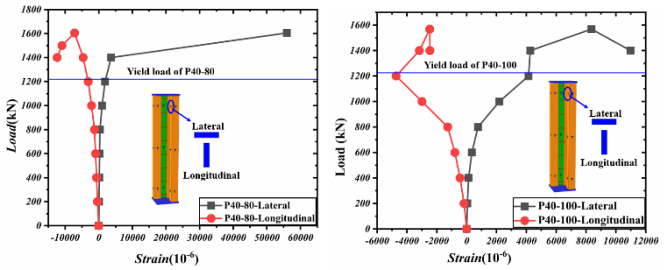

(c) P40-80 (d) P40-100

Fig. 13 The eccentric load–strain curve

3.2.5. The effect of the eccentricity

Reference [28], which the authors also published, contains the test results on L-RACFST columns with an 80mm loading eccentricity. In order to determine the impact of the eccentricity, the test results of specimens with a 40mm eccentricity were compared with the reference data. In Fig. 14, the comparison curve is displayed. It is evident that as eccentricity increases, the specimens' peak loads gradually decrease. This makes sense because a higher eccentricity corresponds to a higher bending moment and a lower axial load capacity.

Additionally, the specimens' stiffness curve gradually declines when the RCA replacement rate exceeds 40%. Although the ductility curve has no clear-cut law, when the replacement ratio of RCA is greater than 40%, the ductility generally decreases slowly. This is due to the test error of the specimen with a 20% replacement ratio of RCA.

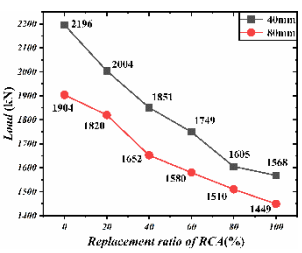

(a) Load comparison

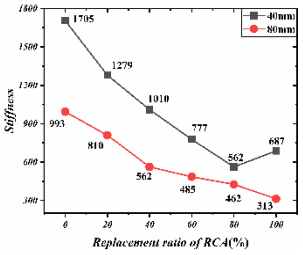

(b) Stiffness comparison

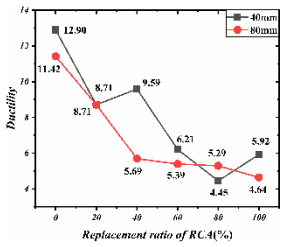

(c) Ductility comparison

Fig. 14 The comparison curve

4. Numerical simulation

4.1. Numerical models

The finite element analysis program ANSYS was used in this study to simulate the test procedure and the behaviors of the columns. The stiffeners, connection plates, and steel tubes were all modeled using SHELL181 elements. The RAC was modeled using SOLID65 details. Steel tubes and RAC adopted "surface to surface contact," which are TARGE170 and CONTAL173 elements. Due to the incomplete filling of the RAC, the production, and the transportation of the specimens, the initial imperfection of the specimens is the deviation from the ideal situation, which is caused by the initial bending and welding residual stress. In this study, the initial imperfection of the specimens is set at 1/1000 of the eigenvalue buckling analysis result. The modeled method cited an earlier source[28].Through mesh sensitivity analysis, in order to balance the calculation accuracy and speed, the SHELL181 elements size is determined as 10mm×10mm, and SOLID65 elements size is determined as 30mm×30mm×30mm.The friction coefficient adopted between the contact elements is 0.4[30]. All nodes' degrees of freedom in the X, Y, and Z directions were constrained at the bottom of the L-RACFST columns. All nodes had fixed X and Y degrees of freedom at the top of the L-RACFST columns. The finite element model is displayed in Fig. 15. In the modeling [31-33], the constraining effect of steel tubes on concrete was considered. The RCA of reference [34] constitutive relationship was used.

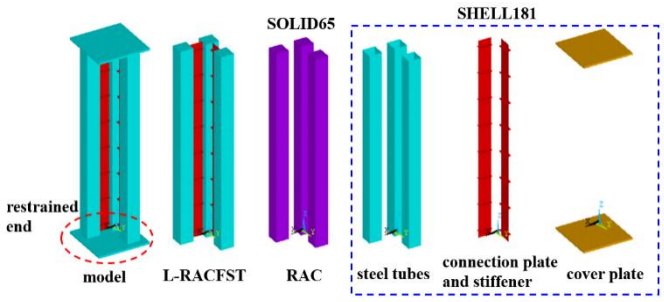

Fig. 15 Finite element models

4.2. The comparison of the failure mode

Fig. 16 depicts the comparison diagram of specimen failure modes. The failure modes of the specimens in both FEM and testing were similar and involved bending deformation of the specimens around the weak axis. The specimens' side mono columns (columns A and C) in FEM exhibit symmetrical deformation, and their side mono columns' deformation is greater than their corner mono columns' (column B). Additionally, the specimens' local buckling positions were comparable. It suggests that the failure mode of the test can be accurately simulated using the FEM.

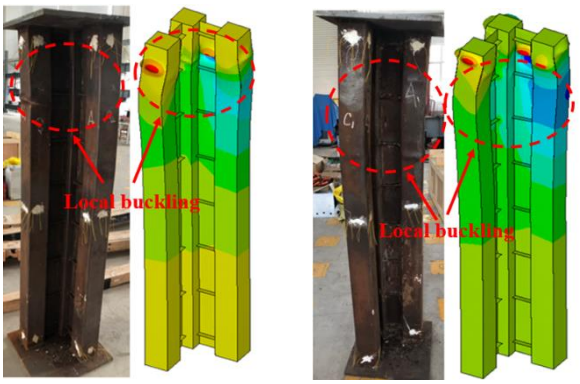

(a) P40-0 (b) P40-20

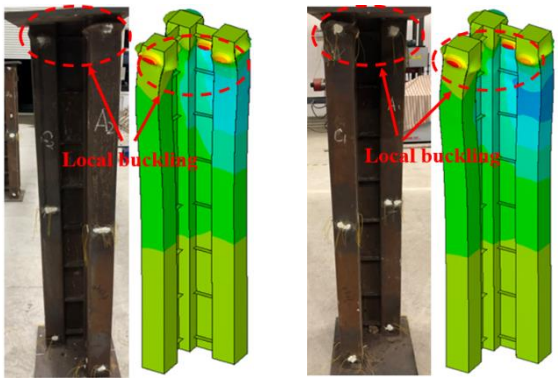

(c) P40-40 (d) P40-60

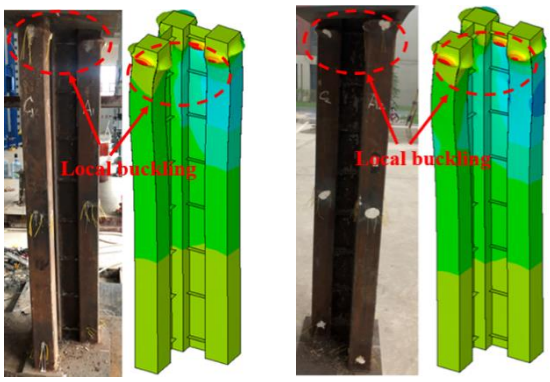

(e) P40-80 (f) P40-100

Fig. 16 Comparison of the failure mode

4.3. Bearing capacity comparison

Table 6
The load value information

Speci-mens	Yield load		$N_{y\text{-FEM}}/N_{y\text{-test}}$	Peak load		$N_{p\text{-FEM}}/N_{p\text{-test}}$
	$N_{y\text{-FEM}}$ (kN)	$N_{y\text{-test}}$ (kN)		$N_{p\text{-FEM}}$ (kN)	$N_{p\text{-test}}$ (kN)	
P40-0	1630	1722	0.95	2251	2196	1.03
P40-20	1568	1535	1.02	2095	2004	1.05
P40-40	1385	1363	1.02	1896	1851	1.02
P40-60	1353	1390	0.97	1781	1749	1.02
P40-80	1226	1236	0.99	1659	1605	1.03
P40-100	1191	1278	0.93	1617	1568	1.03
MV			0.98	*MV*		1.03

The load-displacement comparison curve is shown in Fig. 17. The specimen load value information is displayed in Table 6. As can be seen, the yield load and peak load average errors are within acceptable bounds at 0.98 and 1.03, respectively. These facts suggest that the numerical simulation technique used in this paper can accurately model the L-RACFST columns' capacity for eccentric compression.

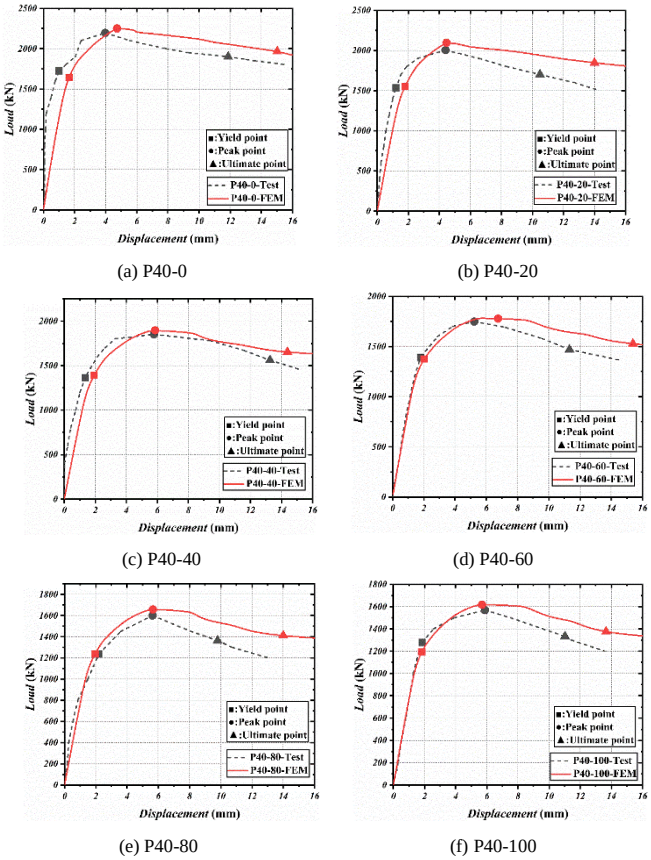

(a) P40-0 (b) P40-20

(c) P40-40 (d) P40-60

(e) P40-80 (f) P40-100

Fig. 17 Comparison of the load-displacement curve

5. Parametric analysis

5.1. The steel strengths effect

This section discusses the impact of the steel strength grades Q235, Q345, Q390, Q420, and Q460 on the specimens' bearing capacity. Fig. 18 depicts the load-steel strengths curve for the specimens. As steel strengths rise, the specimen's bearing capacity also gradually rises. The bearing capacity of the specimens increased by about 35% as steel strength increased from Q235 to Q460. This is because the stronger the steel's tensile strength, the stronger the steel tubes' restraint effect on the RAC, and the steel tubes' improved compressive strength, which increases the specimen's bearing capacity.

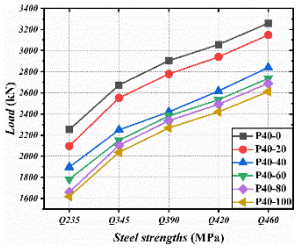

Fig. 18 Load-steel strengths curve

5.2. The steel ratio effect

In this paper, the steel thickness is changed to alter the steel ratio of the specimens. Equation (3) was used to define the steel ratio (D_r).

$$D_r = \frac{A_c}{A_s} \tag{3}$$

where, A_c denotes RAC area and A_s defines steel tube area.

When the steel ratio is altered, the steel tubes, connection plates, and stiffeners also change in thickness. The steel ratio of a mono column is calculated to be 14.44%, 28.60%, 41.48%, 53.08%, and 63.40%, respectively. The steel tubes have a thickness of 3.75, 7.75, 11.75, 15.75, and 19.75mm. The load-steel ratio curve of the specimens is shown in Fig.19 when the steel ratio varies. The bearing capacity of the specimens with replacement ratios of 0% and 100% increased by 175% and 282%, respectively, as the steel ratio increased from 14.44% to 63.40%. It is evident that the specimens' bearing capacity gradually increases as the steel ratio rises. This shows that the restraint effect of steel tubes on RAC is improved as steel tube thickness increases. This is because steel tubes get thicker, their restraining impact on the RAC becomes stronger, and their compressive strength increases, increasing the specimen's bearing capacity.

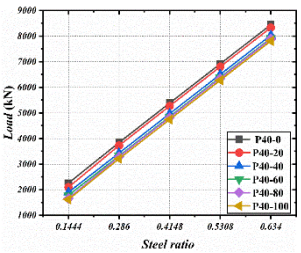

Fig. 19 Load- steel ratio curve

5.3. The effect of the connection plates width

The connection plates in this section are 100, 150, and 200 mm wide. Fig. 20 depicts the load-connection plate width curve. It is evident that the specimens' bearing capacity slightly increases as the connection plate's width increases. This suggests that the connection plate's primary function is to support the steel surface of its connecting surface and increase its stiffness, but that it has little bearing on improving the specimens' bearing capacity. This is because connecting plate width increases, and connecting plate thickness remains constant. This may result in a slight improvement in the stability of the connecting plate, which in turn may result in a slight improvement in the supporting effect of the connecting plate on the mono column, which in turn may result in a slight improvement in the carrying capacity of the L-RACFST columns.

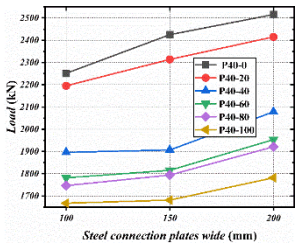

Fig. 20 Load- steel connection plates wide curve

6. Conclusions

Compared to a hollow L-shaped column, the eccentric compression behaviors of specimens with various RCA replacement ratios were investigated in the current research. The specimens' mechanical properties are simulated and examined using the validated numerical simulation. Following is an overview of the study's findings:

(1) Elastic stage, elastoplastic stage, and plastic stage under eccentric load were the three stages of the L-RACFST columns' testing procedure. The specimens tend to enter the plastic stage instantly, revealing a lower degree of ductility when the RCA replacement ratio is greater than 40%. The overall instability failure of the L-RACFST columns is the ultimate failure, and the replacement ratio of RCA has little bearing on the ultimate failure mode. Localized buckling inward and outward of the steel tubes leads to the failure mode of the hollow L-shaped column.

(2) The specimens' bearing capacity decreases with an increase in the replacement ratio of RCA. The specimens' bearing capacity degrades more quickly when the RCA replacement ratio exceeds 40%. The specimen with a replacement ratio of 100% has a bearing capacity reduction of about 29% compared to the specimen with a replacement ratio of 0%.

(3) The L-RACFST columns' ductility and stiffness gradually decline as RCA's replacement ratio rises; the decline rate is slower when RCA's replacement ratio is higher than 40%. The ductility coefficient decreased by 54%, and the stiffness coefficient decreased by 60% as the replacement ratio of RCA increased from 0% to 100%.

(4) As eccentricity rises, the L-RACFST columns' bearing capacity gradually declines. This is also supported by the research findings of reference [28].

(5) Although the connection plate increases the stiffness of the steel tubes, this has little impact on the specimens' ability to support more weight. The L-RACFST columns' bearing capacity can be enhanced by using the engineering design technique of increasing steel strength and ratio. It is not advised to make the connection plate wider to improve the bearing capacity of the specimens.

(6) When taken into account with the reference [28], it is preferable in engineering for the replacement ratio of RCA in the L-RACFST columns to be lower than 40%.

References

[1] Etxeberria M , E Vázquez, A Marí, et al. influence of amount of recycled coarse aggregates and production process on properties of recycled aggregate concrete[J]. Cement & Concrete Research, 2007, 37(5):735-742.

[2] Corinaldesi V , Moriconi G . Influence of mineral additions on the performance of 100% recycled aggregate concrete[J]. Construction & Building Materials, 2009, 23(8):2869-2876.

[3] Xiao J Z , Jia-Bin L I , Sun Z P , et al. Study on Compressive Strength of Recycled Aggregate Concrete[J]. Journal of Tongji University, 2004, 32(12):1558-1561.

[4] Olek, Jan, Behnood, et al. Predicting modulus elasticity of recycled aggregate concrete using M5 ' model tree algorithm[J]. Construction and Building Materials, 2015.

[5] Wdeeing P A，Rasheeduzzafar，Khan A. Recycied concrete-a source for new aggregate. Cement Concrete and Aggregates，1984，6（1）：17-23.

[6] Ridzuan A R M, Ibrahim A, Ismail A M M, et al. Durablity performance of recycled aggregate concrete. Achieving Sustainability in Construction,2005(7):193–202.

[7] Huda S B , Alam M S . Mechanical and Freeze-Thaw Durability Properties of Recycled Aggregate Concrete Made with Recycled Coarse Aggregate[J]. Journal of Materials in Civil Engineering, 2015, 27(10):04015003.

[8] Mahmood W , Khan A U R , Ayub T . Mechanical and Durability Properties of Concrete Containing Recycled Concrete Aggregates[J]. Iranian Journal of Science and Technology, Transactions of Civil Engineering, 2021:1-20.

[9] Shi X S , Wang Q Y , Qiu C C , et al. Experimental Study on the Properties of Recycled Aggregate Concrete with Different Replacement Ratios from Earthquake-stricken Area[J]. Journal of Sichuan University(Engineering ence Edition), 2010, 42:170-176.

[10] Huang Y , Xiao J . Seismic behavior and damage assessment of recycled aggregate concrete-filled steel tube columns[J]. Tongji Daxue Xuebao/Journal of Tongji University, 2013, 41(3):330-335+354.

[11] Mohanraj E K , Kandasamy S , Malathy R . Behaviour of steel tubular stub and slender columns filled with concrete using recycled aggregates[J]. Journal of the South African Institution of Civil Engineering, 2011, 53(2):31-38.

[12] A W L , B Z L A , C Z T , et al. Mechanical behavior of recycled aggregate concrete-filled steel tube stub columns after exposure to elevated temperatures - ScienceDirect[J]. Construction and Building Materials, 2017, 146:571-581.

[13] Liu W , Cao W , Zhang J , et al. Mechanical Behavior of Recycled Aggregate Concrete-Filled Steel Tubular Columns before and after Fire[J]. Materials, 2017, 10(3):274.

[14] Liu, Feng, Liao, et al. Seismic performance of recycled aggregate concrete-filled steel tube columns[J]. Journal of Constructional Steel Research, 2017.

[15] Dong J F , Wang Q Y , Guan Z W . Structural behaviour of recycled aggregate concrete filled steel tube columns strengthened by CFRP[J]. Engineering Structures, 2013, 48:532-542.

[16] Chen Z P , Chen X H , Ke X J , et al. Experimental study on the mechanical behavior of recycled aggregate coarse concrete-filled square steel tube column. IEEE, 2010.

[17] Wang Y , Jie C , Yue G . Testing and analysis of axially loaded normal-strength recycled aggregate concrete filled steel tubular stub columns[J]. Engineering Structures, 2015, 86(mar.1):192-212.

[18] Tang Y C , Li L J , Feng W X , et al. Seismic performance of recycled aggregate concrete–filled steel tube columns[J]. Journal of Constructional Steel Research, 2017, 133:112-124.

[19] Chen Z H , Rong B , Fafitis A . Axial compression stability of a crisscross section column composed of concrete-filled square steel tubes[J]. Journal of Mechanics of Materials and Structures, 2010, 4(10):1787-1799.

[20] B. Rong, Z. Chen, A. Fafitis, N. Yang. Axial Compression Behavior and Analytical Method of L-Shaped Column Composed of Concrete-Filled Square Steel Tubes[J]. Transactions of Tianjin University, 2012(03):180-187.

[21] Chen Z , Rong B . Research on axial compression stability of L-shaped column composed of concrete-filled square steel tubes[J]. Building Structure, 2009.

[22]B. Rong, Z. Chen, T. Zhou. Research on axial compression strength of L-SHAPED short column composed of concrete-filled square steel tubes[J].Industrial Construction 2009, 39(11), 104.

[23] Zhou T,Chen Z ,Liu H. Seismic behavior of special shaped column composed of concrete filled steel tubes[J]. Journal of Constructional Steel Research, 2012, 75(75):131-141.

[24] Xu M , Zhou T , Chen Z , et al. Experimental study of slender LCFST columns connected by steel linking plates[J]. Journal of Constructional Steel Research, 2016, 127(DEC.):231-241.

[25] Xiong Q , Chen Z , Zhang W , et al. Compressive behaviour and design of L-shaped columns fabricated using concrete-filled steel tubes[J]. Engineering Structures, 2017, 152(dec.1):758-770.

[26] Liu J , Zhou T , Lei Z , et al. Eccentric compression performance of slender L-shaped column composed of concrete-filled steel tubes connected by steel linking plates[J]. Journal of Constructional Steel Research, 2019, 162(Nov.):105675.1-105675.16.

[27] Chen Z , Liu J , Zhou T , et al. Uniaxial Eccentric-Compression Performance Analysis for Double-Plate Connected Concrete-Filled Steel-Tube Composite Columns[J]. Journal of Structural Engineering, 2020, 146(8):04020161.

[28] Ma,T.;Chen,Z.;Du,Y.;Zhou,T.;Zhang,Y.Mechanical Properties of L-Shaped Column Composed of RAC-Filled Steel Tubes under Eccentric Compression .Metals2022,12,953. https://doi.org/10.3390/met12060953

[29] GB/T 50081-2019, Standard for test methods of concrete physical and mechanical properties, Standardization Administration of China, 2019.

[30] Du Y , Zhang Y , Chen Z , et al. Axial compressive performance of CFRP confined rectangular CFST columns using high-strength materials with moderate slenderness[J]. Construction and Building Materials, 2021, 299(4):123912.

[31] Yang Y, Han L. Compressive and flexural behaviour of recycled aggregate concrete filled steel tubes (RACFST) under short-term loadings[J].Steel & Composite Structures,2006, 6 (3): 257-284.

[32] Yang Y. Theoretical research on load-deformation relations of recycled aggregate concrete-filled steel tubular members[J]. Industrial Construction,2007, 37 (012): 1-6.

[33] Xiao J, Lan Y. Investigation on the Tensile Behavior of Recycled Aggregate Concrete [J].Journalof building materials,2006 (02): 154-158.

[34] Li J,Chen Z,Du Y,et al.Study on constitutive model of core concrete of recycled aggregate concrete filled steel tubular columns under compression[J].Industrial Construction, 2021,51(05):108-115+15.